Investigations of Nonlinear Optical Effects and Ultrafast Laser Induced Plasma in Nanostructured Media

by

Suchand Sandeep C. S.

Thesis submitted to the Jawaharlal Nehru University
for the award of the degree of
Doctor of Philosophy

Raman Research Institute
Bangalore – 560 080
March 2010

DECLARATION

I hereby declare that this thesis is composed independently by me at the Raman Research Institute, Bangalore, under the supervision of Dr. Reji Philip. The subject matter presented in this thesis has not previously formed the basis of the award of any degree, diploma, associateship, fellowship or any other similar title.

Suchand Sandeep C. S.

CERTIFICATE

This is to certify that the thesis entitled ***"Investigations of Nonlinear Optical Effects and Ultrafast Laser Induced Plasma in Nanostructured Media"*** submitted by Suchand Sandeep C. S. for the award of the degree of DOCTOR OF PHILOSOPHY of Jawaharlal Nehru University is his original work. This has not been published or submitted to any other university for any other degree or diploma.

Prof. Ravi Subrahmanyan	Dr. Reji Philip
(Center Chairperson)	(Thesis Supervisor)
Director	Associate Professor
Raman Research Institute	Raman Research Institute
Bangalore – 560080	Bangalore – 560080

Acknowledgements

The years I spent at RRI, I am sure, would count among the most important phases of my life. Over and above the good fortune of working in my field of interest, the deep rooted fascination I acquired towards it over the years leaves me with a sense of happy contentment, for which I feel totally indebted to Reji. His quality of being a thorough and meticulous experimentalist has never failed to impress me. He has been a kind and considerate mentor all throughout, providing support and encouragement in matters relating to the lab, career and personal life. His sweet way of dealing with people has deeply influenced me. Another of his very unique traits which I cannot but mention is his very neat sense of humour. I remember the many evening tea sessions, made vibrant by his presence. He was an integral part of my Bangalore life and I am extremely thankful to him for being the fabulous guide that he was and an absolute friend!

It is always nice to be part of a group, and I feel very privileged to have belonged to the LAMP group. I cherish the bourgeoning interactions I had with the group members. I express my heartfelt thanks to Hema for her solid support and encouragement. Also to Andal, for her insightful thoughts and advices. I feel very lucky to have had someone so pleasant, caring and encouraging as her, in my advisory panel. My thanks, also to Sadiq, for the fruitful discussions I was pleased to have with him. I am very thankful to Ravi, the institute director, for his encouragement and support rendered during the course of my stay at RRI.

I am thankful to Pratibha, who was in my advisory committee, for the valuable suggestions and encouragement that helped me a lot. My heartfelt thanks to Udayashankar for his ever encouraging words. I remember the fun time I had with him during the shooting of a small scientific movie for the Agastya Foundation. I thank Lakshminarayanan for his wise advices and well wishes. My special thanks to Prof. Madhusudhana, for introducing me to the wonderful field of liquid crystals and recommending me for the Italian MIUR project with Prof. F. Simoni. My thanks to K. A. Suresh and N. Kumar for the motivational discussions.

I am thankful to Prof. T. Pradeep for kindling my fascination to the world of nanoscience and nanotechnology. I remember with gratitude the warm hospitality rendered to me during my various visits to his lab. My special thanks to prof. Simoni, for introducing me to the field of NLO of liquid crystals. The project work under his guidance was a warm experience, as well as the comfortable and enjoyable stay in Italy.

I am very much indebted to GRK, DM and MK for initiating my fascination with high intensity laser field studies. The VSRP project I did in the Atmol group of TIFR was the turning point in my career. Thanks to all Atmol group members, especially, Vinod, Rajeev, Anand, Sandhu and Aditya. I thank Prof. C. Vijayan for introducing me to the attractions of nonlinear optics. I am thankful to Prof. T. S. Natarajan, my mentor during my MSc days for the confidence he had in me. My thanks also to Prof. V. P. N. Nampoori, who helped me with insightful suggestions during my second year comprehensive viva.

I remember with gratitude the many useful discussions I had with many caring professors, including Prof. D. V. G. L. N. Rao, Prof. D. N. Rao, Dr. Sainath, and Prof. Thyagarajan.

I thank all my collaborators. P. M. Ajayan, B. Karthik, Eswaramoorthi, P. A. Joy, M. R. Anantharaman, A. V. Adhikari, V. Kumar, B. L. V. Prasad, Liana Luchetti, K. Nandakumar, D. P. Mahapatra, K. S. Shankunni, K. Chandrashekaran, Umesh, Joseph, Adarsh, and Sreekumar are some who necessarily require mention. The student collaborators I have worked with include Sreekumaran Nair, Shibu, Nuja, Pramod, Manjunatha, Muthukumar, Shivarama Krishnan, Sai Krishna, Samal, Virginia, Ambika, Venkatesan, Narayanan, Shijumon, Swapna, Rani and Bobby. It was a refreshing experience working with you all.

My special thanks to Krishna, the administrative officer, RRI, for the various helps received from him. Thanks to Marisa and Radha who are in administrative charge of the efficient running of the PhD program. I also thank Ram Subrahmaniyam for the various helps rendered. I thank everyone in the purchase department, for the valuable help given. I thank the library staff for maintaining the very good and comfortable library.

My thanks to all staff in the computer section, accounts, stores, reception, canteen, and above all, the security. Special thanks to Mr. Jayaraman for the wonderful job done and keeping RRI a very safe place.

I thank the workshop staff, who transformed the designs given them into reality with precision. Special thanks to Narayanaswami, Achankunju, and Mohandas for their extremely skilled jobs. Also, thanks to Dasan of the glass blowing section, Ram, and Mani for helping out with occasional jobs. My thanks also to the E & B section, especially Sasidharan, who came to our rescue many times.

I remember with gratitude and pleasure the time spent with Anija, Jinto and Karthik. They were the 'all-in-all' of the lab. They were more like my family. Anija was like my sweet and caring sister, who was my strong support and help in my initial days at RRI. Her brilliant way of dealing with problems has impressed me many times. I thank Karthik for his ever-appreciating good nature. His enthusiasm about his work, no matter how small, I think, is something worth assimilating. Jinto, my senior since my MSc days, has been a source of wonderful company and help. I admire him for the cleverness and sincerity that he puts into every job. His enthusiasm that never wanes is another quality I admire.

My grazie to Ricardo, Francesco, Agneese, Matteo, Daniele, Luigino, Karen, Kato, and Oda for making my life outside India very memorable. I enjoyed the time spent with you immensely, and the quality scientific contributions have been an asset!

Among the many important others who made my life at RRI most pleasant and memorable include Augustine, Smijesh, Subhadra, Preethi, Jimmy, Nadeer, Deepthi, Prakash, Remya, Sindhya, Rossamma, Priya, Sunita, Deepa, Arun Kumar, Ajesh, Kishore, Aravindan, Aparna, Anand, Benoy, Mohesh, Sreekanth, Aasif, Milan, Naresh, Balamurugan, Vinitha, Sunil, Archana, Ajit, Sreeranjini, Ravi, Ceegan, Praveen, Manu, Vaishakh, Nimi, Sanjay, Sundar, Raghavan, Lakshmi, Dhanalakshmi, Yaser, Nithin, Rahul, Revathi, Arthur, Bushra, Harsha, Bejoy, Soumya and many others. I remember the enjoyable time spent with you in gratitude!

My batchmates, seniors, and juniors were an integral part of my RRI life. From the campus to the hostel, the life with you has been wonderful. I thank my seniors Kripa, Arun, Ganesh, Vishwa, Reshmi, Chandreyee, Navinder, U. Khan, Divya, Amit, Atish, and Dipanjan for their love and support. My special gratitude to my batchmates, Rahul, Raju, Alpana, Shanthanu, and Mohanpriya. I remember with pleasure the great times I had with my junior friends, SeungHyun, Jyothi, Shabeeb, Suresh, Sijo, R. K, Rakesh, Nagu, Bhibhu, Bharat, Satyam, Madhukar, Ravi, Radhika, K. L. P, Swaminathan, Piyush, Deepak, Nandan and Hari.

Special thanks to Prabhu, Nagaraj, Meena, Poornima, Latha, and Harini for their valuable help with the administration and technical works.

Shiva and Manju are real assets to the group! I thank them for the tremendous help they provided throughout.

I thank Preetha, Niranajan, Nirmal, and parents of Preetha and Reji for their wonderful hospitality and love, for including me as one among the family. I truly cherish my time spent with you all.

I thank my little puli sisters, Lakshmi, Sonia and Rose for being the life and energy of the lab during my thesis writing. Without you three the thesis wouldn’t have taken this form.

I thank all my teachers, from primary school to date. I owe a lot to them as it is their care, love and constant encouragement that helped me to reach where I am today.

My big thanks to my little brother, Sangeeth. He has been a pillar of constant support. In no words can I express my deep gratitude and love to my parents. They have always been there for me, whenever in need. I can proudly say that the best assets that I have in my life are my brother and my parents. Without them this thesis would have never become a reality. Finally, thanks to all my friends who have been a part of my life, who have made me what I am.

TABLE OF CONTENTS

1. Introduction

2. Nonlinear optical properties of metal nanoparticles and nanowires

3. Fine structure in spatial self-phase modulation patterns: at a glance determination of the sign of optical nonlinearity in highly nonlinear films

6. X-ray emission from ultrafast laser induced plasma in planar liquid jets

7. X-ray emission from ultrafast laser induced plasma in a Nickel target

Synopsis

The interaction of electromagnetic radiation with matter is the basis of most of the processes observed in nature, and this phenomenon has always aroused the curiosity of mankind. Under ordinary circumstances the optical properties of a material remain unchanged, regardless of the intensity of light falling on it. However, this is not true at higher intensities where the optical properties become a function of the input light intensity. With the development of science and technology newer sources of light as well as novel forms of matter have emerged, enabling a deeper study of light-matter interaction. Advances in laser technology during the last two decades have resulted in lab-scale, tabletop lasers which routinely generate pulses few-femtoseconds in duration and multi-terawatt in peak power. This has opened up new domains for scientific exploration by accessing the exotic aspects of light-matter interaction at high intensities. Moreover, in addition to providing rich scientific insights, the interaction of intense laser pulses with solids, liquids and gases have many technological applications as well.

Ultrafast light bursts, comprising a few oscillation cycles of electromagnetic fields, even with relatively low pulse energy, when focused, give rise to unprecedented light intensity levels with extreme temporal resolution. A light pulse is termed ultrashort (or ultrafast) if its temporal duration is less than a picosecond. At moderate intensities ($< 10^{12}$ W/cm^2) the electric field of the interacting electromagnetic radiation is much weaker than the static atomic Coulomb fields. In this regime the atomic quantum states get only moderately perturbed for non-resonant excitations, and resonant electron excitation is characterized by bound-bound transitions. Conventional Nonlinear Optics deals with optical processes in this regime. Light intensities larger than 10^{12} W/cm^2 are considered intense, whose electric field is strong enough to affect most atomic and molecular systems non-perturbatively. At intensities above 10^{14} W/cm^2 electrons are liberated from atoms and molecules by multi-photon excitations and tunneling through the Coulomb barrier. Higher fields suppress the Coulomb barrier potential further and free the bound electrons to the continuum over the barrier. Under such high irradiation matter will exist in the ionized state, known as plasma.

In this thesis, an experimental investigation of the interaction of moderately intense and intense laser pulses with novel forms of matter, namely metal nanostructures and plasmas, is presented. Initially, the nonlinear optical properties of metal nanostructures are investigated using moderate intensity laser pulses. A new method for estimating the sign of refractive optical nonlinearity in a nonlinear film using a CW laser is then presented. The use of white-light z-scan for measuring the spectral dispersion of optical nonlinearity in a silver nanoparticle solution is discussed afterwards. Later on, the focus of the study shifts to the application of intense laser pulses for creating plasmas in solid and liquid targets, and their spectroscopic study in the x-ray region. For the experiments, we used a He-Ne laser, 7 ns laser pulses from an Nd:YAG laser, and 300 ps, 20 ps and 100 fs laser pulses made available from an ultrafast Ti:Sapphire laser.

A general introduction to the nonlinear optical properties of matter in a strong laser field is presented in chapter 1. Depending on the light intensity the medium shows a nonlinear response that is either moderate or extreme. In this chapter various nonlinear processes such as sum frequency generation, harmonic generation, parametric amplification, optical Kerr effect, optical phase conjugation, stimulated Raman and Brillouin scattering and multiphoton absorption are briefly mentioned. The chapter gives a brief overview of the generation of ultrafast laser pulses. Q-switching and mode-locking methods are discussed. The chirped pulse amplification (CPA) technique used for amplifying ultrafast pulses is explained. Applications of ultrashort laser pulses like ultrafast spectroscopy and TeraHertz frequency generation are mentioned. Furthermore, a general description of intense laser-matter interaction and some of the fascinating applications are presented in this chapter.

A study of the nonlinear optical properties of metal nanoparticles and nanowires is presented in chapter 2. Nanostructures are of interest in optics, and metal nanostructures in particular, because of the surface plasmon resonances they exhibit in the visible region of the electromagnetic spectrum. Various mechanisms controlling the nonlinear light transmission, like saturable absorption, two- and three-photon absorption and reverse saturable absorption are discussed initially. Subsequently, the nonlinear transmission behaviour of Ag@ZrO_2-PVA nanocomposites, and Te and Ag_2Te nanowires, measured by the z-scan technique, are discussed in detail. These results show that metal nanostructures possess a large potential for optical limiting applications. In general, the combination of different limiting mechanisms improves the overall limiting performance. The excellent optical limiting properties of nanoparticle-embedded solid-state thin films indicate the possibilities of the design and fabrication of commercially viable optical limiters. Towards the end of the chapter, measurement of the third order nonlinear susceptibility ($\chi^{(3)}$) of silver nanoparticles using the degenerate four-wave mixing (DFWM) experiment in the folded boxcars geometry is discussed. Results show that silver nanoparticles have very good figure of merit (F) values for third order optical nonlinearity.

In chapter 3, a fast and simple method to determine the sign of the nonlinear coefficient n_2 in films with high nonlinearity is presented. The technique is similar to the conventional z-scan, except that no aperture is necessary here to determine the sign of the refractive nonlinearity. The method can be considered as a 'visualization' of the z-scan technique for highly nonlinear films. It exploits the effect of spatial self-phase modulation (SPM) and the role of wavefront curvature that leads to a specific far field pattern that is dependent on the sign of n_2. When a Gaussian laser beam passes through a thin nonlinear medium like a liquid crystal, the laser beam can induce an unusually large refractive index modulation due to molecular reorientation, and the far field pattern appears as a set of concentric bright and dark diffraction rings. Since the number of SPM principal rings is directly related to the value of the induced birefringence, the method proposed allows a simple evaluation of both the sign (by means of the SPM fine structure) and the magnitude (by counting the SPM principal rings) of n_2. The method is independent of the type of nonlinearity that causes the ring pattern, as demonstrated by our measurements in different types of nematic cell, and is expected to work for every kind of highly nonlinear medium.

Chapter 4 discusses a recent application of the femtosecond white-light continuum (WLC) for measuring the spectral dispersion of optical nonlinearity in materials. The dispersion of the two-photon absorption coefficient in the 500-700 nm region in silver nanoparticles is measured using this method. Nonlinear phenomena like self-phase modulation, stimulated Raman scattering, cross- and induced-phase modulation and self-focusing are responsible for WLC generation in a nonlinear medium. When projected onto a screen, the femtosecond continuum appears to the eye as a white disk, often surrounded by a distinct concentric rainbow-like pattern. White-light continuum finds potential applications in femtosecond time resolved spectroscopy, optical pulse compression, seeding of optical parametric amplifiers, optical coherence tomography, frequency metrology, and linear and nonlinear microscopy. Of the several liquid media we investigated for generating white-light continuum, CCl_4 and water are found to be the most efficient. Normalized z-scan curves for a range of wavelengths (500-700 nm) are obtained for silver nanoparticle samples from a single open aperture WLC z-scan. The experimental data obtained is successfully fitted to the standard nonlinear transmission equations, and the dispersion of the two-photon absorption coefficient in the wavelength range studied is determined.

The laser system and the diagnostic equipment used for plasma investigations are discussed in detail in chapter 5. The equipment include the ultrafast CPA laser system (Ti:Sapphire), high vacuum chamber, solid target manipulator, target motion controller, mechanical laser pulse picker, X-ray and -ray detectors, and multichannel analyzer. At high laser intensities, air itself will act as a nonlinear medium, and hence a vacuum environment is essential for background free measurements. Our vacuum chamber is provided with a differential pumping arrangement, and can be pumped to a pressure of 10^{-6} Torr. The intensity autocorrelation method for pulse width measurement, knife-edge technique and imaging for beam spatial profile determination, calibration of the x-ray and γ-ray detectors, and time-gating of the detectors also are discussed in this chapter.

In chapter 6, the plasma experiments conducted in thin planar liquid jets in ambient conditions are discussed. Intense electromagnetic radiation is known to emanate from laser-produced plasmas. Laser-produced plasma is thus a compact source of pulsed radiation, and can be extended to a wide variety of industrial and scientific applications. In this chapter we discuss the spectroscopic study of x-ray emission from an ultrafast laser-induced plasma, generated in thin planar liquid jets of approximately 250 μm thickness. Laser pulses of 100 fs duration are focused to the jet to obtain intensity levels close to 10^{16} W/cm^2. Tunnel ionization is the dominant ionization mechanism at this intensity regime. A general description of various mechanisms leading to plasma production by ultrafast laser pulses is presented. Some important physical parameters of the plasma like Debye length and plasma frequency are explained. Energy transfer mechanisms like inverse Bremsstrahlung, resonance absorption and vacuum heating are discussed. Plasma experiments conducted in thin planar liquid jets of pure de-ionized water, a colloidal solution of silver nanoparticles, and an aqueous solution of silver nitrate are presented. Results show that even in the absence of a vacuum, it is possible to get a substantial amount of soft x-rays from an ultrafast laser-produced plasma. A novel way of enhancing the x-ray emission yield and emission energy range by the incorporation of metal nanoparticles into the liquid used in the jet is presented.

The plasma experiments conducted in Nickel targets under high vacuum conditions (10^{-6} Torr) is given in chapter 7. The target is irradiated at an intensity of 10^{15} W/cm^2. The x-ray emission in the range of 30 keV to 200 keV is measured using a NaI(Tl) detector. The detector is gated in synchronization with the laser to reduce the cosmic ray background. From the x-ray spectrum obtained, the electron temperature of the nickel plasma is calculated.

Chapter 8 presents the general conclusions drawn from the work done for this thesis, and some future perspectives.

Publications

Communicated:

1. Dispersion of the optical nonlinearity in silver nanoparticles measured by the white-light z-scan technique
   C. S. Suchand Sandeep, Deepa Kamath and Reji Philip
2. Enhanced x-ray emission from ultrafast laser irradiated silver nanoparticle solutions
   C. S. Suchand Sandeep and Reji Philip

Patents:

1. An optical limiting device with the highest known laser damage threshold and method of preparation thereof.
   T. Pradeep, A. Sreekumaran Nair, Reji Philip and Suchand Sandeep C. S.
   Indian patent 1273/CHE/2005 published on 2007-07-27

Published (included in the thesis):

1. Optical limiting properties of Te and Ag_2Te nanowires
   C. S. Suchand sandeep, A.K. Samal, T. Pradeep, Reji Philip, Chem. Phys. Lett., **485**, 326 (2010).
2. Fine structure in the spatial self phase modulation pattern: at a glance determination of the sign of optical nonlinearity in highly nonlinear films
   Liana Lucchetti, C. S. Sandeep Suchand, and Francesco Simoni, Journal of Optics A: Pure and Applied Optics, **11**, 034002 (2009).

Published (not included in the thesis):

1. Study of optical properties and effective three-photon absorption in Bi-doped ZnO nanoparticles
   B. Karthikeyan, C. S. Suchand Sandeep, Reji Philip, and M. L. Baesso, Journal of Applied Physics, **106**, 114304 (2009).
2. Optical Limiting Properties of Hydrophobic Poly(etherimide) Membranes Embedded with Isolated and Aggregated Gold Nanostructures

V. D’Britto, C. S. Suchand Sandeep, R. Philip and B. L. V. Prasad, Colloids and Surfaces A: Physicochem. Eng. Aspects, **352**, 7983 (2009).

3. Synthesis and characterization of a new NLO active donor-acceptor type conjugated polymer derived from 3,4-diphenylthiophene
   Manjunatha. M. G, A. V. Adhikari, Pramod Kumar Hegde, C. S. Suchand Sandeep, and Reji Philip, Journal of Polymer Research - Online First - August 2009.
4. Nonlinear optical properties of (Pb1-xSrx)TiO3 thin films
   D. Ambika, V. Kumar, C. S. Suchand Sandeep, and Reji Philip, Applied Physics B, **97**, 661 (2009).
5. Optical characterization of a new donor–acceptor type conjugated polymer derived from 3,4-diphenylthiophene
   Manjunatha. M. G, A. V. Adhikari, Pramod Kumar Hegde, C. S. Suchand Sandeep, and Reji Philip, Journal of Maretial Science, **44**, 6069 (2009).
6. Nonlinear Optical Studies on New Conjugated Poly{2,2'-(3,4-dialkoxythiophene-2,5-diyl)bis[5-(2-thienyl)-1,3,4-oxadiazole]}s
   Pramod Kumar Hegde, A.Vasudeva Adhikari, Manjunatha. M.G, C. S. Suchand Sandeep, and Reji Philip, Accepted in Journal of Applied Polymer Science – May 2009.
7. Optical and nonlinear absorption properties of Na doped ZnO nanoparticle dispersions
   B. Karthikeyan, Suchand Sandeep C. S., T. Pandiyarajan, P. Venkatesan, and Reji Philip, Applied Physics Letters, **95**, 023118 (2009).
8. The synthesis of high coercivity cobalt-in-carbon nanotube hybrid structures and their optical limiting properties
   T N Narayanan, C. S. Suchand Sandeep, M M Shaijumon, Pulickel M Ajayan, Reji Philip, and M R Anantharaman, Nanotechnology, **20**, 285702 (2009).
9. Synthesis and nonlinear optical characterization of new poly{2,2'-(3,4-didodecyloxythiophene-2,5-diyl)bis[5-(2-thienyl)-1,3,4-oxadiazole]}
   Pramod Kumar Hegde, A.Vasudeva Adhikari, Manjunatha M.G., C. S. Suchand Sandeep and Reji Philip, Synthetic Metals, **159**, 1099 (2009).
10. Optical properties and ultrafast optical nonlinearity of Yb3+ doped Sodium Borate and Bismuthate glasses

B. Karthikeyan, C. S. Suchand Sandeep, Jaemine Cha, Hiromichi Takebe, Reji Philip, and S. Mohan, Journal of Applied Physics, **103**, 103509 (2008).

11. An optical limiter based on ferrofluids
    Swapna S. Nair, Jinto Thomas, C. S. Suchand Sandeep, M. R. Anantharaman, and Reji Philip, Applied Physics Letters, **92**, 171908 (2008).
12. Structural and non-linear optical properties of self-assembled SnO2 doped Silicon nanorings formed by pulsed laser ablation
    J. R. Rani, V. P. Mahadevan Pillai, C. S. Suchand sandeep, and Reji philp, Electrochem. Solid-State Letters, **11**, K73 (2008).
13. Optical and nonlinear optical properties of copper nanocomposite glasses annealed near the glass softening temperature
    B. Karthikeyan, M Anija, C. S. Suchand Sandeep, Muhammed Nadeer T M and Reji Philip, Optics Communications, **281**, 2933 (2008).
14. Excitonic Transitions and Off-resonant Optical Limiting in CdS Quantum Dots Stabilized in a Synthetic Glue Matrix
    Pushpa Ann Kurian, C. Vijayan, K. Sathiyamoorthy, C. S. Suchand Sandeep and Reji Philip, Nanoscale Research Letters, **2**, 561 (2007).
15. Ultrafast optical power limiting in free-standing Pt-Polyvinyl Alcohol nanocomposite films synthesized in situ
    B. Karthikeyan, M. Anija, P. Venkatesan, C. S. Suchand Sandeep and Reji Philip, Optics Communications, **280**, 482 (2007).
16. Nonlinear optical properties of MeV and keV ion beam synthesized Ag nanoclusters
    B. Joseph, C. S. Suchand Sandeep, B.R. Sekhar, D.P. Mahapatra and Reji Philip, Nuclear Instruments and Methods in Physics Research B, **265**, 631 (2007).
17. Observation of three-photon absorption and saturation of two-photon absorption in amorphous nanolayered Se/As2S3 thin film structures
    K V Adarsh, K S Sangunni, C. S. Suchand Sandeep, Reji Philip, S Kokenyesi and V Takats, Journal of Applied Physics, **102**, 026102 (2007).
18. Two-photon-assisted excited state absorption in nanocomposite films of PbS stabilized in a synthetic glue Matrix
    Pushpa Ann Kurian, C Vijayan, C. S. Suchand Sandeep, Reji Philip and K Sathiyamoorthy, Nanotechnology, **18**, 075708 (2007).

19. Sol-gel synthesis and nonlinear optical transmission in $Zn(1-x)Mg(x)O$, $(x<0.2)$ thin films
    C. S. Suchand Sandeep, Reji Philip, R. Satheeshkumar and V. Kumar, Applied Physics Letters, **89**, 063102 (2006)

1

Introduction

Light, which provides us visual information about the world we live in, has always aroused the curiosity of mankind. Under ordinary circumstances the optical properties of a material are unchanged, regardless of the intensity of light falling on it. This however is not true at higher intensities where the optical properties become a function of the input light intensity. In this chapter, the basic ideas of nonlinear optics, ultrafast laser pulse generation, and the physics and applications of the interaction of intense light with matter are discussed.

1.1 Nonlinear optics

Electromagnetic radiation interacts with matter primarily through the valence electrons in the outer orbitals {1}. This interaction creates electric dipoles leading to a macroscopic polarization of the medium. For small field strengths this induced polarization is proportional to the applied electric field. When an electromagnetic wave propagates through a dielectric medium, the electric displacement can be written as,

$$D = \varepsilon E \qquad \text{- (1.1)}$$

where ε is the permittivity tensor and E is the electric field. (The electric displacement, electric field and polarization are vector quantities. However for the sake of simplicity, they are considered as scalar quantities in the following discussion). The permittivity tensor can be written in terms of the permittivity of free space (ε_0) and relative permittivity (ε_r) as,

$$\varepsilon = \varepsilon_0 \varepsilon_r \qquad - (1.2)$$

The electric displacement can also be written as,

$$D = \varepsilon_0 E + P \qquad - (1.3)$$

where P is the electric polarization (electric dipole moment density). From the above equations, we can write,

$$P = \varepsilon_0 \left(\varepsilon_r - 1\right) E = \varepsilon_0 \chi E \qquad - (1.4)$$

where $\chi = \varepsilon_r - 1$, is called the electric susceptibility tensor (or simply electric susceptibility) of the medium. In the nonlinear regime, the expression for the polarization should be modified to a power series as {1},

$$P = \varepsilon_0 \left(\chi^{(1)} E + \chi^{(2)} EE + \chi^{(3)} EEE + ...\right) \qquad - (1.5)$$

where $\chi^{(1)}, \chi^{(2)}$, and $\chi^{(3)}$ are the linear, quadratic (second-order), and cubic (third-order) susceptibility tensors, respectively. Substitution of equation 1.5 into Maxwell's equations leads to a set of nonlinear differential equations that involve terms with high-order-powers of the optical electric field strength. These terms are responsible for various observed coherent optical frequency-mixing effects. In other words, in the nonlinear case, the re-radiation coming from the dipoles do not faithfully reproduce the sinusoidal electric field that generates them. As a result, the distorted re-radiated wave contains frequencies different from that of the original wave {2}. In sections 1.2 and 1.3, we describe some of the most commonly observed second- and third-order nonlinear optical effects.

1.2 Second-order nonlinearities

The second-order susceptibility $\chi^{(2)}$ is responsible for second harmonic generation, sum and difference frequency generation, and optical parametric amplification. The above-mentioned second-order nonlinear effects are produced by two waves, which interact to produce a third wave. Conservation of momentum and photon energy are always required in these processes. The optical fields of these waves are coupled to one another through the second-order susceptibility. The coupling provides the mechanism for the exchange of energy among the interacting fields. In centro-symmetric crystals, $\chi^{(2)}$ is zero; therefore second-order nonlinear processes are generally possible only in materials that lack inversion symmetry {3}.

1.2.1 Sum and difference frequency generation

In this process, two waves of frequencies ω_1 and ω_2 with comparable intensity interact nonlinearly to produce a wave at a third frequency ω_3. The polarization in this case can be written as,

$$P(\omega_3) = \varepsilon_0 \chi^{(2)} E(\omega_1) E(\omega_2) \qquad - (1.6)$$

where $\omega_3 = \omega_1 + \omega_2$. Similarly a wave at the difference frequency $\omega_3 = \omega_1 - \omega_2$ may also be generated ($\omega_1 > \omega_2 > \omega_3$).

1.2.2 Second harmonic generation (SHG)

This is a special case of frequency mixing in which the initial waves have the same frequency, $\omega = \omega_1 = \omega_2$ and $\omega_3 = 2\omega$. The induced polarization takes the form

$$P = \varepsilon_0 \left(\chi^{(1)} E \sin(\omega t) + \tfrac{1}{2} \chi^{(2)} EE \left(1 - \cos 2\omega t\right) + ... \right) \qquad - (1.7)$$

according to equation 1.5, with $E = E_0 \sin(\omega t)$. The presence of the second term involving 2ω in the above expression shows that a wave having twice the fundamental frequency can be formed during the nonlinear process.

1.2.3 Parametric amplification

Parametric amplification refers to the coupled growth of two waves in the presence of a strong wave, which is referred to as the pump. When a strong pump with frequency ω_P co-propagates in a nonlinear medium with a signal beam of frequency ω_S, energy from the pump gets transferred to the signal and to an idler frequency (ω_i) by difference frequency generation. The frequency relationship in such a process can be written as $2\omega_P = \omega_S + \omega_i$. For parametric amplification to occur efficiently, a phase matching condition needs to be satisfied, that depends on the propagation constants of the fields as {3},

$$\Delta k = 2k_p - k_s - k_i \qquad \text{- (1.8)}$$

where k_p, k_s and k_i are the propagation constants of the pump, signal, and idler. The refractive index inside the nonlinear material depends on the wavelength, the direction of propagation, and on the polarization of the waves. Hence it is generally possible, by using birefringence and dispersion, to find conditions under which equation 1.8 is satisfied. A key advantage of parametric amplification is its wide bandwidth. With the pump providing input at the fixed frequency, small changes of refractive index around phase matching condition will change the signal and idler frequencies such that a new phase matching condition is achieved.

1.3 Third-order nonlinearities

Third-order nonlinearities involve the nonlinear susceptibility tensor $\chi^{(3)}$ in equation 1.5. This term governs many nonlinear phenomena like third harmonic generation, optical Kerr effect, stimulated Raman scattering and stimulated Brillouin scattering. In general, $\chi^{(3)}$ couples together four frequency components: in other words, three fields interact to produce a fourth field.

$$P(\omega_4) = \varepsilon_0 \chi^{(3)} E(\omega_3) E(\omega_2) E(\omega_1) \qquad \text{- (1.9)}$$

In a lossless medium the susceptibility coefficients of $\chi^{(3)}$ are real. In this case, the primary nonlinear optical effects are the generation of new frequency components and the intensity dependent refractive index change (Kerr effect). In third-order interactions involving absorption, the imaginary part of $\chi^{(3)}$ describes Raman and Brillouin scattering and two-photon absorption {2}.

1.3.1 Third harmonic generation (THG)

The third harmonic is generated by an intense beam at frequency $\omega = \omega_1 = \omega_2 = \omega_3$ and $\omega_4 = 3\omega$. The expression of a sinusoidal electric field raised to the cubic power will include a term $\sin^3(\omega t)$ which can be written as $\frac{3}{4}\sin(\omega t) - \frac{1}{4}\sin(3\omega t)$ which indicates the creation of the third harmonic at 3ω.

1.3.2 Optical Kerr effect

The third-order nonlinearity can lead to an intensity dependence of the refractive index which is known as the optical Kerr effect. The change in refractive index is proportional to the time average of the optical field squared and is given by {4},

$$\Delta n = n_2 I(r,t) \qquad - (1.10)$$

where $I(r,t)$ is the intensity of the incident beam. The spatial part $I(r)$ gives rise to self-focusing, and the temporal part $I(t)$ gives rise to a nonlinear phase delay leading to self-phase modulation.

1.3.3 Optical phase conjugation

It is a third-order nonlinear interaction, producing a light beam that is the spatial complex conjugate of one of the waves incident on the nonlinear medium. A phase conjugate wave will have exactly the time reversed phase of the incident wave. Optical phase conjugate waves can be generated from various nonlinear optical processes such as four-wave mixing, backward-stimulated scattering, special three wave mixing in a second-order nonlinear crystal {5} etc. Because of their wavefront-reconstruction ability, the optical phase conjugation technique has several applications of which aberration correction for coherent light transmission through inhomogeneous media is the most important. In laser oscillators and amplifiers, phase conjugate mirrors can be used as the rear cavity-reflector, to give an output with higher brightness and smaller beam divergence. It is also used in cavityless devices, laser target-aiming systems, laser weapon systems, laser identification and rescue systems and laser real-time holographic systems {5}.

1.3.4 Stimulated Raman scattering (SRS)

SRS is caused by the interaction of a laser beam with the molecular vibrational modes. A pump beam of frequency ω_P drives the nonlinear interaction, to provide amplification at $\omega_P - \omega_0$, where ω_0 is the frequency of the molecular vibration. Amplification occurs due to the interaction of the Stokes photons with the laser photons in the medium, which results in the stimulation of additional Stokes photons coherent with the incident Stokes photons. SRS is used in diverse areas such as spectroscopy, coherent frequency conversion, signal amplification, beam combining, and beam cleanup {1,6}.

1.3.5 Stimulated Brillouin scattering (SBS)

Brillouin scattering is related to the interaction between an incident optical wave and the elastic acoustic wave in a transparent medium {5}. The scattered light can be thought of as a Doppler-shifted reflection from an acoustic wavefront, or as the scattering of a photon from an acoustic phonon. The frequency shift of the scattered light is dependent on the scattering angle and the acoustic velocity in the medium. In laser scattering from an acoustic disturbance, the incident laser and Brillouin scattered waves superpose to form a traveling beat wave with frequency Ω and wave vector $\mathbf{K}$, which satisfies the momentum and energy conditions, $\mathbf{k}^{'} = \mathbf{k} \pm \mathbf{K}$ and $\omega^{'} = \omega \pm \Omega$, where $\left(\omega^{'}, \mathbf{k}^{'}\right)$ represents the scattered wave and $(\omega, \mathbf{k})$ represents the incident wave. If the laser intensity is sufficiently high, this beat wave can coherently drive the acoustic wave through electrostrictive and thermal forces. The enhanced acoustic wave scatters the incident laser radiation more strongly, which in turn leads to a stronger beat wave. This mutual reinforcement results in an amplified Brillouin wave and this process is known as stimulated Brillouin scattering.

1.3.6 Two-photon absorption

Two-photon absorption (2PA) is the simultaneous absorption of two photons of identical or different frequencies in order to excite a molecule/atom from one state to another. The energy difference between the lower and upper states involved is equal to the sum of the energies of the two photons. A detailed discussion on two-photon absorption and related phenomena is presented in chapter 2.

1.4 Ultrafast laser pulse generation

Laser, an acronym for *"light amplification by stimulated emission of radiation"*, is a device that effectively makes use of the stimulated emission process, to generate intense, coherent radiation. The electromagnetic radiation thus generated is usually monochromatic, highly directional, and has a high intensity.

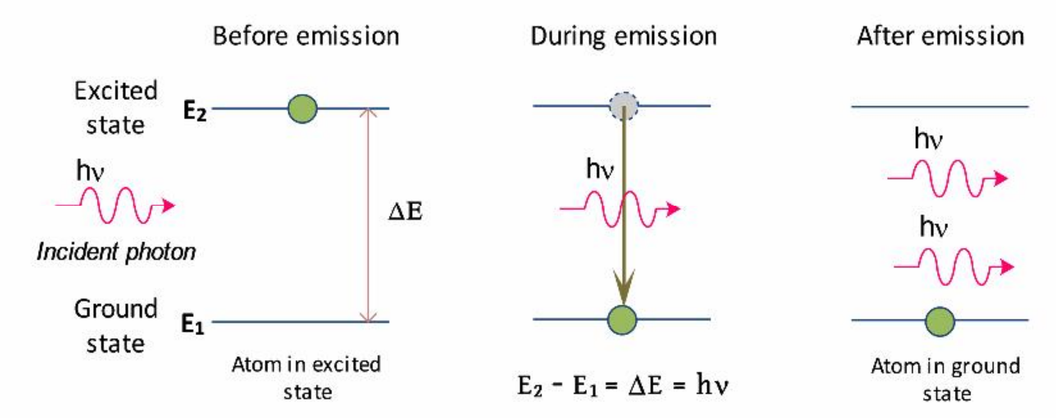

Figure 1.1: The stimulated emission process.

There are different kinds of lasers, which can amplify radiation at wavelengths ranging from the far infrared region, merging with millimeter waves or microwaves, up through the visible region and extending now to the vacuum and extreme ultraviolet (VUV & EUV), and even to the x-ray regions {7}. Lasers come in a great variety of forms, using many different laser materials, and many different kinds of pumping or excitation techniques. Broadly they can be classified into two categories, namely continuous wave (CW) lasers and pulsed lasers. Lasers can also be classified based on the active medium used, such as solid state lasers, semiconductor lasers, gas lasers etc. In the following subsection we discuss the two main techniques used to generate short and ultrashort laser pulses, namely Q-switching and mode-locking.

1.4.1 Q-switching

In the technique of Q-switching we allow a laser pumping process to build up much above the usual population inversion inside the laser cavity, while keeping the cavity itself from oscillating by removing the cavity feedback or greatly increasing the cavity losses; in effect by blocking or removing one of the end mirrors. The quality factor Q is defined as the ratio of energy stored in the cavity to the energy loss per cycle. Consequently, the higher the quality factor, the lower the losses. Thus by removing the cavity feedback, the losses are increased and the system has a low Q-value at this state. Then, after a large population inversion has been developed in the active medium, the cavity feedback is restored, or the cavity quality factor is "switched" back to its usual large value, using some suitably rapid modulation method. The result is a very short, intense burst of laser output, which dumps all the accumulated population inversion in a single short laser pulse, typically only a few nanoseconds long {8}.

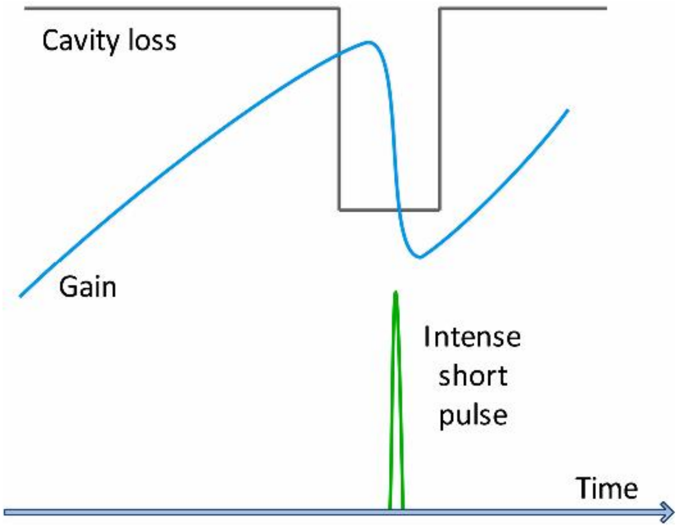

Figure 1.2: Q-switching technique used for the generation of nanosecond laser pulses.

The three most commonly used Q-switching techniques are electro-optic Q-switching, acousto-optic Q-switching and passive saturable absorber Q-switching. In electro-optic Q-switching an electro-optic modulator, consisting of an electro-optic crystal, which becomes birefringent under the influence of an applied electrical voltage, is used to introduce the controllable cavity loss. A fast high voltage signal applied across the crystal reduces the cavity losses thereby producing a short intense pulse of a few nanoseconds duration. The acousto-optic Q-switching technique makes use of an acousto-optic modulator, in which a refractive index grating produced by a radio frequency (RF) acoustic wave, Bragg-diffracts the light out of the laser cavity. Passive Q-switching uses a saturable absorber inside the laser cavity. The pumping process builds up laser inversion until the gain inside the cavity exceeds this absorption, and laser oscillation begins to develop inside the cavity. This oscillation at some relatively low level then rapidly saturates the absorber and thus opens up the cavity, leading to the development of a rapid and intense laser pulse.

1.4.2 Mode-locking

In the absence of frequency selective elements inside the laser resonator, the laser generally oscillates simultaneously on many resonator modes within the spectral-gain profile of the active medium. In this “multimode operation” no phase relations exist between the different oscillating modes. Mode-locking establishes a coupling between the phases of these simultaneously oscillating modes, resulting in a coherent superposition of the *mode amplitudes,* which leads to the generation of intense, ultrashort output pulses. Mathematically the Fourier transform of a large number of frequency components with the same phase gives an infinite series of short pulses in time {9}.

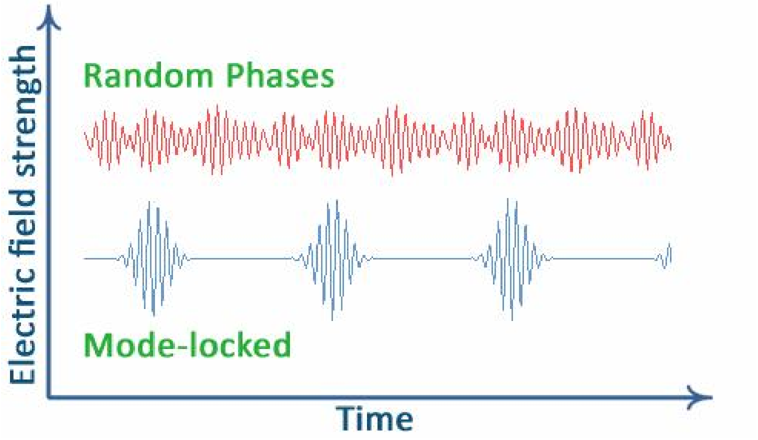

Figure 1.3: Mode-locking.

In a laser cavity, these modes are equally spaced. The electric field distribution with N such modes in phase can be written as {10},

$$E(t)=\sum_{n=0}^{N-1}E_n e^{i(\omega_0+n\Delta\omega)t}\propto\left(\frac{e^{iN\Delta\omega t}-1}{e^{i\Delta\omega t}-1}\right)e^{i\omega_0 t}=\frac{\sin(N\Delta\omega t/2)}{\sin(\Delta\omega t/2)}e^{i\omega_0 t} \qquad \text{- (1.11)}$$

where ω_0 is the central frequency and Δω is the mode spacing, given by c/2L, where L is the cavity length. In order to get a short pulse, a very large number of cavity longitudinal modes should be locked together. The shortest pulsewidth that can be achieved from a lasing medium of linewidth $\Delta\nu_g$ is $\frac{1}{\Delta\nu_g}$ {11}.

The intensity of the mode-locked output from the laser is given by,

$$I(t)=\left|E(t)\right|^2\propto\frac{\sin^2(N\Delta\omega t/2)}{\sin^2(\Delta\omega t/2)} \qquad \text{- (1.12)}$$

There are two types of mode-locking techniques in use, namely active mode-locking and passive mode-locking. In active mode-locking, an active element is inserted into the cavity, which modulates the cavity losses. This element will now introduce an amplitude modulation on each of the longitudinal modes, thereby creating sidebands. A global phase-locking will be introduced by these sidebands in the cavity ultimately leading to the mode-locking of the laser. In passive mode-locking, a saturable absorber is introduced into the laser cavity. The association of this saturable absorber with the saturable active medium leads to a natural mode-locking of the laser. Another commonly used passive method is the Kerr-lens mode-locking (KLM), which is a self-mode-locking phenomenon. KLM is based on the occurrence of self-focusing by the intensity dependent index of refraction (the Kerr effect) in the laser active medium. In this technique, the amplifying medium decreases the loss of the stronger intensity peaks of the cavity by modifying the transverse structure of the laser wave selectively with respect to the intensity {12}. A schematic of the Kerr-lens mode locking technique is shown in figure 1.4.

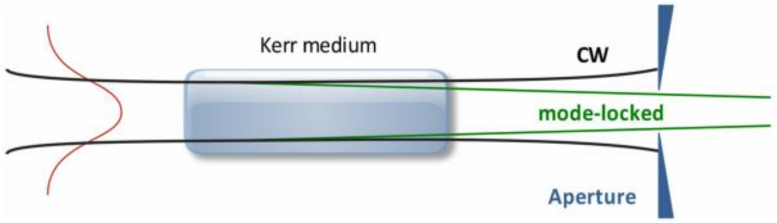

Figure 1.4: Kerr lens mode-locking.

The self-locking of modes was first observed accidentally in a laser where the amplifying medium consisted of a Ti:sapphire crystal pumped by an Ar^+ laser. It was initially called *"magic mode-locking"* but later described in terms of Kerr-lens mode-locking. As a high intensity pulse passes through the Ti:sapphire crystal, the crystal acts as a lens (Kerr lens) and self-focusing of the beam takes place. Maximum self-focusing occurs when the pulse intensity is a maximum i.e., when the laser is fully mode-locked. An aperture will be placed in the laser cavity at an appropriate position so that the cavity losses are minimum when maximum self-focusing occurs. In this condition the laser will automatically mode-lock. Thus the Kerr-lens and the aperture act together as an ideal fast saturable absorber where the saturation is produced by the intensity dependent self-focusing through a physical aperture.

As long as no sufficient intensity fluctuation occurs in the cavity to create strong Kerr-lens effects, the continuous wave (generally known as the *free-running* mode) regime prevails over the pulsed regime. So there should be an initiating mechanism, which creates an intense pulse, which triggers off the process. Usually an acousto-optic modulator is used for this purpose, which switches the laser from the free-running regime to the pulsed regime. Once the laser gets switched to the mode-locked state, the acousto-optic modulator can be turned off.

The intensity I(t) being a rapidly varying function of time, the change of refractive index as a function of intensity, following the equation $n = n_0 + n_2 I(t)$, implies a rapid change of the phase of the pulse in time. This self-modulation of the phase broadens the spectrum further, shortening the pulse more in time. However the spectral broadening enhances group velocity dispersion (GVD), as different frequencies travel at different velocities inside the laser medium. This results in a temporal broadening of the pulse. Precise balancing of self-phase modulation with

GVD gives rise to a pulse, which travels back and forth in the cavity, with its shape and size unaltered. Hence it is essential to tune the cavity GVD of Kerr-lens mode-locked lasers for reliable operation. GVD compensation is usually achieved by using a pair of prisms, or by using suitably chirped cavity end mirrors.

1.5 Amplification of ultrafast laser pulses

Amplification of ultrafast laser pulses is not an easy task as the intensities of these pulses normally exceed the damage thresholds of typical amplifying media. The technique that is widely used nowadays to overcome this issue is called chirped pulse amplification (CPA) {13}. In CPA, an ultrashort laser pulse from the oscillator is stretched in time using a pair of gratings that are arranged such that the low-frequency components travel a shorter path compared to the high-frequency components. The pulse is now positively chirped, i.e., the high-frequency component lags behind the low-frequency component, and has a longer pulse duration than the original by a factor of 10^3 to 10^5. Then the stretched pulse, the intensity of which is sufficiently low compared to the intensity limit of gigawatts per square centimeter (typical damage threshold of the active medium), is safely introduced to the gain medium and amplified by a factor of 10^6 or more. Finally, the amplified laser pulse is recompressed back to the original pulsewidth through the reverse process, i.e., by introducing a negative chirp to the pulse using a grating compressor.

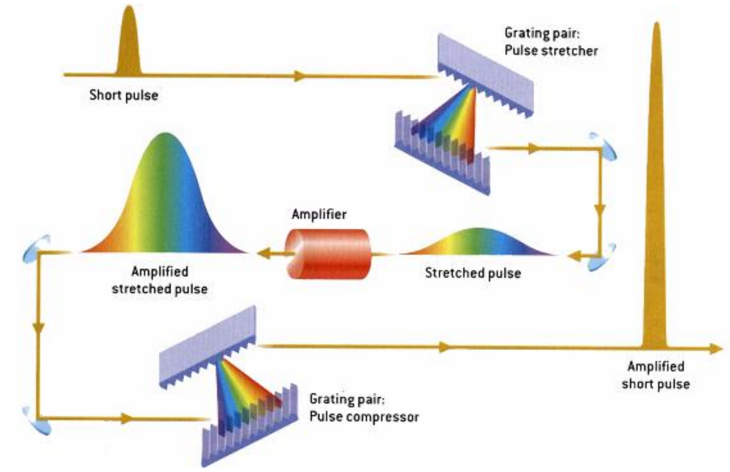

Figure 1.5: The concept of chirped pulse amplification in a solid-state amplifier. (Picture curtsy: University of Michigan)

For our experiments, we used the spectra physics Ti:sapphire oscillator (Tsunami, Spectra Physics) which is pumped by a frequency doubled CW diode pumped Nd:YVO_4 laser (Millennia Pro, Spectra Physics). The oscillator produces 100 fs laser pulses of about 1 nJ energy per pulse. The pulses are stretched to about 300 ps in an all-reflective stretcher and amplified in a regenerative cavity followed by a double-pass cavity, both of which have Ti:sapphire crystals as the gain medium. The pulse is compressed right after amplification by introducing a negative dispersion using a grating compressor. A schematic of our ultrafast CPA laser system used for the experiments is shown in figure 1.6. More details about the laser system can be found in chapter 5.

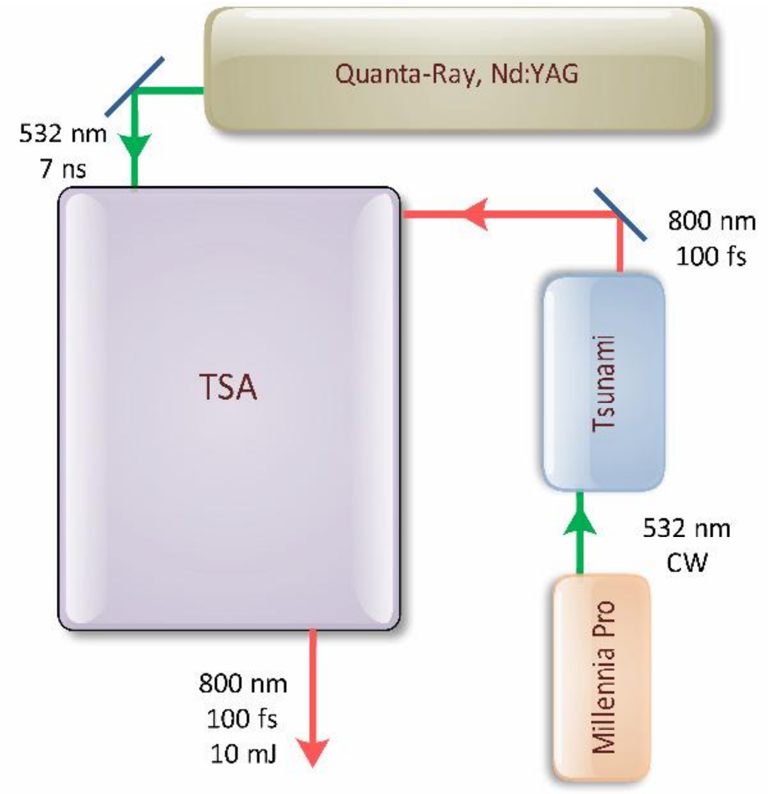

Figure 1.6: Schematic of the ultrafast CPA laser used for the experiments.

1.6 Applications of ultrafast pulses

Femtosecond laser pulses are ideal tools for investigating many ultrafast processes, such as molecular vibrations and evolution of transition states in chemical reactions {14,15}. With femtosecond pump-probe spectroscopy we can study the temporal evolution of these fundamental ultra-short processes. In this technique a powerful light pulse interacts with the sample and excites it into a non-equilibrium state. The sample thereafter relaxes towards a new equilibrium state, which can be mapped by sending a second pulse (much weaker), called a probe, onto the sample. The delayed weak pulse probes the change in the optical property induced by the pump. By varying the time delay between the pump and the probe, many material parameters such as occupation numbers, carrier density, and molecular orientation can be measured. Another technique called impulsive stimulated Raman scattering can be used to analyze vibrational motions in a material medium {16}. And of late, using femtosecond pulses, researchers have generated electro-magnetic pulses of *TeraHertz* frequency {17}. This novel source has opened completely new fields of application, for example, time resolved x-ray spectroscopy, short pulse radar, and far infrared coherent spectroscopy.

Being extremely short, femtosecond pulses can often serve to characterize the fastest electronic components where purely electronic means fail. Similarly, with femtosecond pulses very short acoustic pulses can be produced and launched into materials for diagnostic purposes. Femtosecond spectroscopy is a widely used tool for the study of complex biological and chemical systems {18}.

1.7 Intense laser-matter interaction

Nonlinear optics, discussed in section 1.1, deals with optical processes at low and moderate intensities ($< 10^{12}$ W/cm^2). The electric field of the interacting EM radiation is much weaker than the static atomic Coulomb fields in this case. Therefore the atomic quantum states are only moderately perturbed for non-resonant excitations. Bound-bound transitions are the prevailing mechanism for resonant electron excitation at these intensity levels.

The behavior of atoms in intense laser fields ($>10^{13}$ W/cm^2) is very different. In this case the electron does not remain bound and atoms begin to get ionized. The electrons released are then immediately caught in the laser field, and oscillate with a characteristic energy, which then dictates the subsequent interaction physics. There are different ionization pathways, depending on the strength of the incident electric field.

1.7.1 Multi-photon ionization

According to Einstein's theory of photoelectric effect, electrons are emitted from the surface of solids in response to the incident light when each photon carries an energy $\hbar\omega$ which matches the work function of that material {19}. But with short pulse lasers, multi-photon ionization occurs in materials, expressed by the condition $n\hbar\omega = I_p$. Instead of one very energetic photon, an electron absorbs n photons of moderate energy and is subsequently ejected. According to perturbation theory, the n-photon ionization rate is given by {20},

$$\Gamma_n = \sigma_n I_L^n \qquad \text{- (1.13)}$$

The cross section σ_n obviously decreases with n, but the I_L^n dependence ensures that an n^{th} order ionization event will eventually occur provided that the intensity is high enough (in the range 10^{13} – 10^{14} W/cm^2). This is the intensity regime between the perturbative and strong-field regimes of light-matter interaction.

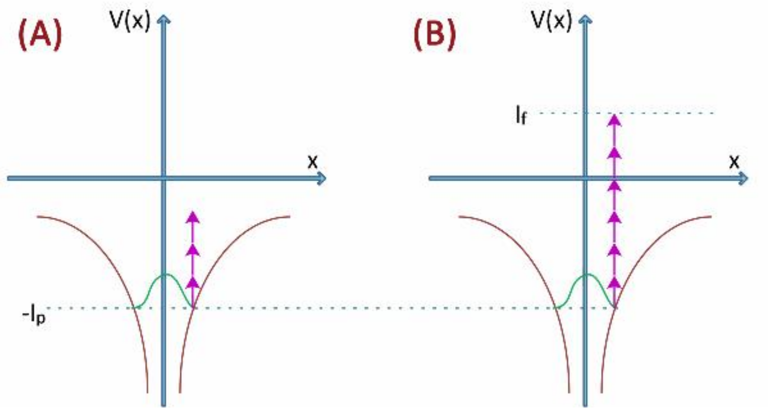

Figure 1.6: (A) Schematic of multi-photon ionization (MPI). An electron with binding energy E_{ion} simultaneously absorbs n photons and is released from the atom with minimal kinetic energy. (B) Above-threshold ionization (ATI): the electron absorbs more photons than necessary for ionization, leaving the atom with significant momentum.

This physically appealing picture went almost unchallenged until the late 1970s, when experimentally determined electron energy spectra started to reveal distinct peaks beyond the ionization energy E_{ion}, separated by the photon energy

$\hbar\omega$ {21,22}. This remarkable effect, known as *above-threshold ionization* (ATI), allows an electron to absorb more photons than strictly necessary to free it from the atom. The final kinetic energy of the electron, by an extended version of Einstein's formula, is

$$E_f = (n+s)\hbar\omega - E_{ion} \qquad \text{- (1.14)}$$

where n is the number of photons needed for multi-photon ionization and s is the excess photons absorbed. This process still conserves momentum because it takes place in the field of the parent ion.

1.7.2 Tunneling and over-the-barrier ionization

An important assumption in perturbative multi-photon ionization is that the atomic binding potential remains undisturbed by the laser field. At intensities above 10^{14} W/cm^2, the laser field becomes strong enough to distort the Coulomb field felt by the electron. This case was first considered by Keldysh (1965) {23}, who introduced a parameter γ separating the multi-photon and tunneling regimes, given by,

$$\gamma = \omega_L \sqrt{\frac{2E_{ion}}{I_L}} \sim \sqrt{\frac{E_{ion}}{\Phi_{pond}}} \qquad \text{- (1.15)}$$

where,

$$\Phi_{pond} = \frac{e^2 E_L^2}{4m\omega_L^2} \qquad \text{- (1.16)}$$

is the so called *ponderomotive potential* {24} of the laser field, expressing the effective quiver energy acquired by an oscillating electron. Tunneling and over-the-barrier processes are applied for strong fields of intensities above 10^{14} W/cm^2 for which $\gamma < 1$. For multi-photon ionization $\gamma > 1$.

In the intensity regime of 10^{14} W/cm^2 to 10^{15} W/cm^2 tunnel ionization predominates, in which the Coulomb barrier becomes suppressed due to the interaction with the strong laser field. Quantum mechanically, the electron may tunnel through this barrier with some finite probability (Given by Keldysh's formula) {25}. At still higher intensities, greater than 10^{15} W/cm^2, the electric field amplitude of the laser is so high that it suppresses the Coulomb barrier below the energy level corresponding to the binding energy of the electron. When the barrier falls below E_{ion}, the electron will escape spontaneously. This is called *over-the-barrier ionization* {26}. The minimum value of the laser field that is required for inducing over-the-barrier ionization can be obtained by equating the maximum value of the modified atomic potential, in the presence of the laser field, to the binding energy of the electron.

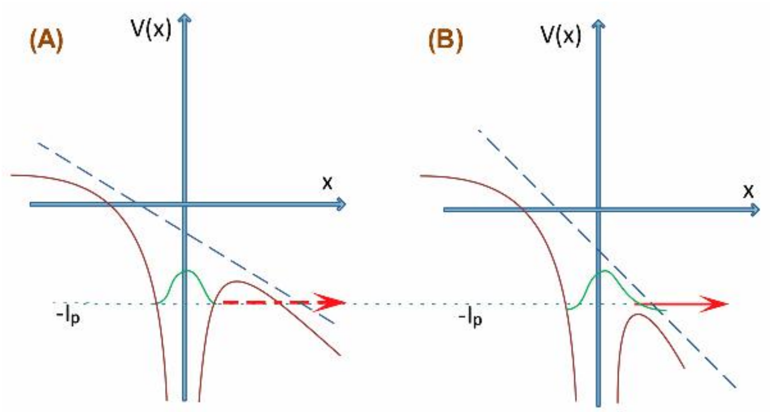

Figure 1.7: Tunneling and over-the-barrier ionization schemes.

1.7.3 Electrons in intense laser fields

In an intense laser field, the electrons kicked out from the atoms will get accelerated, and they will oscillate at the frequency of the field. This is called *Quiver motion* of the electron. The energy gained by the electrons from the laser field is transferred to the plasma when they are damped by collisions. The magnitude of the quiver velocity is given by,

$$v_{osc} = \frac{eE}{m\omega} \propto \left(I\lambda^2\right)^{1/2} \qquad - (1.17)$$

and the quiver energy can be written as,

$$U_{osc} = \frac{1}{2} m v_{osc}^2 \qquad - (1.18)$$

These energetic electrons are capable of causing ionization when they collide with neutral atoms. The collisional ionization is especially strong in solids, forming a hot plasma at the focal point.

When there are gradients in the field amplitude, the electrons do not experience a uniform sinusoidal field all over their orbit but a varying field amplitude along it. This results in a non-linear force called the *ponderomotive force* that tends to push electrons away from the regions of strong field. The ponderomotive force averaged over an oscillation can be obtained as,

$$F_P = -\frac{e^2}{4m\omega^2}\nabla E^2(x) = -\nabla U_P \qquad \text{- (1.19)}$$

where E is the oscillating electric field and U_P is the ponderomotive energy. This same force enables tweezing action in optical tweezers. In plasma, ponderomotive force acts mainly on the electrons, as it is dependent on the spatial extent of the electron orbits. Consequently, it tends to create charge separation and hence produces an electrostatic disturbance in the plasma. It is known that the ponderomotive force creates electrostatic plasma waves (wake field acceleration), thus playing a pivotal role in tabletop particle accelerators.

When, instead of isolated atoms and molecules, an intense field encounters a ‘solid-density’ of particles in the focal volume, the electrons and ions interact among themselves and several other phenomena, including further ionization and absorption mechanisms unique to this state, emerge {27}. Thus, at the focal volume of the laser, matter exists as a soup of electrons and ions with a dominant collective behavior. This is termed the ‘*plasma*’ state, the fourth state of matter.

The study of the behavior of matter under extreme light irradiation is rewarding because of its many relevant scientific and technological possibilities. For instance, the process of high harmonic generation has several applications, as it can generate coherent x-rays from a visible 1 eV laser. It can be understood in a simple manner as the recombination of a highly excited electron with the core ion, as the electron repeatedly returns to the core during the cyclic oscillation by the light wave {28}. In recent studies, harmonics as high as 3000 have been measured from a solid surface at ‘relativistic intensities’ of 10^{19} W/cm^2 {29}.

1.8 Applications of intense laser–matter interactions

Intense laser – matter interactions have a variety of fascinating applications such as attosecond pulse generation, laser fusion, relativistic nonlinear optics, laser wake field acceleration etc. Temporal beating of superposed high harmonics obtained by focusing a femtosecond laser pulse in a gas jet can produce a train of very short intensity spikes of the time scale of attoseconds, depending on the relative phases of the harmonics {30}. Using such attosecond pulses, it may be possible to capture electronic motion inside atoms, molecules and condensed matter in real time, enabling nanoscopy simultaneously with attosecond time resolution {31}.

When an intense laser pulse shorter than an ion oscillation period is used for laser-matter interaction, the electrons get displaced whereas the ions remain static due to inertia. This charge separation provides an electrostatic force that sets up electron plasma oscillations at the plasma frequency (ω_p). The alternating regions of net positive and negative charge result in the electrostatic ‘wake field’ plasma, a wave that propagates at a phase velocity close to that of light. For appropriately phased electrons, the acceleration becomes continuous leading to high energies. This particular technique of particle acceleration is known as laser wake field acceleration (LWFA). LWFA can provide an acceleration gradient of 200 GV/m in comparison to conventional accelerators that can only provide 20 MV/m. In principle, this would allow a reduction in the size of particle accelerators from kilometers to millimeters {32}.

At very high laser intensities, the electrons in the medium get accelerated to relativistic velocities. For a laser of wavelength 1 μm, the intensity required for this is approximately 10^{18} W/cm^2. At such high velocities, the electrons become more massive and their nonlinear response becomes sluggish. Correspondingly, the plasma frequency also reduces, thus making a usually opaque region transparent. Some of the relativistic nonlinear effects observed include self-focusing of light (with more exciting characteristics compared to its sub-relativistic counterpart), self-channeling, hole-boring transparency and soliton formation {33}.

Intense laser produced plasmas can generate subpicosecond x-ray pulses under the right conditions. The plasma x-ray emission extends over a broad spectral range and arises mainly from continuum emissions in the high-density plasma. Such a plasma source can be very efficient because almost 90% of the excitation laser energy can be coupled into the solid target and used for heating the target electrons to high temperatures {34}. Duration of the x-ray pulse is of the order of picoseconds to nanoseconds, which is much shorter than that of a conventional light source such as an x-ray tube. This feature is helpful in taking snapshot images of rapidly moving materials with high spatial and temporal resolutions.

It is possible to access pressure, temperature and density conditions similar to those encountered in intra-stellar matter from ultrashort, ultraintense laser – matter interactions. Thus, by these laser experiments, it is possible to obtain ‘astrophysics on a tabletop’, with good repeatability and reproducibility. The levels of ionization and temperature achieved enable the simulation of intra-stellar and intra-planetary matter. Opacity of stellar matter, phase transition routes, gamma ray bursts, synthesis of particles at extremely high temperatures and pressures etc can be studied by laboratory astrophysics {35,36}.

1.9 Outline of the thesis

This thesis consists of experimental work related to moderate and high intensity laser-matter interaction. A general introduction to these fields is given in this chapter. Chapter 2 elaborates nonlinear optical measurements done on metallic nanostructures. In chapter 3, a simple, fast method to find out the sign of refractive nonlinearity in thin nonlinear films is discussed. Chapter 4 is a study of the spectral dispersion of nonlinearity in metal nanoparticles, using a white-light continuum source. Chapter 5 describes the instrumentation used for intense laser-matter interaction. Laser induced x-ray emissions from a planar liquid jet and a novel way to enhance the x-ray emission are discussed in chapter 6. Chapter 7 is a study of laser induced x-ray emission from a Nickel target. Chapter 8 contains the conclusions drawn from the studies and some future perspectives.

References

1. *Handbook of Nonlinear Optics*, R. L. Sutherland, Second Edition, Marcel Dekker, New York (2003).
2. *Solid-State Lasers*, W. Koechner and M. Bass, Springer-Verlag, New York (2003).
3. *Nonlinear Optics*, R. W. Boyd, Second Edition, Academic press, San Diego, CA (2003).
4. *Ultrafast Optics (Wiley Series in Pure and Applied Optics)*, A. Weiner, Wiley, Hoboken (2009).
5. *Physics of Nonlinear Optics*, Gung S. He and Song H. Liu, World Scientific, Singapore (1999).
6. *Laser Spectroscopy: Volume 2: Experimental Techniques*, W. Demtroder, Fourth Edition, Springer-Verlag, Berlin Heidelberg (2008).
7. *Lasers*, A. E. Seigman, University Science Books, California (1986).
8. *Laser Fundamentals*, W. T. Silfvast, Second Edition, Cambridge University Press, Cape Town, South Africa (2004).
9. *Femtosecond Laser Pulses: Principles and Experiments*, C. Rulliere, Springer, New York (1998).
10. *Investigation of Nonlinear Effects Induced in Condensed Matter by Intense Laser Fields*, M. Anija, PhD Thesis, Raman Research Institute (2007).
11. *Solid-State Laser Engineering*, W. Koechner, Springer Science+Business Media, New York (2006).
12. *Kerr lens mode-locking*, T. Brabec, Ch. Spielmann, P.F. Curly, and F Krausz, Opt. Lett., **17**, 1292 (1992).
13. *Compression of amplified chirped optical pulses*, C. D. Strickland and G. Mourou, Opt. Comm., **56**, 219 (1985).
14. *Laser Spectroscopy*, P. Hannaford, Springer Science+Business Media (2005).
15. *Chemical Reactions and Their Control on Femtosecond Scale: XXth Solvay Conference on Chemistry*, P. Gaspard and I. Burghardt (Eds.), Wiley, Hoboken, NJ (1997).
16. *Ultrafast Laser Pulse Phenomena*, J. C. Diels and W. Rudolf, Academic Press, San Diego, California (1996).
17. *Terahertz Optoelectronics*, K. Sakai, Springer-Verlag, Berlin, Heidelberg (2005).
18. *Ultrafast Laser Pulses in Biology and Chemistry*, M. Braun, P. Gilch, and W. Zinth, Springer-Verlag, Berlin, Heidelberg (2008).

19. *Optics*, A. Ghatak, Third Edition, Tata McGraw-Hill, New Delhi (2005).
20. *Short Pulse Laser Interactions with Matter: An Introduction*, P. Gibbon, Imperial College Press, London (2005).
21. *Free-free transition following six-photon ionization of Xenon atoms*, P. Agostini, F. Fabre, G. Mainfray, and G. Petite, Phys. Rev. Lett., **42**, 1127 (1979).
22. *Multiphoton ionization above the threshold,* Y. Gontier, M. Poirier, and M. Trahin, J. Phys. B: At. Mol. Phys., **13**, 1381 (1980).
23. *Ionization in the field of a strong electromagnetic wave*, L.V.Keldysh, Sov. Phys. JETP, **20**, 1307 (1965).
24. *Progress in Optics: Volume 31,* E. Wolf, Elsevier Science Publisher B.V., Amsterdam, The Netherlands (1993).
25. *Concerning the theory of impact ionization in a semiconductor*, L. V. Keldysh, Sov. Phys. JETP, **21**, 1135 (1965).
26. *Atoms, solids, and plasmas in super-intense laser fields*, D. Batani, C. J. Joachain, and S. Martellucci, Kluver Academic/Plenum, New York (2001).
27. *Interactions of ultra-intense laser light with matter*, C. J. Joshi and P.B. Corkum, Phys. Today, **48**, 36 (1995).
28. *Plasma perspective on strong-field multiphoton ionization*, P. B. Corkum, Phys. Rev. Lett., **71**, 1994 (1993).
29. *Bright multi-keV harmonic generation from relativistically oscillating plasma surfaces,* B. Dromey, S. Kar, C. Bellei, D. C. Carroll, R. J. Clarke, J. S. Green, S. Kneip, K. Markey, S. R. Nagel, P. T. Simpson, L. Willingale, P. McKenna, D. Neely, Z. Najmudin, K. Krushelnick, P. A. Norreys, and M. Zepf, Phys. Rev. Lett., **99**, 085001 (2007).
30. *Observation of a train of attosecond pulses from high harmonic generation*, P. M. Paul, E. S. Toma, P. Breger, G. Mullot, F. Augé, Ph. Balcou, H. G. Muller, and P. Agostini, Science **292**, 1689 (2001).
31. *Attosecond science*, P. B. Corkum and F. Krausz, Nature Physics **3**, 381 (2007).
32. *Electron acceleration by a wake field forced by an intense ultrashort laser pulse*, V. Malka, S. Fritzler, E. Lefebvre, M. M. Aleonard, F. Burgy, J. P. Chambaret, J. F. Chemin, K. Krushelnick, G. Malka, S. P. D. Mangles, Z. Najmudin, M. Pittman, J. P. Rousseau, J. N. Scheurer, B. Walton, A. E. Dangor, Science, **298**, 1596 (2002).

33. *Optics in the relativistic regime*, G. Mourou, T. Tajima, and S. V. Bulanov, Rev. Mod. Phys., **78**, 309 (2006).
34. *Generation of efficient ultrafast laser-plasma x-ray sources*, M. M. Murnane, H. C. Kapteyn, and R. W. Falcone, Phys. Fluids B, **3**, 2409 (1991).
35. *Frontiers in High Energy Density Physics: The X-games of Contemporary Science,* National Research Counsel of the National Academics, National Academies Press, Washington Dc, (2003).
36. *Set the controls for the heart of the Sun*, S. J. Rose, Contemp. Phys. **45**, 109(2004).

2

Nonlinear optical properties of metal nanoparticles and nanowires

Nanostructures are receiving substantial attention from researchers recently. They are of particular interest in optics and nonlinear optics due to the applications arising out of their enhanced responses to an applied electromagnetic (EM) field. Metal nanostructures are very promising among these, particularly because of the surface plasmon resonances they exhibit in the visible region of the EM spectrum. In this chapter the nonlinear transmission behaviour of a few metal nanostructures measured by the z-scan technique is discussed in detail. From Degenerate Four Wave Mixing (DFWM) experiments the third-order nonlinear susceptibility ($\chi^{(3)}$) *of silver nanoparticles also has been determined.*

2.1 Introduction to nanoscience and nanotechnology

The word '*nano*' from which this relatively new field derives its name is a prefix denoting a scale of 10^{-9}. Nano comes from the Greek word '*nanos*' meaning '*dwarf*'. Properties of materials of nanometric dimensions are significantly different from those of atoms and bulk materials. They effectively form a bridge between bulk materials and their atomic or molecular counterparts. Nanoscience is the study of the properties and phenomena associated with nanoscale materials. The suitable control of the properties of nanometer scale structures can lead to new sciences as well as new devices and technologies. Nanotechnology is the application of nanoscience, especially to industrial and commercial objectives. The underlying theme of nanotechnology is miniaturization.

Bulk materials have physical properties regardless of size, but at the nanoscale, size-dependent properties are often observed. Thus, the properties of materials change as their size approaches the nanoscale and as the percentage of atoms at the surface becomes significant. For materials larger than one micrometer in size, the percentage of atoms at the surface is insignificant in relation to the number of atoms in the bulk of the material. The interesting and sometimes unexpected properties of nanoparticles are therefore largely due to the large surface area of the material, which dominates the contributions made by the small bulk of the material. An excellent example of this is the absorption of solar radiation in photovoltaic cells, which is much higher in materials composed of nanoparticles than it is in thin films of continuous sheets of material {1}.

In this chapter we discuss the nonlinear optical properties of metallic nano particles and clusters. A cluster is an entity consisting of a few to a few hundred thousand atoms, packed densely with arbitrary external shape and structural arrangement. Clusters represent an intermediate stage in the transition from atoms or small molecules to the bulk or to the solid state. '*Metal clusters*' are composed of materials which in the bulk state are classified as metals with high density of electronic states near the Fermi level. In the state of clusters, they may not exhibit metallic properties {2}. Metal clusters that are large enough to posses a well defined conduction band, and hence, are able to manifest plasmon resonance and classical electron charging behaviour, are termed '*metal nanoparticles*' {3}. The interaction of the large fraction of the surface atoms with the surrounding medium gives rise to new interesting properties.

Clusters are generally classified into three size regimes. '*Very small clusters*' are those clusters, which typically have a size less than a nanometer. The number of atoms in such a cluster is usually between 2 to 20. In the case of very small clusters, the surface and inner volume are indistinguishable. If the diameter of the cluster is in the 1-3 nm range, it is a '*small cluster*'. For small clusters the ratio of the number of atoms on the surface of the cluster to that in the interior of the cluster will be between 50% and 90%. Small clusters normally consist of 20 to 500 atoms per cluster. Clusters of 3-100 nm diameter are categorized as '*large clusters*'. They contain typically about 500 to 10^7 atoms.

The electrical and optical properties of clusters strongly depend on their size, shape and the surrounding medium. Small and large clusters are usually approximated as spheres and spheroids respectively, if they are in free form. If they are embedded or supported, they are assumed to be ellipsoids and caps {2}. The geometry of very small clusters depends sensitively on their size and might vary from planar to complex three-dimensional structures. The experimental variety of cluster geometries (sizes and shapes) and surroundings makes it difficult to formulate a general theory which can explain all features of their optical response.

The optical properties of metal nano clusters are interesting in different size regimes. There are two different kinds of cluster size effects: *intrinsic effects* - concerning specific changes in volume and surface material properties - and *extrinsic effects* – which are size-dependent responses to external fields or forces irrespective of the intrinsic effects. For large clusters electrodynamic theory can be applied using bulk optical constants (extrinsic size effects) {2}. The dielectric functions of clusters with diameter larger than 10 nm are usually close to those of the bulk material and are size independent. For small clusters, the optical functions become size-dependent (intrinsic size effects). Spherical- and ellipsoidal- jellium models {4} can account qualitatively for many important experimental features of small and very small clusters. More detailed molecular - orbital calculations can also be applied in the case of very small clusters.

2.1.1 The surface plasmon resonance (SPR)

'*Plasmons*' are collective oscillations of the conduction electrons of a metal at optical frequencies. They are the *quasi-particles* resulting from the quantization of *plasma oscillations* (periodic oscillation of charge density in a conducting medium like plasma or metal) in metals or semiconductors, similar to photons that arise from the quantization of electromagnetic fields (a quasi-particle is a particle like entity that can be thought as a single particle moving through a system of interacting particles, surrounded by a cloud of other particles which are being dragged along or pushed apart by the single particle with the resultant effect that the entire entity moves like a free particle).

Plasmons play a determining role in the optical properties of metals. In most metals the plasmon frequency is in the ultraviolet so that visible light reflects from them, making them shiny. The plasmon energy is estimated as,

$$E_p = \hbar\omega_p \qquad \text{- (2.1)}$$

where $\omega_p = \sqrt{ne^2/m\varepsilon_0}$ is the plasma frequency with n being the free electron density, e the charge of the electron, m its mass and ε_0 the permittivity of free space. Those plasmons that are confined to the surface and interact strongly with light resulting in a polariton are known as '*surface plasmons*'. Polaritons are quasi-particles resulting from strong coupling of electromagnetic waves with an electric or magnetic dipole-carrying excitation. Surface plasmons occur at the interface of a material with different dielectric constants.

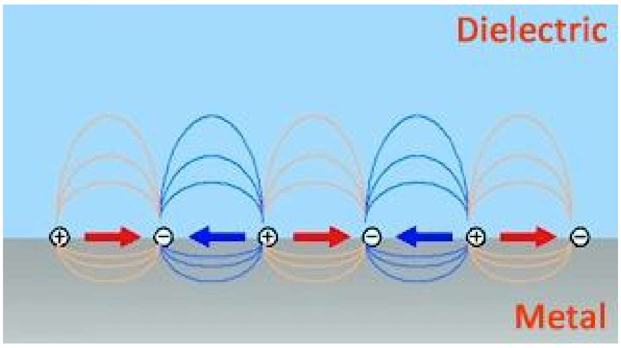

Figure 2.1: Schematic representation of an electron density wave propagating along a metal/dielectric interface. The charge density oscillations and associated electromagnetic fields are called surface plasmon-polariton waves.

When subjected to external electromagnetic radiation, the conduction electrons in a bulk metal behave as a relaxator system, whereas when the metal is in the form of spherical clusters, they behave like an oscillator system with polarization charges at the cluster surface giving rise to a linear restoring force that determines the energy eigen frequencies of the system. These are interpreted as classical *surface plasmon frequencies*. Although all the electrons oscillate with the positive ion background, the main effect producing the restoring force is the surface polarization {2}. The resonant position of the multipolar surface plasmon polariton eigen frequencies is given by the expression (in the quasi-static limit of Mie theory applied to electrically neutral clusters),

$$\omega_L = \omega_p \frac{1}{\sqrt{1+\left(\frac{L+1}{L}\right)\varepsilon_m}} \qquad \text{- (2.2)}$$

where L is the order of the multipole and ε_m is the dielectric constant of the surrounding medium.

For spherical metal clusters where the cluster radius is much less than the wavelength of the interacting electromagnetic field ($r<<\lambda$), the extinction cross section given by Mie theory is,

$$\sigma_{ext}(\omega) = 9\frac{\omega}{c}\varepsilon_m^{3/2}V_0 \frac{\varepsilon_2(\omega)}{\left|\varepsilon_1(\omega)+2\varepsilon_m\right|^2+\varepsilon_2^2(\omega)} \qquad \text{- (2.3)}$$

where the phase retardation and effects of higher multipoles are neglected. V_0 is the particle volume, ε_m is the dielectric function of the embedding medium that is assumed to be frequency independent over the spectral range of interest, and $\varepsilon_1(\omega)$ and $\varepsilon_2(\omega)$ are the real and imaginary parts of the dielectric constant of the spherical metal cluster. Here the extinction cross section is due to the dipolar absorption only {2}. Hence the expression gives the absorption cross section of the dipolar surface plasmon. The absorption peak occurs when $\left|\varepsilon_1(\omega)+2\varepsilon_m\right|^2+\varepsilon_2^2(\omega)$ is a minimum. $\varepsilon_1(\omega)$ determines the peak position and also influences the width of the resonant absorption. Steep $\varepsilon_1(\omega)$ spectra give sharp resonances whereas relatively flat $\varepsilon_1(\omega)$ gives broad absorption bands. Small $d\varepsilon_1(\omega)/d\omega$ and large $\varepsilon_2(\omega)$ smear out the resonances. Noble metals exhibit sharp resonances, and silver in particular shows a pronounced surface plasmon resonance in vacuum due to small $\varepsilon_2(\omega)$ at 3.6 eV. By embedding the metal nanoclusters in transparent dielectric materials their surface plasmon resonance frequencies can be tuned, as the plasmon resonance positions depend on the refractive index of the surrounding material. Hence if the embedding matrix is changed, the plasmon resonance position shifts, and by the systematic variation of ε_m the characteristic spectroscopic fingerprints of the cluster can be obtained. This technique is called *immersion spectroscopy*.

Noble metals like silver (Ag) and gold (Au) have completely filled 4d and 5d bands and just one electron in the 5s and 6s bands respectively in the solid bulk form. Atomic number of bulk Ag is 47 with the outermost orbital configuration as $4d^{10}$, $5s^1$; and for Au it is 79 with the $4f^{14}$, $5d^{10}$, $6s^1$ configuration. When these metals form nanoclusters, distinct energy bands are formed which are not seen in metals.

2.2 The nonlinear light transmission phenomenon

Depending on the characteristic response of a medium to the frequency of light, the transmission of light gets affected by the scattering, refraction or absorption by the medium. For instance, when the intensity of the input light is such that the corresponding electric field is sufficient to evoke the otherwise small nonlinear terms in the dipole oscillation, it modifies the properties of the medium, affecting light transmission. The change in transmittance of a medium as a function of the input light intensity or fluence is referred to as nonlinear light absorption or nonlinear light transmission. At sufficiently high intensities, the probability of an absorber absorbing more than one photon before relaxing to the ground state can be enhanced. A few major mechanisms that control nonlinear light transmission are discussed in detail in the following subsections.

2.2.1 Saturable absorption

Saturable absorption is a property of materials where the absorption of light decreases with increasing light intensity. At sufficiently high incident light intensity, atoms or molecules in the ground state of a saturable absorber material become excited into an upper energy state at such a rate that there is insufficient time for them to decay back to the ground state before the ground state becomes depleted, and the absorption subsequently saturates.

A simple kinetic model can often be used when the saturation is considered in terms of depletion of the ground state concentration. Thus, under the steady state,

$$\frac{dN}{dt}=\frac{\sigma I}{h\nu}(N_g-N)-\frac{N}{\tau}=0 \qquad \text{- (2.4)}$$

where N is the concentration of excited state molecules, N_g is the undepleted ground state concentration, σ is the absorption cross section, hν is the photon energy, and τ is the lifetime of the excited state population. Assuming that the absorption coefficient α is proportional to the ground state population, $\alpha=\sigma(N_g- N)$, we get the following equation describing the saturation,

$$\alpha=\alpha_0\frac{1}{1+\left(\tau\sigma I/h\nu\right)}=\alpha_0\frac{1}{1+\left(I/I_s\right)} \qquad \text{- (2.5)}$$

where $I_s=h\nu/(\sigma\tau)$ is the saturation intensity and $\alpha_0=\sigma N_g$ is the linear absorption coefficient. The case described by the above equation is often referred to as homogeneous saturation {5}.

In the case of a two-level system with inhomogeneously broadened states and hole burning, it has been found that the saturation can be described by {6},

$$\alpha=\alpha_0\frac{1}{\left(1+\left(I/I_s\right)\right)^{0.5}} \qquad \text{- (2.6)}$$

The main applications of saturable absorbers are in passive mode locking and Q-switching of lasers, i.e., in the generation of short pulses {7}. The key parameters for a saturable absorber are its wavelength range (where it absorbs), its dynamic response (recovery time), and its saturation intensity and fluence (at what intensity or pulse energy it saturates). Saturable absorbers are also useful for purposes of nonlinear filtering outside laser resonators, e.g., cleaning up pulse shapes, and optical signal processing.

2.2.2 Two-photon absorption (2PA)

The process of the transition of a system from the ground state to a higher level by the simultaneous absorption of two photons from an incident radiation field is termed two-photon absorption. Two photons of frequency ω of the incident field are simultaneously absorbed by the system to make the transition to a state that is approximately resonant at 2ω. A schematic representation of two-photon absorption can be found in figure 2.2.

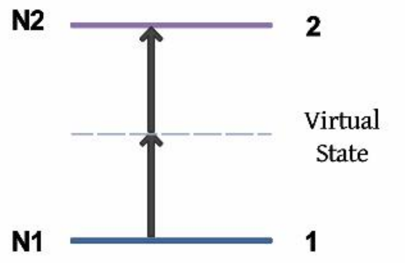

Figure 2.2: Schematic representation of two-photon absorption.

The intermediate level being virtual, the two photons should be simultaneously absorbed making the process sensitive to the instantaneous optical intensity of the incident radiation. The two-photon absorption process is proportional to the square of the input intensity. The propagation of laser light through the system describing the optical loss is given by,

$$\frac{dI}{dz} = -\alpha I - \beta I^2 \qquad \text{- (2.7)}$$

where α is the linear absorption coefficient (which can be very small) and β the two-photon absorption coefficient. β is a macroscopic parameter that characterizes the material and is related to the individual molecular two-photon absorption cross section σ_2 through,

$$\sigma_2 = \frac{\hbar\omega\beta}{N} \qquad \text{- (2.8)}$$

where N is the number density of the molecules in the system and ω is the incident radiation frequency. It is the imaginary part of the third-order nonlinear susceptibility of the system that determines the strength of the two-photon absorption. The relation between the two-photon absorption coefficient and the third-order susceptibility of a centrosymmetric system for linearly polarized incident light is given as,

$$\beta = \frac{3\pi}{\varepsilon_0 n^2 c\lambda} \mathrm{Im}[\chi^{(3)}_{xxxx}(-\omega;\omega,\omega,-\omega)] \qquad \text{- (2.9)}$$

Since the physical quantity that is measured is the transmitted energy in a typical light transmission measurement, the transmittance is conveniently defined as the ratio of the transmitted and incident energies. For a pulsed laser beam that is spatially and temporally Gaussian, the transmittance T in the presence of two-photon absorption is given as {8},

$$T = \frac{(1-R)^2 \exp(-\alpha L)}{\sqrt{\pi} q_0} \int_{-\infty}^{\infty} \ln[1 + q_0 \exp(-\tau^2)] d\tau \qquad \text{- (2.10)}$$

where R is the Fresnel reflection at the interface of the material with air, α the linear absorption coefficient and L the length of the medium. q_0 is given by,

$$q_0 = \beta(1-R) I_0 L_{eff} \qquad \text{- (2.11)}$$

where I_0 is the peak on-axis intensity incident on the material and L_{eff} is the effective length of the medium given as,

$$L_{eff} = \frac{1-\exp(-\alpha L)}{\alpha} \qquad \text{- (2.12)}$$

2.2.3 Three-photon absorption (3PA)

The process of the transition of a system from the ground state to a higher level by the simultaneous absorption of three photons from an incident radiation field is termed as three-photon absorption (3PA). The schematic representation is given in figure 2.3.

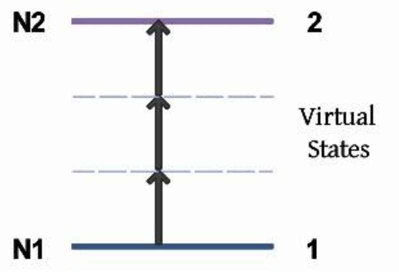

Figure 2.3: Schematic representation of three-photon absorption.

3PA is a fifth-order nonlinear process, and the propagation equation for a medium having significant three-photon absorption is given as,

$$\frac{dI}{dz} = -\alpha I - \gamma I^3 \qquad \text{- (2.13)}$$

where α is the linear absorption coefficient, which can be typically small, and γ is the three-photon absorption coefficient. For a centrosymmetric system and linearly polarized light, γ is related to the imaginary part of the fifth-order susceptibility through {8},

$$\gamma = \frac{5\pi}{\varepsilon_0{}^2 n^3 c^2 \lambda} \operatorname{Im}[\chi^{(5)}_{xxxxxx}(-\omega;\omega,\omega,\omega,-\omega,-\omega)] \qquad \text{- (2.14)}$$

The transmittance of a system with three-photon absorption, when the incident laser is spatially and temporally Gaussian, is given as,

$$T = \frac{(1-R)^2 \exp(-\alpha L)}{\sqrt{\pi}\, p_0} \int_{-\infty}^{\infty} \ln[\sqrt{1 + p_0{}^2 \exp(-2\tau^2)} + p_0 \exp(-\tau^2)] d\tau \qquad \text{- (2.15)}$$

where

$$p_0 = \sqrt{2\gamma(1\text{-}R)^2 I_0{}^2 L'_{eff}} \qquad \text{- (2.16)}$$

where I_0 is the peak on-axis intensity incident on the material and L'_{eff} is the effective length in the medium given as,

$$L'_{eff} = \frac{1-\exp(-2\alpha L)}{2\alpha} \qquad - (2.17)$$

2.2.4 Reverse saturable absorption

Reverse saturable absorption (RSA) is a two-step, sequential one-photon absorption process as shown schematically in figure 2.4. In this case the medium has a resonant linear absorption for the incident laser beam, and some of the molecules in the ground state are excited to an excited state 2. For a properly chosen medium, it is possible that the excited molecules make another transition from the excited state 2 to a higher excited state 3 via another one-photon absorption. (In polyatomic molecules in fact a 5-level model may be considered, which involves both singlet and triplet states).

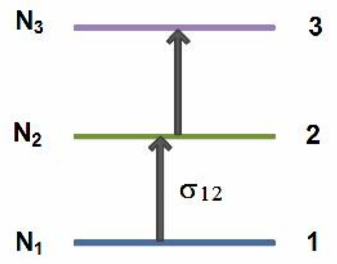

Figure 2.4: Schematic representation of reverse saturable absorption.

The possibility of this process depends on the number of molecules N_2 at the first excited state 2, the incident intensity I, and the excited state absorption cross section σ_{23}. On the other hand N_2 is related to N_1 and I by the relation,

$$N_2 \propto \sigma_{12} N_1 I \qquad - (2.18)$$

where σ_{12} is the cross-section of the transition from the ground state to state 2. As can be seen from this relation, the number of molecules in state 2 (N_2) continuously grows with the incident intensity I and the one-photon sequential absorption from state 2 to state 3 becomes more significant, provided that the cross section σ_{23} of this transition is considerably larger than σ_{12}. Under the steady-state condition, the intensity change of the laser beam in the nonlinear medium along its propagation direction can be expressed as,

$$\frac{dI}{dz} = -\sigma_{12}\left(N_1 - N_2\right)I - \sigma_{23}N_2 I \qquad - (2.19)$$

In the simplest case, it can be assumed that $N_1 >> N_2$, $N_3 = 0$, and $N_1 = N_0$, where N_0 is the number density of the absorbing molecules. Then according to equation 2.18, the above equation can be rewritten as,

$$\frac{dI}{dz} = -\sigma_{12}N_0 I - b\sigma_{12}\sigma_{23}N_0 I^2 \qquad - (2.20)$$

or

$$\frac{dI}{dz} = -\alpha_0 I - \beta' I^2 \qquad - (2.21)$$

where b is a proportionality coefficient, and the linear absorption coefficient α_0 and nonlinear absorption coefficient $\beta'$are defined as,

$$\alpha_0 = \sigma_{12}N_0 \qquad - (2.22)$$

$$\beta' = b\sigma_{12}\sigma_{23}N_0 \qquad - (2.23)$$

Equation 2.21 is similar to equation 2.7 for two-photon absorption. Hence it can be solved using the same treatment and the values of the excited state cross sections can be calculated using equations 2.22 and 2.23.

2.2.5 Free carrier absorption

Once free carriers are generated by linear absorption in semiconductors, they may experience phonon-assisted absorption to higher-lying (lower-lying) states in the conduction (valence) band. This process is called free carrier absorption. In the weak absorption regime, the attenuation may be described by,

$$\frac{dI}{dz} = -\alpha I - \sigma_c N_c(I) I \qquad - (2.24)$$

where $N_c(I)$ is the intensity dependent carrier density, and σ_c is the free carrier absorption cross-section. σ_c is related to the electronic properties via the relation,

$$\sigma_c = \frac{e^2}{\varepsilon_0 n_0 c m^* \omega^2 \tau} \qquad - (2.25)$$

where m* is the effective carrier mass and τ is the free carrier life time (mean collision time). Note that it has the $1/\omega^2$ dependence of a high-frequency conductivity and thus is most important for infrared radiation in semiconductors. The free carrier density is governed by a rate equation given by,

$$\frac{\partial N_c}{\partial t} = \frac{\alpha I}{\hbar\omega} - \frac{N_c}{\tau_c} \qquad - (2.26)$$

where τ_c is the free carrier relaxation time due to electron–hole recombination and carrier diffusion. In the general case, equations 2.24 and 2.25 must be solved numerically to determine the transmittance of the material. When the incident pulse is short compared to the carrier relaxation time, the latter term may be neglected in equation 2.26, and these equations may be integrated over time to obtain the fluence attenuation equation,

$$\frac{\partial F}{\partial z} = -\alpha\left(1 + \frac{F}{2F_s}\right)F \qquad - (2.27)$$

where $F_s = \hbar\omega/\sigma_c$ is the saturation fluence. (Note that the cross-section involved in this definition of saturation fluence is the free carrier absorption cross-section and not the linear absorption cross-section as in the discussion of SA and RSA in polyatomic molecules above.) For excitation with a pulsed Gaussian beam, the transmittance is given by {8},

$$T = \frac{(1-R)^2 \exp(-\alpha L)}{q} \ln(1+q) \qquad - (2.28)$$

where $q=(1-R)\left[1-\exp(-\alpha L)\right]F_0/2F_s$. The value of F_s can be found out from the appropriate theoretical fit to the experimental data, from which the free carrier cross section can be calculated.

2.2.6 Nonlinear scattering (Induced thermal scattering)

Optically induced scattering can also have an effect on the nonlinear transmission in a system. This is a common nonlinear phenomenon associated with nanomaterials {9}. The scattering process can spread the incident light into a larger spatial dimension thereby reducing the intensity of the direct transmitted beam. There are three major mechanisms that are believed to be responsible for the nonlinear scattering of incident light in a system. The first possibility is the generation of solvent bubbles (in a liquid sample). In this case, the sample absorbs the incident photons and transfers the generated thermal energy to the surrounding solvent. The solvent in turn evaporates to form bubbles. There will be a large refractive index discontinuity at the vapour–solvent interface, and hence the vapour bubbles scatter the incident light effectively {10}. The scattering cross section increases significantly with increasing size of the vapour bubbles and it is an intensity-dependent quantity since the size of the gas bubbles is nonlinearly related to the incident energy density. Since the evaporation time of typical solvents is generally of the order of nanoseconds, this process is more effective for excitation with nanosecond laser pulses.

In some cases, the refractive index of the surrounding solvent or the interface between the particles and the surrounding liquid may vary due to the absorption of laser radiation and the subsequent thermal energy transfer. Such dielectric constituents with a refractive index discontinuity or mismatch, formed in the nanosecond excitation time scales, can play the role of scattering centers as well. The difference of this process with the first one is the absence of bubble formation. This type of a process is more likely to happen in samples dissolved in non-volatile solvents.

The third possibility is the direct ionization of the sample and the subsequent production of microplasmas in the focal region. The microplasmas formed will strongly scatter the input radiation from its normal transmission path, thereby resulting in a nonlinear decrease in the measured transmitted light. Especially for metal nanoparticles, if the wavelength of the incident beam is in the surface plasmon absorption band, strong photon absorption can make the particles form microplasma states, and hence serve as scattering centers. Compared with the long formation time of the other two processes, the sublimation of particles can be completed in the sub-nanosecond range, resulting in a faster nonlinear transmission response. However this process needs much higher incident intensity than solvent evaporation.

2.3 Experimental measurement of nonlinear transmission

Of late, the open aperture z-scan technique {11} has become quite popular for nonlinear transmission measurements. In the open aperture z-scan experiment, a laser beam is first focused using a lens. The direction of beam propagation is taken as the z-axis, and the focal point is considered as $z = 0$. The z value increases towards either side of the focal point, but the sign will be negative on one side and positive on the other (similar to a number line). The sample is now placed in the beam at a position (z) between the lens and the focal point, and the transmitted laser energy is measured. Then the sample is moved in small steps towards the focus and beyond, and the transmission is measured at each step. At each of these positions the sample will experience a different laser intensity, and the intensity will be a maximum at the focus. Thus the open aperture z-scan is essentially a sample transmission measurement, the data being continuously taken while the sample is slowly translated from a position before the focus to a position after the focus. A schematic of the open aperture z-scan setup can be seen in figure 2.5.

If a spatially Gaussian laser beam is used, then each z position will correspond to an input laser energy density (fluence) of $4(\ln 2)^{1/2}E_{in}/\pi^{3/2}\omega(z)^2$ where E_{in} is the input laser pulse energy, and $\omega(z)$ is the beam radius. $\omega(z)$ is given by $\omega(0)[1+(z/z_0)^2]^{1/2}$ where $\omega(0)$ is the beam radius at the focus, and $z_0 = \pi\omega(0)^2/\lambda$ is the Rayleigh range (diffraction length), where λ is the excitation wavelength. Thus from the open aperture z-scan data, it is possible to draw a graph between the input laser fluence and the sample transmission. The nature of this graph will reveal the absorptive nonlinearity of the system.

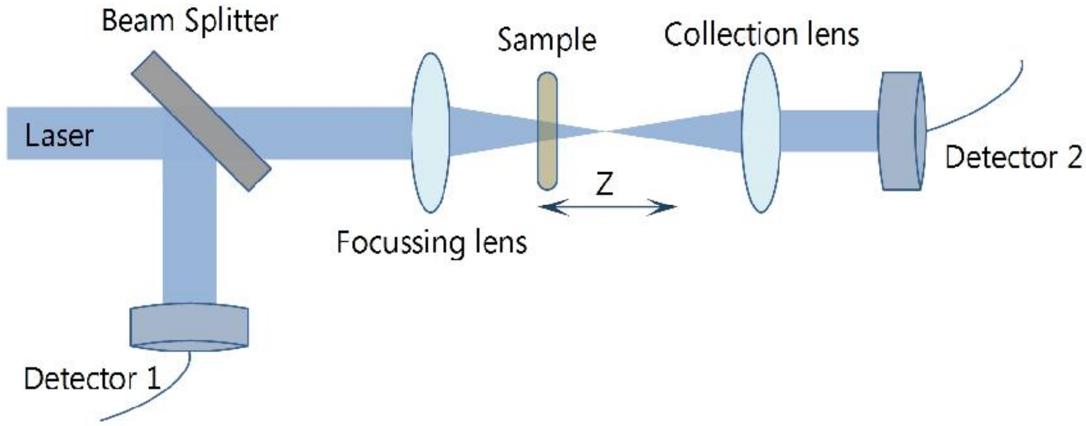

Figure 2.5: Schematic of the open aperture z-scan setup.

In our experiment a plano-convex lens of 20 cm focal length was used to focus the laser beam. Samples in liquid form were taken in a 1 mm glass cuvette (Hellma GmBH) and film samples were loaded as such on a programmable linear translation stage. The input energy reaching the sample and the energy transmitted by the sample were measured using two pyroelectric energy probes (RjP 735, Laser Probe Inc.). The laser pulse-to-pulse energy fluctuations were generally less than ±5% and were monitored by the reference energy probe. The interval between successive laser pulses was kept sufficiently large (about one second) to allow complete thermal relaxation of the excited sample between adjacent laser pulses. The energy meter outputs were digitized with the help of a digital storage oscilloscope, which was interfaced to a PC using the serial port (RS-232). The experiment was completely automated using a C++ program written in the Linux platform. The stepper motor was controlled through the parallel port of the PC using appropriate drivers developed in-house. The nonlinear scattering in the samples was measured with the help of a third photo detector (UDT 10 - photo diode), kept at an angle of about 45 degrees and 4 cm away from the front surface of the sample. A detailed schematic of the experimental setup can be seen in figure 2.6.

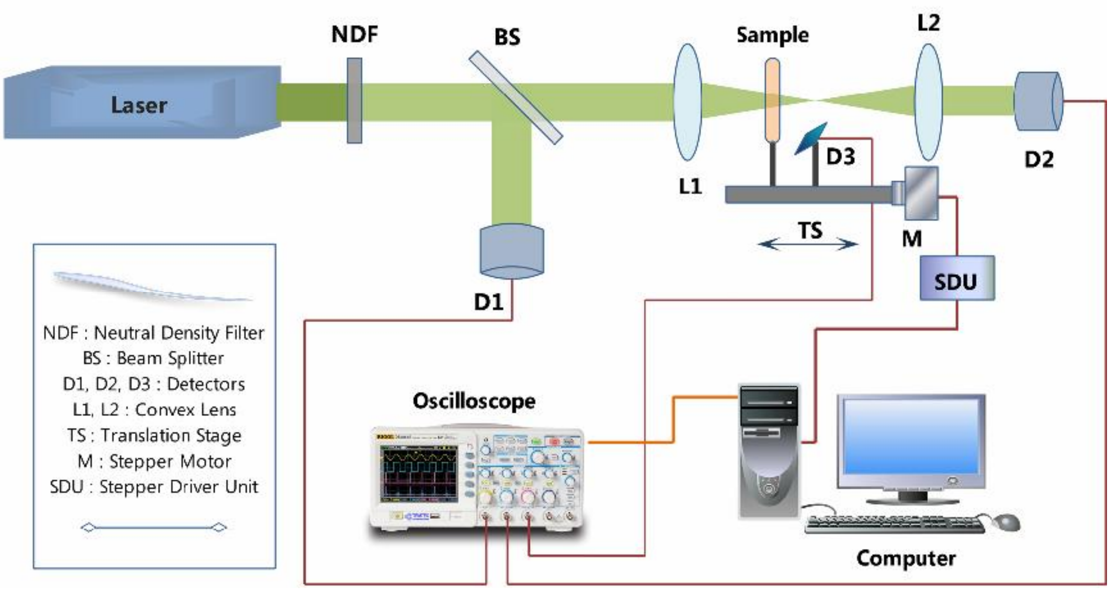

Figure 2.6: Detailed schematic of the z-scan experimental setup.

2.4 Nonlinear transmission in Ag@ZrO$_2$-PVA core-shell nanocomposites

In this section, we discuss features of nonlinear optical transmission measured in Ag@ZrO$_2$ clusters embedded in poly vinyl alcohol (PVA) films. These are core-shell nanoparticles prepared using the wet chemical method {12}. Core-shell nanoparticles are a class of nanostructures, which have a well-defined core as well as a shell, both in the nanometer size range. These are synthesized by encapsulating the nanometal core within a shell of desired material or by coating the nanometal core by suitable shell material {13}. Details of the synthesis of Ag@ZrO$_2$ core-shell nanoparticles can be found in reference 12. To prepare the nanocomposites, Ag@ZrO$_2$ solution is mixed with an equal amount of PVA solution (prepared by dissolving PVA in water at 60 °C) and then the mixture is layered on a solid support. It is then allowed to evaporate under ambient conditions and a thin solid film of the core-shell nanoparticle/polyvinyl alcohol composite material is obtained. Figure 2.7 shows the absorption spectrum of the prepared film. As can be seen from the figure, the plasmon absorption maximum is at 426 nm. The redshift of the peak from 400 nm (absorption maximum of bare Ag nanoparticles of similar size) is due to the dielectric shell surrounding the metal core. The absorption peak shift is dependent on the shell thickness {14}.

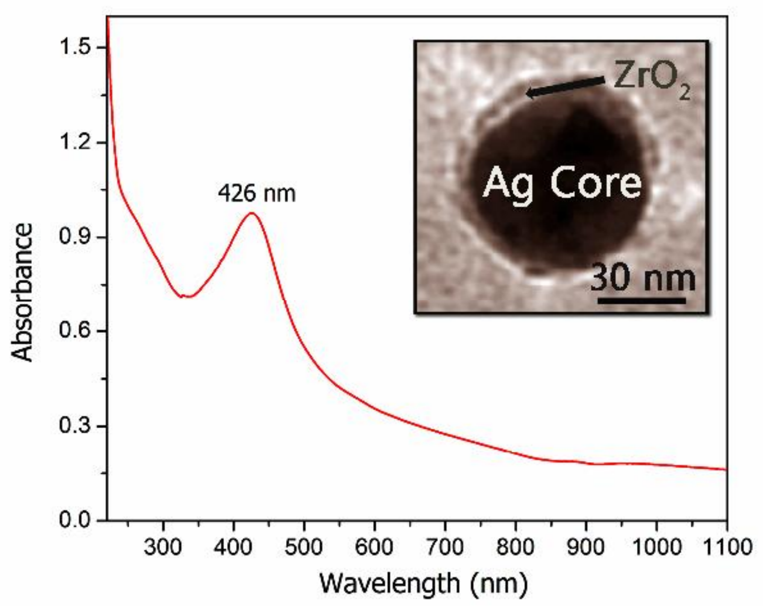

Figure 2.7: Optical absorption spectrum of Ag@ZrO$_2$ - PVA nanocomposite. The absorption spectrum peaks at 426 nm for a 3 nm ZrO$_2$ shell thickness. Inset shows the transmission electron micrograph of a single nanoparticle.

The transmission electron micrograph (TEM) of the sample given in the inset of figure 2.7 is an expanded image of a single nanoparticle with Ag core and ZrO$_2$ shell, depicting a typical particle size of about 50 nm and a shell thickness of 3 nm. It must be noted that the shell covers the core completely. The linear transmission of the film used for the z-scan experiment was 74% at 532 nm.

We used 7 nanosecond pulses from a Q-switched, frequency doubled Nd:YAG laser emitting at the wavelength of 532 nm (2.33 eV) for investigating the nonlinear transmission properties of these nanoparticles. The intensity dependent transmission was measured using the automated open aperture z-scan set-up discussed above. Figure 2.8(A) shows the z-scan curve obtained for a prepared film of 100 micrometer thickness. Figure 2.8(B) is the corresponding fluence vs. normalized transmission curve, derived from the z-scan data. As the transmission decreases at higher input fluences, the film obviously behaves as an optical limiter. The optical limiting threshold (fluence value at which the normalized transmittance drops to a value of 0.5) is found to be 6.47x10^4 J/m^2.

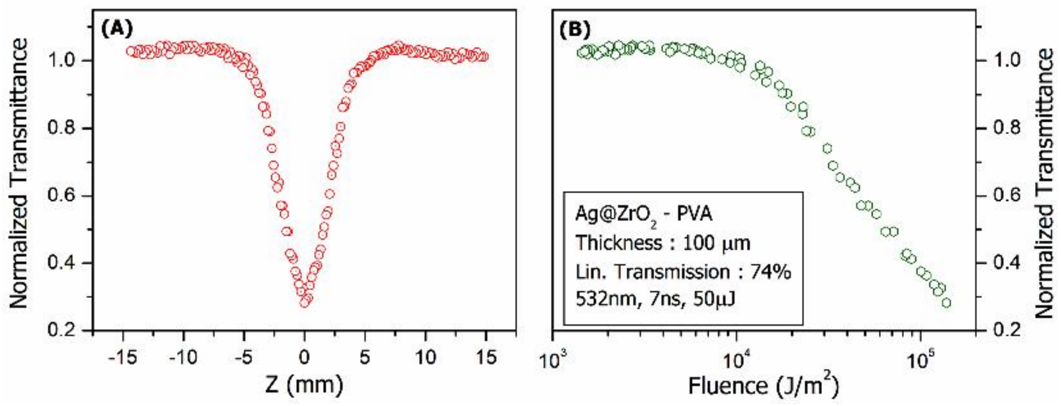

Figure 2.8: (A) The open-aperture z-san curve obtained for the Ag@ZrO$_2$ - PVA nanocomposite film. (B) The corresponding optical limiting curve derived from the z-scan data.

Figure 2.9 is a plot of the input fluence vs the output fluence obtained from the Ag@ZrO$_2$ – PVA nanocomposite film. The straight line in the graph represents a linear transmission behaviour.

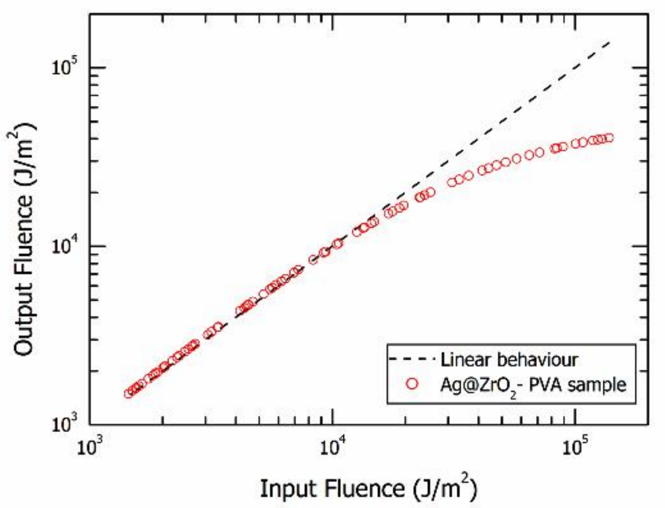

Figure 2.9: Input fluence vs. output fluence for the Ag@ZrO$_2$ - PVA film (red circles). The dashed line is for a linear transmission behaviour.

The z-scan curves obtained are somewhat peculiar (when compared to the conventional z-scan curves obtained from benchmark optical limiting materials like pthalocyanines, carbon nanotubes, fullerenes etc.) in that initially (i.e., at moderate fluences) the transmission increases slightly, before the dip due to optical limiting sets in. It appears that this happens from a saturation of the surface plasmon absorption. The optical limiting seen in the film at higher input fluences can have contributions from two-photon absorption, reverse saturable absorption and nonlinear scattering. Considering the fact that the sample has some absorption at the excitation wavelength (532 nm) and there exists a strong absorption at the two-photon level of 266 nm (as depicted from the UV-Vis absorption spectrum of the film), it can be deduced that the first two processes above contribute to the nonlinear absorption. To learn whether induced thermal scattering (nonlinear scattering) has a contribution to the observed nonlinear transmission, we did a measurement of the laser light scattered by the samples during the z-scan. This was done by keeping a sensitive photodiode on the translation stage, close to the sample, during the experiment. Some amount of nonlinear scattering was observed when the sample was at and near the beam focus. Figure 2.10 shows the nonlinear scattering observed from the film at the excitation wavelength of 532 nm. The scattered and transmitted signals look comparable in the graph because normalized quantities are used for plotting. In absolute terms, the scattered intensity seen by the photodiode is relatively smaller compared to the transmitted intensity seen by the pyroelectric detector.

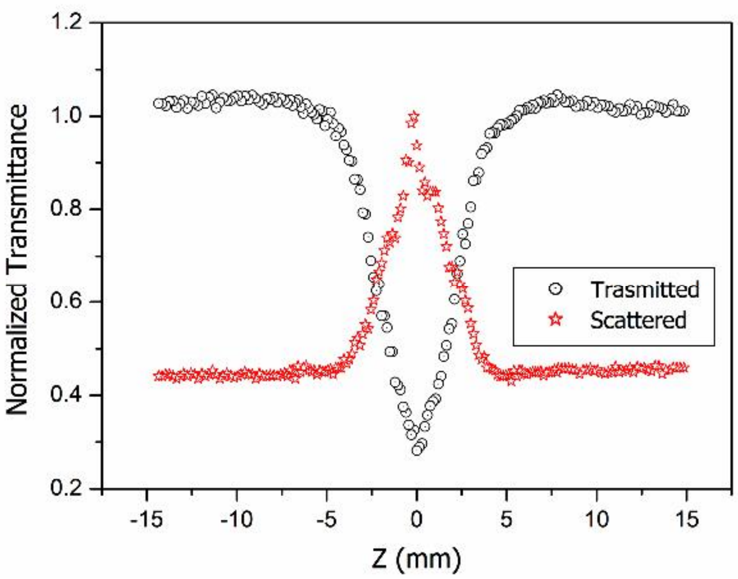

Figure 2.10: Nonlinear scattering observed in the Ag@ZrO$_2$ - PVA film when excited with 532 nm, 7 ns laser pulses.

Therefore the nonlinearity observed can be considered as a combination of three processes: first the SPR saturation, which contributes to a saturation at moderate fluences, then an effective two-photon absorption (comprising of genuine two photon absorption and reverse saturable absorption) and finally nonlinear scattering. The last two effects are responsible for the optical limiting behaviour. Therefore an effective nonlinear absorption coefficient $\alpha(I)$, given by,

$$\alpha(I)=\frac{\alpha_0}{1+\left(\frac{I}{I_s}\right)}+\beta_{eff}I \qquad -(2.29)$$

can be considered, where α_0 is the unsaturated linear absorption coefficient at the wavelength of excitation, I is the input laser intensity, and I_s is the saturation intensity (intensity at which the linear absorption drops to half its original value). β_{eff} is the effective nonlinear extinction coefficient with contributions from two photon absorption, reverse saturable absorption and nonlinear scattering. For calculating the transmitted intensity for a given input intensity, the propagation equation,

$$\frac{dI}{dz'}=\left[\left(\alpha_0\middle/1+\left(I\middle/I_s\right)\right)+\beta_{eff}I\right]I \qquad -(2.30)$$

was numerically solved. Here z' indicates the propagation distance within the sample. From the best fit obtained, the saturation intensity and the effective nonlinear extinction coefficient can be calculated. Figure 2.11 shows the best fit obtained for the z-scan data. The simulated curve is not fully smooth, as we have incorporated the input laser energy fluctuations in the experiment also into the simulation. The value of saturation intensity obtained from the best fit to the experimental data is $8\text{x}10^{11}$ W/m^2, and the value of the effective nonlinear extinction coefficient is $1.9\text{x}10^{-9}$ m/W.

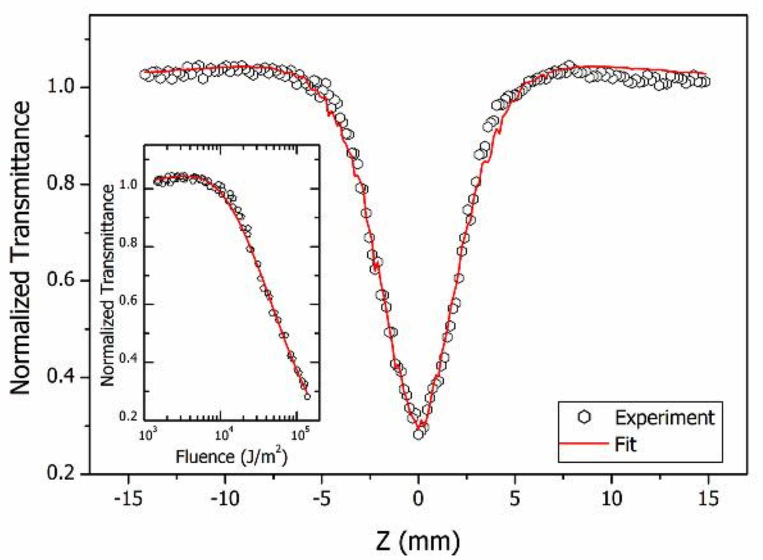

Figure 2.11: The z-scan curve with numerical fitting. Hollow circles are experimental z-scan data and the solid line is the theoretical fit to the data simulated using equation 2.30. Inset shows the corresponding fluence graph.

We investigated the nonlinear transmission of the Ag@ZrO_2 - PVA film at 1064 nm also, using 8 nanosecond pulses. The film showed strong optical limiting at this wavelength as well. In this case, since the SPR of the sample is far away from the excitation wavelength, no saturation behaviour is observed at the moderate fluences. The optical limiting observed has contributions from nonlinear scattering and three-photon absorption. The obtained z-scan curve fits well to an effective three-photon absorption and equation 2.15 was used for numerically fitting the z-scan data. The value of the effective three-photon absorption coefficient obtained is $3.2\text{x}10^{-22}$ m^3/W^2. The absorption spectrum of the film indicates a two-photon induced excited state absorption as the cause for optical limiting at this wavelength. The z-scan curve obtained along with the appropriate 3PA fit is shown in figure 2.12.

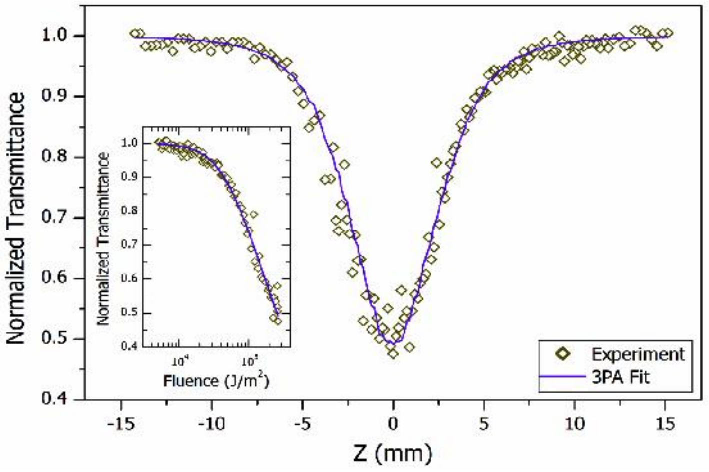

Figure 2.12: Z-scan curve obtained for the Ag@ZrO$_2$ - PVA film under 1064 nm, 8 ns excitation. The solid line is the 3PA fit to the experimental data. Inset shows the corresponding optical limiting curve.

We further investigated the film using 100 femtosecond pulses at 800 nm as well as at 400 nm. The sample showed strong optical limiting at these wavelengths also. As the z-scan measurement is a single pulse measurement, this implies that some components of the nonlinearity associated with the Ag@ZrO$_2$ - PVA samples are ultrafast in nature. This makes the Ag@ZrO$_2$ – PVA sample a potential candidate for ultrafast photonic switching applications. The results obtained for 400 nm, 532 nm, 800 nm and 1064 nm excitation is compiled in figure 2.13.

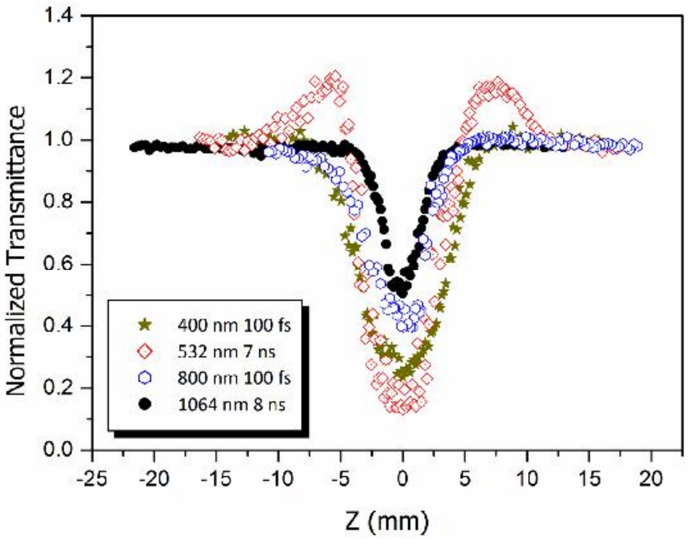

Figure 2.13: Broad band, broad pulsewidth optical limiting characteristics of the Ag@ZrO$_2$ - PVA film.

Similarly, the laser pulsewidth dependence of optical limiting was studied at an excitation wavelength of 800 nm, for 100 fs, 20 ps and 300 ps pulse durations. The same input fluence was used in all these measurements. The corresponding z-scan curves can be seen in figure 2.14. It is found that within these pulsewidth values the nonlinearity is highest for the shortest pulse used.

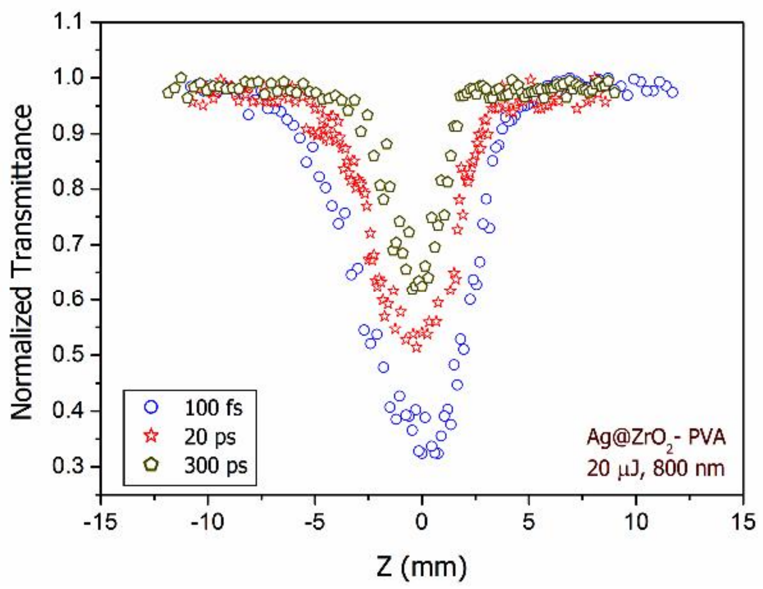

Figure 2.14: Optical limiting seen in the Ag@ZrO$_2$ - PVA film for different input laser pulsewidths.

The above measurements reveal the potential of Ag@ZrO$_2$ - PVA films as a broad wavelength, broad pulse optical limiter. Laser damage threshold measurements conducted on the film show that it has one of the highest laser damage thresholds reported for solid-state optical limiters. For instance, the damage threshold at 1064 nm was found to be 33 J/cm^2 for 8 nanosecond pulses {15}. In terms of dynamic range and frequency bandwidth, this sample is one of the best optical limiters reported in literature so far.

2.5 Nonlinear transmission in tellurium (Te) and silver telluride (Ag$_2$Te) nanowires

The optical limiting properties of a few metal nanowires (Cu, Co, Ni, Pd, Pt and Ag) have been studied recently by Pan and colleagues {16} using 7 ns laser pulses, and results obtained at 532 and 1064 nm indicate that they have broadband optical limiting capabilities. The observed optical limiting in some of them is comparable to or better than that of carbon nanotubes (CNTs). Taking cue from this report, we studied the nonlinear absorption properties of tellurium (Te) and silver telluride (Ag_2Te) nanowires suspended in water. The sample synthesis details can be found in reference 17 {17}. Silver telluride is a semiconductor which can be doped to give both n-type and p-type properties. It has the potential to act as a photonic as well as an electronic device, which will be of significance in optoelectronic systems. Ag_2Te is also known to show a large magnetoresistance. A chemical route was followed for the synthesis of these anisotropic structures. The absorption spectra of the prepared Te and Ag_2Te nanowires are shown in figure 2.15. In general, the absorption spectrum of Te nanowires has two characteristic peaks; peak I and peak II. Peak I appears in the range of 250-350 nm, and it is due to the transition from p-bonding valence band to the p-antibonding conduction band. Peak II appears around 600-850 nm, and it is due to the transition from p-lone pair valence band to the p-antibonding conduction band {17,18}.

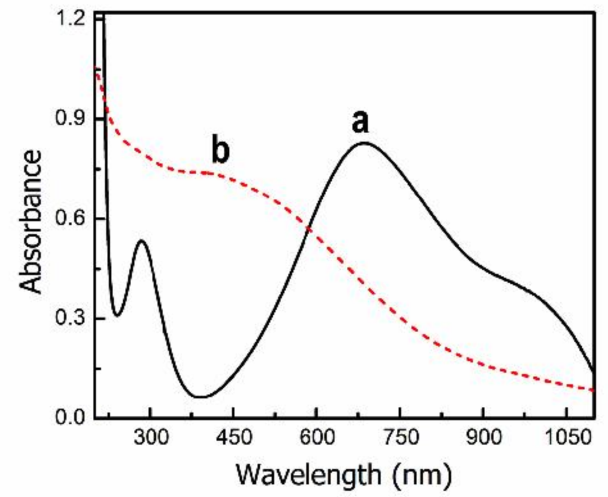

Figure 2.15: Absorption spectrum of the prepared (a) Te nanowires, (b) Ag_2Te nanowires.

In this synthesis, peak I appeared at 284 nm and peak II appeared at 685 nm. Ag_2Te nanowires show a broad peak at 480 nm. It is interesting to note that for Te nanowires the absorbance is nearly the same at the optical excitation wavelengths of 532 and 1064 nm. In general, such a feature can be advantageous in the design of broadband optical limiters.

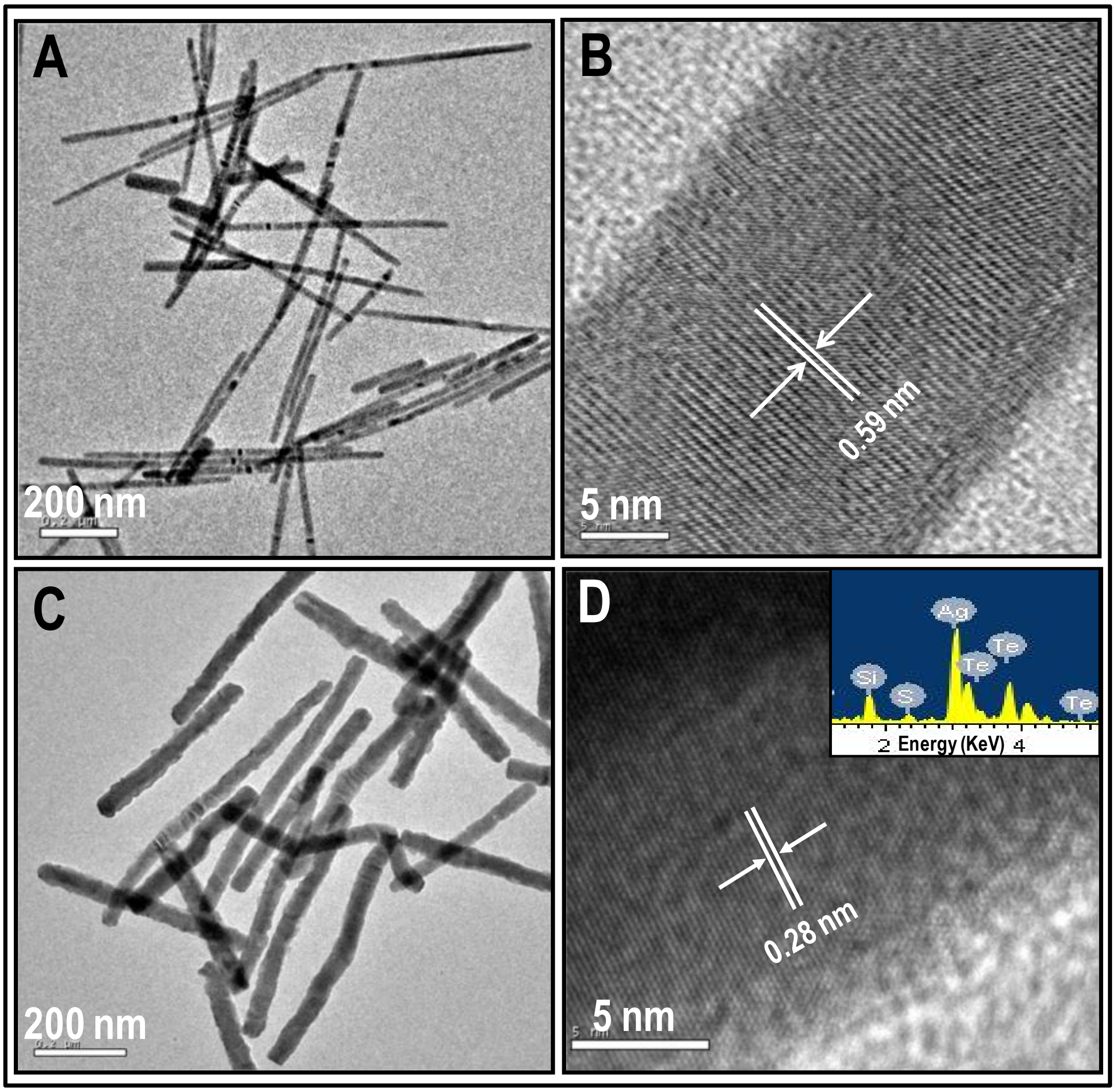

Figure 2.16: (A) Large area TEM image of Te nanowires, (B) lattice resolved HRTEM image of the body of a single Te nanowire, (C) large area TEM image of Ag_2Te nanowires, and (D) lattice resolved HRTEM image of the body of a single Ag_2Te nanowire. Inset of D shows EDAX spectrum of Ag_2Te nanowires.

Figure 2.16(A) depicts a large area TEM image of Te nanowires. All the nanowires are found to be uniform in size. The length and width of the Te nanowires are around 600 and 20 nm, respectively. Figure 2.16(B) shows lattice resolved HRTEM image of the body of a single nanowire. The interplanar distance is found to be 0.59 nm, corresponding to the (001) plane of Te. There are no dislocation and planar defects on the nanowires, indicating that these are single crystalline. Figure 2.16(C) shows the large area TEM image of Ag_2Te nanowires and figure 2.16(D) shows the lattice resolved HRTEM image of the body of a single Ag_2Te

nanowire. The inter planar spacing is found to be 0.28 nm, corresponding to the (220) lattice plane of Ag_2Te nanowire. Inset of figure 2.16(D) shows the EDAX spectrum of Ag_2Te which confirms the presence of silver. The Si and S peaks are due to the glass substrate and sodium dodecyl sulfate (SDS) surfactant used in the synthesis of nanowires, respectively.

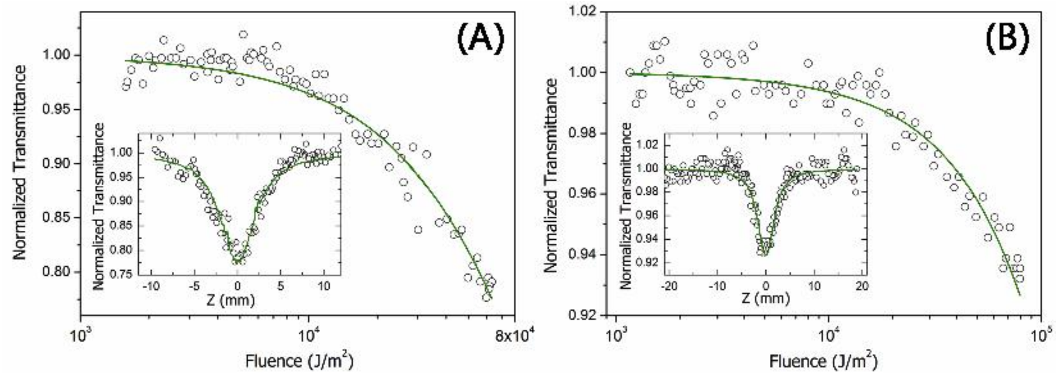

Figure 2.17: Nonlinear absorption in Te nanowires at (A) 532 nm and (B) 1064 nm. Insets show the corresponding z-scan curves. Circles are data points and solid curves are numerical fits using equation 2.30.

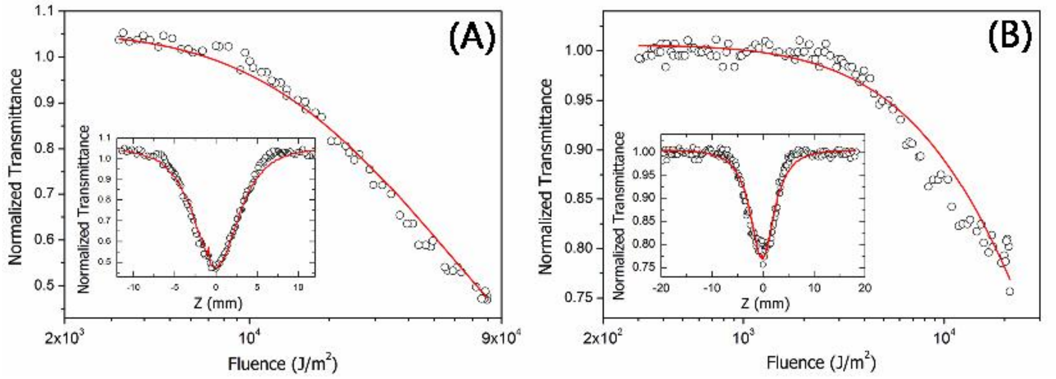

Figure 2.18: Nonlinear absorption in Ag_2Te nanowires at (A) 532 and (B) 1064 nm. Insets show the corresponding z-scan curves. Circles are data points and solid curves are numerical fits using equation 2.30.

Figures 2.17(A) and 2.17(B) show the optical limiting curves obtained for Te nanowires for 532 and 1064 nm excitations, respectively. Figures 2.18(A) and 2.18(B) are similar results for Ag_2Te nanowires. At 1064 nm excitation the limiting is relatively weaker in both cases. The samples were taken in 1 mm cuvettes for the z-scan measurements. The linear transmission values were 75% and 70% at 532 nm and 80% and 77% at 1064 nm, for Te and Ag_2Te respectively.

In general, optical limiting behavior of a medium can have contributions from effects such as RSA, free-carrier absorption, two- or three-photon absorption (2PA, 3PA), self-focusing, self-defocusing, thermal blooming, and nonlinear scattering. Similar to the previous observation by Pan et.al. {16} in other metal nanowires, we also noticed nonlinear scattering from the present Te and Ag_2Te samples (figures 2.19(A) and 2.19(B)). The scattered light was detected by an uncalibrated photodiode while transmitted light was detected by a calibrated pyroelectric detector. The scattered and transmitted intensities look comparable in the graphs because normalized quantities are used for plotting. In absolute terms, the scattered intensity seen by the photodiode is much smaller than the transmitted intensity seen by the pyroelectric detector.

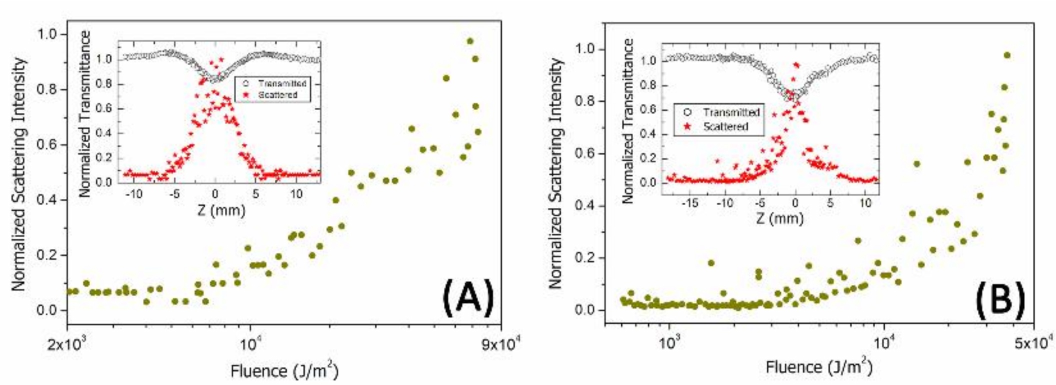

Figure 2.19: Nonlinear scattering in Ag_2Te nanowires for excitation at (A) 532 nm and (B) 1064 nm.

The fact that nonlinear scattering was relatively weaker in comparison to the nonlinear absorption was evident while trying to fit experimental data to the standard nonlinear transmission equations also. Similar to the case of $Ag@ZrO_2$ – PVA films, it turned out that there are two predominant causes for the nonlinearity: one is a saturation of the ground state absorption, and the other is an absorption by the excited state. Saturable absorption is more obvious in the z-scan curves obtained for samples of higher concentration, as seen in figure 2.20. The first graph is for a transmission value of 50% while the second is for 60% and the last is for 75%, when taken in a 1 mm cuvette. Saturation absorption behavior is clearly evident in the T=50% sample, as “humps” flanking the “valley” in the z-scans.

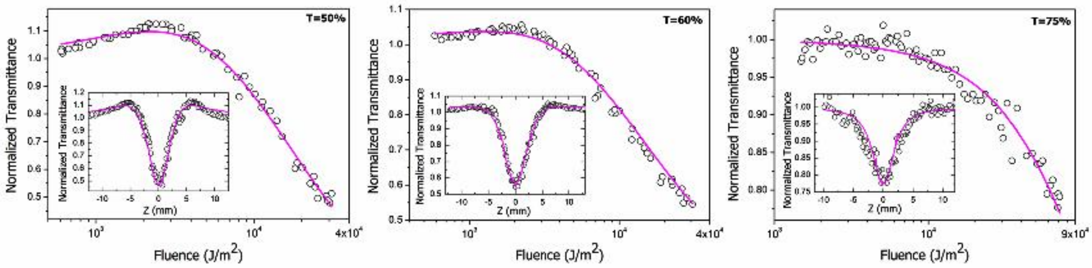

Figure 2.20: Nonlinear transmission behavior of Te nanowires at different concentrations.

Therefore an effective nonlinear absorption coefficient $\alpha(I)$, given by equation 2.29, can be considered. For calculating the transmitted intensity for a given input intensity, the propagation equation, equation 2.30, was numerically solved. By determining the best-fit curves for the experimental data, the nonlinear parameters could be calculated, which are given in table 2.1.

Wavelength (nm)	Te Nanowire			Ag_2Te Nanowire		
	α (m^{-1})	I_s (W/m^2)	β_{eff} (m/W)	α (m^{-1})	I_s (W/m^2)	β_{eff} (m/W)
532	287.68	$1.6x10^{13}$	$3.8x10^{-11}$	356.67	$1.8x10^{12}$	$1.5x10^{-10}$
1064	223.14	$1.9x10^{13}$	$1.7x10^{-11}$	261.36	$2.5x10^{13}$	$1.6x10^{-10}$

α = Linear absorption coefficient, I_s = Saturation Intensity, β_{eff} = Nonlinear extinction coefficient.

Table 2.1: Linear and nonlinear optical properties of Te and Ag_2Te nanowires at the studied concentrations.

It is seen that for both excitation wavelengths of 532 nm and 1064 nm, while β_{eff} is in the order of 10^{-11} m/W for Te, it is one order of magnitude higher at 10^{-10} m/W for Ag_2Te. Thus an obvious enhancement in the nonlinearity has been achieved from the presence of nano Ag in the composite. In comparison, when excited using 7 ns laser pulses at 532 nm, Bi nanorods gave a β_{eff} value of 10^{-11} m/W {19}, Cu nanocomposite glasses were between 10^{-12} to 10^{-10} m/W {20}, Au-Ag core-shell nanoparticles were between 10^{-10} to 10^{-9} m/W {21}, and CdS quantum dots were at 10^{-9} m/W {22}. The relatively lower optical limiting efficiency in the case of the Te nanowire sample can be a consequence of the lower nonlinear scattering seen in the Te nanowires.

In conclusion, reverse saturable absorption is found to be the major contributor to the observed optical limiting in Te and Ag_2Te nanowires, with a relatively minor contribution from nonlinear scattering. The nonlinear extinction coefficient measured in Ag_2Te nanowires is one order of magnitude larger than that in Te nanowires. These values are comparable to the values obtained earlier in certain other metal and semiconductor nanosystems. Occurrence of optical limiting at both wavelengths indicates the potential of these samples to be used as broadband optical limiters.

2.6 Third-order nonlinear susceptibility ($\chi^{(3)}$) measurements in silver nanoparticles

For noble metals, in particular gold and silver, the optical properties are determined by the 5d and 6s–p (conduction) band electrons. The outermost d and s electrons of the constituent atoms together form a total of six bands, with five of them (the d bands) fairly flat and lying a few eV below the Fermi level, while the sixth band (the s–p band) is almost free electron-like: roughly parabolic with an effective mass very close to that of an electron. Nanoparticles of noble metals exhibit the surface plasmon resonance (SPR) in an electromagnetic field, which is a collective oscillation of the conduction electrons occupying states near the Fermi level. A singular property of the SPR is that it leads to a large local field enhancement within the metal particle. This effect can be appreciable with laser excitation, where the electric field associated with the electromagnetic radiation is quite high. In the quasi-static limit the local field inside a spherical particle E_{loc} is related to the applied field E_0 by $E_{loc} = [3\varepsilon_m(\omega)/(\varepsilon_m(\omega) + 2\varepsilon_d(\omega))]E_0 = f(\omega)E_0$, where ε_d is the dielectric constant of the surrounding medium; $f(\omega)$ is defined as the local field factor. At the SPR peak the local field factor has the maximum value, given by $|f_{max}(\omega p)|^2 = |3\varepsilon_1/2\varepsilon_2|^2$. Since the real part of the dielectric constant is larger than the imaginary part in noble metals, they experience strong local field enhancements upon laser irradiation. Therefore, the effective third-order nonlinear susceptibility $\chi^{(3)}(\omega)$ will be strongly enhanced in the SPR region.

It has been shown that there are three major electronic contributions to the Kerr nonlinearity in metal nanoparticles {23}. The first one, $\chi^{(3)}_{\text{intra}}$, is derived from the intra-band conduction electrons in the s–p band. It originates totally due to the confinement of the free electrons, and is strongly size dependent. The second is from inter-band transitions between the d-bands and the conduction band which occurs when the photon energy is larger than a gap energy, $E_g = \hbar\omega_g$. Inter-band transitions can saturate leading to a mostly imaginary and negative $\chi^{(3)}_{\text{inter}}$, and this contribution is size and shape independent down to very small sizes of about 2.5 nm. The third and most important contribution $\chi^{(3)}_{\text{he}}$ arises from hot electrons. By photoexcitation, conduction electrons can be easily elevated to temperatures of several hundred degrees as their specific heats are very small {24}, generating hot electrons. It takes a few picoseconds for these electrons to thermalize with the lattice. During this time, the Fermi–Dirac electron distribution is modified, since part of the one-electron levels below the Fermi level is emptied and part of those above is occupied. This leads to a modification of the dielectric constant $\varepsilon(\omega)$, and the main contribution to the incremental $\delta\varepsilon_m$ will be from those states in the Brillouin zone for which the energy difference between the Fermi level and the d-bands is close enough to the excitation energy. Writing $\varepsilon(\omega) = \varepsilon_X + \varepsilon_L + \varepsilon_D$ where ε_D is the Drude contribution of the free electrons and ε_X and ε_L are components of $\varepsilon_{\text{inter}}$ with the suffixes denoting the X and L points of the Brillouin zone, respectively, we have $\delta\varepsilon(\omega) \cong (\partial\varepsilon_L/\partial T)\delta T$ where δT is the change in temperature of the free electrons. This modification of $\varepsilon(\omega)$ results in a transient re-distribution of the equilibrium plasmon band: the absorption around the peak is reduced and that at the wings is increased. This transient reduction in absorption is generally referred to as ‘plasmon band bleach’ in literature {25, 26}.

Degenerate four wave mixing (DFWM) is the experimental technique mostly used for measuring the third-order susceptibility ($\chi^{(3)}$) of samples. In the following section, we describe essential features of the DFWM method, and experimental results of $\chi^{(3)}$ measurements in silver nanoparticles.

2.6.1 The degenerate four-wave mixing (DFWM) experiment

In the four wave mixing process, three coherent waves are incident on a nonlinear medium, and a fourth wave (the phase conjugate) is generated. This phase conjugate wave is dependent on a coupling coefficient κ that is proportional to the effective $\chi^{(3)}$ for the interaction. Hence measurements of the phase conjugate intensity can yield the $\chi^{(3)}$ tensor components of the medium {27}. If the three incident waves have the same frequency, then it is known as a degenerate four wave mixing process. This is a popular method for characterizing third-order nonlinear materials. Using various combinations of polarizations for the three beams employed in this experiment, it is possible to measure all of the independent tensor components of the $\chi^{(3)}$ of an isotropic material.

Forward and backward geometries can be used for the DFWM measurement depending on the choice of the experimental conditions {28}. The schematics for the forward and backward four wave mixing geometries are shown in figure 2.21.

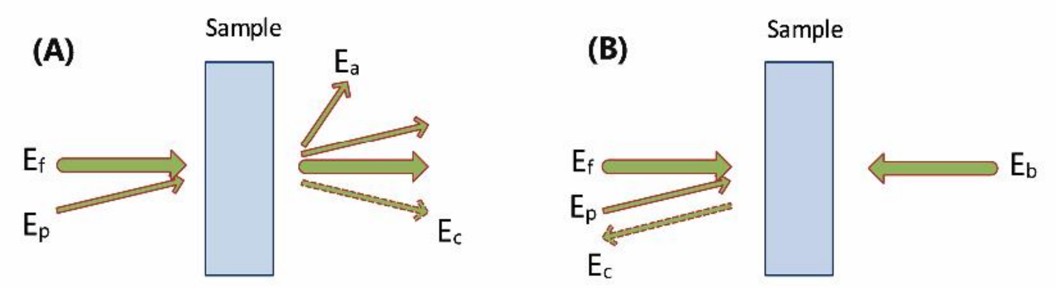

Figure 2.21: Schematic for degenerate four wave mixing experiment. A) Forward geometry. B) Backward geometry.

The forward DFWM involves one pump beam (E_f) and one probe beam (E_p). The probe beam is incident on the sample from the same side and overlaps with the pump inside the sample. The output waves are the transmitted pump and probe, a conjugate wave (E_c) and a fourth wave called the auxiliary wave (E_a). In the backward DFWM geometry, there are two pump beams which are counter propagating (labeled in the figure as E_f and E_b). The probe beam is incident on the sample at a small angle to the direction of the forward pump beam. A fourth beam is generated, which is the signal beam. It is phase-conjugate to the probe beam, and propagates exactly opposite to the probe beam direction.

Another popular geometry of the forward DFWM is the '*Folded Boxcars*' configuration. In this case, the incident beam is split into three and these three beams are aligned such that they form three corners of a square, as shown in figure 2.22. The diametrically opposite beams are the pump beams, which have the same intensity. The third beam is the probe, which has a much lower intensity compared to the pump beams. These three beams will interact nonlinearly when focused on to the sample to generate a fourth beam, which is the signal beam. It will appear at the fourth corner of the square, as shown in figure 2.22.

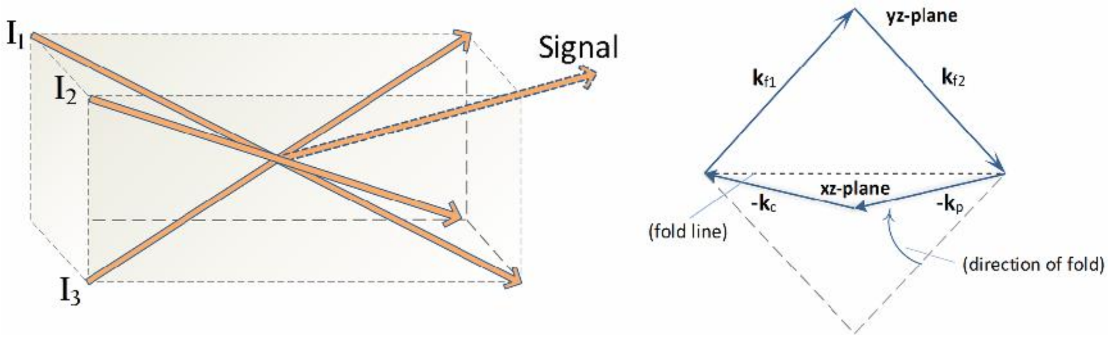

Figure 2.22: Folded Boxcars form of forward DFWM. The phase matching diagram illustrating the folded box is also shown.

Measurement of $\chi^{(3)}$ by the DFWM technique has several advantages. The samples to be analyzed can be in a variety of forms, and for isotropic materials, all the independent $\chi^{(3)}_{ijkl}$ can be measured in a single experimental setup. The phase conjugate signal can easily be distinguished by the spatial separation from the other interacting beams. The phase conjugate signal has a cubic dependence on the pump laser intensity ($I_c \propto I^3$) which can easily be checked for verifying the experimental setup. Moreover, the temporal evolution of the nonlinearity can also be measured by introducing a delay line in one of the incident beams {27}.

2.6.2 DFWM in isotropic media

For a centrosymmetric (isotropic) medium, the interaction of the three input waves in DFWM will generate a third-order polarization oscillating at the same frequency ω given by {8},

$$P_c^{(3)} = 6\varepsilon_0 \chi_{\text{eff}}^{(3)} A_{\text{f}} A_{\text{b}} A_{\text{p}}^* \exp[i(\mathbf{k}_{\text{f}} + \mathbf{k}_{\text{b}} - \mathbf{k}_{\text{p}}).\mathbf{r}] \qquad \text{- (2.31)}$$

where

$$\chi_{\text{eff}}^{(3)} = \hat{e}_c \cdot \boldsymbol{\chi}^{(3)}(-\omega;\omega,\omega,-\omega) : \hat{e}_{\text{f}} \hat{e}_{\text{b}} \hat{e}_{\text{p}}^* \qquad \text{- (2.32)}$$

The polarization is proportional to the conjugate (negative frequency component) of the probe wave so that the net frequency is ω. Since $\mathbf{k}_{\text{f}} = \mathbf{k}_{\text{b}}$ and $\mathbf{k}_{\text{p}}=-\mathbf{k}_{\text{c}}$; the DFWM process is automatically phase matched.

Similar third-order polarizations can be written for the other three waves. Because of permutation symmetry for this nonresonant process, they will all have the same $\chi_{\text{eff}}^{(3)}$. The third-order polarization couples the four waves. Substituting the expressions for the nonlinear polarization into the wave equation and employing the slowly varying amplitude approximation yields four first-order coupled differential equations that describe the spatial evolution of the waves in this process. The usual case involving strong pump beams of approximately equal amplitude allows one to ignore the pump beam equations. This is the nondepleted pump regime where A_{f} and A_{b} are approximately constant throughout the medium. The equations for the probe and conjugate waves are then given by,

$$\frac{dA_p}{dz} = i\kappa A_c^* \qquad \text{- (2.33)}$$

and $$\frac{dA_c^*}{dz} = i\kappa^* A_p \qquad \text{- (2.34)}$$

where $$\kappa = \frac{3\omega}{n_0 c} \chi_{\text{eff}}^{(3)} A_{\text{f}} A_{\text{b}} \qquad \text{- (2.35)}$$

is called the coupling coefficient. Here n_0 is the refractive index of the sample. In deriving these equations, it is assumed that the angle θ between the probe and forward pump beams is small. Otherwise, the left-hand side of equations 2.32 and 2.33 should be multiplied by $\cos\theta$. Using the boundary conditions, $A_p(0)$ is nonzero and $A_c(L) = 0$, the solutions to the above coupled equations can be obtained as,

$$A_p(z) = \frac{\cos\left(|\kappa|(z-L)\right)}{\cos\left(|\kappa|L\right)} A_p(0) \qquad \text{- (2.36)}$$

and

$$A_c(z) = -i\frac{\kappa \sin\left(|\kappa|(z-L)\right)}{|\kappa|\cos\left(|\kappa|L\right)} A_p^*(0) \qquad \text{- (2.37)}$$

The conjugate reflectance is given by the ratio of intensities of the conjugate beam and the input pump beam, I_c/I_p, and it is given by,

$$R = \tan^2|\kappa|L \qquad \text{- (2.38)}$$

For small values of $|\kappa|L$, which is the experimental condition in most of the cases, the conjugate reflectance can be written as,

$$R \cong \left(|\kappa|L\right)^2, \text{ when } |\kappa|L \ll 1 \qquad \text{- (2.39)}$$

In the case of an off-resonant measurement, under the usual conditions, where $I_f = I_b = I_{pump}$,

$$R \cong \left(|\kappa|L\right)^2 = \left(\frac{3\pi L}{\varepsilon_0 n_0^2 c\lambda}\right)^2 \left(\chi_{\text{eff}}^{(3)}\right)^2 I_{pump}^2 \qquad \text{- (2.40)}$$

Here n_0 is the linear refractive index of the sample of length L and λ is the wavelength of the interacting light.

It is easier to measure the intensity of the conjugate beam rather than the reflectance. If the probe intensity is related to the pump intensity by $I_p = \eta I_{pump}$, then the phase conjugate intensity can be written as, $I_c = \eta|\kappa L|^2 I_{pump}$. The data can thus be fitted to an equation of the form,

$$I_c = bI_{pump}^3 \qquad \text{- (2.41)}$$

and

$$\chi_{\text{eff}}^{(3)} = \frac{\varepsilon_0 n_0^2 c\lambda}{3\pi L}\sqrt{\frac{b}{\eta}} \qquad \text{- (2.42)}$$

The coefficient b can be determined by the least-squares fit of equation 2.41 to the data. However this requires precise measurements of the pump intensity. i.e., the beam 1/e^2 radius and, for pulsed lasers, the pulse width, must be measured with high accuracy, which is a different task. Therefore it is more common to make measurements with respect to a standard reference sample whose $\chi^{(3)}$ is known, to avoid the need to characterize these laser parameters precisely.

In such relative measurements, the same experiment described above is performed on a standard, well-characterized reference also, in addition to the sample, under identical conditions. The peak intensity is proportional to the average power or pulse energy, the measurement of which is more straightforward. Thus to within a proportionality constant that is the same in both measurements, of the sample and of the standard, the conjugate power or energy or the conjugate reflectance data can be fitted to a formula of the form

$$I_c = b\mathrm{E}_{pump}^3 \qquad \text{- (2.43)}$$

where $\mathrm{E}_{\mathrm{pump}}$ is the pump pulse energy. Once both the sample and the reference data have been fitted to the formula of the form of equation 2.43, the sample susceptibility is given by

$$\chi^{(3)} = \chi_R^{(3)}\left(\frac{b}{b_R}\right)^{1/2}\left(\frac{n_0}{n_R}\right)^2\left(\frac{L_R}{L}\right) \qquad \text{- (2.44)}$$

where the subscript R refers to the reference quantities.

For samples that have a linear absorption at the laser wavelength used for the experiment, the phase conjugate signal will be modified. In this case the linear absorption coefficient must be taken into account to extract the true value of the third-order susceptibility. For measurements where $|\kappa| L \ll \alpha L \ll 1$, the effective $\chi^{(3)}$ can be found using the equation {8},

$$\chi^{(3)} = \chi_R^{(3)} \left(\frac{b}{b_R} \right)^{1/2} \left(\frac{n_0}{n_R} \right)^2 \left(\frac{L_R}{L} \right) \left(\frac{\alpha L \mathrm{e}^{(\alpha L/2)}}{1 - \mathrm{e}^{(-\alpha L)}} \right) \qquad \text{- (2.45)}$$

Here α is the linear absorption coefficient of the sample. The reference is assumed to have no linear absorption at the excitation wavelength.

2.6.3 $\chi^{(3)}$ measurements in silver nanoparticles

We employed the folded forward boxcars geometry for our degenerate four wave mixing experiments. 7 ns laser pulses at 532 nm were used for the experiment. Absorptive type neutral density filters were used to change the intensity of the input laser beam. Colloidal silver nanoparticles of about 30 nm average size were prepared through the wet chemical method {29}. For this, stock 10^{-3} M silver nitrate solution and a stock 1% tri-sodium citrate solution were prepared by dissolving appropriate amounts of the respective salts in doubly distilled water. 200 ml of the prepared $AgNO_3$ solution was heated to boiling, and to this 10 ml of the 1% tri-sodium citrate solution was added drop by drop with vigorous magnetic stirring. Heating and stirring were continued for about 6 minutes, till the color change became evident (pale yellow). The colloidal solution obtained was then rapidly cooled in a water-bath. The UV-Vis absorption spectrum of the nanoparticle colloidal solution is given in figure 2.23. The formation of the nanoparticles was confirmed by the SPR peak at 409 nm in the absorption spectrum. The mechanism of the reaction can be expressed as follows,

$$4Ag^+ + C_6H_5O_7Na_3 + 2H_2O \rightarrow 4Ag + C_6H_5O_7H_3 + 3Na^+ + H^+ + O_2 \uparrow$$

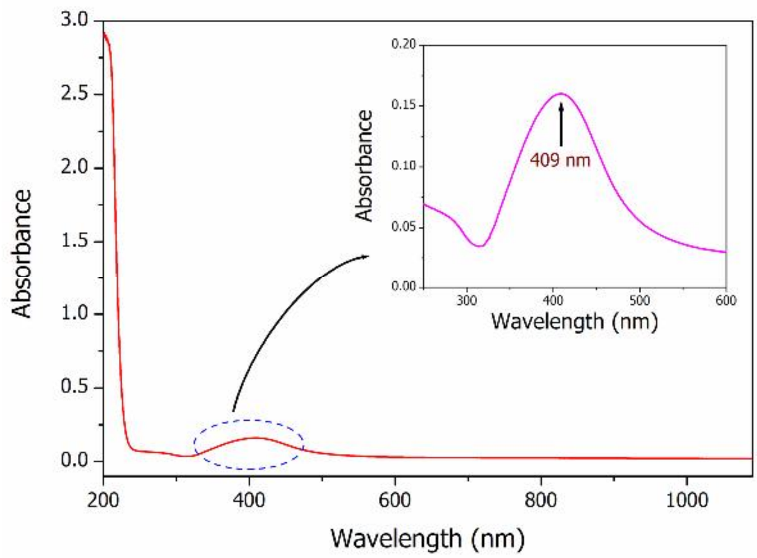

Figure 2.23: Absorption spectrum of the prepared silver nanoparticles. The SPR peak wavelength is 409 nm (inset).

The nanoparticle colloidal solution was taken in a 2 mm glass cuvette. The linear transmission of the sample was 78%. The input energy was monitored using a pyroelectric energy probe, and the generated signal beam was measured in the far field using a calibrated photodiode. HPLC grade carbon disulphide (CS_2) purchased from Merck was used as the reference sample.

Figure 2.24(A) shows the variation of the DFWM signal as a function of the pump intensity, obtained for the reference sample, CS_2. The DFWM signal obtained for the silver nanoparticles is shown in figure 2.24(B). The signal is proportional to the cubic power of the input intensity as given by the equation,

$$I(\omega) \propto \left(\frac{\omega}{2\varepsilon_O c n^2}\right)\left|\chi^{(3)}\right|^2 L^2 I_0^3(\omega) \qquad - (2.46)$$

where, $I(\omega)$ is the DFWM signal intensity, $I_o(\omega)$ is the pump intensity, L is the length of the sample and n is the refractive index of the medium. The solid curve in the figure is the cubic fit to the experimental data.

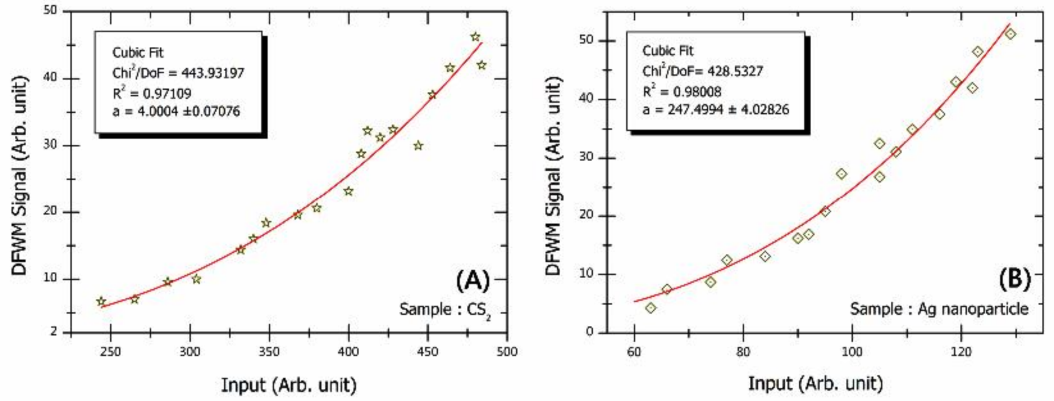

Figure 2.24: DFWM signal obtained in CS_2 (A) and silver nanoparticle (B) samples.

The third-order susceptibility $\chi^{(3)}$ of the sample can then be calculated from the equation,

$$\chi^{(3)} = \chi_R^{(3)} \left[\frac{\left(I \big/ I_0^3 \right)}{\left(I \big/ I_0^3 \right)_R} \right]^{\frac{1}{2}} \left[\frac{n}{n_R} \right]^2 \frac{L_R}{L} \left(\frac{\alpha L}{\left(1 - e^{-\alpha L}\right) e^{-\alpha L/2}} \right) \qquad \text{- (2.47)}$$

where the subscript 'R' refers to the standard reference, CS_2. '$\chi^{(3)}_R$' is taken to be 2.8x 10^{-20} m^2/V^2 {8}. The value of $\chi^{(3)}$ obtained is 28.16x10^{-20} m^2/V^2 (2.01x10^{-11} esu). The figure of merit of nonlinearity, F, given by $\chi^{(3)}/\alpha$ is calculated to be 2.27x10^{-21} m^3/V^2 (1.62x10^{-11} esu cm). F is a measure of nonlinear response that can be achieved for a given absorption loss in the medium. The F value is useful for comparing the nonlinearity of different materials when excited in spectral regions of non-zero absorption. The $\chi^{(3)}$ values obtained are comparable with those obtained in poly vinyl carbazole (10x10^{-20} m^2/V^2) {30}, carbon nanotubes (0.59x10^{-11} esu) {31}, and poly-1,6-heptadiester (6x10^{-11} esu) {32}. Much higher values of $\chi^{(3)}$ of the order of 10^{-6} to 10^{-9} esu are reported in semiconductor quantum dots, nanoparticles, conjugated polymers and organometallics, when excited resonantly {33–37}. In our experiment, the excitation used is off-resonant (78% transmission for 2 mm sample thickness, ie., linear absorption coefficient of 124 m^{-1} (1.24 cm^{-1})). Off-resonant excitations often result in reduced $\chi^{(3)}$ values. However the figure of merit value obtained is comparable to the highest F values reported in literature {34,38,39}. The F values reported for resonant excitation measurements are generally an order of magnitude lower (~10^{-12} esu cm) {33,36,40,41} than the value obtained in the present experiment. Larger F values are desirable in optical signal processing applications.

2.7 Conclusions

The results obtained from the above experiments show that metal nanostructures possess a large potential for nonlinear optical applications. From open-aperture z-scan experiments Ag@ZrO_2-PVA nanocomposites are found to exhibit very good broadband optical limiting activity at different excitation pulsewidths, with a remarkably high laser damage threshold. Te and Ag_2Te nanowires in solution also show good optical limiting. In general, the combination of different limiting mechanisms improves the overall limiting performance in these materials. The excellent optical limiting properties of nanoparticle-embedded solid-state thin films open up a way to design and fabricate commercially viable optical limiters. Degenerate four wave mixing experiments in silver nanoparticles reveal a high figure of merit (F) values for third-order nonlinearity, which will have potential applications in photonic devices and optical signal processing.

References

1. *Enhancement of polycrystalline silicon solar cells using ultrathin films of silicon nanoparticle*, M. Stupca, M. Alsalhi, T. Al Saud, A. Almuhanna, and M. H. Nayfeh, Appl. Phys. Lett., **91**, 063107 (2007).
2. *Optical Properties of Metal Clusters*, U. Kreibig and M. Vollmer, Springer-Verlag, Berlin, (1995).
3. *Metal nanoparticles: Synthesis, Characterization, and Applications*, D. L. Feldheim, and C. A. Foss Jr., Marcel Dekker, New York (2002).
4. *Dynamical polarizability of small metal particles: self-consistent spherical jellium background model*, W. Ekardt, Phys. Rev. Lett. **52**, 1925 (1984).
5. *Lasers*, A. E. Siegman, University Science, Mill Valley, CA. (1986).
6. *Strong-field saturation effects in laser media*, D. H. Close, Phys. Rev., **153**, 360 (1966).
7. *An analysis of saturable absorbers*, M. Hercher, Appl. Opt. **6**, 947 (1967).
8. *Handbook of Nonlinear Optics*, R. L. Sutherland, Second Edition, Marcel Dekker, New York (2003).
9. *Inorganic and hybrid nanostructures for optical limiting*, J. Wang and W. J. Blau, J. Opt. A: Pure and Appl. Opt., **11**, 024001 (2009).
10. *A review of optical limiting mechanisms and devices using organics, fullerenes, semiconductors and other materials*, L. W. Tutt and T. F. Boggess, Prog. Quantum Electron., **17**, 299 (1993).
11. *Sensitive measurement of optical nonlinearities using a single beam*, M. Sheik-Bahae, A.A. Said, T.H. Wei, D.J. Hagan, and E.W. Van Stryland, IEEE J. Quantum Electron., **QE-26**, 760 (1990).
12. *ZrO_2 bubbles from core-shell nanoparticles*, A. Sreekumaran Nair, Renjis T. Tom, V. Suryanarayanan and T. Pradeep, J. Mater. Chem., **13**, 297 (2003).
13. *Synthesis of luminescent thin-film CdSe/ZnSe quantum dot composites using CdSe quantum dots passivated with an overlayer of ZnSe*, P. S. M. Danek, K. F. Jensen, C. B. Murray, and M. G. Bawendi, Chem. Mater., **8**, 173 (1996).
14. *Redox catalysis using Ag@SiO_2 colloids*, T. Ung, L. M. Liz-Marzan, and P. Mulvaney, J. Phys. Chem. B, **103**, 6770 (1999).

15. *An optical limiting device with the highest known laser damage threshold and method of preparation thereof*, T. Pradeep, A. Sreekumaran Nair, R. Philip and Suchand Sandeep C. S., Indian patent 1273/CHE/2005 published on 2007-07-27.
16. *Optical limiting properties of metal nanowires*, H. Pan, W. Chen, Y. P. Feng, W. Ji, and J. Lin, Appl. Phys. Lett., **88**, 223106 (2006).
17. *Controlled synthesis of crystalline tellurium nanorods, nanowires, nanobelts and related structures by a self-seeding solution process*, U. K. Gautama and C. N. R. Rao, J. Mater. Chem., **14**, 2530 (2004).
18. *Tellurium nanowire-induced room temperature conversion of graphite oxide to leaf-like graphenic structures*, T. S. Sreeprasad, A. K. Samal, and T. Pradeep, J. Phys. Chem. C, **113**, 1727 (2009).
19. *Nonlinear optical scattering and absorption in bismuth nanorod suspensions*, S. Sivaramakrishnan, V. S. Muthukumar, S. S. Sai, K. Venkataramanaiah, J. Reppert, A. M. Rao, M. Anija, R. Philip, and N. Kuthirummal, Appl. Phys. Lett., **91**, 093104 (2007).
20. *Optical and nonlinear optical properties of copper nanocomposite glasses annealed near the glass softening temperature*, B. Karthikeyan, M. Anija, C. S. Suchand sandeep, T. M. Muhammad Nadeer, and R. Philip, Opt. Commun., **281**, 2933 (2008).
21. *$Au_xAg_y@ZrO_2$ core-shell nanoparticles: synthesis, characterization, reactivity and optical limiting*, A. S. Nair, V. Suryanarayanan, T. Pradeep, J. Thomas, M. Anija, and R. Philip, Mater. Sci. Eng. B, **117**, 173 (2005).
22. *Excitonic transitions and off-resonant optical limiting in CdS quantum dots stabilized in a synthetic glue matrix*, P. A. Kurian, C. Vijayan, K. Sathiyamoorthy, C. S. Suchand Sandeep, and R. Philip, Nanoscale Res. Lett., **2**, 561 (2007).
23. *The optical kerr effect in small metal particles and metal colloids: The case of gold*, F. Hache, D. Ricard, C. Flytzanis, and U. Kreibig, Appl. Phys. A, **47**, 347 (1988).
24. *Generation of nonequilibrium electron and lattice temperatures in copper by picosecond laser pulses*, G. L. Eesley, Phys. Rev. B, **33**, 2144 (1986).
25. *Picosecond dynamics of silver nanoclusters. photoejection of electrons and fragmentation*, P. V. Kamat, M. Flumiani, and G. V. Hartland, J. Phys. Chem. B, **102**, 3123 (1998).

26. *Electron dynamics of passivated gold nanocrystals probed by subpicosecond transient absorption spectroscopy*, S. L. Logunov, T. S. Ahmadi, M. A. El-Sayed, T. J. Khoury, and R. L. Whetten, J. Phys. Chem. B, **101**, 3713 (1997).
27. *Optical Phase Conjugation,* R. A. Fisher, Academic Press Inc., San Diego, CA. (1983).
28. *Generation of a phase-conjugate wave in the forward direction with thin Na-vapor cells*, C. V. Heer and N. C. Griffin, Opt. Lett., **4**, 239 (1979).
29. *Adsorption and surface-enhanced Raman of dyes on silver and gold sols*, P. C. Lee and D. Meisel, J. Phys. Chem., **86**, 3391 (1982).
30. *Third-order nonlinear optical susceptibility of polymers based on carbazole derivatives*, I. Fuks, B. Derkowska, B. Sahraoui, S. Niziol, J. Sanetra, D. Bogdal, and J. Pielichowski, J. Opt. Soc. Am. B, **19**, 89 (2002).
31. *Third-order optical nonlinearity of the carbon nanotubes*, X. Liu, J. Si, B. Chang, G. Xu, Q. Yang, Z. Pan, S. Xie, and P. Ye, Appl. Phys. Lett., **74**, 164 (1999).
32. *A 160-femtosecond optical image processor based on a conjugated polymer*, C. Halvorson, A. Hays, B. Kraabel, R. Wu, F. Wudl, and A. J. Heeger, Science, **265**, 1215 (1994).
33. *Nonlinear optical properties of novel low-bandgap polythiophenes*, W. Schrof, S. Rozouvan, T. Hartmann, H. Möhwald, V. Belov, and E. Van Keuren, J. Opt. Soc. Am. B, **15**, 889 (1998).
34. *Large third-order optical nonlinearity in Au:SiO_2 composite films near the percolation threshold*, H. B. Liao, R. F. Xiao, J. S. Fu, P. Yu, G. K. L. Wong, and P. Sheng, Appl. Phys. Lett. **70**, 1 (1997).
35. *DFWM study of thin films containing surface-modified CdS nanoparticles,* T. Yamakia, K. Asaia, K. Ishigurea, K. Sanob and K. Emab, Synth. Met., **103**, 2690 (1999).
36. *Nonlinear optical properties of lead sulfide nanocrystals in polymeric coatings*, S. W. Lu, U. Sohling , M. Mennig, and H. Schmidt, Nanotechnology, **13**, 669 (2002).
37. *Large third-order optical nonlinearity in Au:TiO_2 composite films measured on a femtosecond time scale*, H. B. Liao, R. F. Xiao, H. Wang, K. S. Wong, and G. K. L. Wong, Appl. Phys. Lett., **72**, 1817 (1998).
38. *Optical nonlinearities of a high concentration of small metal particles dispersed in glass: copper and silver particles*, K. Uchida, S. Kaneko, S. Omi, C. Hata, H. Tanji, Y.

Asahara, A. J. Ikushima, T. Tokizaki, and A. Nakamura, J. Opt. Soc. Am. B, **11**, 1236 (1994).

39. *Third-order nonlinear optical property of a polyphenylene oligomer: poly (2,5-dialkozyphenylene)*, J. Wu, J. Yan, D. Sun, F. Li, L. Zhou, and M. Sun, Opt. Comm., **136**, 35 (1997).
40. *Ultrafast optical switching in a silver nanoparticle system*, H. Inouye, K. Tanaka, I. Tanahashi, T. Hattori, and H. Nakatsuka, Jpn. J. Appl. Phys., **39**, 5132 (2000).
41. *Nonlinear Optical properties of Au:*TiO_2 *multilayer composite films*, S. W. Yu, H. B. Liao, W. J. Wen, and G. K. L. Wong, Int. J. Mod. Phys. B, **19**, 2616 (2005).

3

Fine structure in spatial self-phase modulation patterns: at a glance determination of the sign of optical nonlinearity in highly nonlinear films

A fast and simple method to determine the sign of the nonlinear coefficient n_2 in films with high nonlinearity is presented. The method is similar to z-scan but does not require an aperture. It exploits the effect of spatial self-phase modulation and the role of wavefront curvature that leads to a specific far field pattern that is dependent on the sign of n_2 and on the sample position. The method can be considered a 'visualization' of the z-scan for highly nonlinear films. Application to nematic liquid crystals under different experimental conditions confirms the results predicted by theory.

3.1 Introduction

In this chapter we discuss a fast and easy method we devised to determine the sign of optical nonlinearity in thin nonlinear films {1}. Liquid crystals were used as samples for measurement. In general, materials that simultaneously possess some properties typical of liquids and some others typical of solids are termed liquid crystals. These are materials that show mesomorphic (of intermediate form) states, which are aggregation states that lie in between the solid phase and the liquid phase {2}. Most of the time liquid crystals show anisotropic physical properties. Liquid crystals are mainly divided into two categories, namely, thermotropic liquid crystals and lyotropic liquid crystals, depending on the phase inducing factors. In thermotropic liquid crystals, changing the temperature of the system induces the phase transitions. Majority of the liquid crystalline compounds fall in this category. Lyotropic liquid crystalline phases are shown by amphiphilic molecules (molecules which have a hydrophilic and hydrophobic part) dissolved in a solvent. In this case changing the relative concentration of various components of the molecule brings about the phase transitions {3}.

In a mesomorphic compound, the chemical composition produces an orientational order of the molecules. The liquid crystalline phases are generally distinguished by the degree of molecular order they present. In the *'nematic phase'* there exists an orientational order, but no positional order. On the average, molecules align their axes along a preferred direction and hence rotational symmetry around this direction can be found. This will in turn become a locally uniaxial phase. The *'smectic phase'* is characterized by a layered structure. This is more ordered than the nematic phase. If a material posses both nematic and smectic phases, the latter will appear at lower temperatures. The *'cholesteric phase'* is generally considered a chiral nematic phase where the preferred molecular direction is subjected to helical distortion. This phase shows some similarities with the smectic phase as a layered structure sometimes can be identified {4}.

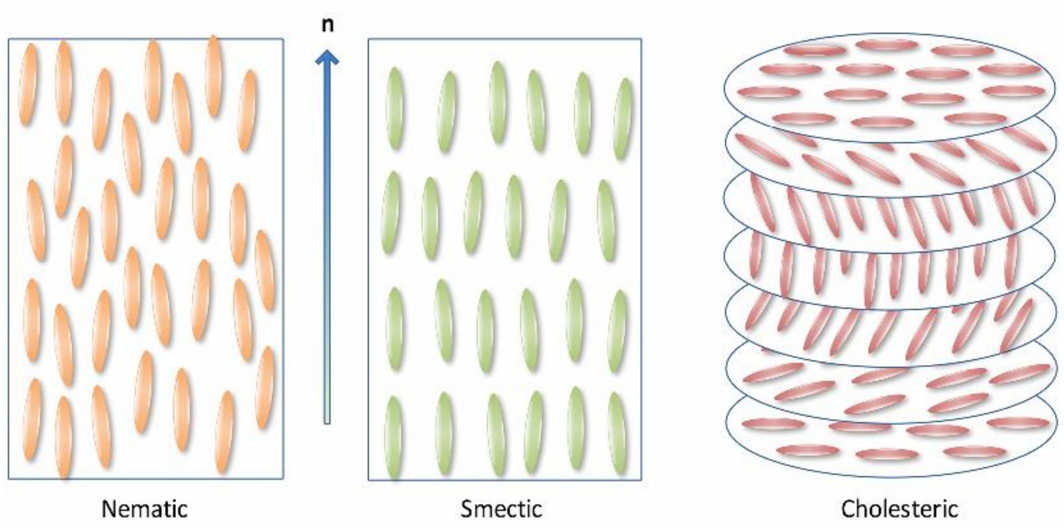

Figure 3.1: Nematic, smectic and cholesteric phases exhibited by liquid crystals.

In all liquid crystals, a preferred local molecular orientation can be found and its direction is usually indicated by a unit vector **n** called "director". This represents the average direction in a small volume, containing many molecules to make a meaningful averaging. The three commonly used director alignments determined by the boundary conditions of the liquid crystals are *homeotropic (HOM), planar* (PLAN) or *homogenous,* and *hybrid* alignments.

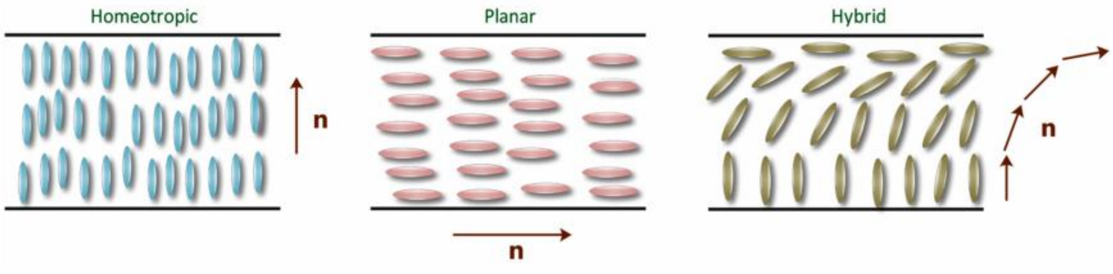

Figure 3.2: Homeotropic, Planar, and Hybrid alignments of liquid crystals.

In homeotropic alignment the director is normal to the surface. In the planar sample, the director alignment is tangential to the boundary. The planar and the homeotropic samples will have uniform alignment in the whole volume. On the contrary, the hybrid alignment is a distorted configuration created by homeotropic orientation at one boundary and planar orientation at the other boundary. Such a hybrid liquid crystal sample is referred to as HAN cell (Hybrid Aligned Nematic). Some other configurations used are the *twisted* and *supertwisted* ones, which are common in display applications {5}. These are often obtained by doping the nematic liquid crystal with a chiral compound (such as a cholesteric compound) and using planar alignments at both the boundaries. The experiments described in this chapter are done on nematic liquid crystal samples of homeotropic and planar alignment.

3.2 Spatial self-phase modulation in thin nonlinear films

When a Gaussian laser beam passes through a nonlinear medium, it may exhibit a characteristic diffraction ring pattern resulting from spatial self-phase modulation (SPM) {6}. In general in a liquid crystal medium, the laser beam can induce an unusually large refractive index modulation due to molecular reorientation {2}. The resulting spatial self-phase modulation on the laser beam usually yields a diffraction pattern in the form of many concentric rings.

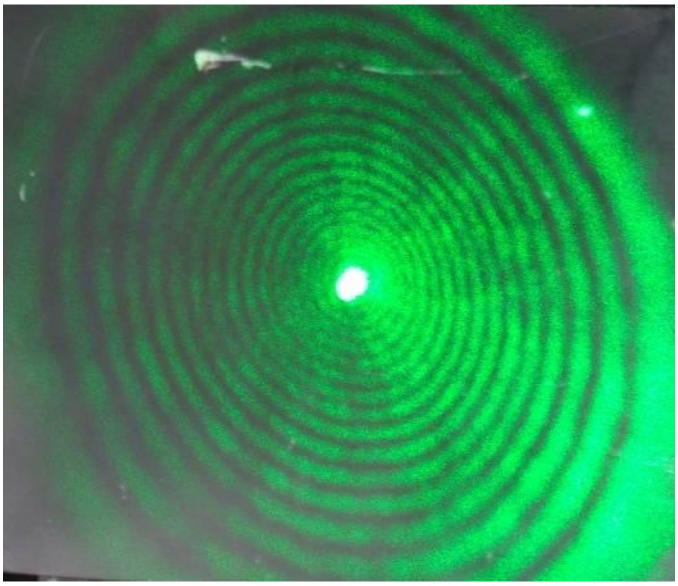

Figure 3.3: SPM rings observed in pentyl-cyanobiphenyl (5CB) nematic liquid crystal.

Self-phase modulation is a consequence of the difference in nonlinear refractive index at different radial positions of a beam due to its non-uniform spatial intensity profile. The variation of the refractive index not only produces different light speeds leading to self-focusing or self-defocusing {7}; but also induces changes in the optical path of each part of the beam. Since the manifestation of SPM is closely related to the temporal and spatial behavior of a light beam, the analysis of the patterns produced by a thick sample becomes very complicated. This is mainly due to the fact that SPM and self-focusing (or self-defocusing) effects can generally coexist in a thick sample and the theoretical treatment becomes rather complex. For the sake of simplicity, we consider only thin nonlinear samples for the analysis in this chapter.

In the case of a thin sample, where self-focusing and self-defocusing effects can be neglected, we can describe the SPM phenomenon caused by a Gaussian beam as diffraction of light through a circular aperture, which introduces a phase shift depending on the local light intensity. The circular aperture corresponds to the beam width on the sample, while the phase shift profile is due to the nonlinear response of the medium. Following the classical theory of Franhoffer diffraction {8} we can write the light field in rectangular coordinates as,

$$U(P) = C\int_A E_i e^{-ik(p\xi+q\eta)} d\xi d\eta \qquad - (3.1)$$

where *(p,q)* is the coordinate of a point P in the diffraction pattern, *(ξ,η)* is the coordinate of a typical point in the aperture and C is a constant. E_i is the incident electric field and *k* is the wave vector of the incident electromagnetic radiation.

For a circular aperture, it is more convenient to use polar coordinates to represent the light field. Let *(ρ,θ)* be the polar coordinates of a typical point in the aperture. We can write,

$$\rho\cos\theta = \xi\,, \qquad \rho\sin\theta = \eta \qquad - (3.2)$$

and let *(ω,ψ)* be the coordinates of a point P in the diffraction pattern referred to the geometrical image of the source. Defining

$$\omega\cos\psi = p\,, \qquad \omega\sin\psi = q \qquad - (3.3)$$

it follows that $\omega = \sqrt{p^2+q^2}$ is the sine of the angle which the direction *(p,q)* makes with the central direction *p=q=0*. If *a* is the radius of the circular aperture, the diffraction integral now can be written as,

$$U(P) = C\int_0^a\int_0^{2\pi} E_i(\quad e^{-ik\rho\omega\cos(\theta-\psi)}\, d\theta d \qquad - (3.4)$$

For an incident Gaussian beam, the electric field can be written as {8},

$$E_i = E_0 e^{-\left(\frac{r^2}{w^2}\right)} e^{-\left(\frac{ikr^2}{2R}\right)} \qquad - (3.5)$$

where *r* is the radial distance of a point on the wave front from the center of the beam, *w* is the beam width, and *R* is the radius of curvature of the wave front. As we can see from the equation, for a Gaussian beam, the intensity is a function of *r*. Hence the nonlinear phase shift introduced at the aperture should also be a function of *r*. If this nonlinear phase shift can be represented by $\varphi_{NL}(r)$, equation 3.4 must be multiplied by a phase factor of $e^{-i\varphi_{NL}}$ {9}.

$$U(P) = C\int_0^a \int_0^{2\pi} E_i(\quad e^{-ik\rho\omega\cos(\theta-\psi)} e^{-i\varphi_{NL}} \; d\theta d \qquad \text{- (3.6)}$$

Using the standard Bessel functions,

$$J_n(x) = \frac{i^{-n}}{2\pi}\int_0^{2\pi} e^{ix\cos\beta} e^{in\beta} d\beta \qquad \text{- (3.7)}$$

we get,

$$U(P) = 2\pi C E_0 \int_0^a J_0(k \;\; w\, e^{-\left(\frac{\rho^2}{w^2}\right)} e^{-\left(\frac{ik\rho^2}{2R}\right)} e^{-i\varphi_{NL}(} \quad d \qquad \text{- (3.8)}$$

Since $w \approx \alpha$, the diffraction angle; the light intensity at far field can be written as,

$$\Im(\alpha) = \left(\frac{2\pi}{D}\right)^2 I_0 \left| \int_0^a J_0(k \;\; \alpha \quad e^{-\left(\frac{\rho^2}{w^2}\right)} e^{-ik\left(\frac{\rho^2}{2R}\right)} e^{-i\varphi_{NL}(} \;\; d \right|^2 \qquad \text{- (3.9)}$$

where D is the distance from the sample.

3.3 Numerical simulations

Considering a Gaussian beam with beam waist *w* and radius of curvature R propagating through a thin nonlinear film of thickness d, the transmitted intensity can be described using equation 3.9 as,

$$I(\alpha) = \left(\frac{2\pi}{D}\right)^2 I_0 \left| \int_0^\infty r dr J_0(k\alpha r) e^{-\left(\frac{r^2}{w^2}\right)} e^{-ik\left(\frac{r^2}{2R}\right)} e^{-i\varphi_{NL}(r)} \right|^2 \qquad \text{- (3.10)}$$

where $k = 2\pi/\lambda$, r is the radial co-ordinate, α is the diffraction angle and J_0 is the zeroth order Bessel function. φ_{NL}, the nonlinear phase shift induced by a plane wave, can be described as {2},

$$\varphi_{NL} = \frac{2\pi}{\lambda}\int_0^d \delta n dz \qquad - (3.11)$$

Here δn is the refractive index variation seen by the incident wave. In the present case however the nonlinear phase shift is also a function of the transverse co-ordinate r ($\varphi_{NL}(r)$) because of the Gaussian intensity profile, and hence we should modify the above equation as,

$$\varphi_{NL}(r) = \frac{2\pi}{\lambda}\int_0^d \delta n(r,z) dz \qquad - (3.12)$$

so that we can write the Fraunhofer diffraction integral for the present case as,

$$I(\alpha) = \left(\frac{2\pi}{D}\right)^2 I_0 \left| \int_0^\infty r dr J_0(k\alpha r) e^{-\left(\frac{r^2}{w^2}\right)} e^{-ik\left(\frac{r^2}{2R} + \int_0^d \delta n(r,z) dz\right)} \right|^2 \qquad - (3.13)$$

It can be seen from the above equation that the observed diffraction ring pattern is governed by the phase factor φ_r which contains two terms: the first accounts for the wave front curvature while the second accounts for the optical nonlinearity of the sample. Far above the onset of the nonlinear response, the latter term dominates the phase factor and the ring pattern can be described neglecting the wavefront curvature. In such a situation, only the SPM principal rings are present. In contrast, just above the nonlinear response threshold both terms in the phase factor become comparable and their interference gives rise to a smaller, fine ring pattern at the center of the principal rings (see figure 3.4). Only one or a few principal rings will be present for the 'just above threshold' condition. The small ring pattern disappears when the sample is placed right at the focus where the curvature is infinite (plane wave).

The nonlinear phase shift contribution is related to the intensity-dependent refractive index of the material. If we assume a Kerr nonlinearity, the refractive index changes can be represented as $\delta n(r,z) = n_2 I(r,z)$. This change is practically independent of the propagation coordinate (thin sample approximation), and we can write the nonlinear phaseshift term as,

$$\int_0^d \delta n(r,z)dz \approx Be^{\left(\frac{-2r^2}{w^2}\right)} \qquad \text{- (3.14)}$$

The quantity B is defined as, $B = \Delta n \times d$, where Δn is the maximum induced variation of the refractive index and d is the thickness of the sample. Using the above equation, the Fraunhofer diffraction integral can be simplified as,

$$I(\alpha) = \left(\frac{2\pi}{D}\right)^2 I_0 \left| \int_0^\infty rdrJ_0(k\alpha r)e^{-\left(\frac{r^2}{w^2}\right)} e^{-ik\left(\frac{r^2}{2R}+B\exp\left(\frac{-2r^2}{w^2}\right)\right)} \right|^2 \qquad \text{- (3.15)}$$

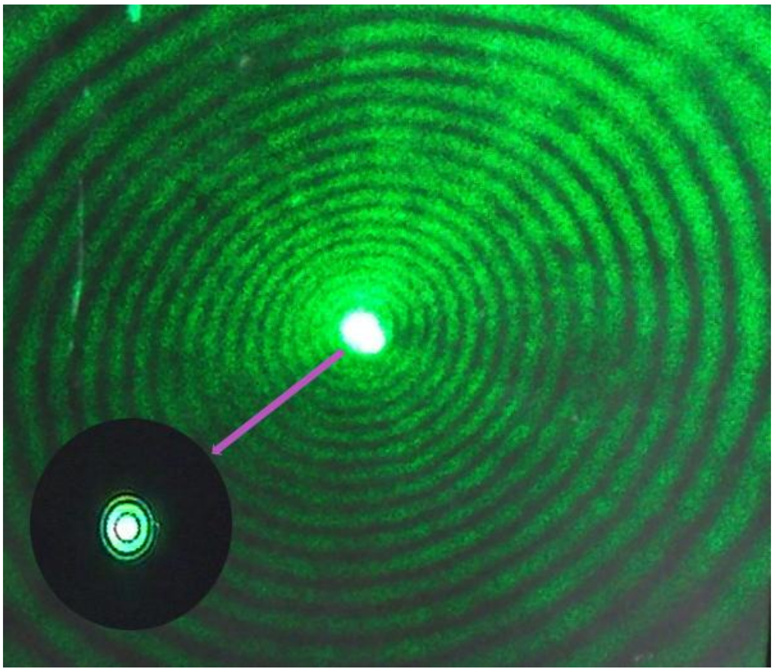

Figure 3.4: Photograph showing the principal SPM ring pattern and the central fine ring structure.

We did numerical simulations based on equation 3.15 for the condition of comparable phase terms, to fully characterize the SPM fine structure and its dependence on the different parameters appearing in the equation {1}. In the simulations, R is the wavefront curvature, w is the beam width and B is the maximum index variation multiplied by the cell thickness. The sign of the parameter B represents the sign of the optical nonlinearity of the sample. We have used reasonable values for the parameters in the Fraunhofer integral. For instance, B = 0.6 μm means that for a typical cell thickness of 60 μm, the maximum induced variation of the refractive index is about 0.01, which is actually a reasonable value for nematic liquid crystals. The effects of beam width and curvature (magnitude and sign) and optical nonlinearity (again magnitude and sign) have been considered.

Figure 3.5 shows the simulations showing the dependence of the ring pattern on the magnitude of the radius of curvature of the beam.

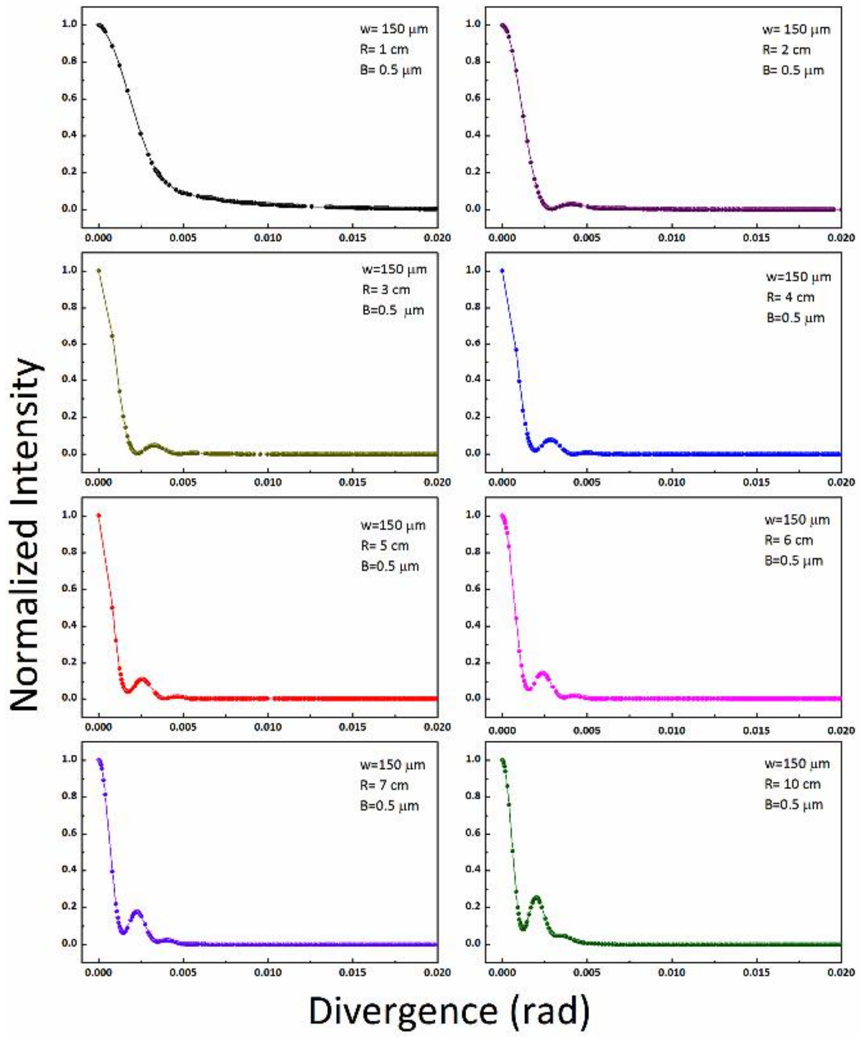

Figure 3.5: Diffraction ring intensity pattern as a function of the radius of curvature (R) of the beam.

Figure 3.6 shows the variation of the intensity pattern with the magnitude of the nonlinearity of the sample. It can be seen that with the increase of nonlinearity, the second ring also increases in intensity. These results confirm the fact that the ring fine structure is strongly related to the magnitudes of the radius of curvature of the beam and the nonlinearity.

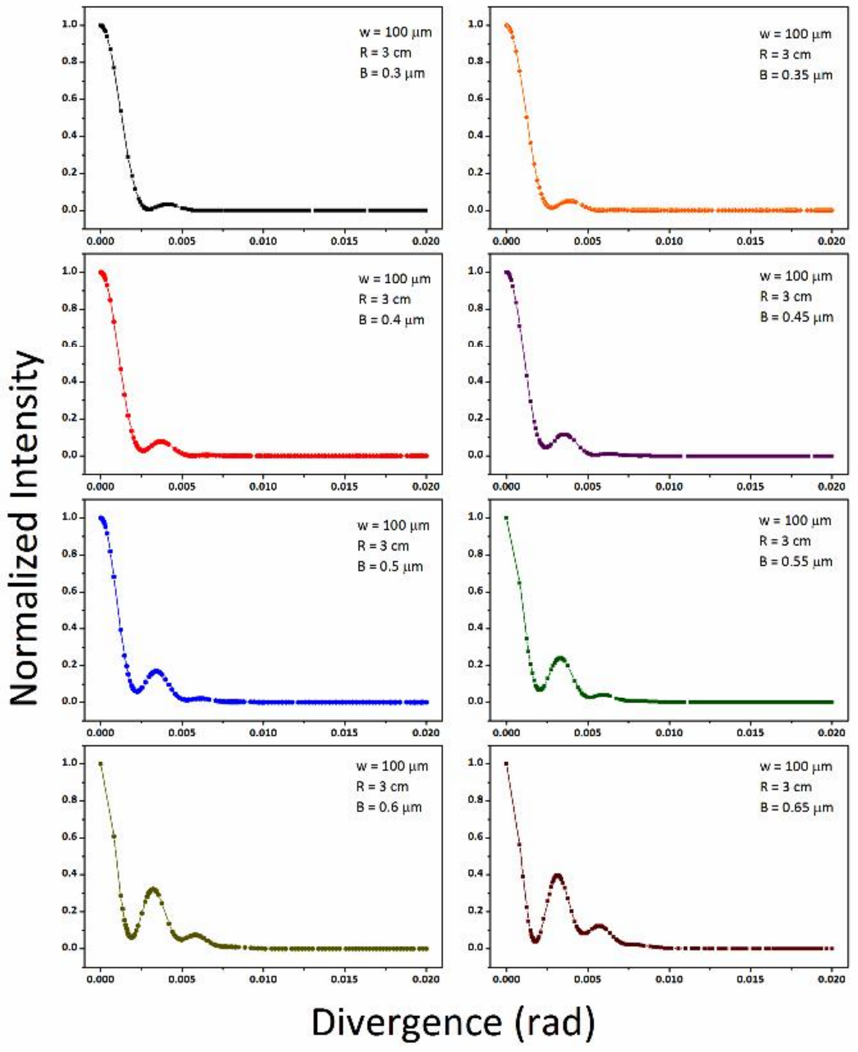

Figure 3.6: Diffraction ring intensity pattern as a function of the nonlinearity (B) of the sample.

The effect of the signs of radius of curvature and nonlinearity are considered in figure 3.7. Simulations show that when both have the same sign, the distribution of the fine ring structure is characterized by a central bright spot surrounded by another ring of lower intensity (figure 3.7(A) and 3.7(B)). When they have opposite signs, the distribution changes to a dark central spot surrounded by a bright thick ring (figure 3.7(C) and 3.7(D)). These results are presented in table 3.1. Since R is fixed by the position of the cell with respect to the lens focus, and the spatial distribution of the small rings can be rapidly evaluated by the eye, this fine ring pattern structure can be used to visually identify the sign of the nonlinearity exhibited by the sample.

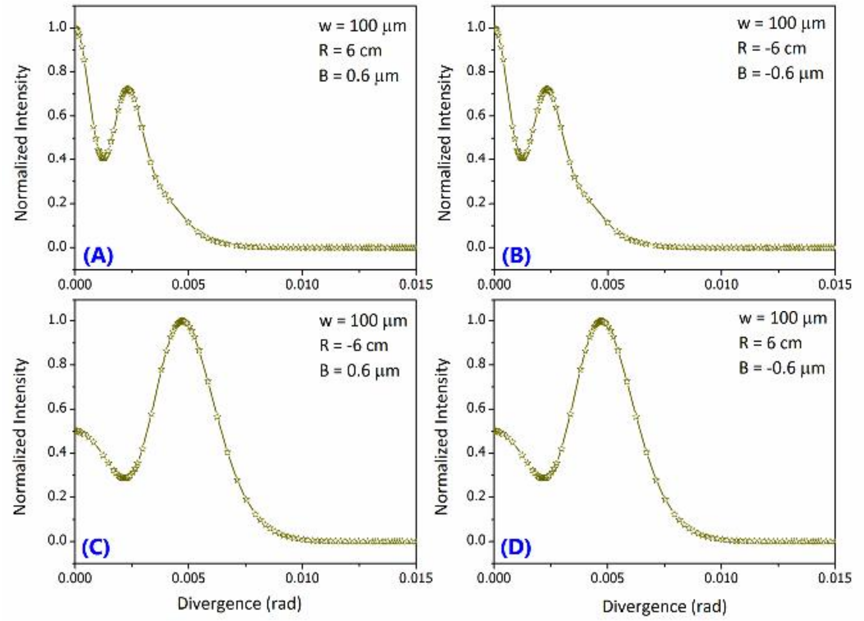

Figure 3.7: Computer simulations showing the spatial distribution of the small low divergence rings for different signs of R and *B*. When both the beam curvature and the induced nonlinearity are either positive (A) or negative (B), the far field fine structure distribution consists of a central bright spot surrounded by a ring. If either *B* or R change sign, the intensity distribution changes to a dark center surrounded by a bright ring ((C) and (D)).

R	n_2	**Fine ring spatial distribution**
Positive	Positive	Central bright spot
Positive	Negative	Central dark spot
Negative	Negative	Central bright spot
Negative	Positive	Central dark spot

Table 3.1: Effect of the signs of beam curvature and optical nonlinearity on the fine ring pattern in the far field.

The magnitude of the nonlinearity can be found out from the number of the principal SPM rings. In the simplest situation, when the sample is at the focus, the nonlinear phase shift given by equation 3.12 can be written as,

$$\delta\varphi(r) = \delta\varphi_0 e^{-2\left(\frac{r}{\omega}\right)^2} \qquad \text{- (3.16)}$$

which means that the wave front suffers a phase shift dependent on the transverse coordinate. Since in the focal waist of a Gaussian beam, the plane wave approximation is fulfilled, we can write the wave vector as $\mathbf{k} = k_z \mathbf{z}$, while the nonlinear phase shift gives rise to a transverse component of **k** given by

$$k_\perp = \frac{d\left(\delta\varphi(r)\right)}{dr} \qquad \text{- (3.17)}$$

Because of the Gaussian shape of equation 3.16 there are two different values of r, which correspond to the same slope of δφ(r), that is, to the same $k_\perp$. It means that these portions of the wave front travel in the same direction and can interfere. Therefore, the interference maxima and minima occur when

$$\delta\varphi(r_1) - \delta\varphi(r_2) = m\pi \qquad \text{- (3.18)}$$

where *m* is an integer, which is even for maxima and odd for minima.

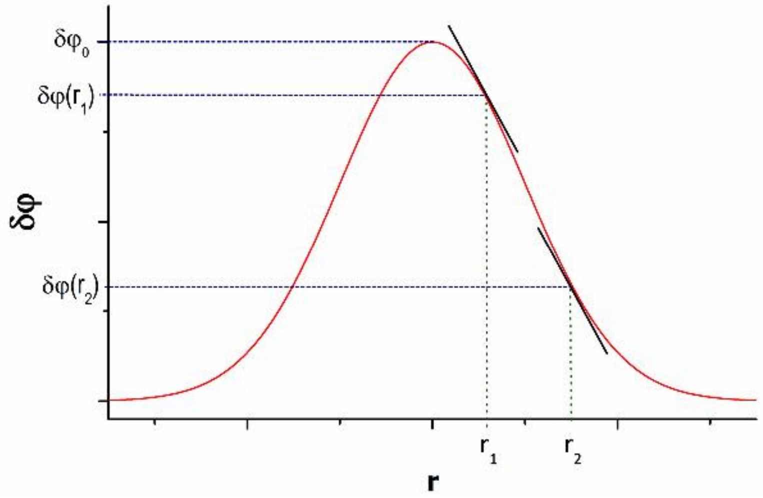

Figure 3.8: Radial distribution of nonlinear phase shift induced on a Gaussian beam.

The interference pattern will appear as bright and dark rings in the far field. The maximum phase shift $\delta\varphi_0$ can easily be related to the number of rings,

$$\delta\varphi_0 = \delta\varphi(0) - \delta\varphi(\infty) = N2\pi \qquad - (3.19)$$

or

$$N = \frac{\delta\varphi_0}{2\pi} \qquad - (3.20)$$

Even though this is a qualitative description, it can be considered a good approximation when N is large, taking into account that the experiment uncertainty is $\approx 2\pi/(N \times 2\pi) = 1/N$.

From equation 3.11, it can be seen that the maximum phase shift in a sample induced by a planar wave is given by

$$\delta\varphi_0 = \frac{2\pi}{\lambda}\delta n_0 d, \qquad - (3.21)$$

where d is the sample thickness. Using equations 3.20 and 3.21, the nonlinear refractive index can be related to the total number of rings as,

$$\delta n_0 = \frac{N\lambda}{d} \qquad - (3.22)$$

Hence if one knows the incident laser wavelength and the sample thickness, the nonlinear refractive index can be found by counting the principal SPM rings formed.

3.4 Experimental

An experimental test of the proposed method for the determination of the sign of the optical nonlinearity can be easily realized. For this, a highly nonlinear film is moved through the focus of a Gaussian beam from a point before the focus where the beam curvature is negative, to a point after the focus where the curvature is positive. During this motion the changes in the distribution of the small rings pattern is carefully observed.

Three different kinds of sample have been tested, all of which are liquid crystalline materials:

Sample 1: Homeotropic cells with both surfaces treated with a solution of dimethyl octadecyl[3-(trimethoxysilyl)-propyl] ammonium chloride (DMOAP) and isopropyl alcohol. The nominal thickness of the cells, fixed by mylar spacers, is 100 μm. Empty cells have been filled with nematic pentyl-cyanobiphenyl (5CB) in the isotropic phase and then slowly cooled down to room temperature.

Sample 2: Homeotropic doped cells with both surfaces treated with DMOAP and isopropyl alcohol. The nominal thickness of the cells, fixed by mylar spacers, is 23 μm. Empty cells have been filled with a mixture of the nematic 5CB doped with the azo-dye, methyl-red (MR), with a weight concentration of 0.1% in the isotropic phase and then slowly cooled down to room temperature.

Sample 3: Planar cells with only one surface treated with poly-vinyl alcohol and rubbed to obtain strong planar anchoring. The nominal thickness of the cells, fixed by mylar spacers, is again 23 μm. Empty cells have been filled with a mixture of the nematic 5CB and MR (0.1% by weight) following the usual procedure used for the other two kinds of sample.

The last type of cell has only one of the two glass substrates covered by the surfactant, because this procedure yields samples with a good alignment and a surface with weak anchoring, which enhance the optical nonlinear response {10}.

The laser source used for the measurements was a frequency doubled Nd:YVO_4 CW laser with λ = 532 nm (Verdi, Coherent), focused by a 22 cm plano-convex lens to a diameter of ~100 μm near the sample. The laser beam falls on the sample at normal incidence, and in the case of planar cells, it irradiates the untreated surface and enters the sample as a pure e-wave. The incident laser power is of the order of 0.1 mW for the planar cells, 10 mW for the homeotropic doped cells, and 100 mW for the homeotropic undoped nematic cells. These values correspond to intensities of about 3 W/cm^2, 30 W/cm^2, and 300 W/cm^2 respectively. In planar cells a static bias (variable typically between 1.2 and 2.5 V) is applied between the substrates. The ring pattern generated is displayed on a screen 1.8 m away and is captured with a CCD camera for detailed analysis. A schematic of the experimental setup is given in figure 3.9.

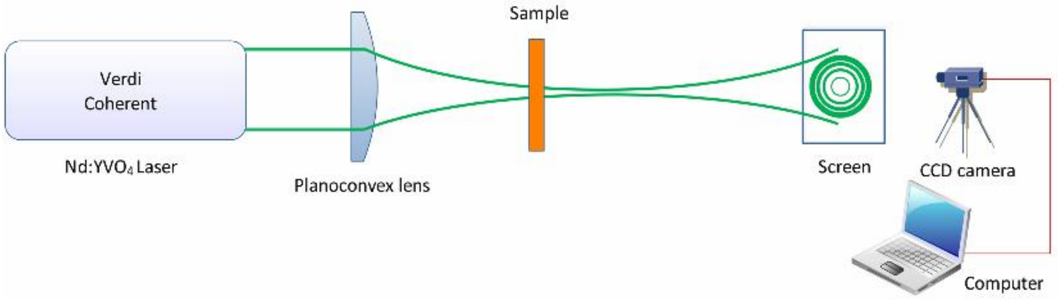

Figure 3.9: Experimental setup for recording the SPM ring patterns.

3.5 Results and discussion

The low divergence rings typical of the SPM fine structure are clearly visible in all the samples analyzed, and in each case we fitted the experimental intensity distribution using equation 3.15, with *B* as a fitting parameter. The patterns obtained from the three different types of cell are described below in detail.

3.5.1 Undoped homeotropic cells

Santamato and Shen have reported the field-curvature effect on the diffraction ring pattern of a laser beam dressed by spatial self-phase modulation in a nematic film {9}. The intensity required to observe the small rings must slightly overcome the optical Fredericks threshold. The expected nonlinearity is positive since under light irradiation the refractive index changes from n_o to a higher value between n_o and n_e. When the cell is before the focus ($R < 0$) the distribution is characterized by a dark central spot surrounded by an intense ring, whereas when the cell is after the focus ($R > 0$) the distribution changes to a central bright spot surrounded by a ring of lower intensity. According to the simulations and table 3.1, this corresponds to a positive induced optical nonlinearity. The intensity distribution fitted to equation 3.15 is shown in figure 3.10. The fitting parameter *B* is positive, as expected. The value of *B* found by the fitting procedure corresponds to a maximum induced birefringence (Δn) of about 0.007 and to a nonlinear coefficient (n_2) of the order of 10^{-5} cm^2/W, which is typical of the giant optical nonlinearity of liquid crystals responsible for SPM in this kind of cell {2}.

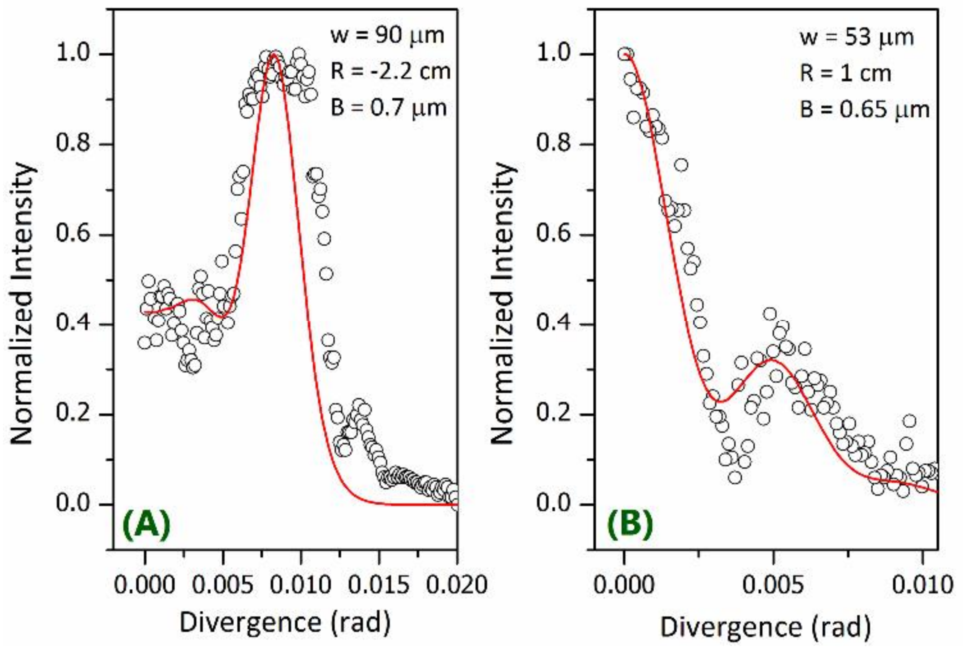

Figure 3.10: Experimental far field intensity distribution of the small rings in the case of undoped homeotropic cells. The line represents the fit based on equation 3.15. The cell lies before the beam focus (negative beam curvature) in (A), and after the focus (positive curvature) in (B).

3.5.2 Homeotropic cells doped with methyl red

In this case the presence of the absorbing dye produces, at the intensity used, a nonlinear response of thermal nature. The optical nonlinearity associated to this kind of response is expected to be positive because dn_0/dT is a growing function of T; that is, the ordinary refractive index increases with the sample temperature. Since the incident Gaussian beam has a maximum intensity at its centre, the cell temperature will be higher in this region and lower in the beam wings, with the refractive index following the same trend.

The spatial distribution of the low divergence rings is shown in figure 3.11 for both positions of the cell with respect to the lens focus. Again, negative curvature corresponds to a dark central spot surrounded by an intense ring, and positive curvature corresponds to a central bright spot surrounded by a ring of lower intensity, which is in agreement with an induced nonlinearity of positive sign. Also, the sign of B derived by fitting the intensity curve with equation 3.15 is positive, as expected.

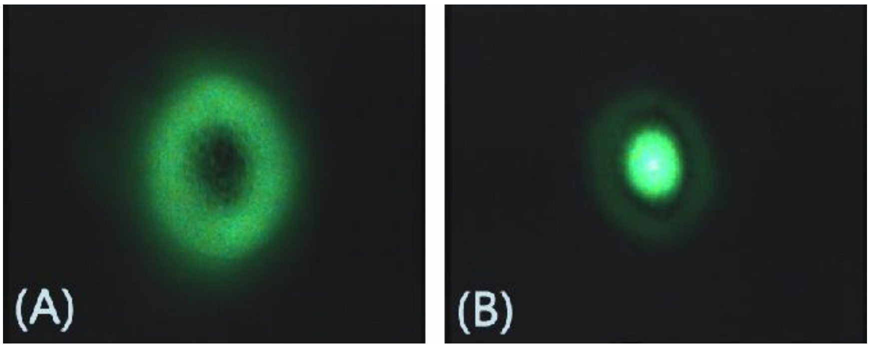

Figure 3.11: Spatial distribution of the fine structure rings in the case of doped homeotropic cells. Negative curvature corresponds to a dark central spot surrounded by an intense ring, and positive curvature corresponds to a central bright spot surrounded by a ring of lower intensity. The induced optical nonlinearity is positive and has a thermal origin.

3.5.3 Planar cells doped with methyl red

In the case of planar cells, both SPM principal rings and fine structure can be obtained only when an external bias is switched on and is kept lower than the Fredericks threshold voltage {11}. The behaviour of the spatial distribution of the low divergence rings is different with respect to that of homeotropic samples. This time, when the cell is before the focus ($R < 0$), the distribution is characterized by a central bright spot surrounded by a ring of lower intensity, whereas if the cell moves beyond the focus ($R > 0$) the distribution changes to a dark central spot surrounded by an intense ring. According to the simulations, this corresponds to a negative induced optical nonlinearity. The occurrence of a negative nonlinear response in planar cells is in agreement with the phenomenological model proposed by Lucchetti et.al. {11}. The model states that the incident light modulates the effective internal voltage acting on the surface charge density of ions in such a way that the external bias produces a director reorientation towards the homeotropic configuration only, corresponding to the centre of the incident Gaussian beam. In this way, the refractive index seen by the incident light is n_e in the beam wings, and has a value between n_o and n_e at the beam centre, which gives rise to self-phase modulation due to a negative nonlinearity. Figure 3.12 shows the distribution of the intensity transmitted by the cells in the two positions: before (figure 3.12(A)) and after (figure 3.12(B)) the lens focus. Note that these are reversed with respect to the curves shown in figure 3.10. The fitting parameter *B* is negative, as expected. Its value is -0.8 μm in one case and -0.7 μm in the other. This corresponds to a maximum induced birefringence (Δn) of about 0.03, which means a nonlinear coefficient n_2 of the order of 10^{-2} cm^2/W, consistent with the recently observed nonlinear response of planar cells of 5CB doped with methyl red {11}.

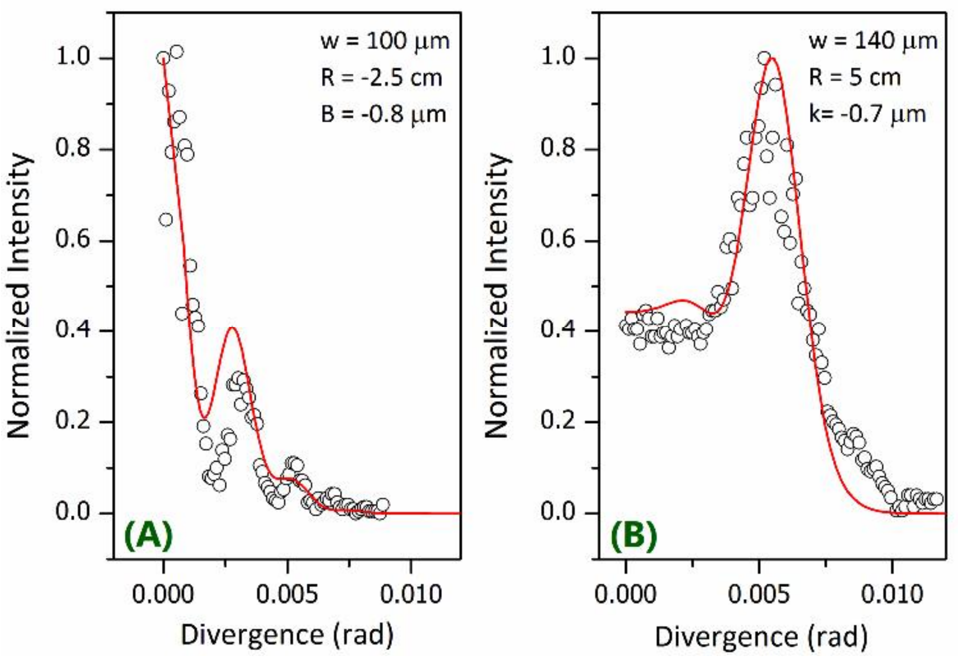

Figure 3.12: Experimentally determined far field intensity distribution of the small rings in the case of a planar cell of 5CB doped with MR placed before (A) and after (B) the lens focus. Solid lines represent theoretical fits with equation 3.15. In this case the induced optical nonlinearity is negative.

3.6 Conclusions

In conclusion, we have devised a fast and easy method to determine at a glance the sign of the optical nonlinearity of highly nonlinear film samples. The technique is similar to the conventional z-scan {12} except for the fact that no aperture is necessary to determine the sign of the nonlinearity. Since the number of SPM principal rings is directly related to the value of the induced birefringence, the method proposed allows a simple evaluation of both the sign (by means of the SPM fine structure) and the value (by counting the SPM principal rings) of n_2. The method is independent of the type of nonlinearity that causes the ring pattern, as demonstrated by measurements in different types of nematic cell, and is expected to work for every kind of highly nonlinear medium.

References

1. *Fine structure in spatial self-phase modulation patterns: at a glance determination of the sign of optical nonlinearity in highly nonlinear films*, L. Lucchetti, S. Suchand, and F. Simoni, J. Opt. A: Pure Appl. Opt., **11**, 034002 (2009).
2. *Nonlinear Optical Properties of Liquid Crystals and Polymer Dispersed Liquid Crystals*, F. Simoni, World Scientific, (Series on Liquid Crystals – Vol. 2), Singapore (1997).
3. *Introduction to Liquid Crystals Chemistry and Physics*, P. J. Collings and M. Hird, Taylor & Francis Inc., Philadelphia (1997).
4. *The Surface Physics of Liquid Crystals,* A. A. Sonin, Gordon and Breach Publishers, Luxembourg (1995).
5. *Liquid Crystals*, H. Stegemeyer (Ed.), Springer, New York (1994).
6. *Laser-induced diffraction rings from a nematic-liquid-crystal film*, S. D. Durbin, S. M. Arakelian, and Y. R. Shen, Opt. Lett., **6**, 411 (1981).
7. *Nonlinear Optics,* R. W. Boyd, Second Edition, Academic Press, San Diego, CA (2003).
8. *Principles of Optics*, M. Born and E. Wolf, Pergamon Press, Oxford (1980).
9. *Field-curvature effect on the diffraction ring pattern of a laser beam dressed by spatial self-phase modulation in a nematic film,* E. Santamato, and Y. R. Shen, Opt. Lett., **9**, 564 (1984).
10. *Colossal optical nonlinearity in dye doped liquid crystals*, L. Lucchetti, M. Di Fabrizio, O. Francescangeli, and F. Simoni, Opt. Comm., **233**, 417 (2004).
11. *Surface-induced nonlinearities of liquid crystals driven by an electric field*, L. Lucchetti, M. Gentili, and F. Simoni, Phys. Rev. E, **78**, 061706 (2008).
12. *Sensitive measurement of optical nonlinearities using a single beam*, M. Sheik-Bahae, A. A. Said, T.H. Wei, D. J. Hagan, and E. W. Van Stryland, IEEE J. Quantum Electron., **26**, 760 (1990).

4

Spectral dispersion of optical nonlinearity: Nondegenerate z-scan with a supercontinuum light source

Measurement of the spectral dispersion of ultrafast optical nonlinearities requires an expensive broadband light source like the optical parametric amplifier (OPA). Recently, the use of a white-light continuum for this purpose was proposed and demonstrated. There are two advantages to this approach: the ultrafast OPA is not necessary and the entire data can be obtained in a single measurement. One disadvantage is the relatively lower S/N ratios involved. In this chapter we present the use of a femtosecond supercontinuum source for measuring the spectral dispersion of optical nonlinearity in silver nanoparticle solution.

4.1 Introduction to the white-light continuum

The propagation of an intense picosecond or shorter laser pulse through certain media leads to one of the most spectacular phenomena in nonlinear optics, viz the super-broadening of the pulse to a spectral continuum, which in most cases spans hundreds of nanometers in wavelength. When this supercontinuum covers the whole visible range, it appears white and is often referred to as a while-light continuum (WLC). Even though the temporal coherence of such a broadened pulse is low, the spatial coherence remains high {1}. Various processes are responsible for supercontinuum generation. The main processes involved are self-, induced-, and cross-phase modulations, multi-photon parametric processes, and Raman scattering {1}.

Figure 4.1: (A) White-light continuum generated in water using 800 nm, 100 fs laser pulses. (B) The continuum dispersed using a grating.

The mechanism determining the spectral width of continuum emission is quite intriguing. At present it is generally accepted that the main mechanism in ultrafast continuum generation is strong self-phase modulation (SPM) enhanced by self-steepening of the pulse. A shortcoming of this theory is its prediction of stronger SPM in media with higher Kerr nonlinearity, a trend that is not observed. For instance, the continuum generated in water (a widely used medium) is among the broadest observed, despite the low Kerr nonlinearity of water {2}.

4.2. Mechanisms of supercontinuum generation

4.2.1 Self-phase modulation (SPM)

When an intense laser pulse propagates through a medium, the optical Kerr effect results in a change in the refractive index of the medium, which in turn changes the phase and frequency of the incident laser pulse. The intensity dependent refractive index can be written as,

$$n(I) = n_0 + n_2 I(t) \qquad \text{- (4.1)}$$

where $I(t)$ is the intensity of the incident laser pulse, n_0 is the linear component of refractive index and $n_2 I(t)$ is the nonlinear component of refractive index. Therefore the instantaneous phase of the pulse is given by,

$$\phi(t) = \omega_0 t - k.L = \omega_0 t - \frac{2\pi}{\lambda_0} n(I) L \qquad - (4.2)$$

which can be written as,

$$\phi(t) = \omega_0 t - \frac{2\pi}{\lambda_0} n_0 L - \frac{2\pi}{\lambda_0} n_2 I(t) L \qquad - (4.3)$$

where ω_0 is the frequency, λ_0 is the wavelength of the incident pulse, and L is the length of the medium.

The instantaneous frequency is the time-derivative of the instantaneous phase, given by,

$$\omega(t) = \frac{d\phi(t)}{dt} = \omega_0 - \frac{2\pi}{\lambda_0} n_2 L \frac{dI}{dt} \qquad - (4.4)$$

so that,

$$\omega(t) = \omega_0 - \Delta\omega(t) \qquad - (4.5)$$

where $\Delta\omega(t) = \frac{2\pi L n_2}{\lambda_0} \frac{dI}{dt}$

Thus the intensity dependent refractive index results in a frequency sweep of the pulse in time. The plot of ω(t) against t shows the frequency shift experienced by the pulse. In a material with a positive nonlinear refractive index coefficient (n_2), the leading edge of a Gaussian pulse shifts to higher frequencies ("bluer" wavelengths) and the trailing edge to lower frequencies ("redder" wavelengths).

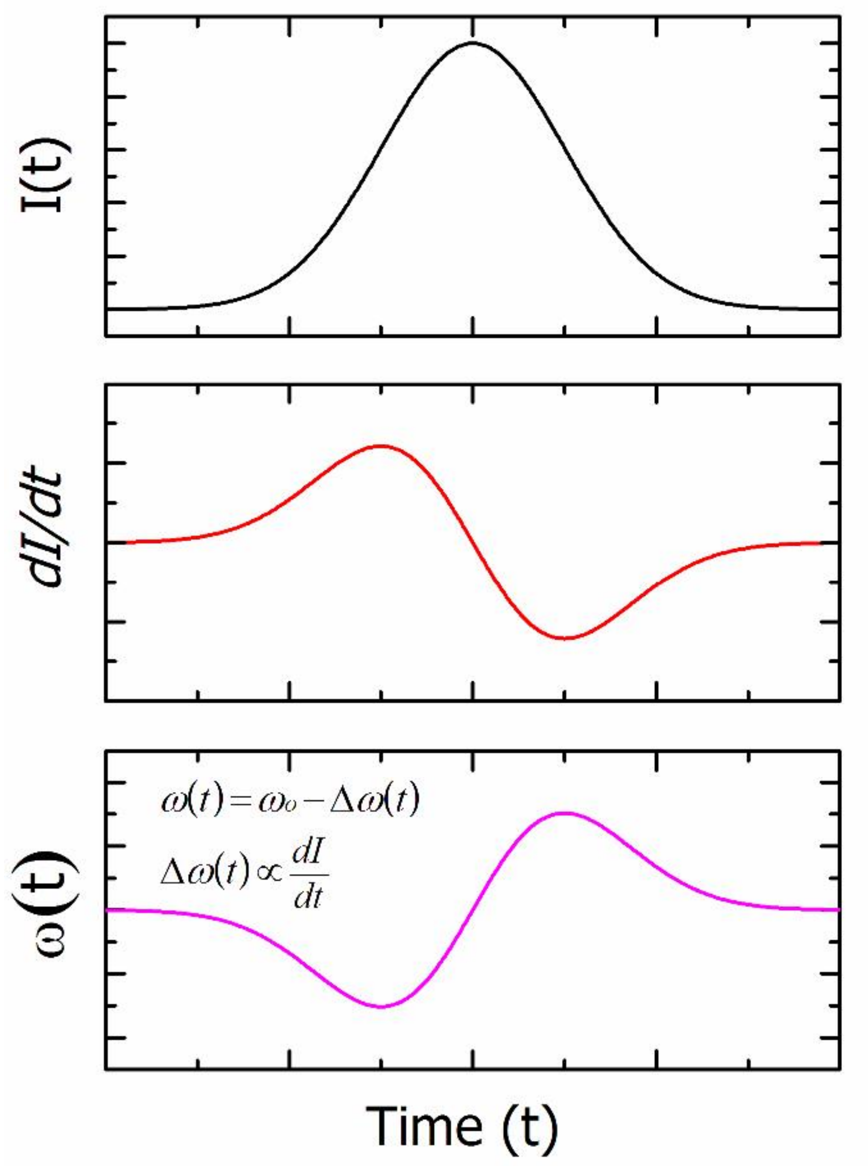

Figure 4.2: An ultrafast light pulse propagating through a nonlinear medium experiences a frequency shift in time.

Thus self-phase modulation introduces a band of new frequencies to the spectrum and is considered as one of the major mechanisms involved in the supercontinuum generation phenomenon.

4.2.2 Stimulated Raman scattering (SRS)

When a laser excites a coherent vibrational mode in a molecule, stimulated Raman scattering (SRS) occurs. The primary SRS lines may generate their own

Raman lines, thereby introducing new spectral components. SRS is an important process that competes and couples with SPM.

4.2.3 Cross-phase modulation and induced-phase modulation

In cross-phase modulation (XPM) the phase of a coherent beam is modified by another beam, both of which interact through a nonlinear medium. When the interference between SRS and SPM causes a change in the emission spectrum, it is known as stimulated Raman scattering cross-phase modulation (SRS-XPM). Similarly the interference between second harmonic generation (SHG) and SPM can result in the modification of the emission spectrum and is referred to as second harmonic generation cross-phase modulation (SHG-XPM). A process closely related to XPM, called induced-phase modulation (IPM), occurs in media disrupted by SPM {1,3}. When a weak probe pulse is sent into this disrupted system, the phase of the probe pulse at different frequencies will get modulated by the time variation of the nonlinear index of refraction originating from the primary intense pulse.

In addition to these processes, non-degenerate four-photon parametric generation usually occurs simultaneously with the SPM process {1}. Photons at the laser frequency parametrically generate photons at the Stokes and anti-Stokes frequencies, which are emitted in an angular pattern due to the required phase matching condition.

4.2.4 Self-focusing

Self-focusing is believed to play a part in continuum generation in extended media {4,5}. It is a well known phenomenon that arises in the propagation of a spatially non-uniform laser beam in a Kerr medium, in which the index of refraction is given by $n(I)=n_0+n_2I(r)$.

For a CW Gaussian beam, catastrophic self-focusing occurs at powers that exceed the critical power $P_{crit}=3.77\lambda_0^2/8\pi n_0 n_2$ where λ_0 is the laser wavelength. The Gaussian beam then collapses to a singularity at a distance

$$z_f(P) = \frac{0.367ka_0^2}{\left[\left(\sqrt{P/P_{crit}} - 0.852\right)^2 - 0.0219\right]^{1/2}} \qquad \text{- (4.6)}$$

where P is the beam power, k is the wave number, and a_0 is the input beam's radius at the 1/e level of intensity.

For a laser pulse the instantaneous beam power (P) varies with time. In the slowly varying envelope approximation (which is valid for pulses as short as approximately 10 optical cycles, or 30 fs at 800 nm) and in the absence of absorption and dispersion, self-focusing can be described in terms of the moving-focus model {4}. The laser pulse is then viewed as consisting of a longitudinal stack of infinitely thin transverse slices that propagate independently from one another at the pulse's group velocity. Each slice behaves according to its own power; the slices with power exceeding P_{crit} undergo a collapse at a distance. Because the position of the self-focus depends on power, various slices will collapse at different positions. When the pulse is much shorter than the self-focusing distance, the first slice to self-focus is the most powerful slice at the center of the pulse. This implies that an intensity spike develops initially at the center of the pulse during self-focusing.

Medium dispersion can be important for the self-focusing of ultrashort pulses. During self-focusing an ultrashort pulse broadens spectrally because of SPM, but the new frequency components travel at different speeds due to group velocity dispersion (GVD). This causes a reduction of peak power during self-focusing, such that a higher input power is required for the onset of catastrophic self-focusing. Therefore P_{crit} is higher for ultrashort pulses compared to that for long pulses. GVD during self-focusing can also result in a temporal splitting of the pulse.

It was experimentally found that the power threshold for continuum generation in gases coincides with the critical power for self-focusing. This is not surprising, considering that the onset of catastrophic self-focusing at critical power leads to a drastic increase in intensity. Self-focusing can also lead to the generation of free electrons, which contributes a negative term to the nonlinear index of refraction. This may ultimately stop self-focusing by canceling the Kerr index. The connection between continuum generation and self-focusing suggests that free electrons may be involved in continuum generation. Measurements with a new experimental technique confirm that continuum generation is triggered by self-focusing and reveal a strong dependence of the continuum on the band gap of the medium. A band gap threshold is found, below which the medium cannot generate a continuum. Above this threshold, the width of the continuum increases with the band gap.

4.3 Features and applications of the supercontinuum

The first observation of white-light continuum dates back to the late 1960's, when Alfano and Shapiro focused powerful picosecond pulses into glass samples {6}. The continuum they observed covered the visible spectral range and extended into the near infrared. In 1983 Fork et. al. generated the first femtosecond continuum by focusing powerful 80 fs pulses into an ethylene glycol film; the resultant continuum ranged from the ultraviolet to the near infrared {7}. Corkum et. al. then demonstrated continuum generation in gases using femtosecond pulses {8}. The general characteristics of the femtosecond continuum are as follows: its spectral width depends on the medium in which it is generated, its spectrum is modulated, its polarization is in the same direction as the polarization of the input pulse, and its anti-Stokes frequency components lag the Stokes components {1}. The femtosecond continuum exhibits a smaller beam divergence than the picosecond continuum. When it is projected onto a screen the femtosecond continuum appears to the eye as a white disk, often surrounded by a distinct concentric rainbow-like pattern (due to conical emission). The term "white-light continuum" refers to the low-divergence, central part of the beam and excludes the conical emission.

Potential applications of white-light continuum include femtosecond time resolved spectroscopy, optical pulse compression for generation of ultrashort pulses, seeding of optical parametric amplifiers, optical coherence tomography, LIDAR, frequency metrology, and linear and nonlinear microscopy {1,9,10}.

4.4 White-light continuum generation

To generate a white-light continuum, an intense ultrafast laser pulse is required. We used the mode-locked output from a chirped pulse amplified (CPA) Ti:Sapphire femtosecond laser system for our experiments (Tsunami and TSA-10, Spectra Physics). The laser system was capable of generating 100 fs pulses of 10 mJ energy at the fundamental wavelength {11}. The repetition rate of the system was 10 Hz. For the continuum generation experiment, laser pulses of 6 mJ energy were focused onto a 5 cm long liquid cell using a 10 cm focal length lens. Various media viz; water, silver nanoparticle colloidal solution (Ag:NP), carbon tetrachloride (CCl_4), sodium chloride solution (NaCl, different concentrations), zinc nitrate solution $Zn(NO_3)_2$, Di-methyl formamide (DMF), nickel chloride solution ($NiCl_2$), etc were tried as samples for white-light continuum generation. Spectra of the white-light continuum generated were taken using a fiber optic spectrometer (AvaSpec 2048, Avantes BV), which has a working wavelength range of 340-1100 nm. The resolution of the spectrometer was about 0.8 nm. A short wavelength pass filter was used to cut off wavelengths above 720 nm to filter out the strong pump pulse (800 nm) from the spectra. The obtained spectra are presented in figure 4.3.

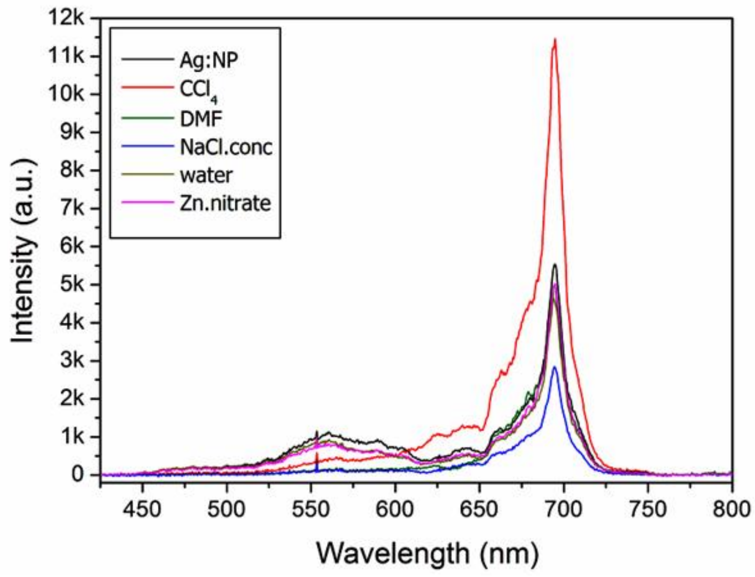

Figure 4.3: White-light continuum generated using different liquid media.

From the spectra obtained it is found that water and CCl_4 are the most efficient among the media used for continuum generation. A colloidal system of silver nanoparticles in water also seems to be a promising candidate. It is seen that increasing the concentration of the salts in an ionic solution used for white-light generation results in a weaker spectrum (figure 4.4).

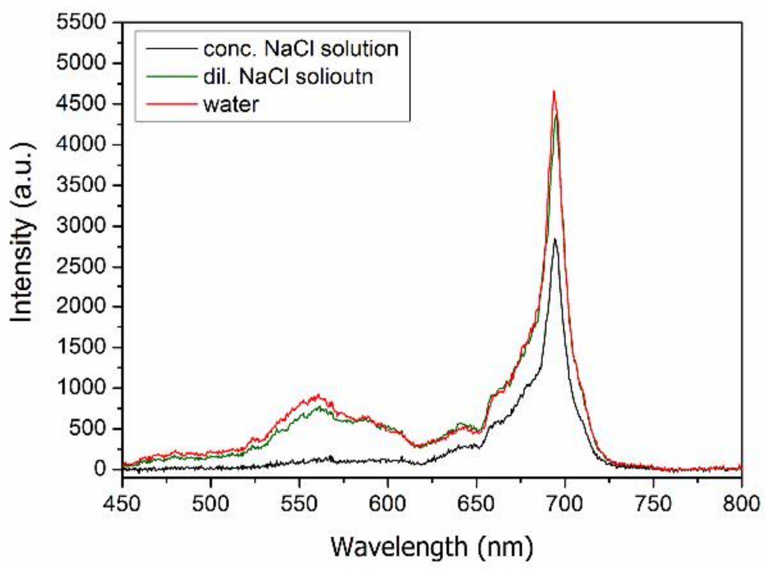

Figure 4.4: Comparison of WLC spectra obtained using water and two different concentrations of aqueous NaCl solution.

Even though the total white-light yield was better in CCl_4, we preferred to use water for our experiments, as the emission at the lower wavelengths was higher in water.

4.5 The White-light continuum z-scan experiment

In the white-light z-scan experiment, the conventional monochromatic light source is replaced by an intense WLC source. This method provides for an absolute measurement of the spectral dispersion of the nonlinearities of the sample under investigation, and adds to the sensitivity of the normal z-scan technique {12–17}. The white-light z-scan is much more versatile than the conventional single-wavelength z-scan. The energy detector used in the conventional z-scan measurement is here replaced with a single shot CCD spectrometer so that the spectral content of the transmitted beam is accurately measured for each z position. Thus the nonlinearity coefficient for each wavelength can be calculated from a single z-scan measurement by using a WLC source for the experiment.

A schematic of the experimental set up used in this work is given in figure 4.5. White-light continuum is generated by focusing the pump beam (800 nm, 100 fs, 6 mJ pulses from a Ti:Sapphire laser) using a lens of focal length 10 cm, to a water cell of 5 cm length. Another lens of 10 cm focal length is used to collimate the white-light continuum generated. A short wave pass filter is used to filter out the strong laser line from the generated spectra. After re-collimation, the conical emissions are removed by placing an aperture in the beam path, which restricts the output to the central white-light continuum region. This continuum beam is then focused onto the sample using another convex lens and the sample is moved along the beam propagation direction as is usually done in the conventional open aperture z-scan technique. Light transmitted through the sample is fed to a fiber optic spectrometer and the spectrum obtained is recorded for each z position of the sample.

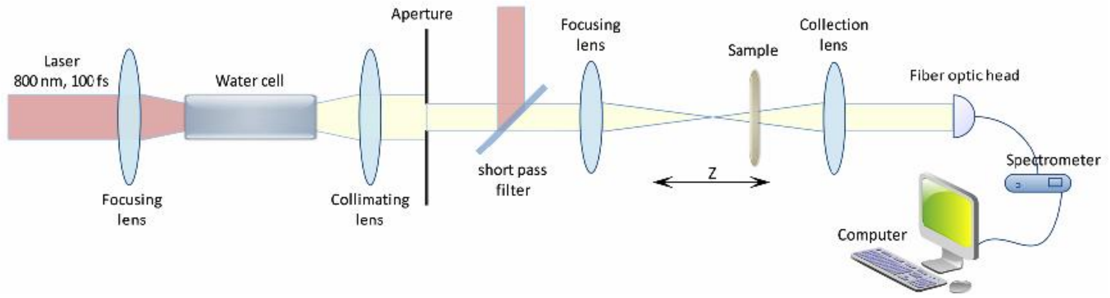

Figure 4.5: Schematic diagram of the white-light z-scan experimental setup.

Each wavelength in the supercontinuum pulse will be focused slightly differently in the sample due to chromatic aberration. Therefore to preserve the degeneracy of the experiment we repeated the measurement by focusing the WLC using an achromatic doublet, but could not find any appreciable difference in the finally obtained dispersion curves.

We measured the nonlinear absorption of silver nanoparticles at different wavelengths in a single z-scan run, using this technique. The silver nanoparticles used for the experiments were synthesized by the reduction of $AgNO_3$ with tri-sodium citrate. Details of the nanoparticle synthesis can be found in chapter 2. A surface plasmon resonance observed at 410 nm confirms the formation of silver nanoparticles. The prepared particles were of approximately 30 nanometer in size.

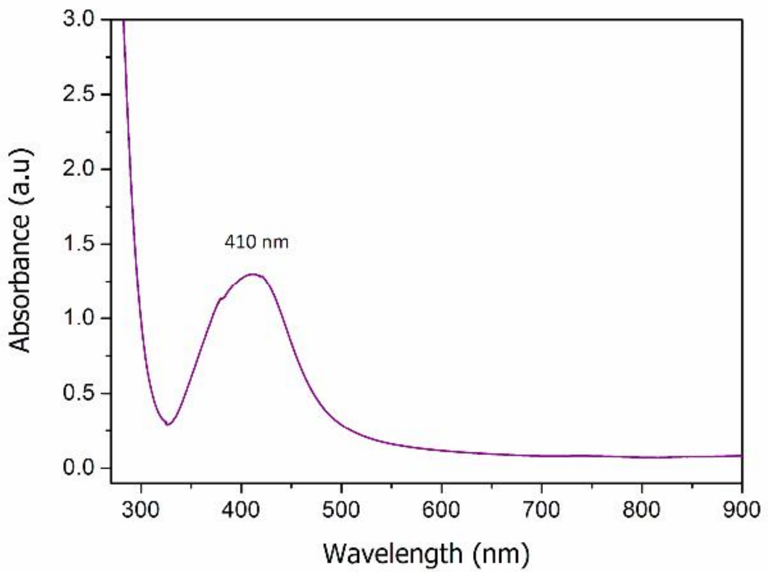

Figure 4.6: Absorption spectrum of the synthesized silver nanoparticles.

Since the data collected at each z position contained information over a wavelength range of at least 200 nm, analyzing them manually was virtually impossible. Hence we developed a program in LabVIEW™ to select any desired wavelength from the set of measured spectra and then obtain a z-scan curve for that wavelength. After obtaining the z-scan curves for several such closely lying wavelengths, the experimental data was numerically fitted to the standard nonlinear transmission equations. From the theoretical fits to the data, the corresponding nonlinear absorptive mechanisms were deduced and the nonlinear absorption coefficients were calculated. Screenshots of the LabVIEW™ program used for the data analysis can be seen in figures 4.7 and 4.8.

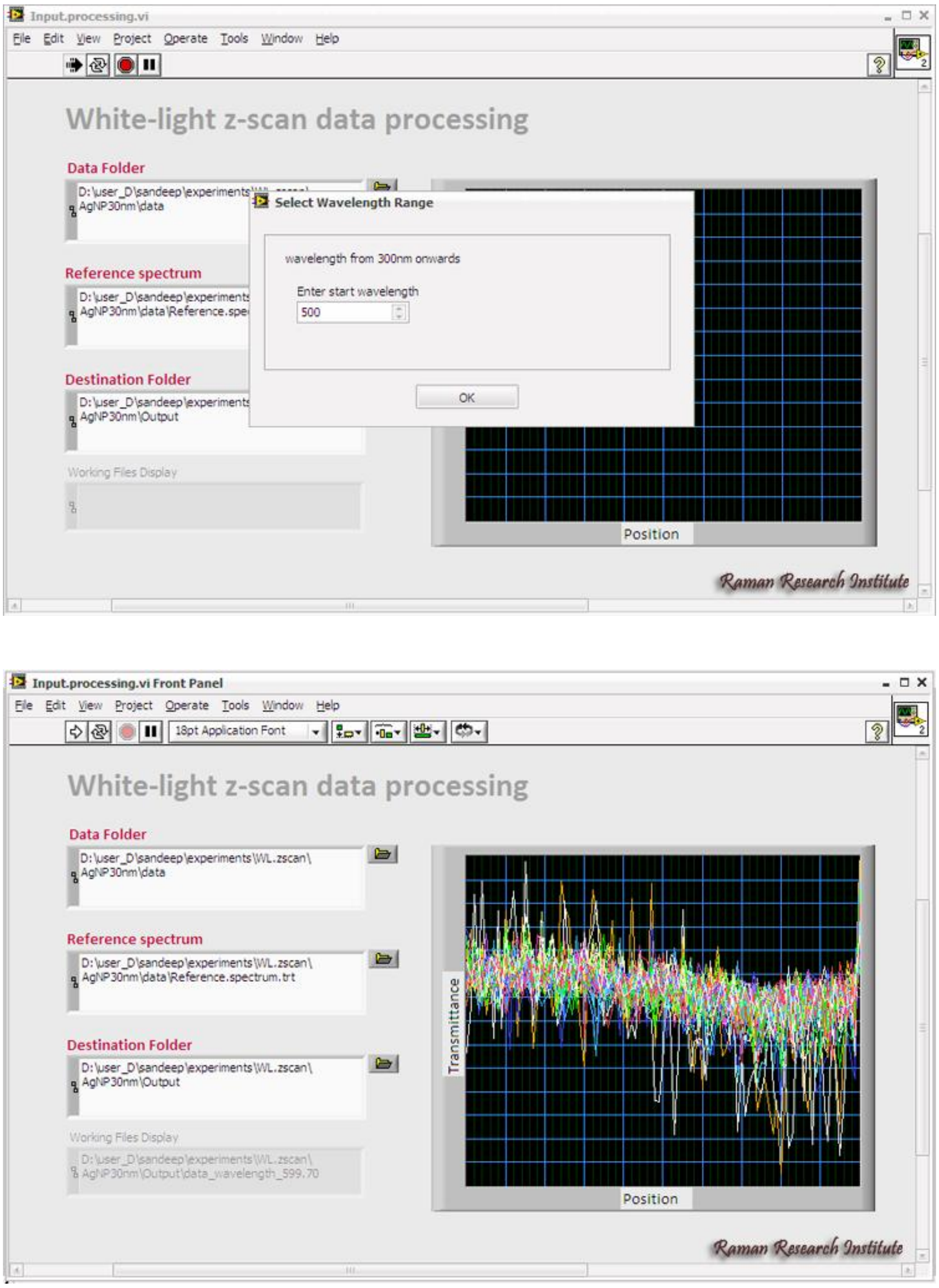

Select Wavelength Range

wavelength from 300nm onwards

Enter start wavelength: 500

OK

Data Folder: D:\user_D\sandeep\experiments\WL.zscan\AgNP30nm\data

Reference spectrum: D:\user_D\sandeep\experiments\WL.zscan\AgNP30nm\data\Reference.spectrum.trt

Destination Folder: D:\user_D\sandeep\experiments\WL.zscan\AgNP30nm\Output

Working Files Display: D:\user_D\sandeep\experiments\WL.zscan\AgNP30nm\Output\data_wavelength_599.70

Figure 4.7: Screenshots of the LabVIEW$^{\text{TM}}$ program used for carrying out the data analysis.

In the present measurements, white-light z-scan data for a silver nanoparticle solution was obtained for the range of wavelengths from 500 nm to 700 nm. The nonlinear transmission curves obtained for all the wavelengths in this range were found to fit well to the two-photon absorption (2PA) nonlinear equations (described in detail in chapter 2). A LabVIEW$^{\text{TM}}$ module was developed for fitting the obtained z-scan data to the 2PA equation. A screenshot of this program is shown in figure 4.8.

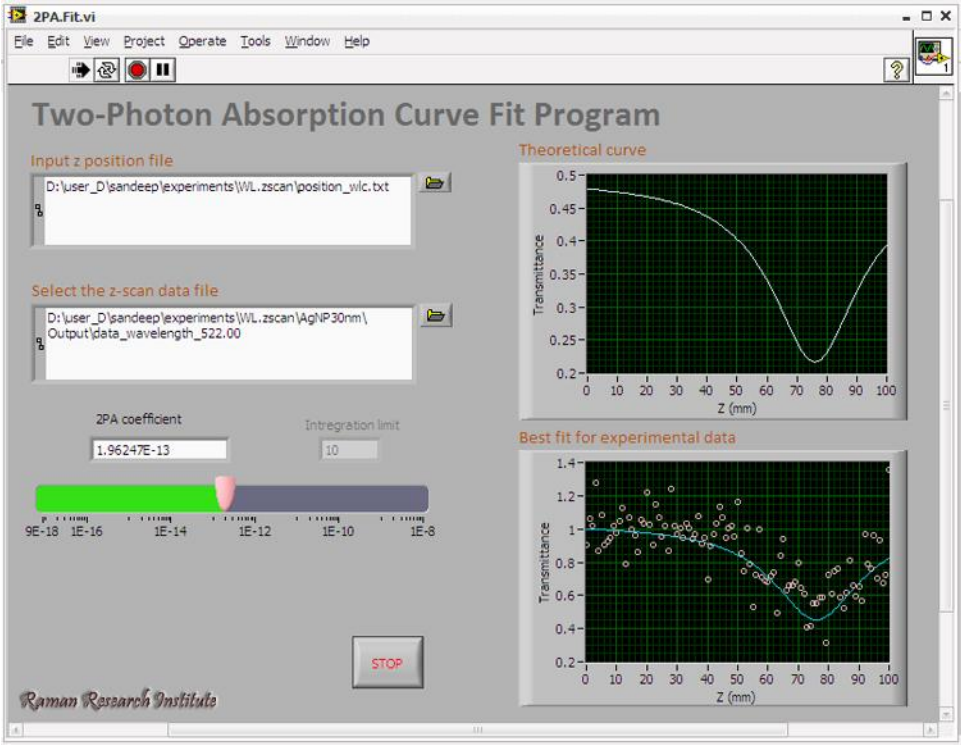

Input z position file
D:\user_D\sandeep\experiments\WL.zscan\position_wlc.txt

Select the z-scan data file
D:\user_D\sandeep\experiments\WL.zscan\AgNP30nm\Output\data_wavelength_522.00

2PA coefficient
1.96247E-13

Intregration limit
10

Figure 4.8: The LabVIEW™ program used for fitting the obtained data.

The 2PA coefficients could thence be extracted for this range of wavelengths from the white-light z-scan curves. The spectral dispersion of the 2PA coefficients was then plotted. The plot shows a decrease in the magnitude of the nonlinearity towards the longer wavelength region. This spectral dispersion of nonlinearity in the 500-700 nm range approximately follows the strength of one-photon absorption in the corresponding two-photon wavelength region of 250 to 350 nm.

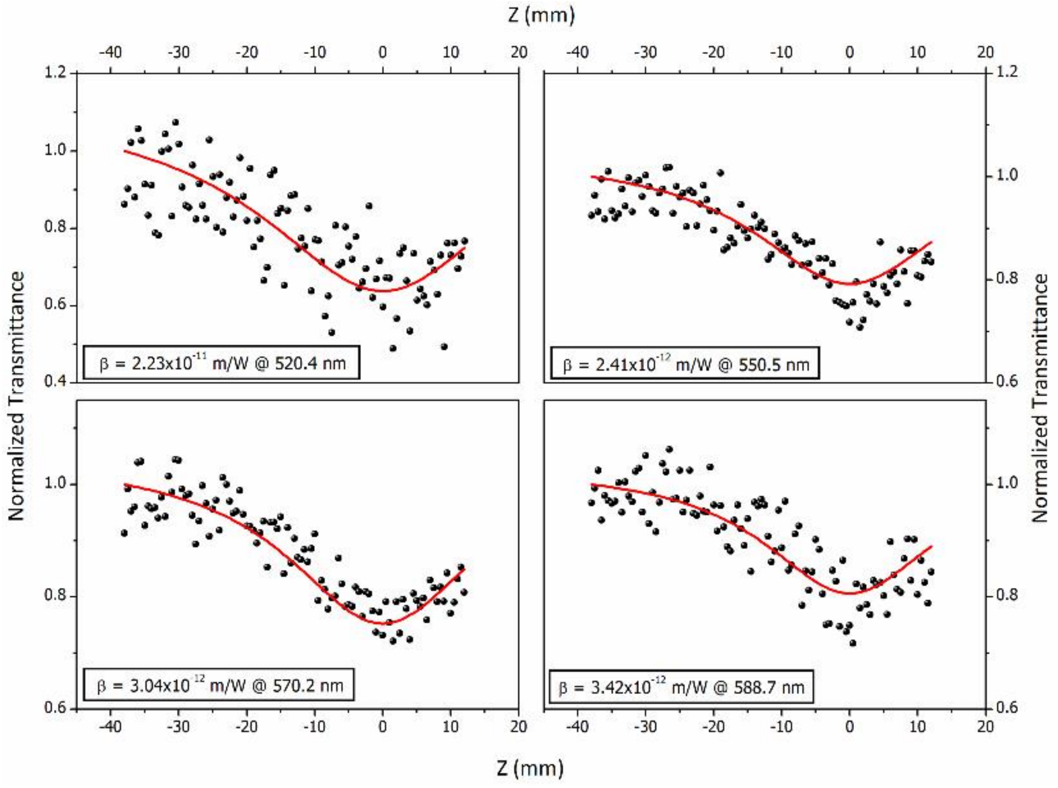

Figure 4.9: Normalized transmission curves for four different wavelengths in the 500-600 nm range obtained for silver nanoparticles using WLC z-scan.

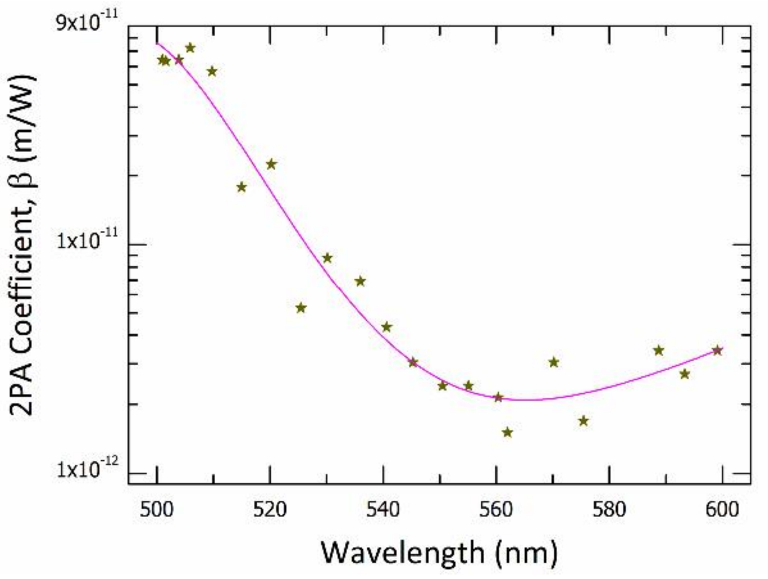

Figure 4.10: Calculated dispersion curve of the 2PA coefficient in silver nanoparticles for the range of 500-600 nm. The continuous line is drawn as an aid to the eye.

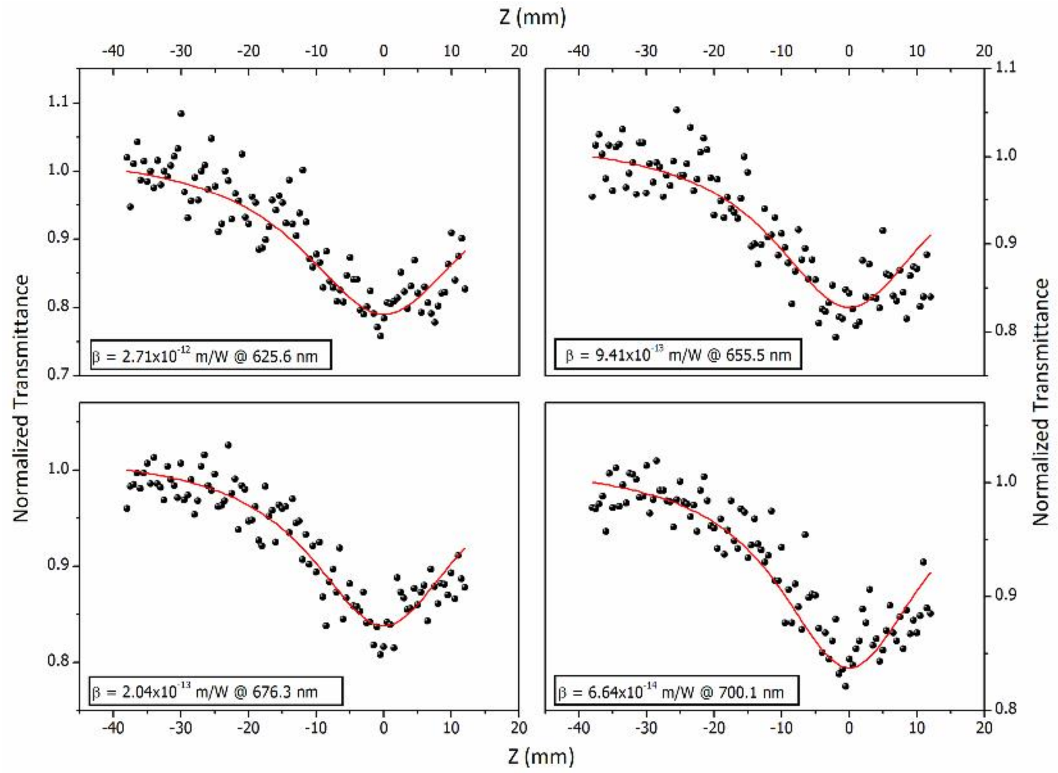

Figure 4.11: Normalized transmission curves for four different wavelengths in the 600-700 nm range obtained for silver nanoparticles using WLC z-scan.

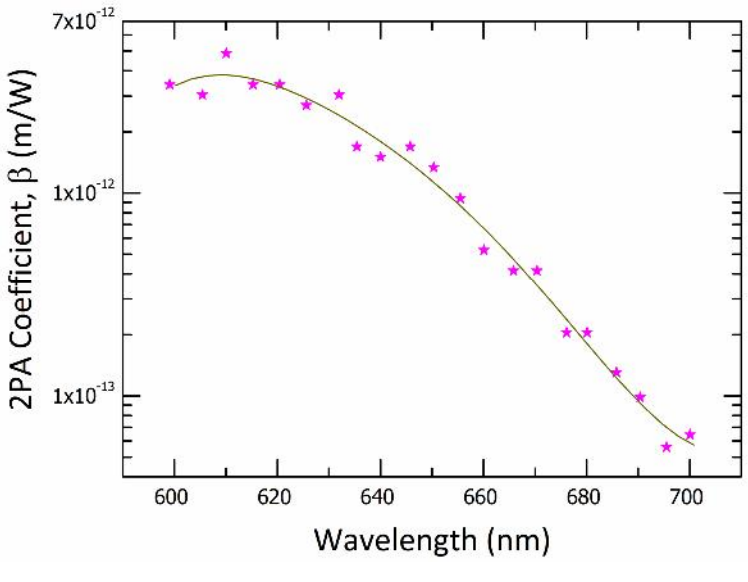

Figure 4.12: Calculated dispersion curve of the 2PA coefficient in silver nanoparticles for the range of 600-700 nm. The continuous line is drawn as an aid to the eye.

4.6 Conclusions

We investigated a number of liquid media for generating white-light continuum, of which CCl_4 and water are found to be the most efficient under the present experimental conditions. Normalized transmission curves for a range of wavelengths have been obtained in a single measurement for silver nanoparticle samples using the open aperture WLC z-scan. The experimental data obtained is successfully fitted with the nonlinear transmission equation, which shows the occurrence of two-photon absorption in the wavelength range of 500-700 nm. The advantages of the white-light z-scan technique over conventional z-scan technique in measuring the spectral dispersion of optical nonlinearities is highlighted.

References

1. *The Supercontinuum Laser Source*, R. R. Alfano (Ed.), Springer-Verlag, New York (1989).
2. *Band-gap dependence of the ultrafast white-light continuum*, A. Brodeur and S. L. Chin, Phys. Rev. Lett., **80**, 4406 (1998).
3. *Induced spectral broadening of a weak picosecond pulse in glass produced by an intense picosecond pulse*, R. R. Alfano, Q. X. Li, T. Jimbo, J. T. Manassah, and P. P. Ho, Opt. Lett., **11**, 626 (1986).
4. *Ultrafast white-light continuum generation and self-focusing in transparent condensed media*, A. Brodeur and S. L. Chin, J. Opt. Soc. Am. B, **16**, 637 (1999).
5. *Physical Factors Limiting the Spectral Extent and Band Gap Dependence of Supercontinuum Generation*, M. Kolesik, G. Katona, J.V. Moloney, and E.M.Wright, Phys. Rev. Lett., **91**, 043905 (2003).
6. *Emission in the region 4000 to 7000 Å via four-photon coupling in glass*, R. R. Alfano and S. L. Shapiro, Phys. Rev. Lett., **24**, 584 (1970).
7. *Femtosecond white-light continuum pulses*, R. L. Fork, C. V. Shank, C. Hirlimann, R.Yen, and W. J. Tomlinson, Opt. Lett., **8**, 1(1983).
8. *Supercontinuum generation in gases*, P. B. Corkum, C. Rolland, and T. Srinivasan Rao, Phys. Rev. Lett., **57**, 2268 (1986).
9. *Progress in Ultrafast Intense Laser Science II*, K. Yamanouchi, S. L. Chin, P. Agostini, and G. Ferrante (Eds.), Springer-Verlag, Berlin Heidelberg (2007).
10. *Advances in Atomic, Molecular, and Optical Physics: Volume 53*, G. Rempe and M. O. Scully (Eds.), Academic Press, London, UK (2006).
11. *Tsunami – user's manual*, Revision B, Spectra Physics (1999).
12. *New technique for degenerate two-photon absorption spectral measurements using femtosecond continuum generation*, G. S. He, T. C. Lin, P. N. Prasad, R. Kannan, R. A. Vaia, and L. S. Tan, Opt. Exp., **10**, 566 (2002).
13. *Z-scan measurements using femtosecond continuum generation*, L. De Boni, A. A. Andrade, L. Misoguti, C. R. Mendonça, and S. C. Zilio, Opt. Exp., **12**, 3921 (2004).
14. *White-light continuum z-scan technique for nonlinear materials characterization*, M. Balu, J. Hales, D. J. Hagan, and E. W. Van Stryland, Opt. Exp., **12**, 3820 (2004).

15. *Highly Efficient White Light Generation from Barium Fluoride*, A. K. Dharmadhikari, F. A. Rajgara, N. C. S. Reddy, A. S. Sandhu and D. Mathur, Opt. Exp., **12**, 695 (2004).

16. *Femtosecond filamentation and supercontinuum generation in silver-nanoparticle-doped water*, C. Wang, Y. Fu, Z. Zhou, Y. Cheng, and Z. Xub, Appl. Phys. Lett., **90**, 181119 (2007).

17. *Degenerate z-scan measurements with white-light continuum*, L. De Boni, A. A. Andrade, D. S. Dos Santos Jr, L. Misoguti, O. N. Oliveira Jr., C. R. Mendonça, S. C. Zilio, Annals of Optics, **5**, XXVI ENFMC (2003).

5

Instrumentation for the intense laser field–condensed matter interaction studies

The instrumentation work carried out for performing the intense laser plasma experiments is presented. The laser system used and pulse characterization techniques employed are described in detail. X-ray and γ-ray detection schemes and calibration methods are discussed. Electronic circuits designed and fabricated for the experiments are presented.

5.1 Introduction

The work described in chapters six and seven is an experimental study of the absorption and emission processes in laser-driven condensed media plasmas. These describe the measurement of x-ray emissions from solid targets and liquid jets. In this chapter, the laser systems and the necessary experimental and diagnostic equipment organized for these studies are discussed in detail. At high laser intensities, air itself will act as a nonlinear medium, and hence a vacuum environment is essential for background free measurements. For x-ray emission studies, a minimum working pressure of 10^{-3} Torr is necessary to prevent air from absorbing the emissions and affecting the plasma expansion. Vacuum is essential for the plasma to attain high temperatures as well, since energy transfer to the ambient air has to be avoided. For the detection of ions generated from the plasma, a vacuum of the order of 10^{-6} Torr will be necessary. Therefore a high vacuum chamber, originally designed for laser-microdroplet interaction experiments, was modified to conduct the intense laser-solid target interaction studies. A high vacuum compatible solid target manipulator and its control electronics were used together with the vacuum chamber.

5.2 The Ti:sapphire laser system

The ultrafast laser system used for the experiments is essentially a combination of four different lasers. The main components of the laser system and a brief description of each are presented below.

5.2.1: Millennia Pro - the pump laser

The pump laser used for the ultrafast oscillator is a frequency doubled, all solid-state Nd:vanadate (Nd:YVO_4) continuous wave laser capable of producing 5.2 W output power at 532 nm (Millennia Pro-S, Spectra Physics). The Nd:vanadate crystal is pumped by a diode laser (809 nm, 40 W) coupled to the crystal via an optical fiber module. The fundamental emission from the vanadate crystal is frequency doubled to produce 532 nm, using a Lithium Triobate (LBO) crystal. The output beam has a TEM_{00} spatial intensity distribution with a nominal beam width of 2.3 mm.

5.2.2: Tsunami - the ultrafast oscillator

The ulftrafast oscillator (Tsunami, Spectra Physics) consists of a folded cavity with an acousto-optic modulator (AOM) and active feedback for generation of ultrashort pulses by regenerative mode-locking technique. Dispersion compensation of the laser cavity is achieved with a pair of prisms, and the wavelength can be tuned with an adjustable slit. The lasing material is a one centimeter long Ti:sapphire crystal rod. The crystal is pumped by a continuous wave diode pumped, frequency doubled Nd:YVO_4 laser (Millenia Pro, Spectra Physics) at 532 nm with an output power of up to 5.2 W. The ultrafast oscillator produces Gaussian pulses of approximately 100 fs duration at a repetition rate of 82 MHz. The output wavelength can be tuned from 700 nm to 1000 nm (Tsunami -

broadband version). A maximum average power output of 550 mW can be obtained at 809 nm, which is the peak of the tuning curve.

The titanium ion (Ti^{3+}) is responsible for the laser action of Ti:sapphire. The electronic ground state of the Ti^{3+} ion is split into a pair of vibronically broadened levels as shown in figure 5.1. Absorption transitions occur over a broad range of wavelengths from 400 nm to 600 nm. Fluorescence transitions occur from the lower vibrational levels of the excited state to the upper vibrational levels of the ground state. Although the fluorescence band starts from 600 nm, the lasing action is only possible at wavelengths longer than 670 nm. This is because of the fact that the long wavelength side of the absorption band overlaps the short wavelength end of the fluorescence spectrum. Additionally the tuning range is affected by mirror losses, tuning element losses, pump power and atmospheric absorption.

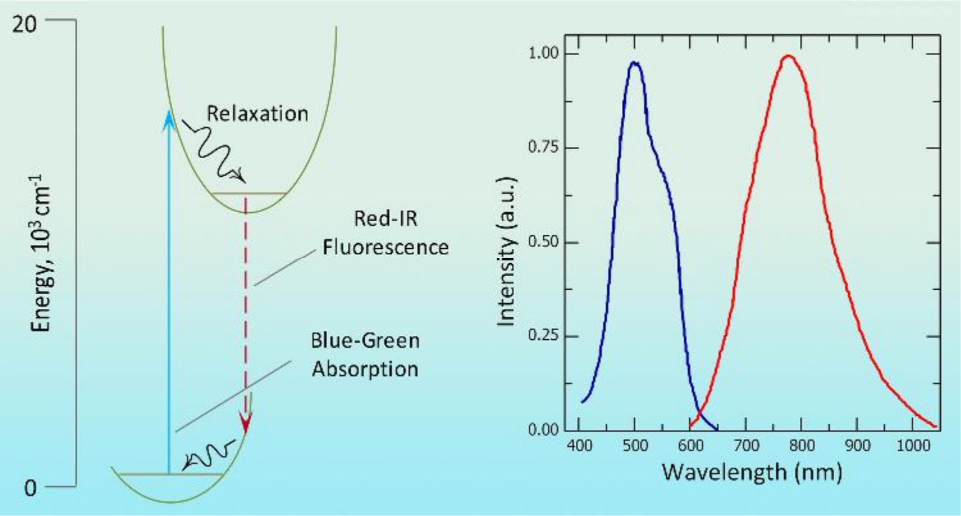

Figure 5.1: Absorption and emission spectra of Ti:Sapphire.

The pulse width tuning characteristics of Ti:sapphire are influenced by factors inherent in the Ti:sapphire material as well as the cavity parameters. The optical components in the laser cavity introduce positive group velocity dispersion (GVD) and cause pulse spreading in addition to that caused by self phase modulation in the Ti:sapphire rod. These effects are compensated with negative GVD, introduced in the cavity with the help of a pair of prisms {1}.

Mode-locking in the Tsunami oscillator is achieved by the use of an AOM module, in a regenerative mode-locking configuration. Unlike conventional active mode-locking, the RF drive signal used to drive the AOM is derived directly from the cavity in the regenerative mode-locking configuration. This removes one of the greatest drawbacks of active mode-locking, i.e., the requirement that the cavity length match the external drive frequency. In regenerative mode-locking the drive signal to the modulator automatically changes depending on the cavity length.

When the laser is switched on, it operates in the continuous wave (CW) mode with oscillations from several longitudinal modes. These are partially phase-locked, and mode beating generates a laser output at a frequency of c/2L. This mode beating is detected by a photodiode and then amplified. Since this signal is twice the required AOM modulation frequency (ω_{ML}), it is divided by two and then the phase is adjusted such that the modulator is always at maximum transmission when the pulse is present. Finally, the signal is reamplified and fed to the AOM.

Figure 5.2: The Tsunami oscillator along with the Millennia pump laser.

5.2.3: The Ti:sapphire chirped pulse amplifier (CPA)

The pulse energy levels (generally in nanojoules) from the Tsunami ultrafast oscillator are sufficient for many applications like multi-photon fluorescence microscopy, femtosecond writing, fluorescence lifetime measurements etc {2,3}. However, it is necessary to have much higher pulse energies (and hence high peak powers) for performing intense laser field experiments. So a regenerative "chirped pulse amplifier" is added to the system for obtaining high energy ultrafast pulses. It is not possible to amplify the ultrashort pulses directly to high energy levels, as this leads to intensities which are above the damage threshold of the amplifying medium. A technique called chirped pulse amplification (CPA) helps us to overcome this difficulty. In the CPA technique, the pulse to be amplified is first stretched in time by a large factor (typically 10,000) in order to reduce the peak power. This pulse can be then safely amplified, and after amplification, can be compressed back nearly to the original input pulse width {4,5}.

In our titanium sapphire amplifier (TSA 10, Spectra Physics), the 100 fs pulses from the femtosecond oscillator are sent to a pulse stretcher, which broadens the pulse to about 300 ps width. An individual pulse is then picked from the 82 MHz pulse train using an electro-optic modulator. The selected pulse is seeded into a regenerative cavity, which contains an optically pumped Ti:sapphire crystal. The principle of regenerative amplification is to confine, by polarization, a single pulse (selected from a mode-locked pulse train), amplify it to an appropriate energy level, and then “cavity dump” the output. The pulse oscillates in the cavity, gaining energy in each trip as it passes through the crystal. After several round trips, the pulse gains sufficient energy and is reflected out of the cavity using an electro-optic switch. Typically an input pulse of energy of a few nanojoules can be amplified to over 5 mJ in a single Ti:sapphire laser rod in the regenerative cavity. The cavity-dumped pulse is then fed to a double-pass linear amplifier for further amplification. The amplified pulse is then sent to a grating compressor, which compresses the pulse back to the original 100 fs width. The TSA-10 generates 100 fs pulses of 10 mJ energy at a repetition rate of 10 Hz.

Pulse stretching and compression in this system is achieved by the use of diffraction gratings. In a pulse stretcher, the input beam is incident on a diffraction grating, causing the different frequencies in the ultrafast laser pulse to disperse. The stretcher gratings are configured in such a way that the bluer frequency components have to travel further through the stretcher than the redder components so that the pulse gets stretched temporally.

Pulse compression is essentially the reverse of pulse stretching. In this case, the gratings are arranged such that the bluer frequencies travel the shortest path, catching up with the redder frequencies and thus compressing the pulse (details of the CPA technique can be found in chapter 1).

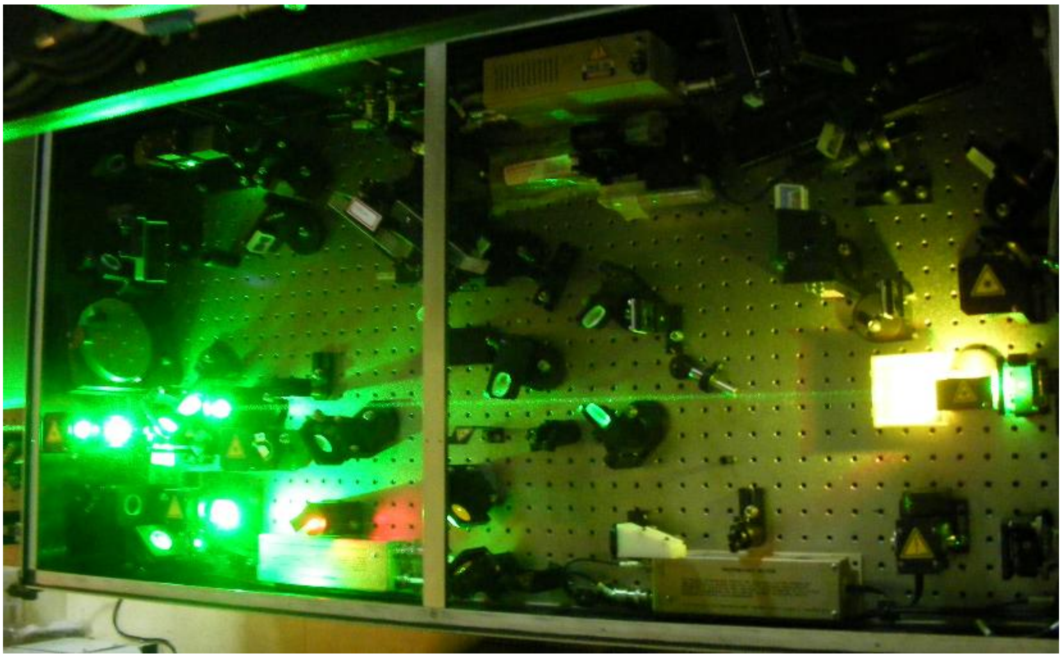

Figure 5.3: The CPA system used for the experiments (view from above).

5.2.4: Quanta Ray – pump laser for CPA

The CPA is pumped by a frequency doubled, Q-switched Nd:YAG laser (Quanta Ray, Spectra Physics) operating at 10 Hz with a nominal pulse width of 7 ns. This flash lamp pumped laser is capable of producing pulses of 275 mJ energy at 532 nm using a KDP crystal for frequency doubling.

5.2.5: Fast electronics: synchronization and delay generator (SDG)

The timings associated with the switching of the Pockels cells in the CPA is very critical. In order to ensure that a single pulse is admitted to the resonator, the input Pockels cell must be switched at the same time, with respect to the mode-locked pulse train. To achieve this, the Pockels cell switching is synchronized to the RF signal generated by the mode-locker of the ultrafast oscillator, using a synchronization and delay generator (SDG) unit. The phase of the switching (the time at which the Pockels cell switches with respect to the pulse train) can also be adjusted: following synchronization, there is a 0-1275 ns delay that allows phase adjustment. The SDG then produces the separate triggers, with adjustable delays, to drive the Pockels cells. The output Pockels cell switches the laser pulse out of the resonator. The pulse must be ejected only after sufficient number of round trips, and hence a delay of approximately 200 ns is employed between the switching of the two Pockels cells.

Figure 5.4: Photograph of the high energy ultrafast laser system used for the experiments.

5.3: Ultrafast laser pulse characterization

5.3.1: Measurement of the pulse width

The measurement of femtosecond pulse durations is always a challenging task, as one cannot use the normal electronic diagnostics for this purpose. The fastest electronic diagnostic tools available today are limited to a few pico seconds (e.g. the streak camera). Once the pulse durations are in the sub-picosecond regime, one employs the light pulse itself to measure its temporal duration in an autocorrelation setup {4}. We make use of the mathematical entity, the correlation function of two functions for this diagnostic technique.

The correlation function of a function *F(t)* is defined as,

$$C(\tau) = \int_{-\infty}^{+\infty} F'(t)F(t-\tau)dt \qquad - (5.1)$$

where $C(\tau)$ is a measurable first order correlation function and *F(t)* is the function to be known. $F'(t)$ is a known test function. In the present case, since it is extremely difficult to produce a test pulse of the same duration as the light pulse, we use the light pulse itself as the test pulse. Such a correlation technique is known as autocorrelation. In this case the laser pulse is split into two and recombined with known, adjustable time delays τ, and their correlation is studied as a function of τ.

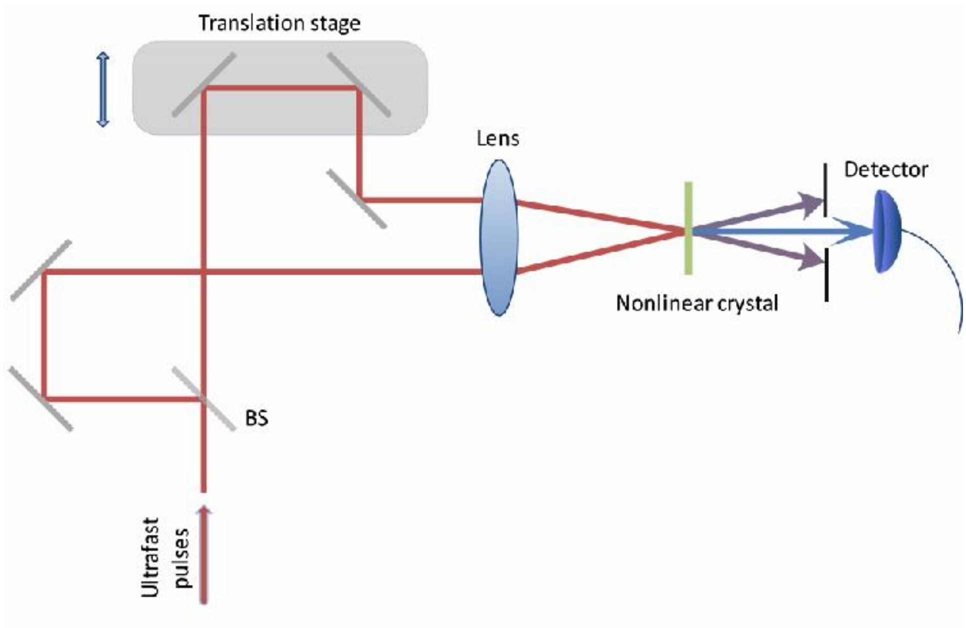

Figure 5.5: Schematic of the second order autocorrelation measurement.

We used the second order autocorrelation (also known as the intensity autocorrelation) technique to measure the temporal width of our ultrafast laser pulse. We choose the intensity autocorrelation technique due to the simplicity in its analysis and the zero background. The easiest way to implement a second order autocorrelation is to study second harmonic generation in a nonlinear crystal as a function of time delay between the two pulses. The experimental setup used for this purpose is shown in figure 5.5.

The incoming laser beam is split into two using a suitable beam splitter. The path length of one of the arms is fixed and other is delayed with respect to the first using an optical delay line. Two mirrors mounted on a translation stage in a retro reflector configuration acts as the optical delay generator. In our setup this translation stage can be moved in steps of 1.25 micrometers, which corresponds to an optical temporal delay of 4 fs. Both beams are then allowed to fall on a SHG nonlinear crystal in a non-collinear geometry, as shown in the schematic. The second harmonic generated in the crystal will be non-collinear with both the beams and hence can be separated using a simple slit, which is then fed to a photodetector. The averaged autocorrelation now will have the form,

$$C(\tau) = K \int_{-\infty}^{+\infty} I(t) I(t-\tau) dt \qquad - (5.2)$$

where K is a constant related to the nonlinear susceptibility of the crystal ($K = \left|\chi^{(2)}\right|^2$) and τ is the relative delay between the two pulses. In this case the crystal does the multiplication of the intensities ($I(t)I(t-\tau)$) during the process of second harmonic generation. Since the detector used is too slow to resolve the variation of intensity in time (we used a slow photodiode which had a pulse rise time of about 40 ns), it will measure only the integrated intensity. In other words, the output from the photo detector readily corresponds to the intensity autocorrelation of the two pulses. From the obtained autocorrelation trace, the input pulse width can be calculated, provided the pulse shape of the input pulse is known. For a Gaussian pulse, the autocorrelation width is $\sqrt{2}$ times the input pulse width, whereas for a sech^2 pulse, the autocorrelation width is 1.543 times the input pulse width {6}. In our case the ultrafast pulse shape is nearly Gaussian, and the pulse width measured using intensity autocorrelation is 93 fs. For the sake of simplicity, the pulse width is taken as 100 fs throughout the discussions in this thesis.

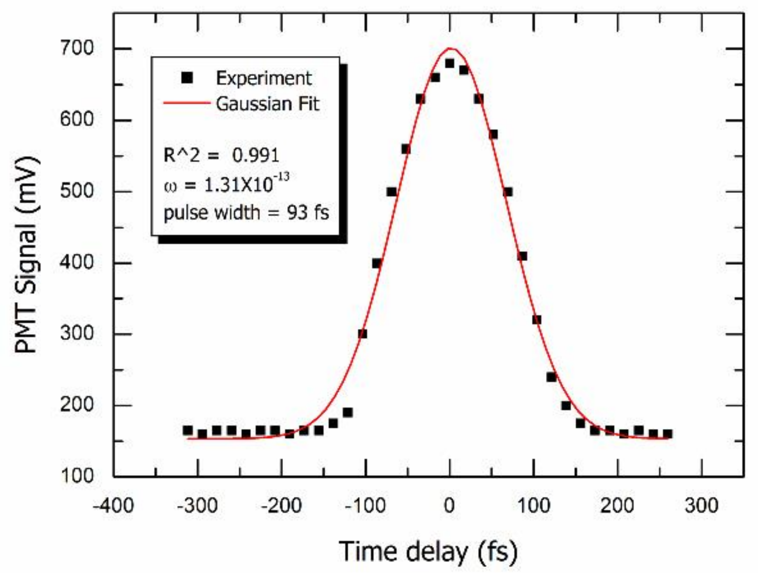

Figure 5.6: Measured intensity autocorrelation of the ultrafast laser.

5.3.2: Spectral characteristics

Since the ultrafast pulse is generated by mode-locking a large number of laser cavity modes, it is broad in the spectral domain. For a Gaussian pulse, the relationship between the spectral and temporal width is given by $\Delta \nu \Delta t \geq 0.441$ {7}, which corresponds to a bandwidth (Δλ) of about 9 nm for a chirp-free pulsewidth (Δt) of 100 fs, at 800 nm wavelength.

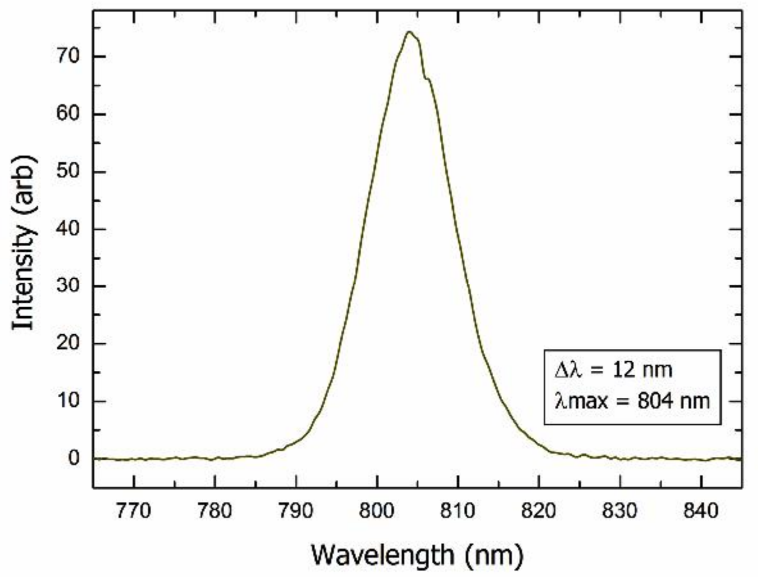

Figure 5.7: Wavelength spectrum of the ultrafast laser pulse.

The spectrum of the ultrafast pulse (output from TSA-10) is measured using a CCD based single shot fiber optic spectrometer (Avaspec 2014, Avantes BV) and the $\Delta\lambda$ obtained is approximately 12 nm (FWHM) at a central wavelength of 804 nm (figure 5.7).

5.3.3: Spatial intensity profile

The cross-sectional intensity profile of a beam is another important parameter, which is crucial in determining the focused spot size as well as the irradiance of the beam. We used a CCD beam profiler (ML3754, Metrolux GMBH) to record the spatial intensity profile of the beam. The beam diameter also can be measured using the beam profiler, by calibrating the pixel size. A Gaussian spatial beam profile is obtained, which is given by,

$$I = I_0 e^{-\left(r^2/\omega^2\right)} \qquad - (5.3)$$

where r is the position along the radial direction of the beam. I_0 is the intensity at r=0, and 2ω is the beam diameter (FWHM). The beam diameter measured using the beam profiler is 7 mm.

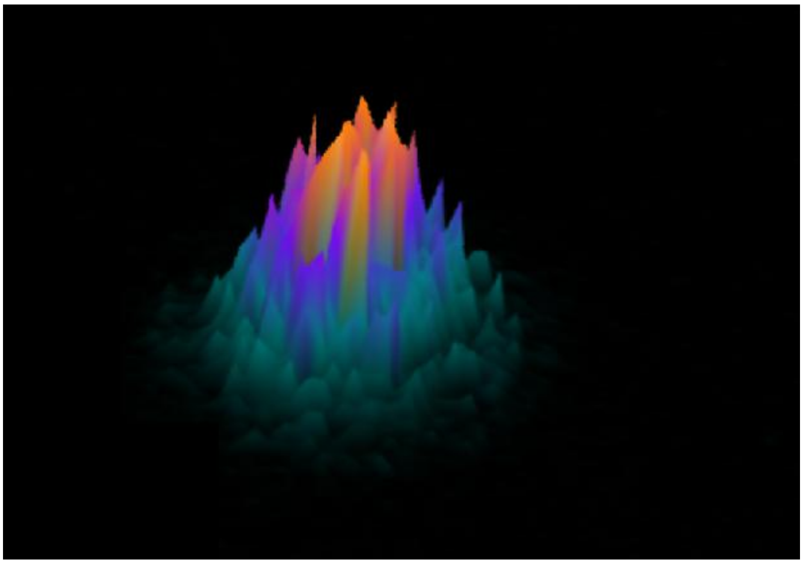

Figure 5.8: Spatial intensity profile of the ultrashort laser pulse.

5.3.4: Beam diameter and spot size measurements

In addition to imaging by the beam profiler, we also used the conventional knife-edge method to determine the beam diameter. In the knife-edge method, a knife-edge is scanned across the transverse profile of the beam and the beam power after the knife-edge is recorded using a photodetector. The detector output corresponds to the integrated intensity, which when differentiated gives the input laser spatial profile.

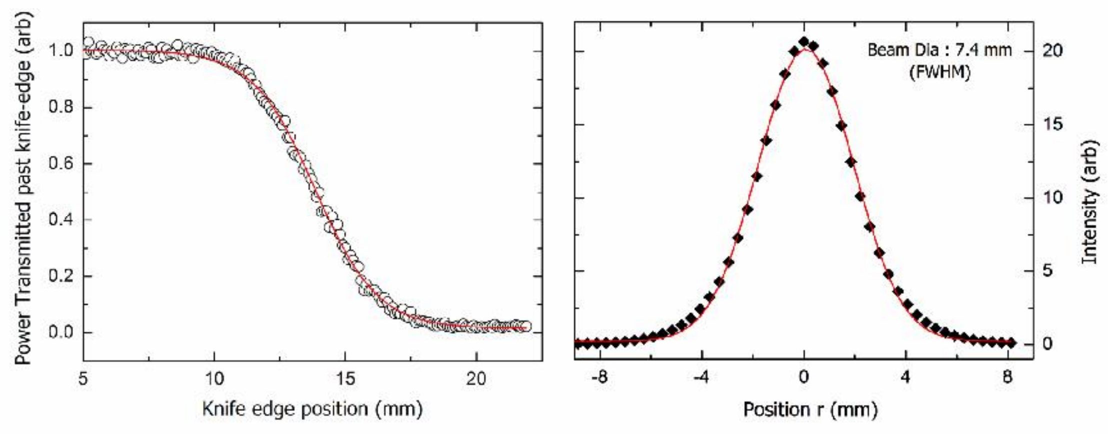

Figure 5.9: Beam diameter measurement using the knife-edge technique.

Assuming the laser spatial profile to be a Gaussian, the beam diameter can be calculated by fitting a Gaussian to the derivative of the photo detector output. The beam diameter calculated using this method is 7.4 mm, which matches well with the value obtained from the beam profiler measurements.

For measuring the spotsize (radius of the beam at the focus) of the beam at the focal point of a focusing lens, the beam diameters at different z positions after the lens along the beam propagation direction are measured. For a paraxial beam of wavelength λ, the beam radius ω at any given point z is given by the equation,

$$\omega(z) = \omega_0 \sqrt{1 + \left(z/z_0 \right)^2} \qquad - (5.4)$$

where ω_0 is the spotsize and z_0 is the diffraction length (Rayleigh range) given by the equation $z_0 = \frac{\pi\omega_0^2}{\lambda}$.

A theoretical fit done using the above equation to the experimental result helps us to extrapolate the curve to the focal point. From the best fit obtained for the experimental data, the value of the spotsize can be obtained. The results from these measurements are presented in figure 5.10.

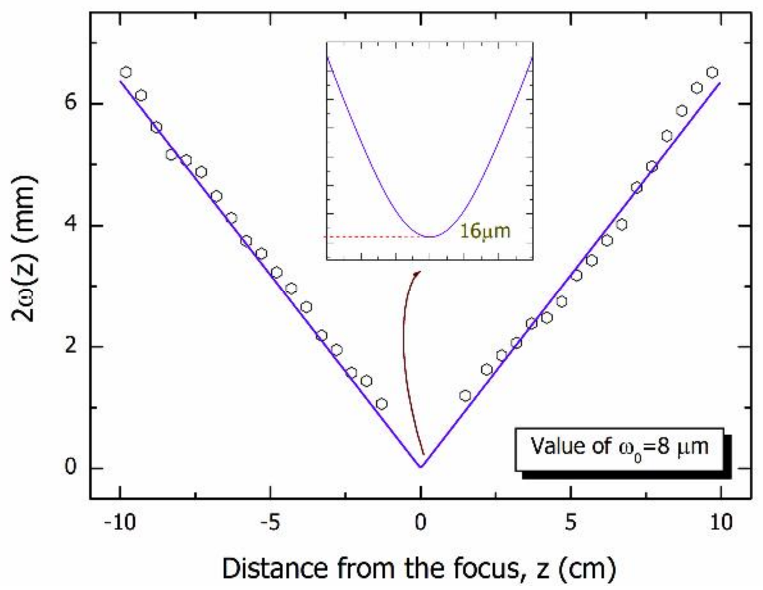

Figure 5.10: Spotsize measurement for the ultrafast laser beam focused by a plano-convex lens of 11 cm focal length at 800 nm.

The measurements were done using a 11 cm focal length (@800 nm) lens and the value obtained for the spotsize is 8 micrometers. This value is used for the calculations in the laser – planar liquid jet experiments discussed in chapter 6.

5.4: The vacuum chamber

The vacuum chamber used is of 1 meter diameter and 40 centimeter height, and has a volume of approximately 300 litres. Such a high volume is not necessary for the experiments reported in this thesis; however we decided to use this chamber because it was available in the lab. It was originally built for liquid droplet – laser interaction studies, and a detailed description of the chamber design can be found in the reference {8}. To make the chamber suitable for solid target studies, we fabricated a high vacuum compatible target manipulator, which was fixed on top of the chamber (details of the solid target manipulator are given in section 5.5).

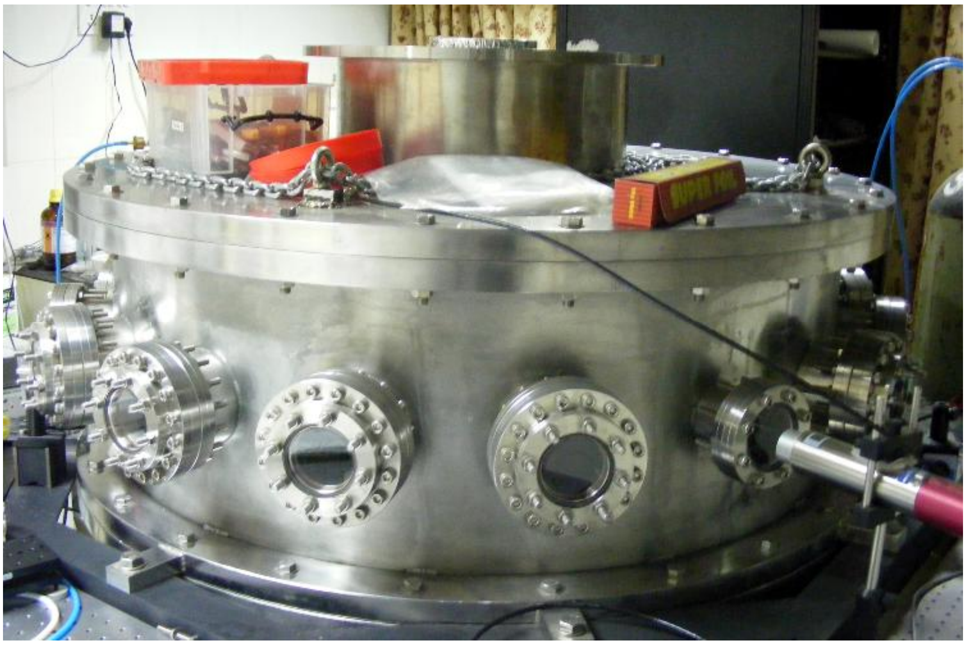

Figure 5.11: The vacuum chamber used for the experiments.

There are 16 ports along the periphery of the chamber as shown in figure 5.11. All ports are centered to the interaction region in the center of the chamber. X-ray, γ-ray and visible emissions can be measured by placing appropriate detectors in front of these ports. This design helps us to take simultaneous measurements of the angular distribution of plasma emission in real time.

To obtain an oil-free vacuum, the chamber is pumped using a turbo molecular pump backed by a dry pump. Oil-free vacuum is preferred for our experiments as continuous pumping using a rotary pump could leave a layer of oil on the target surfaces, which would affect the surface conditions, especially on polished and coated targets. We used a Pfeiffer 2000 l/s turbo molecular pump (TPU 2101 PC) backed by a Pfeiffer 180 l/min (Unidry DBP 050-4) dry pump. The turbo molecular pump is connected to the chamber through an electro-pneumatically actuated gate valve, for isolating the pump from the chamber. Another electro-pneumatically actuated gate valve is used in between the turbo molecular pump and the backing dry pump. Option is provided to connect the backing dry pump to the chamber directly (bypassing the turbo molecular pump) using another manually operated gate valve. This option allows us to use the same backing pump for pumping down the chamber to pre-vacuum levels required for some experiments (like reflectivity studies), completely isolating the turbo molecular pump from the chamber.

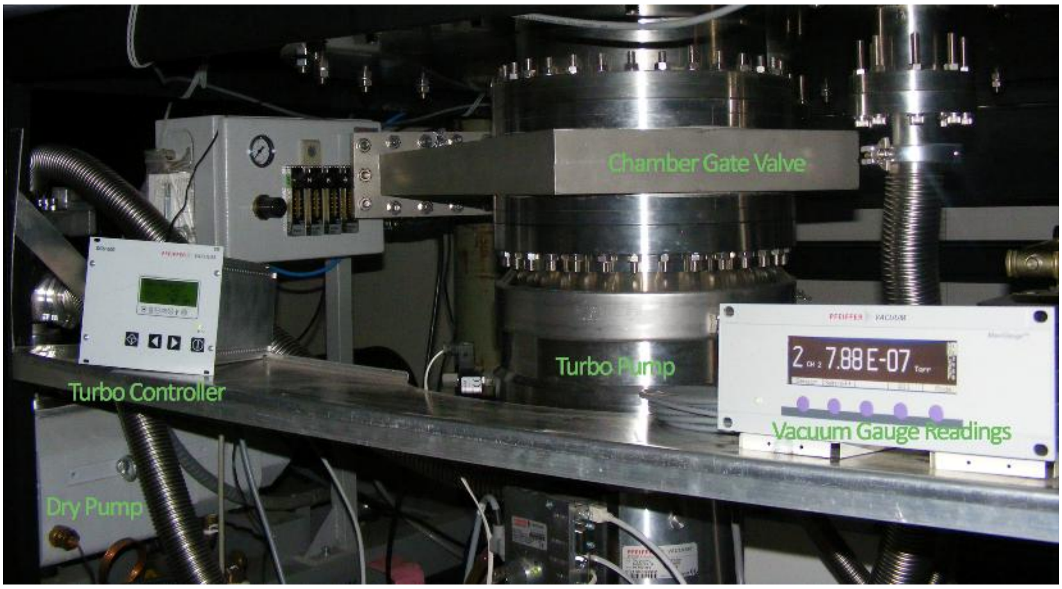

Figure 5.12: Chamber pumping equipment.

The dry pump can evacuate the chamber to a pressure of 5x10^{-2} Torr in about five minutes. A Pirani gauge is used to measure the rough vacuum. The Pirani gauge essentially uses the thermal conduction of the gas to measure the pressure. The gauge head is placed around a heated wire that is exposed to the gas. The resistance of the wire is temperature dependent. When the gas molecules collide with the wire its temperature and hence its resistance decreases. When the pressure in the chamber decreases, the number of colliding molecules decreases and hence the temperature of the wire increases. A calibration of this temperature dependent resistance makes it useful for pressure measurement. The Pirani gauge can be used for measuring a vacuum range of 750 Torr to 3.75x10^{-4} Torr. Lower pressures are measured by using a cold cathode gauge, which has a measuring range of 7.5x10^{-3} Torr to 1.5x10^{-9} Torr. The cold cathode gauge (Penning gauge) is an ionization gauge in which a high voltage discharge produces an electron beam that ionizes the gas in the chamber. These ions will create a current in the anode and the anode current will be proportional to the pressure of the chamber. A magnetic field is applied to increase the path of the charged particles and ionization current. In our experimental setup, the turbo molecular pump in conjunction with the dry pump can pump the chamber pressure down to 5x10^{-6} Torr in about twenty minutes. An ultimate pressure of 5x10^{-7} Torr can be achieved in about an hour.

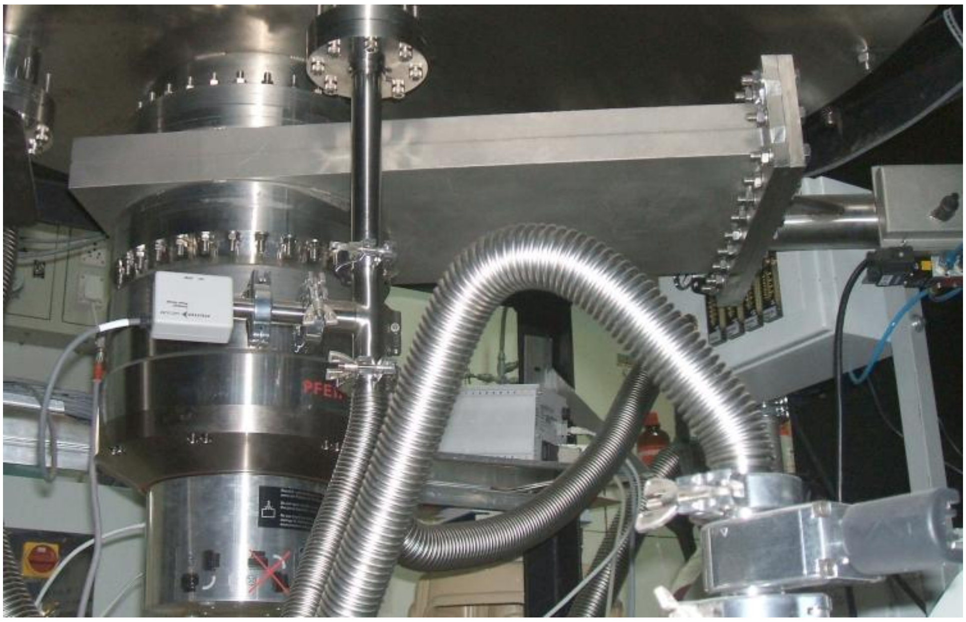

Figure 5.13: View of the vacuum chamber from the bottom side.

5.5: The solid target manipulator

Since the sample kept at the focus gets modified at each laser shot, it is important to move the sample during irradiation, so that the laser sees a fresh sample surface at each shot. In the case of solid targets, a vacuum compatible translation stage is necessary to achieve this. There are two approaches to this problem. One is by placing vacuum compatible XY translation stages, available commercially, inside the vacuum chamber and wiring the connections via a vacuum compatible electrical feed-through. The alternative is to have an ordinary XY translation stage outside the vacuum chamber and couple its translation via a Wilson seal to the vacuum compatible target holder placed inside the chamber. We preferred the second approach as it offers more flexibility and is comparatively cheaper. Also, while the vacuum compatible translation stages have a vacuum limit of 10^{-6} Torr, the second approach gives vacuum levels at least two orders of magnitude higher.

We designed the solid target manipulator in such a way that the target could be moved in the horizontal and vertical directions, in a range of 50 mm in both directions with a positional accuracy of 12.5 micrometers. The 100 CF port on the top of the chamber was used for attaching the solid target manipulator. The schematic of the target manipulator is presented in figure 5.14.

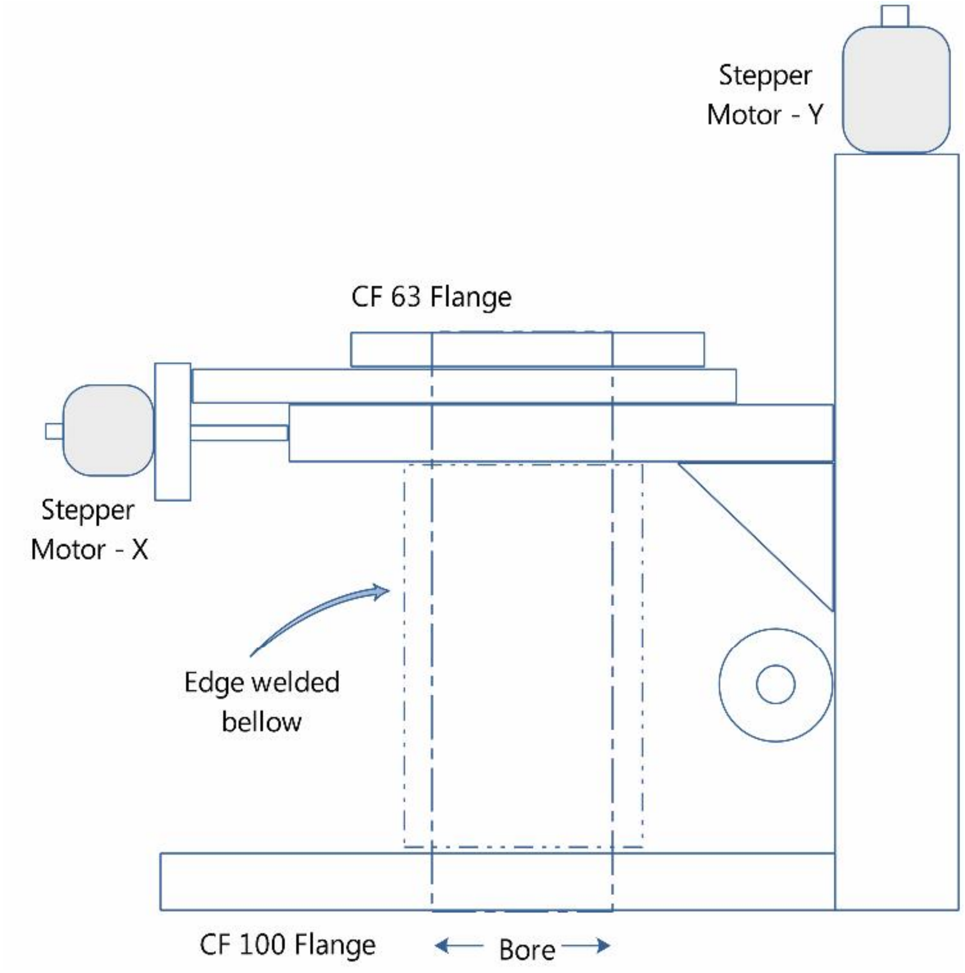

Figure 5.14: UHV compatible solid target manipulator schematic.

Figure 5.15 is the schematic of a Wilson feed-through designed to attach the solid targets to the above mentioned target manipulator. The target can be fixed at the M4 tapped end of a 1 cm stainless steel thick rod, which is attached to a 63 CF blank port using an O-ring Wilson sealed movable joint. This indigenous design allows us to control the target tilt and it gives us more freedom on the Y-axis positioning. Bi-polar stepper motors X and Y control the motion of the target inside the vacuum chamber. The stepper motors used have a full step movement of 1.8 degree per pulse. There is also a provision for the manual control of the manipulator. The leak rate observed under helium leak test for the target manipulator is below 2x10^{-10} cc/sec.

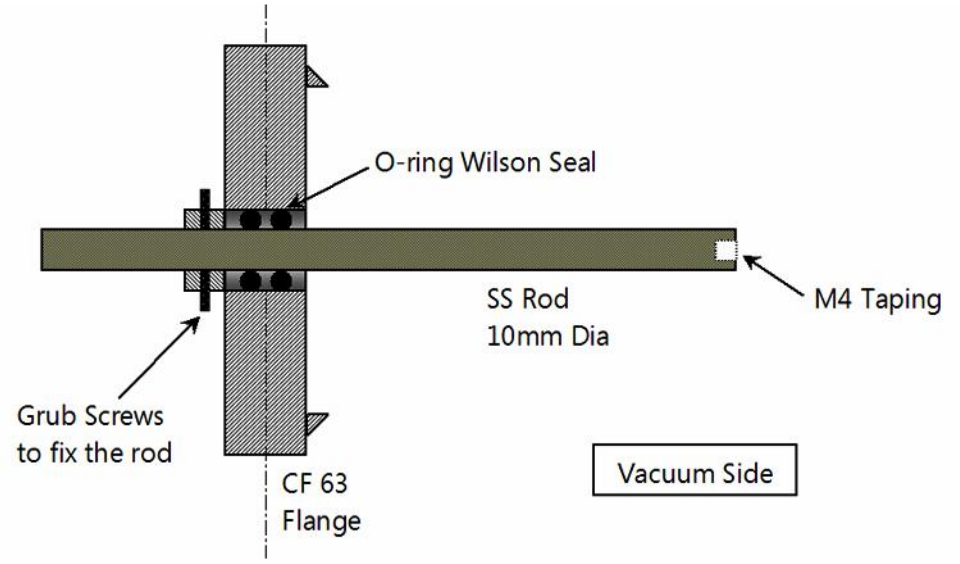

Figure 5.15: Schematic of the Wilson feed-through used to attach the solid targets to the target manipulator.

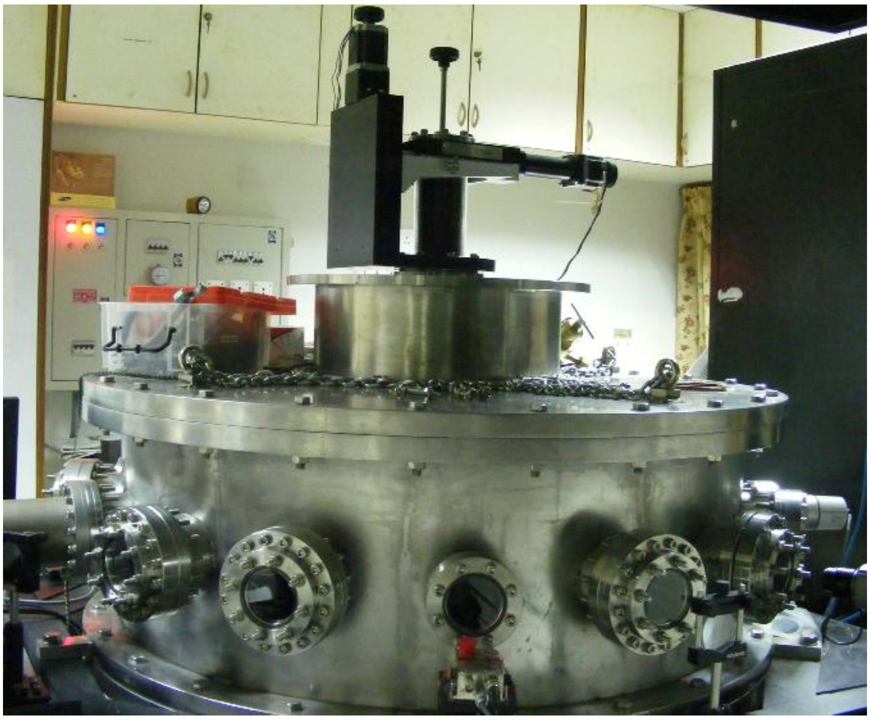

Figure 5.16: A photograph of the vacuum chamber with the solid target manipulator attached on the top CF 100 flange.

5.6: The target motion controller

The stepper motors of the target manipulator need to be controlled and synchronized with the laser for ensuring proper measurements. The motors should be controlled in such a fashion that the manipulator first moves in the X direction, from one end to the other, halting at regular intervals as specified by the user. The laser should be allowed to fall on the target at each stop and the corresponding emission data needs to be taken. When the target reaches one end of the translation stage, the Y motor should be enabled so that the target is shifted vertically to the next line. It should then be moved in the opposite X direction, and so on. We designed and implemented the electronics and software needed to perform these tasks.

We used the LPT port (parallel port) of a PC to send the control signals to the target manipulator and the laser trigger input. An electronic buffer circuit is necessary between the computer and the motor as the stepper motor requires high currents to run, which cannot be sourced by the computer. This circuit should also provide good isolation between the PC and the stepper motors to prevent damage of the PC from high back emfs generated in the motor. In addition the circuit should be capable of selecting the appropriate stepper motor for X or Y movement as per instructions from the PC. The electronics used should be able to provide the current required by the stepper motor (typically around 2 A in our case) and should also have a provision for triggering a relay-energized mechanical shutter, which is used for selecting a single laser pulse from a 10 Hz pulse train. An electronic circuit is designed taking all these factors into account. The circuit diagram can be seen in figure 5.17. A printed circuit board (PCB) is designed for the same using a computer aided design (CAD) software. The PCB design schematic and the populated PCB are shown in figure 5.18.

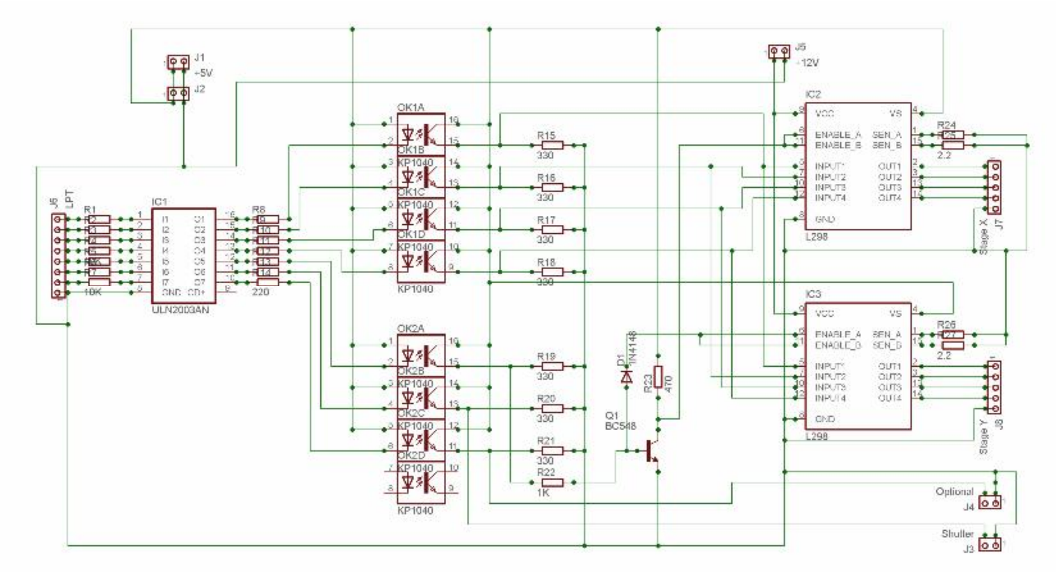

Figure 5.17: Circuit diagram for the XY manipulator controller.

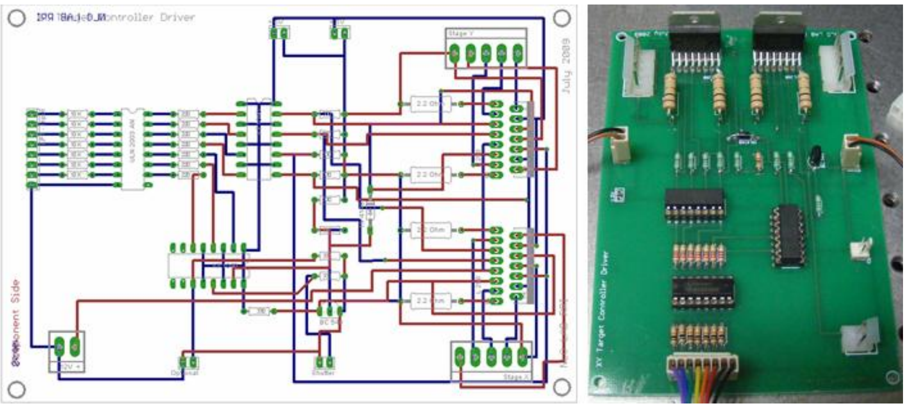

Figure 5.18: Double sided PCB design for the target controller.

The circuit developed is capable of driving both unipolar and bipolar type stepper motors up to a current of 4 A. Provisions for mechanical shutter control and optional trigger outputs are also included in the design. The TTL pulses from the parallel port of the computer are fed to the ULN2003, which contains an array of seven darlington pairs. This acts as a buffer between the parallel port and the next stage of the electronic circuit, thereby limiting the current drawn from the parallel port. The output of this current amplifier is fed to KP1040, which is a four-channel optocoupler. This provides the necessary electrical isolation between the PC and the stepper motor. The first four outputs of the optocoupler are the control signals for the stepper motor. These signals are then fed to the IC L298, which is a dual bridged driver, which is capable of driving high current loads up to 4 A. This IC drives the X translation stage stepper motor. The same signals are fed to another L298, which drives the Y stage. Selection between the two is made by the fifth signal from the parallel port, which is fed to the enable pins of L298. The enable signal to the X translation L298 IC is inverted using an npn transistor. If the fifth signal is low, the enable pin of stage X L298 becomes high thereby enabling the output to the X stepper motor. The stage Y L298 stays disabled at this time as its enable input value stays at low. Subsequently stage Y can be selected by making the fifth signal go high. The sixth signal from the parallel port is used to energize a relay that controls the mechanical shutter. The seventh signal is made available at the connector marked *optional* in the PCB, which can be used to trigger any other optional accessories that need to be controlled using the program.

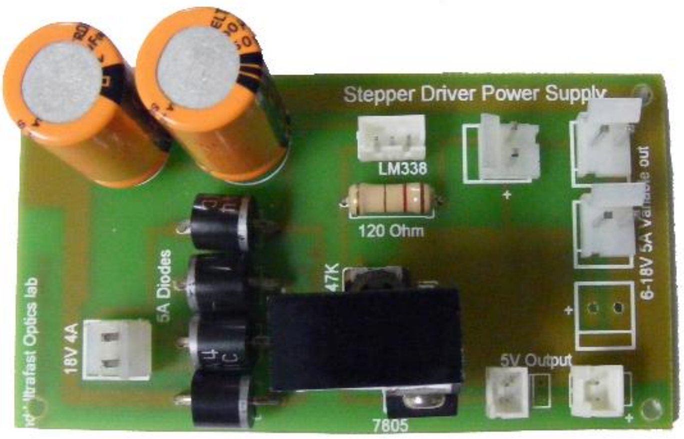

Figure 5.19: Variable, regulated power supply for the target motion controller

A regulated power supply with a variable output from 0 to 18 V with a current capacity of 5 A for the motion controller electronics was also designed and implemented. This includes a separate 5 V regulated output as well for the digital gates included in the stepper controller design. A PCB was designed and fabricated for this circuit. The designed PCB can be seen in figure 5.19. The circuit diagram and a brief description of the same can be found in the appendix.

During the experiment the target has to be moved from position (x_1, y_1) to (x_2, y_2). In this period the laser pulses should be blocked by the mechanical shutter. After moving the target through this definite distance, the laser must be allowed to fall on it by opening the shutter. If the user stops the measurements in between for some reason, the program must store the (x, y) value of the location where the target manipulator was stopped. If the experiment resumes at a later time, it must start from this position. A program was written in LabVIEW^{TM} keeping all these factors in mind. The front panel of the target motion controller program is given in figure 5.20.

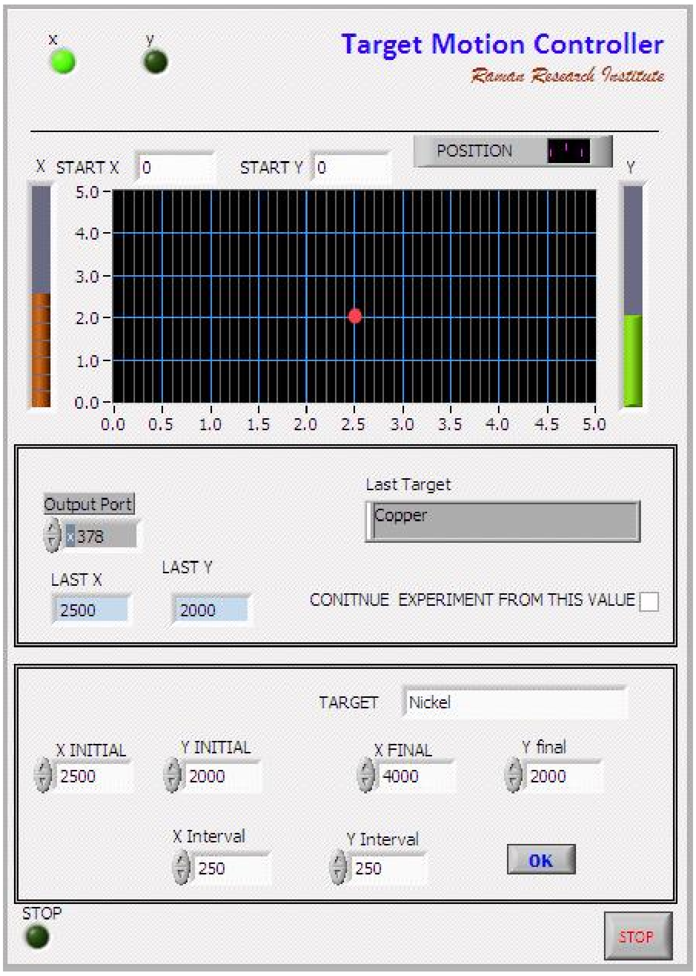

START X 0
START Y 0
Output Port x378
Last Target Copper
LAST X 2500
LAST Y 2000
CONITNUE EXPERIMENT FROM THIS VALUE ☐
TARGET Nickel
X INITIAL 2500
Y INITIAL 2000
X FINAL 4000
Y final 2000
X Interval 250
Y Interval 250

Figure 5.20: Front panel of the target motion control program.

The program will start when the OK button is pressed after entering all the necessary input parameters in the appropriate columns. The live position on the target where the laser is incident is displayed as a red spot in the graph. The two vertical progress bars indicate the progress of the experiment. STOP button can be used to stop the experiment at any point, if required. The VI is developed for targets of 5 cm x 5 cm dimension. For any values of x or y greater than these values, an error message will be displayed, indicating that the target manipulator has reached the limits.

5.7 Solid-state radiation detectors

Solid-state detectors are preferred over gas-filled detectors for measuring high energy radiations as they have material densities three orders of magnitude higher than gases. As the material density increases the number of interaction sites increases, leading to enhanced interaction probabilities so that the detector dimensions are considerably reduced. We chose Si-PIN and NaI(Tl) solid-state detectors for measuring the x-ray and γ-ray emissions from the laser produced plasma. Details of these detectors as well as their calibration methods are discussed below.

5.7.1 Si-PIN : x-ray detector

The depletion region of semiconductor diodes possess properties appropriate for a radiation detection medium. When the radiation deposits energy in a semiconductor detector, an equal number of conduction electrons and holes are created within a few picoseconds along the radiation track. An electric field applied across the detector active volume will ensure that the electron-hole pair created will experience an electrostatic force. Due to this electrostatic force, the electron-hole pair created in the active region will drift to the corresponding electrodes and be collected as the corresponding electrical signal. The number of electron-hole pairs produced corresponds to the incident radiation energy provided the radiation is completely absorbed. The ionization energy for silicon is about 3 eV whereas for gases it is about 30 eV. Hence ten times more number of electron-hole pairs are produced in these solid-state detectors for the same incident radiation as compared to the gas detectors. This is very advantageous in the case of soft x-ray detection, as they do not create many electron-hole pairs.

In the silicon *p-i-n* diode configuration, a high resistivity *i*-region is introduced between the *p* and *n* non-injecting contacts on either surface. This particular configuration helps to reduce the leakage current. Semiconductors generally show a finite conductivity even in the absence of ionizing radiations. Hence there is an inherent leakage current, which may fluctuate enough to suppress signals originating from a true ionizing radiation, if the signal is weak. So to get a better signal to noise ratio, the leakage current should be kept at a minimum and hence a p-i-n configuration is preferred. Another source of leakage current is the thermally induced electron-hole pairs at the depletion layer. This can be controlled by operating the detector at low temperatures. The detectors are usually cooled thermo-electrically or using liquid nitrogen to temperatures of the order of 200 K. Si-PIN detectors are generally used for detecting x-rays in the 1 keV to 100 keV regime. The relatively small number of electron-hole pairs created by a low energy x-ray photon demands maximum reduction in the detector noise level for a faithful detection.

We used two XR-100CR Si-PIN detectors from Amptek for x-ray detection in our measurements. The XR-100CR is a new high performance x-ray detector, preamplifier, and cooler system using a thermoelectrically cooled Si-PIN photodiode as an x-ray detector. Also mounted on the 2-stage cooler are the input field-effect transistors (FET) and a novel feedback circuit. These components are kept at approximately -55 °C, and are monitored by an internal temperature sensor. Cooling the FET reduces its leakage current and increases the transconductance, both of which reduce the electronic noise of the system. The hermetic TO-8 package of the detector has a light tight, vacuum tight thin Beryllium window to enable soft x-ray detection. The Beryllium (Be) window filters low energy photons, thereby reducing low energy background. As the thickness of the Be window increases, the filtering effect increases. So by carefully choosing the Be window thickness, one can strike a balance between the background noise and the detection efficiency. The detector is used in conjunction with an analog linear amplifier, PX2CR (Amptek USA). The standard shaping time constant of the linear amplifier PX2CR is 12 μs, and a higher energy resolution is obtained if 20 μs shaping time is chosen. The detector XR100CR with 7 mm^2 area and 300 μm thickness having a Be window of 0.5 mil (1 mil = 1/1000th of an inch = 25.4 μm) thickness is capable of detecting in the < 1 keV to 30 keV range (pulse shaping time of 20 μs). The other XR100CR detector with 5 mm^2 area and 500 μm thickness has a Be window of 1 mil thickness, and it is capable of detection in the 2 keV to 90 keV range (pulse shaping time of 12 μs). These detectors have an approximate energy resolution of 190 eV. The intrinsic full energy detection efficiencies of these detectors {9} are shown in figure 5.21.

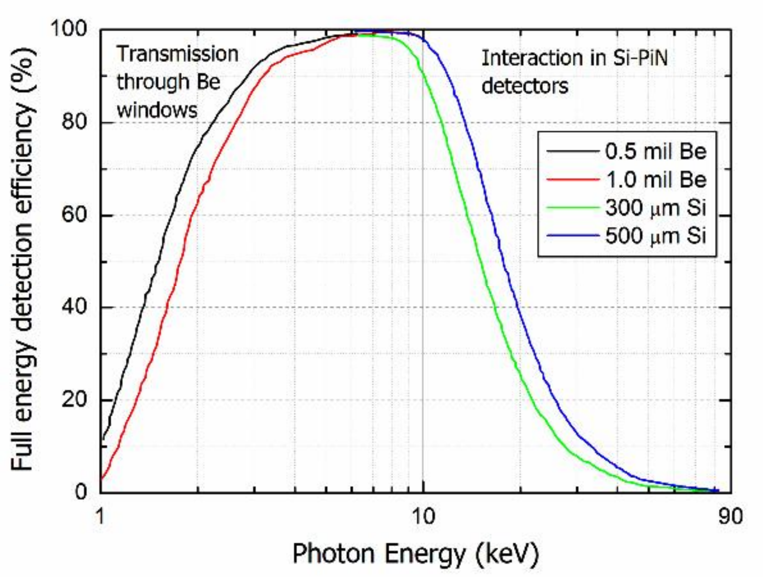

Figure 5.21: Intrinsic full energy detection efficiency of a Si-PIN detector.

Electron-hole pairs created by the radiation, which interacts with the Si near the back contact of the detector, result in fluctuations in charge collection times. These fluctuations will be observed as rise time variations of the voltage step at the output of the charge sensitive preamplifier. As a result the acquired spectra will suffer from increased background counts and a degraded energy resolution. To reduce these effects, a real time discriminator (RTD) option is incorporated in the linear amplifier PX2CR. When RTD is active, the shaped pulses are internally gated and only pulses corresponding to full charge collection are allowed to be sent to the MCA for analysis. The internal threshold of this RTD gating is set around 2 keV. RTD should be inactivated if radiations below 2 keV are to be measured.

5.7.2. NaI(Tl): γ-ray detector

The three important mechanisms of γ-ray interaction with matter that leads to their detection are the *photoelectric effect, Compton scattering and pair production*. As a result of these mechanisms the γ-ray will either completely disappear, or scatter to very large angles. The predominant mode of interaction of x-rays and low energy γ-rays with matter is the photoelectric process. In the photoelectric process the photon will be absorbed by the absorber atom, creating a photoelectron with a kinetic energy equivalent to the difference in energy between the incident photon and the binding energy of the electron. This process is enhanced for materials with higher atomic number and hence most of the γ-ray detectors are made with constituents of high atomic mass. The Compton scattering probability depends on the number of electrons available. Hence the Compton scattering probability per atom increases with the atomic number. Pair production occurs if the γ-ray energy exceeds twice the rest mass energy of an electron (1.02 MeV). The probability of pair production approximately scales as the square of the atomic number of the absorber. The probability of these three interactions as a function of energy is plotted {10} in figure 5.22.

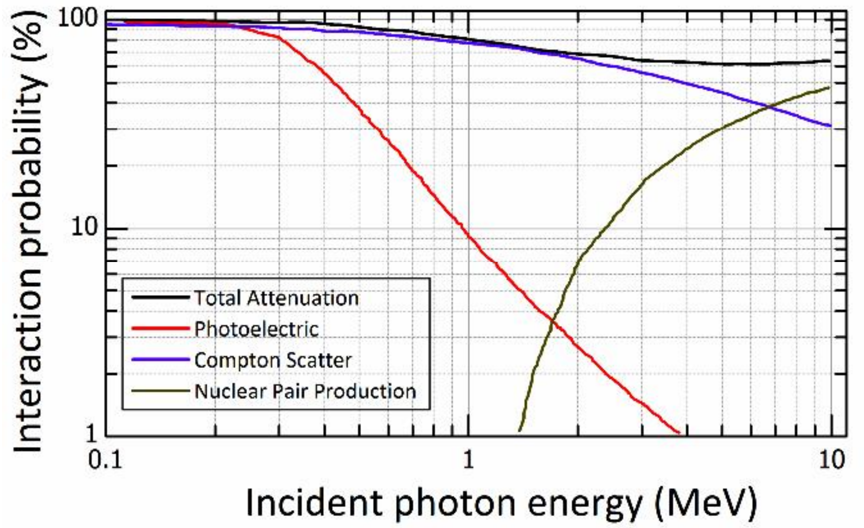

Figure 5.22: Computed interaction probabilities {10} in the 30 mm X 30 mm Amptek make NaI(Tl) detector chosen for the present studies.

Scintillation detectors use crystals that emit light when gamma rays interact with the atoms in the crystals. The intensity of the light produced is proportional to the energy deposited in the crystal by the gamma ray. These detectors are often coupled to a photomultiplier, which converts the light generated to the corresponding electrical signal. The first solid medium used for γ-ray detection is thallium-doped sodium iodide (NaI(Tl)), often known as the sodium iodide detector. Since NaI(Tl) can be produced in large crystals, yielding good efficiency, and it produces intense bursts of light compared to other spectroscopic scintillators, NaI(Tl) still continues to be one of the most widely used scintillation material. The conversion mechanism in a scintillator involves the conversion of the incident γ-ray to the corresponding optical emissions and then the creation of the photoelectrons.

Thus a γ-ray detector should act as a conversion medium for the incident γ-rays to yield one or more fast electrons, and it must act as a conventional radiation detector for the fast electrons. The relatively high atomic number 53 of its iodine constituent ensures that photoelectric effect will be the dominant process in the NaI(Tl) detector. Generally the energy resolution of a radiation detector is determined by the charge collection statistics, electronic noise, variation in the detector response over its active volume, and drift in the operation parameters over time. For the scintillation detectors, the fluctuations in the gain of the photo multiplier tube also is a determining factor of the resolution. Hence the energy resolution of a scintillation detector is basically limited by the photoelectron statistical fluctuations.

We used an Amptek GAMMA-8000 series scintillation detector for γ-ray detection which has a standard 30 mm x 30 mm NaI(Tl) scintillator crystal. It also includes a standard 3 mm PMT and a Cockroft Walton high voltage generator. The scintillation crystal is housed in an anodized aluminium case of thickness 0.5 mm, which reduces the background signals to the detector. The typical energy resolution of this detector is < 7.5% FWHM at 662 keV and < 14% FWHM at 59.5 keV.

5.7.3 Multichannel analyzer (MCA)

The operation of a multichannel analyzer is based on the conversion of the pulse amplitude from a radiation detector to a corresponding digital number. The radiation detector generates electrical signals corresponding to the input radiation and a pulse height analyzer in a radiation detection system records the amplitude distribution of pulses produced by the detector. This is then fed to a linear amplifier, which shapes and increases the amplitude of these pulses to match it with the input of the multichannel analyzer. The key component of an MCA is an analog to digital converter (ADC). These ADCs are designed in such a way that they produce a single output value for each analog pulse presented to their input, which is proportional to the peak amplitude of that pulse and hence named as peak sensing ADCs. The output of the ADC appears in a register that is used to address a digital memory that has addressable locations referred to as the channels into which the spectrum is subdivided. Each channel corresponds to a specific input energy value, which can be calibrated using known spectra from standard radiation sources. The slope and the y-intercept of the straight line of calibration can be determined, if one knows two of the energy lines, preferably those at the initial and final positions of the energy range of interest. A third energy value at the mid point will ensure linear calibration. An ideal MCA will execute a perfectly linear conversion of the pulse height to the channel number. Hence a plot of the pulse height versus the channel number will be a straight line. A lower threshold of the pulse amplitude can be set for the MCA, which helps to suppress the high-count rates from small noise pulses. This threshold is adjustable from the software control of the MCA data acquisition. As described earlier, the signal from the detector is first sent to a linear amplifier so that the signal amplitude is increased to match the set voltage levels of the ADC in the MCA. By increasing the gain of the linear amplifier, the amplitude of each signal can be increased. Hence the corresponding pulse height in the MCA will be increased, thereby changing the slope of the calibration curve. A photograph of the detectors along with respective preamplifiers and MCA can be seen in figure 5.23.

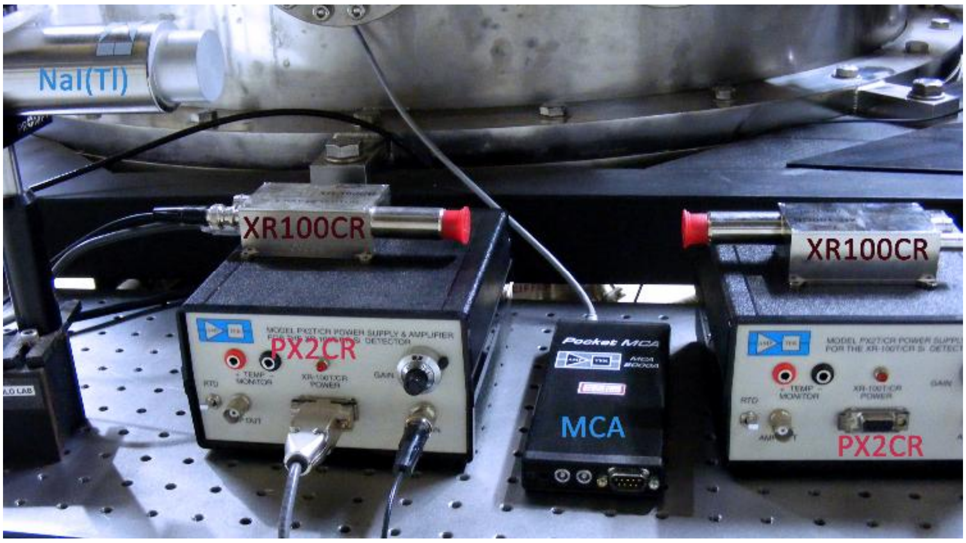

Figure 5.23: A photograph of the x-ray and γ-ray detectors.

The Amptek pocket MCA8000A used in our detector system has software selectable number of channels/memory locations of 16k, 8k, 4k, 2k, 1k, 0.5k, and 0.25k. The number of channels used for recording the spectra will determine its resolution. This MCA which is specially designed for the GAMMA 8000 series detectors, powers the detector electronics as well. The data can be transferred to the PC using a serial port (RS-232) and the acquisition parameters can be selected from the PCMCA software through the same interface.

5.8 Calibration of the solid-state detectors

The MCA only sorts the radiation peaks detected to different channels. In order to assign the energy values of the peaks that are stored in different channels of the MCA, the system needs to be calibrated with a known spectrum of a standard radiation source. Also since the gain control of the preamplifier changes the calibration curve, a re-calibration becomes necessary whenever the gain of the preamplifier is adjusted. This is true in the case of the channel number setting of the MCA as well. Hence a calibration of the detection system becomes necessary at the start of each fresh experiment for a faithful detection of the radiation energy spectrum.

5.8.1 Calibration of the x-ray detector

We used an Americium 241 source for the calibration of the x-ray detector. The standard radiation spectrum {9,11} of Am^{241} is given in figure 5.24. The obtained spectral peaks are compared to this standard and the corresponding energy values are assigned to the channel numbers.

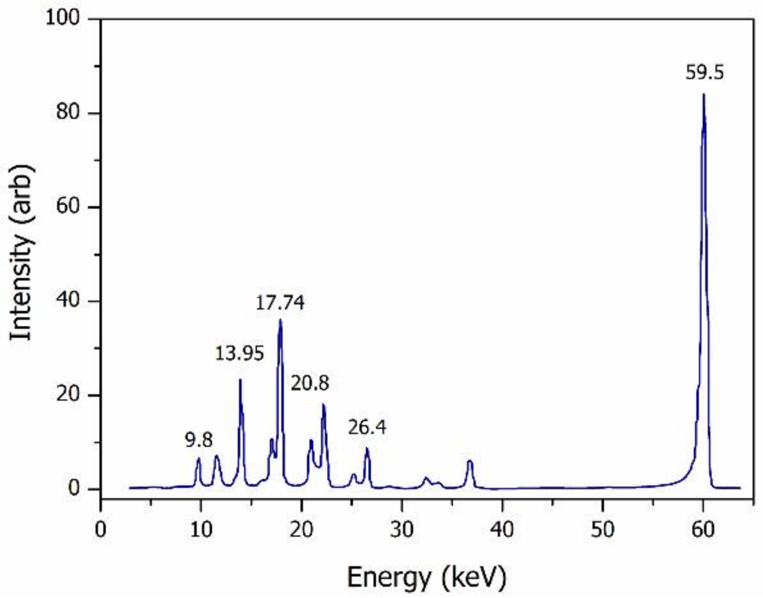

Figure 5.24: Radiation spectrum of Am^{241}.

Americium-241 is a silver-grey colored metal. It decays primarily by alpha particle emission to neptunium-237, which has a half-life of 2,144,000 years. Low energy gamma radiation accompanies these decays, with the 59.5 keV gamma emission being the most prominent. The decay scheme {12} of Am^{241} is shown in figure 5.25.

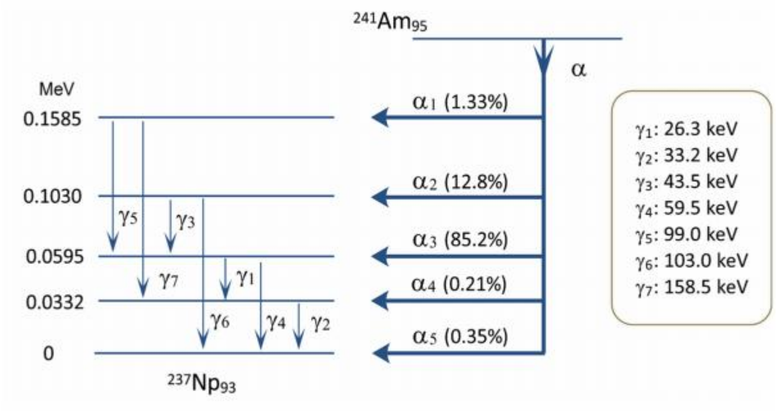

Figure 5.25: Decay scheme of Am^{241}.

The spectra obtained from the Am^{241} source using the 5 mm^2 Si-PiN detector with 1 mil Be window and 500 μm detector thickness are given below. Figure 5.26, 5.27 and 5.28 are the spectra obtained with the linear amplifier gain set to 0.5, 0.7 and 0.9 respectively. The ADC resolution is kept constant at 4096 channels, in all these measurements.

It can be seen that the spectrum shifts to the right giving more resolution to the obtained peaks. The increased gain increases the amplitude of the pulse given to the ADC. Thus a pulse that would have been detected at a lower channel now will be detected at a higher channel, giving the option to discriminate the lower channels to suppress the low amplitude intrinsic noise. It is to be noted that for a chosen ADC resolution, the measurable range decreases with the increase in linear gain.

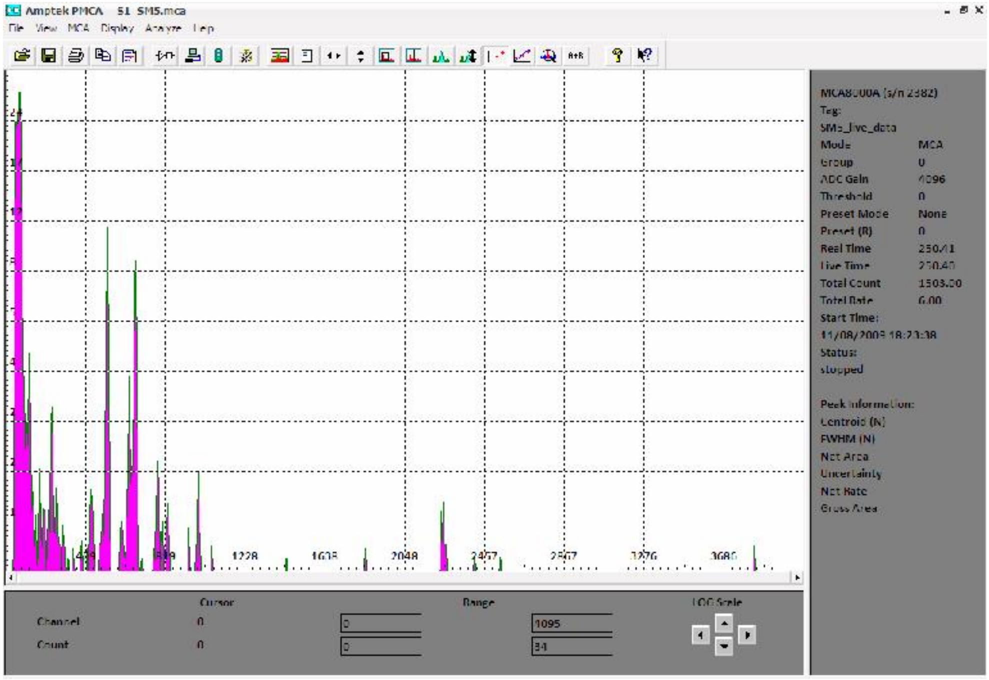

MCA8000A (s/n 2382)
Tag:
SM5_live_data
Mode MCA
Group 0
ADC Gain 4096
Threshold 0
Preset Mode None
Preset (R) 0
Real Time 250.41
Live Time 250.40
Total Count 1503.00
Total Rate 6.00
Start Time:
11/08/2009 18:23:38
Status:
stopped

Peak information:
Centroid (N)
FWHM (N)
Net Area
Uncertainty
Net Rate
Gross Area

Channel 0 0 1095
Count 0 0 34

Figure 5.26: X-ray spectra obtained from Am^{241} with the amplifier gain set to 0.5.

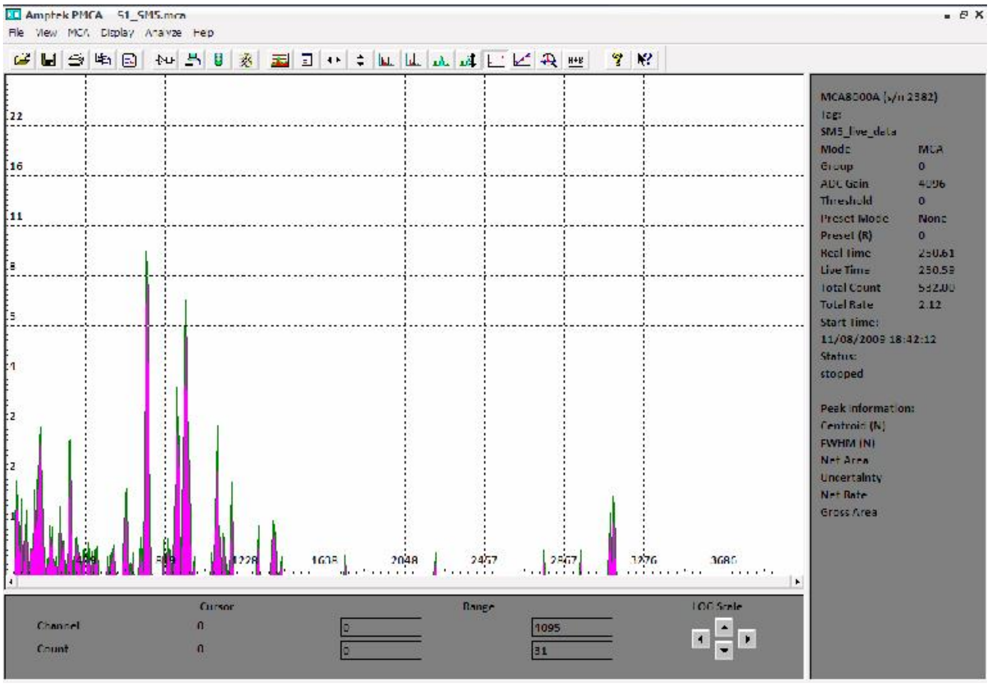

MCA8000A (s/n 2382)
Tag:
SM5_live_data
Mode MCA
Group 0
ADC Gain 4096
Threshold 0
Preset Mode None
Preset (R) 0
Real Time 250.61
Live Time 250.59
Total Count 532.00
Total Rate 2.12
Start Time:
11/08/2009 18:42:12
Status:
stopped

Peak information:
Centroid (N)
FWHM (N)
Net Area
Uncertainty
Net Rate
Gross Area

Channel 0 0 1095
Count 0 0 31

Figure 5.27: X-ray spectra obtained from Am^{241} with the amplifier gain set to 0.7.

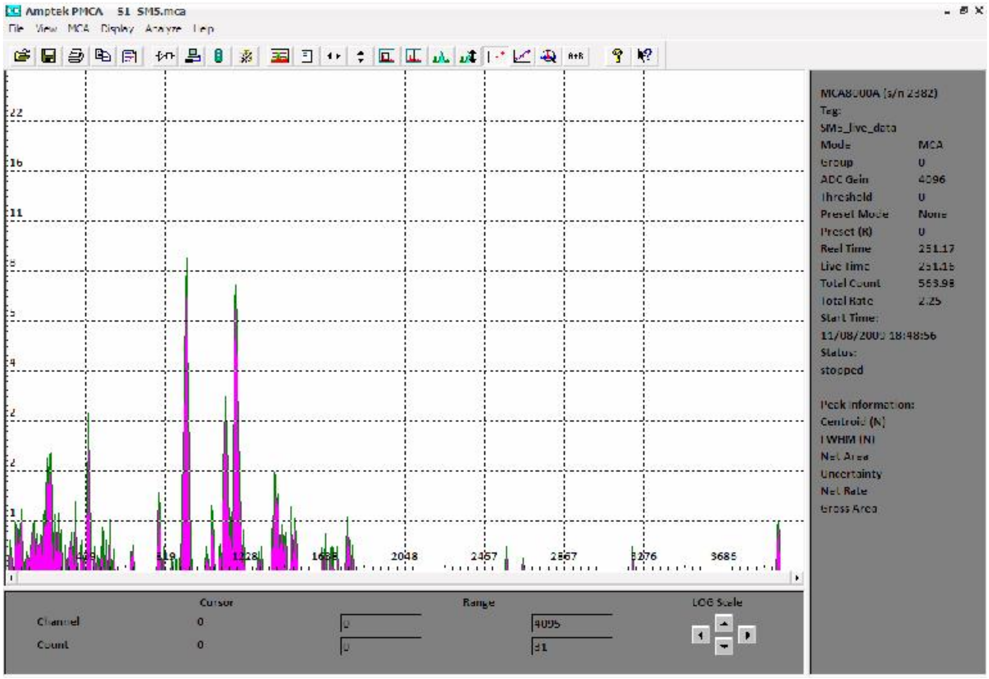

MCA8000A (s/n 2382)
Tag:
SM5_live_data
Mode MCA
Group 0
ADC Gain 4096
Threshold 0
Preset Mode None
Preset (K) 0
Real Time 251.17
Live Time 251.16
Total Count 563.98
Total Rate 2.25
Start Time:
11/08/2009 18:48:56
Status:
stopped

Peak information:
Centroid (N)
FWHM (N)
Net Area
Uncertainty
Net Rate
Gross Area

Channel 0 0 4095
Count 0 0 31

Figure 5.28: X-ray spectra obtained from Am^{241} with the amplifier gain set to 0.9.

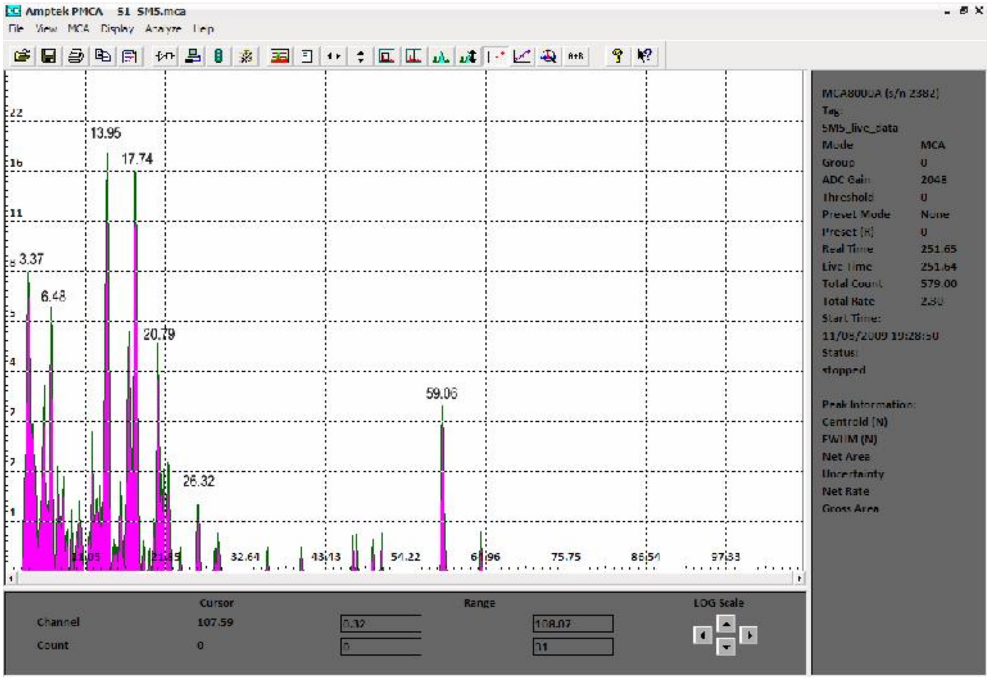

MCA8000A (s/n 2382)
Tag:
SM5_live_data
Mode MCA
Group 0
ADC Gain 2048
Threshold 0
Preset Mode None
Preset (K) 0
Real Time 251.65
Live Time 251.64
Total Count 579.00
Total Rate 2.30
Start Time:
11/08/2009 19:28:50
Status:
stopped

Peak Information:
Centroid (N)
FWHM (N)
Net Area
Uncertainty
Net Rate
Gross Area

Channel 107.59 0.32 108.07
Count 0 0 11

Figure 5.29: Calibrated x-ray spectra obtained from Am^{241} with the linear amplifier gain set to 0.5 and the ADC resolution set to 2048.

Figure 5.29 shows the spectrum obtained after calibration for the linear amplifier setting of 0.5 and an ADC resolution of 2048. The calibrated spectrum obtained from the 7 mm^2 detector with 0.5 mil Be window and 300 μm detector thickness is given in figure 5.30. Since the detector thickness is smaller in this case, the detection efficiency too is lower and hence the spectrum is noisier.

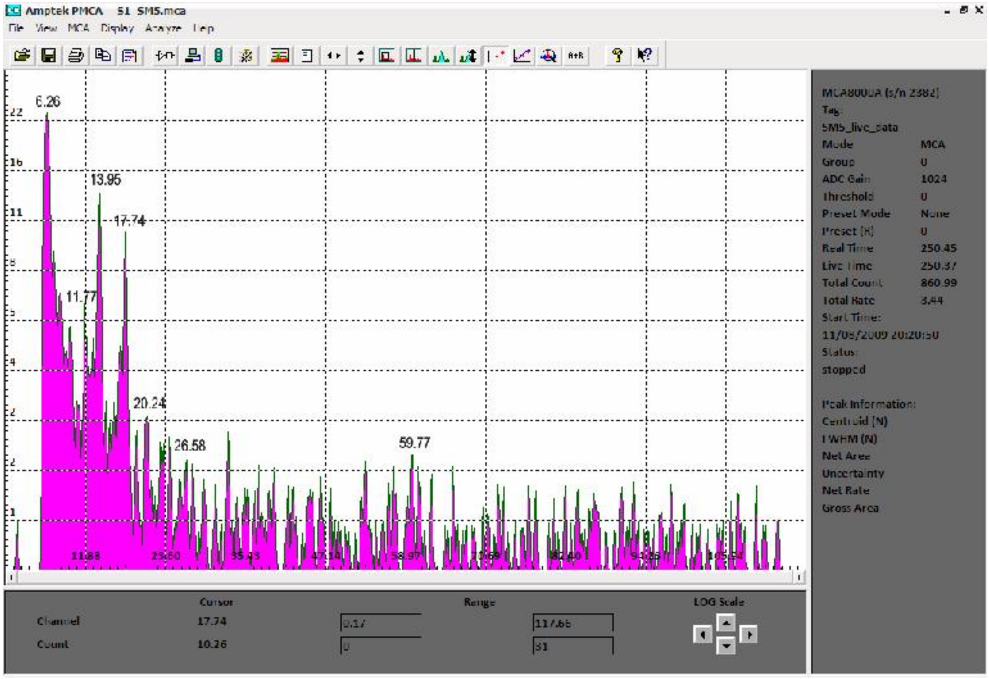

MCA8000A (s/n 2382)
Tag:
SM5_live_data
Mode MCA
Group 0
ADC Gain 1024
Threshold 0
Preset Mode None
Preset (K) 0
Real Time 250.45
Live Time 250.37
Total Count 860.99
Total Rate 3.44
Start Time:
11/05/2009 20:20:50
Status:
stopped

Peak Information:
Centroid (N)
FWHM (N)
Net Area
Uncertainty
Net Rate
Gross Area

Channel 17.74 0.17 117.66
Count 10.26 0 31

Figure 5.30: Calibrated x-ray spectra obtained from Am^{241} with the linear amplifier gain set to 0.5 and the ADC resolution set to 1024. The detector used in this case had a smaller active interaction depth.

5.8.2 Calibration of the γ-ray detector

For the γ-ray scintillation detector calibration, we used Co^{60} and Cs^{137} as the calibration standards. The decay schemes of these two radiation sources {13} are shown in figure 5.31.

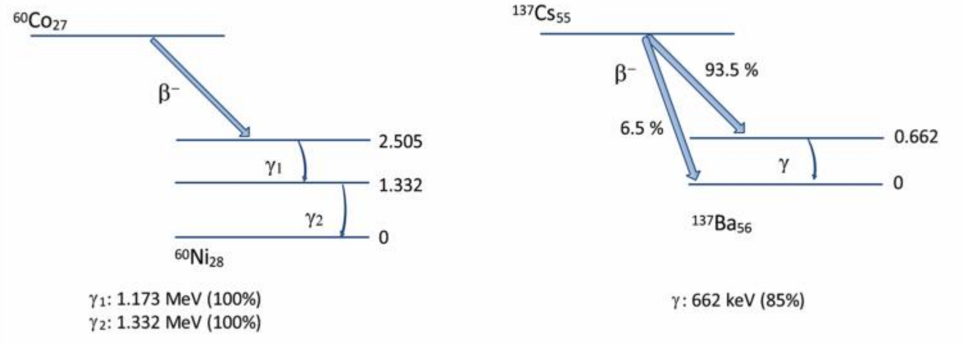

Figure 5.31: Decay scheme for the γ-ray reference sources Co^{60} and Cs^{137}.

The standard radiation spectra of Co^{60} and Cs^{137} are shown in figure 5.32 {10}. The NaI(Tl) detector is first calibrated using the Co^{60} source and the calibration is validated using the Cs^{137} source.

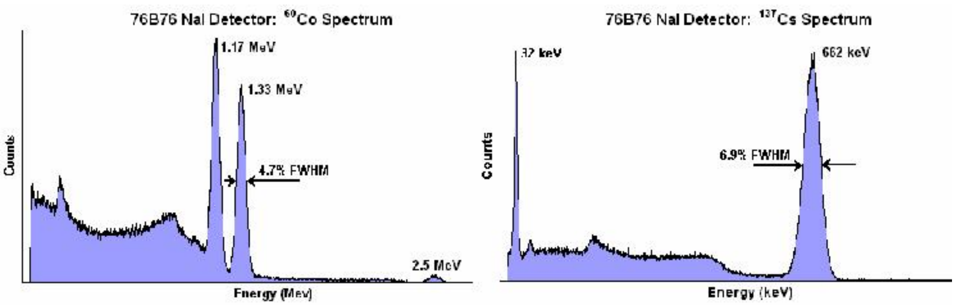

Figure 5.32: Standard emission spectra for the sources Co^{60} and Cs^{137}.

The γ-rays emitted are nearly monoenergetic as nuclear states have well defined energies. Hence any line width obtained for the spectrum is indicative of the detector's resolution rather than any variation in the incident γ-ray energy. The Cs^{137} source which we used to calibrate the γ-ray detector has a strength of 3.3 mCi and the Co^{60} source has a strength of 2.4 mCi.

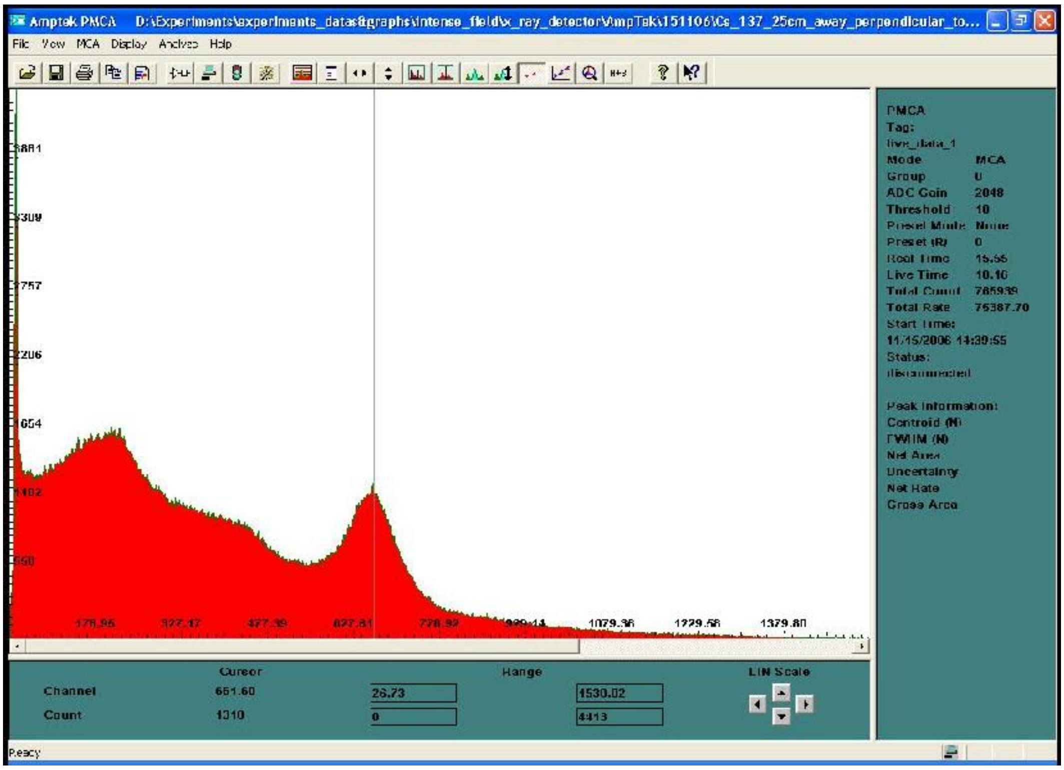

PMCA
Tag:
live_data_1
Mode MCA
Group U
ADC Gain 2048
Threshold 10
Preset Mode None
Preset (R) 0
Real Time 15.55
Live Time 10.10
Total Count 785939
Total Rate 75387.70
Start Time:
11/15/2006 14:39:55
Status:
disconnected

Peak Information:
Centroid (N)
FWHM (N)
Net Area
Uncertainty
Net Rate
Gross Area

Channel 651.60 26.73 1530.02
Count 1310 0 4413

Figure 5.33: Calibration of the NaI(Tl) detector system using Cs^{137}.

5.9 Time gating of the detectors and laser synchronization

The x-ray and γ-ray detectors are susceptible to background radiation noise, which is more so in the case of the NaI(Tl) detector. A carefully chosen time gate can improve the signal to noise ratio. The amptek MCA has two such gating options available. Of the two gates, one is active HIGH TTL compatible and the other is active LOW TTL compatible. When the first gate input is high, the analog input pulses are gated off and the live clock is stopped. In the other gate this happens if the gate input is low. The gating must occur at or prior to the peak of the analog pulse and should extend for at least 1 μs after the peak for optimum performance. MCA gating can be applied also to attain a data accumulation time shorter than one second or for non-integer accumulation times.

The femtosecond laser system works at a repetition rate of 10 Hz, and it would have been ideal if the sample could be moved to a new position for each laser pulse. This means that the target needs to be moved to the next position within 100 ms. But the movement of the target manipulator is rather slow, and can lead to positioning errors if driven fast. This might turn out to be even trickier if the loads on the manipulator are high. Therefore to ensure error free positioning, it is better to allow at least about 500 ms time interval between the successive irradiation of the target. So an external synchronization system becomes necessary for synchronizing the laser triggering, target positioning, MCA gating and data acquisition. Triggering the laser externally at user specified times is a typical solution to this, but not the preferred one in the present case. The pulse to pulse energy stability of the CPA laser system will be ensured only if the crystals are irradiated near a 10 Hz repetition rate, and hence triggering the laser at user specified repetition rates will sacrifice the energy stability of the system. This is due to the fact that the system is optimized to compensate for thermal lensing and associated effects at the repetition rate of 10 Hz. Changing the repetition frequency hence will adversely affect the energy stability of the system. Therefore we chose an alternate method, where we operated the laser at 10 Hz, but used a mechanical shutter to select single pulses from the 10 Hz pulse train at user specified intervals. This shutter is a “pulse picker”, and needs to be synchronized with the 10 Hz laser repetition and the user defined trigger pulses. An electronic circuit was designed and fabricated for this purpose. The circuit diagram and the PCB fabricated can be seen in figure 5.34.

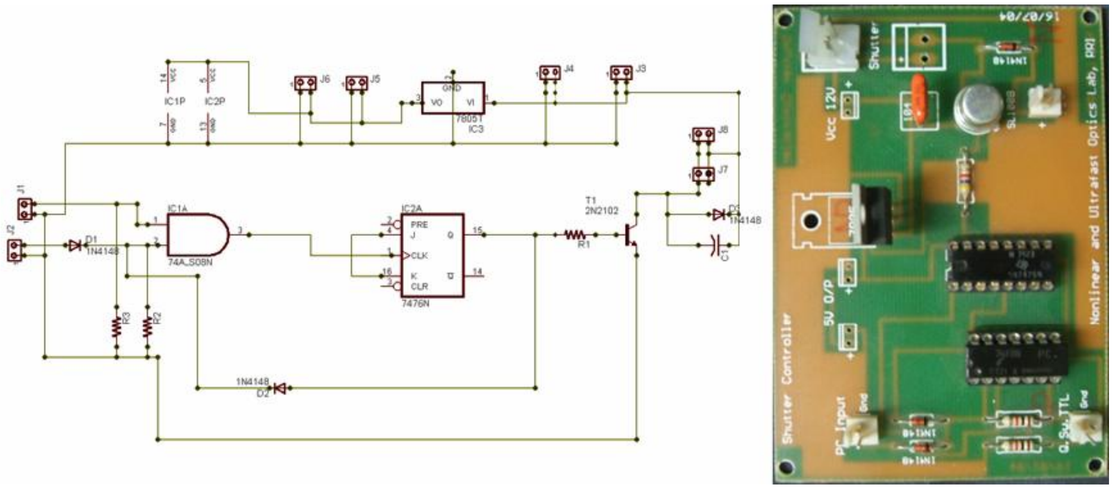

Figure 5.34: The electronic circuit designed for synchronized laser pulse picker.

The heart of the circuit is a 7476 flip-flop. The input from the laser Q-switch and the user trigger are given to an AND gate which energizes the flip-flop and thereby a relay, only when both the pulses are present. The output of the flip-flop is fed back to the input in such a way that the second pulse in the laser train will switch the relay off. A small piece of Aluminium attached to the relay moves across the beam path when the relay is energized, thus acting as the shutter. This indigenous design ensures that a single pulse can be selected from the 10 Hz pulse train at will. A photodiode placed after the shutter acts as the input trigger signal to a function generator wired in the burst trigger mode. We used a 25 MHz function generator (AFG 3022B, Tektronix) for this purpose. The function generator parameters were set such that when triggered, it produces a single pulse of 50 μs duration {14}. This pulse is used as the gating signal for the MCA. The schematic of the experimental setup is shown in figure 5.35.

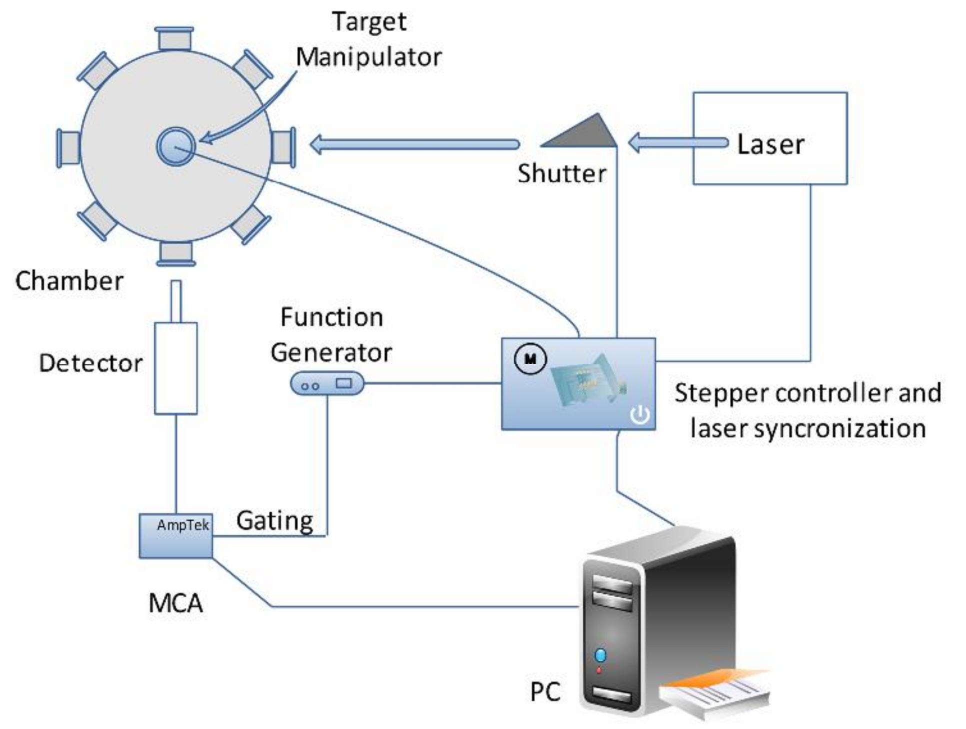

Figure 5.35: Experimental setup for gated, synchronized x-ray measurements from the laser–solid interaction.

5.10: Conclusions

We have developed in-house the entire infrastructure needed for x-ray and γ-ray measurements from intense laser–condensed matter interactions. All the electronics required were developed and fabricated, and the software was coded.

References

1. *Tsunami – User's Manual*, Revision B, Spectra Physics (1999).
2. *Live Cell Imaging: a laboratory manual*, R. D. Goldman and D. L. Spector, Cold Spring Harbor Laboratory Press, Cold Spring Harbor, NY (2005).
3. *Two-photon fluorescence microscope with a hollow-core photonic crystal fiber*, S. P. Tai, M. C. Chan, T. H. Tsai, S. H. Guol, L. J. Chen, and C. K. Sun, Opt. Exp., **12**, 6122 (2004).
4. *Femtosecond Laser Pulses: Principles and Experiments*, C. Rullière, Second Edition, Springer, NY (2005).
5. *Laser fundamentals*, W. T. Silfvast, Second Edition, Cambridge University Press, Cambridge, UK (2004).
6. *Ultrafast Optics*, A. Weiner, John Wiley & Sons Inc., Hobeken, NJ (2009).
7. *Lasers*, A. E. Siegman, University Science Books, Sausalito, CA (1986).
8. *Investigation of Nonlinear Effects Induced in Condensed Matter by Intense Laser Fields,* M. Anija, PhD Thesis, Raman Research Institute (2007).
9. *Amptek XR-100CR Instruction Manual,* Revision 13, Amptek Inc. (2003).
10. *Scintillation Detector & MCA Manual,* Amptek Inc. (2003).
11. *Gamma-Ray Spectrum Catalogue*, Idaho National Laboratory Spectrum Catalogs (1999).
12. *Electromagnetic spectrum of Am*^{241}, P. P. Day, Phys. Rev. Lett., **97**, 689 (1955).
13. *Radiation Detection and Measurement*, G. F. Knoll, John Wiley & Sons Inc., NY (2000).
14. *AFG3000 series Arbitrary/Function Generators Quick Start User Manual*, Tektronix Inc. (2007).

6

X-ray emission from ultrafast laser induced plasma in planar liquid jets

In this chapter we discuss plasma experiments conducted in thin planar liquid jets in ambient conditions. Results show that even in the absence of a vacuum, it is possible to get a substantial amount of soft x-rays from an ultrafast laser produced plasma. We also present a novel way of enhancing the x-ray emission yield and emission energy range by the incorporation of metal nanoparticles into the liquid used in the jet.

6.1 Introduction

Intense electromagnetic radiation is known to emanate from laser-produced plasmas (LPP). Soon after the invention of lasers, the possibility of LPP as a new radiation source was investigated. In particular, technologies such as Q-switching, mode locking, chirped pulse amplification etc., lead to shorter and more powerful laser pulses. Using intense lasers, it is possible to generate radiation pulses extending from TeraHertz frequencies ($\lambda = 100$ μm) to visible light, extreme ultraviolet light (EUV, $\lambda = 10$ nm), x-rays ($\lambda = 0.1$–1 nm) and γ-rays ($\lambda << 0.1$ nm). The emission of these radiations is controlled by optimizing laser-irradiation conditions and target materials {1}. An ultrafast radiation pulse is very useful to observe the dynamics of rapidly moving hot-dense materials such as laser-driven fusion pellets, live organisms, transient phenomena of shock-compressed crystalline matter, and objects of nondestructive inspections {2-5}. LPP radiation is a compact pulse source, and it can be extended to a wide variety of industrial and scientific applications.

In this chapter, we discuss the spectroscopic study of x-ray emission from an ultrafast laser induced plasma generated in thin planar liquid jets of approximately 250 μm thickness. Laser pulses of 100 fs duration are focused to the jet to obtain intensity levels close to 10^{16} W/cm^2. Tunnel ionization is the dominant ionization mechanism at this intensity regime. X-rays in the range of 1.5 keV to 30 keV are recorded and analyzed. The directionality of the x-ray emission is measured and discussed.

6.2 Plasma production by ultrafast laser pulses

In the case of intense laser interactions with a liquid or solid target, the number of atoms exposed to the laser field becomes close to the solid density (10^{23} atoms/cm^3). Even though all the basic ionization mechanisms discussed in chapter one remain valid, there will be several other interactions between the electrons and ions due to the availability of a very large number of atoms. For intensities above 10^{14} W/m^2 the dominant ionization mechanisms will be tunnel ionization and over-the-barrier ionization {6}. The free electrons produced by the ionization process are further accelerated by the electric field of the incident laser. In a solid density material, the electrons accelerated by the quiver motion will collide with the nearby neutral atoms inducing collisional ionization, unlike the less dense atomic systems where the acceleration is uninterrupted. Thus the ionization is much higher in the case of solid density materials. A dense cloud of electrons is formed even before the laser pulse reaches its peak. This electron cloud and the resultant positively charged ions constitute the '*plasma*' [The word '*plasma*' is used to describe a wide variety of macroscopically neutral substances containing many interacting free electrons and ionized atoms or molecules, which exhibit a collective behaviour due to long-range coloumb forces.]. The plasma gets heated up by energy transfer from the exciting electromagnetic wave through various absorption modes (described in detail in section 6.4). This results in further ionization leading to a denser plasma. A diagram showing the various interactions {7} in a laser-produced plasma is given as figure 6.1.

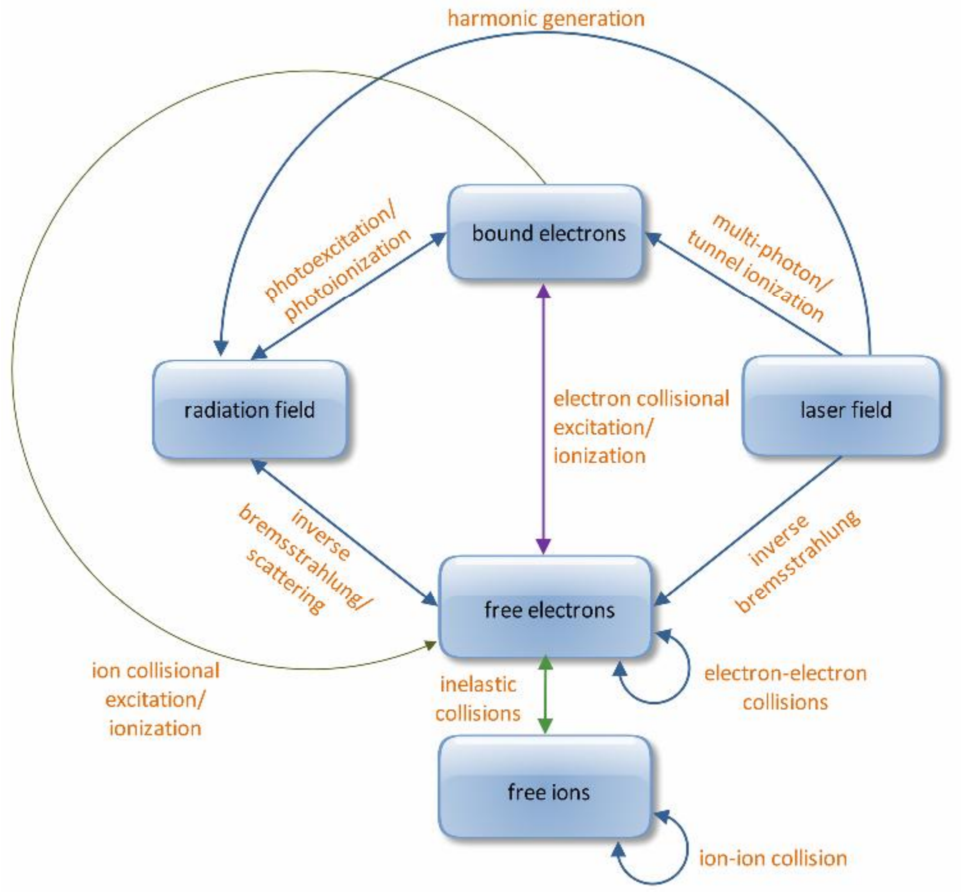

Figure 6.1: A diagram showing various interactions in a laser-produced plasma.

The properties of the plasma are markedly dependent upon particle interactions. The main feature that distinguishes plasma behavior from that of fluids and solids is the existence of collective effects. Due to the existence of long-range electromagnetic forces, each charged particle of the plasma interacts simultaneously with a considerable number of other charged particles, resulting in collective effects. A distinction can be made between *weakly ionized* and *strongly ionized* plasmas in terms of the nature of particle interactions. In a weakly ionized plasma, the charge-neutral interactions dominate over multiple Coulomb interactions (charge-charge interactions). On the other hand when the multiple Coulomb interactions dominate, the plasma can be termed strongly ionized. In fully ionized plasmas, all the particles will be subjected to multiple Coulomb interactions.

6.3 Basic properties of plasma

The fact that some or all the particles in a plasma are electrically charged, and can therefore interact with electromagnetic fields as well as create electromagnetic fields, gives rise to many novel phenomena that are not present in ordinary solids and fluids. Some important properties of the plasma are discussed in the following subsections.

6.3.1 Macroscopic neutrality (Quasi-neutrality)

A plasma is macroscopically neutral in the absence of external forces. This means that under equilibrium conditions with no external forces present, in a volume of the plasma sufficiently large to contain a large amount of particles and yet sufficiently small compared to the characteristic lengths for variation of macroscopic parameters such as density and temperature, the net resulting electric charge is zero. The existence of a very small amount of charge separation over a very short spatial scale for a very small time interval is known as the quasi-neutrality of plasma {8}. In the interior of the plasma the microscopic space charge fields cancel each other, and no net space charge exists over a macroscopic region.

If this macroscopic neutrality was not maintained, the potential energy associated with the resulting Coulomb forces could be enormous compared to the thermal particle kinetic energy. Departures from macroscopic electrical neutrality can naturally occur only over distances in which a balance is obtained between the thermal particle energy, which tends to disturb the electrical neutrality, and the electrostatic potential energy resulting from any charge separation, which tends to restore the electrical neutrality. This distance is of the order of a characteristic length parameter of the plasma, called the *Debye length*. In the absence of external forces, the plasma cannot support departures from macroscopic neutrality over larger distances than this, since the charged particles are able to move freely to neutralize any regions of excess space charge in response to the large Coulomb forces that appear.

6.3.2 Debye Shielding

The Debye length is an important physical parameter for the description of a plasma. It provides a measure of the distance over which the influence of the electric field of an individual charged particle (or of a surface at some nonzero potential) is felt by the other charged particle inside the plasma. The charged particles arrange themselves in such a way as to effectively shield any electrostatic fields within a distance of the order of Debye length. A calculation of the shielding distance was first performed by Debye for an electrolyte and is given by

$$\lambda_D = \left(\frac{\varepsilon_0 kT}{n_e e^2} \right)^{1/2} \qquad - (6.1)$$

It is convenient to define a *Debye sphere* as a sphere inside the plasma of radius λ_D. Any electrostatic fields originated outside a Debye sphere are effectively screened by the charged particles and do not contribute significantly to the electric field inside the sphere. Consequently, each charge in the plasma interacts collectively only with the charges that lie inside its Debye sphere, its effect on the other charges being negligibly small. The first criterion for the existence of the plasma is that its characteristic dimensions of the plasma should be greater than λ_D. Otherwise, there is just not sufficient space for the collective shielding effect to take place, and the collection of the charged particles will not exhibit plasma behavior. The second criterion is that the number of electrons inside the Debye sphere should be very high, i.e. $n_e \lambda_D^3 \gg 1$. This means that the average distance between the electrons, given by $n_e^{-1/3}$, must be very small compared to λ_D. The quantity defined by $g = 1/n_e \lambda_D^3$ is known as the plasma parameter and the condition $g \ll 1$ is called the plasma approximation. This parameter is also a measure of the ratio of the mean inter-particle potential energy to the mean plasma kinetic energy. The number of electrons N_D, inside a Debye sphere can be calculated as

$$N_D = \frac{4}{3} \pi \lambda_D{}^3 n_e = \frac{4}{3} \pi \left(\frac{\varepsilon_0 kT}{n_e^{1/3} e^2} \right)^{3/2} \qquad - (6.2)$$

6.3.3 The plasma frequency

An important plasma property is the stability of its macroscopic space charge neutrality. This is sometimes considered as the third criterion for the existence of a plasma. When a plasma is instantaneously disturbed from the equilibrium condition, the resulting internal space charge fields give rise to collective particle motions that tend to restore the original charge neutrality. These collective motions are characterized by a natural frequency of oscillation known as the *plasma frequency*. Since these are high-frequency oscillations, the ions, because of their heavy mass, are to a certain extent unable to follow the motion of the electrons. The electrons oscillate collectively about the heavy ions, the necessary collective restoring force being provided by the ion-electron Coulomb attraction. The period of this natural oscillation constitutes a meaningful time scale against which can be compared the dissipative mechanisms tending to destroy the collective electron motion.

Consider a plasma initially uniform and at rest, and suppose that by some external means a small charge separation is produced inside it. If the external force is removed instantaneously, the internal electric field resulting from charge separation collectively accelerates the electrons in an attempt to restore the charge neutrality. However, because of their inertia, the electrons move beyond the equilibrium position, and an electric field is produced in the opposite direction. This sequence of movements repeats itself periodically with a continuous transformation of kinetic energy into potential energy and vice-versa, resulting in fast collective oscillations of the electrons about the more massive ions. On the average, the plasma maintains its macroscopic charge neutrality. The angular frequency of these collective electron oscillations, called the (electron) plasma frequency, is given by

$$\omega_{pe} = \left(\frac{n_e e^2}{m_e \varepsilon_0} \right)^{1/2} \qquad \text{- (6.3)}$$

Collisions between electrons and neutral particles tend to damp these collective oscillations and gradually diminish their amplitude. If the oscillations are to be only slightly damped, it is necessary that the electron-neutral collision frequency (ν_{en}) be smaller than the electron plasma frequency,

$$\nu_{pe} > \nu_{en} \qquad - (6.4)$$

where $\nu_{pe} = \omega_{pe} / 2\pi$. Otherwise, the electrons will not be able to behave in an independent way, but will be forced by collisions to be in complete equilibrium with the neutrals, and the medium can be treated as a neutral gas. Equation 6.4 constitutes, therefore, the fourth criterion for the existence of plasma. This criterion can be alternatively written as $\omega\tau > 1$ where $\tau = 1 / \nu_{en}$ represents the average time an electron travels between collisions with neutrals, and ω stands for the angular frequency of plasma oscillations. It implies that the average time between electron-neutral collisions must be large compared to the characteristic time during which the plasma physical parameters are changing.

6.4 Absorption mechanisms in a plasma

Plasma is a strongly absorbing medium. As an electromagnetic wave propagates through a plasma, energy will be transferred from the EM wave to the plasma through different routes. Some of the important energy transfer mechanisms are discussed in the following subsections.

6.4.1 Collisional absorption (Inverse Bremsstrahlung)

Collisional absorption is the main energy transfer mechanism between the laser pulse and the plasma at relatively low intensities. The electrons, while oscillating under the influence of the laser field, collide with the ions, transferring a part of electromagnetic energy to the plasma, thus heating up essentially the plasma electrons to higher temperature {9}. Since these collisions are inelastic, their net result is an equilibration with surroundings – this defines the average or ‘cold’ temperature of the plasma. Here, it has to be noted that the electron-electron and ion-ion collision frequencies are larger compared to the electron-ion collision rates. These provide local thermalization, and essentially a two-fluid description with two distinct temperatures – electrons and ions are in respective local thermal equilibria.

The collisions between similar particles, however, do not cause an effective energy transfer as there is no significant momentum transfer. Collisional behaviour becomes important when the number of electrons in the Debye sphere is less. The electrons performing quiver oscillations in the laser field undergo collisions with the ions thereby converting a part of the coherent oscillation energy into thermal energy of the electrons and thus heating up the plasma.

When an electron of mass m_e moving with a velocity v collides with an ion of charge Ze the change in momentum experienced by the electron is given by the product of Coulomb force and time of interaction (2b/v), with *b* being the impact parameter (the distance of closest approach). The time required to undergo a substantial momentum change such that $\Delta v_{\mathrm{rms}} \sim v$ defines the electron-ion collision frequency γ_{ei}, which is a function of the range of values of v, b and ion density. For a Maxwellian velocity distribution, this collision frequency is given as {10-12}:

$$\gamma_{ei} = \frac{Z n_e e^4 \ln \Lambda}{3(2\pi)^{3/2} \varepsilon_0^2 m_e^{1/2} (k_B T_e)^{3/2}} \qquad - (6.5)$$

Λ being the ratio of the maximum (Debye length) to minimum (largest of the classical distance of closet approach or the De Broglie wavelength of electron) impact parameter. $\ln\Lambda$ is referred to as the Coulomb logarithm {13,14}.

One can obtain the damping caused to an electromagnetic wave passing through a collisional plasma given the elctron-ion collision frequency. From this the amount of collisional absorption suffered by the laser can be found out. Considering the motion of the electron in the laser electric field and incorporating the damping due to the electron-ion collision, the dielectric function of the collisional plasma, for the light frequency ω, can be obtained as:

$$\varepsilon = 1 - \frac{\omega_{pe}^2}{\omega^2 \left(1 + i\frac{\gamma_{ei}}{\omega}\right)} \qquad - (6.6)$$

The dispersion relation for light wave in collisional plasma is given by:

$$\omega^2 = k^2c^2 + \frac{\omega_{pe}^2}{\left(1 + i\frac{\gamma_{ei}}{\omega}\right)} \qquad \text{- (6.7)}$$

The imaginary term in the dispersion relation of uniform plasma indicates the energy damping rate, viz.

$$\omega_i = -\frac{n_e}{2n_{cr}}\gamma_{ei} \qquad \text{- (6.8)}$$

The efficiency of collisional absorption decreases with decrease in the laser pulse width. Equation 6.5 shows that the electron-ion collision rates reduce as the velocity of electrons (T_e) is increased. As the laser pulse intensity becomes greater than 10^{15} W/cm^2, the electron temperature increases significantly {15}, as the rate at which the electrons gain energy is much larger than the rate at which the electrons thrermalize with other electrons {16}. At very high laser intensities, the electron quiver energy will be so large that the quiver velocity dominates the thermal velocity of the electrons. Under this condition collisional absorption is no longer a dominant laser absorption mechanism in plasma {17}. For high density plasma, it is indicated that collisional absorption, with nonlinear terms, is an efficient absorption mechanism {18}.

6.4.2 Collisionless absorption – resonance absorption and vacuum heating

Resonant absorption depends on the collective motion of the particles in the plasma. The collective motion in the plasma is through longitudinal oscillations, with a characteristic frequency. Resonance Absorption is less effective if the plasma spatial density gradient is extremely sharp. This is because plasma waves can be set up only if there is a finite length of the plasma in existence. If the quiver amplitude of the electron in the laser field is greater than the plasma length, no plasma wave can be set up as the electron is taken farther away to the vacuum, breaking the plasma wave in each half cycle of the laser oscillation. Under this condition, another mechanism named ‘vacuum heating’ has to be considered. The principal idea here is that the electrons are dragged into the vacuum on one half of the light period and returned to the target as the light reverses, with a velocity close to the electron quiver velocity. A large number of electrons get accelerated into the target and their kinetic energy is deposited at the over- dense plasma where the laser field cannot penetrate {19}. The ratio of the absorbed power to the incident laser power per cycle in the vacuum heating is given as:

$$f_{VH} = \left(\frac{\eta}{2\pi}\right)\left(\frac{e}{m\omega c\cos\theta}\right)\left(\frac{E_0^3}{E_L^2}\right) \qquad \text{- (6.9)}$$

where $\eta = 1.75(1 + 2v_{th}/v_{osc})$. E_L is the incident laser field and E_0 is the total incident and reflected field {19,20}. In vacuum heating the energy from the laser is directly coupled to the electrons.

6.5 X-ray production in plasma

During the interaction of a high intensity laser with plasma, x-rays are produced {21,22}. For x-ray generation in a laser produced plasma, three emission mechanisms are important, namely bremsstrahlung (free–free transition), radiative recombination (free-bound transition), and radiative de-excitation (bound–bound transition).

Free-free (*ff*) transitions: When a free electron is decelerated by an ion (Coulomb collision), the system emits continuum radiation since both the initial and final states are free electron states. This bremsstrahlung process can be described by,

$$e^- + i \rightarrow e^- + i + \gamma \qquad \text{- (6.10)}$$

where e^- denotes a free electron, i denotes an ion and γ is the emitted photon.

Free-bound (*fb*) transitions: When a free electron is trapped in an orbit of an ion, the excess energy is released in the form of radiation. This process is called radiative recombination. It can be described by,

$$e^- + i_1 \rightarrow i_2 + \gamma \qquad \text{- (6.11)}$$

Here i_1 and i_2 represent different charge states of the ion.

Bound-bound (*bb*) transitions: Electron transition from an upper orbit to a lower orbit yields line emission. However in the case of high Z-atoms several emission lines are possible and due to line broadening (e.g. Doppler) the discrete line emission often changes to a band emission {23}. Bound-bound transitions can be represented by,

$$i_a \rightarrow i_b + \gamma \qquad \text{- (6.12)}$$

where i_a and i_b describe the quantum numbers of the ion states.

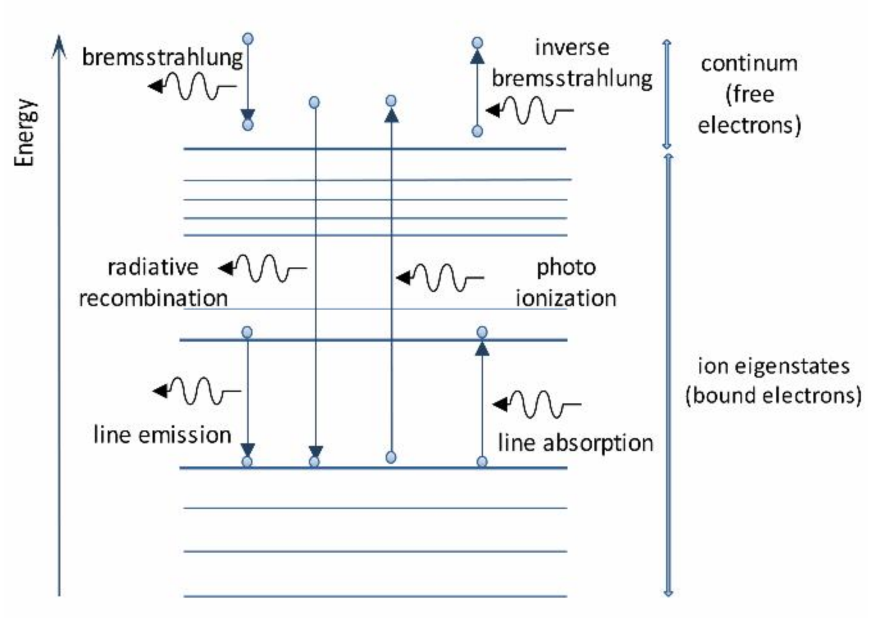

Figure 6.2: Different x-ray production mechanisms in a plasma.

6.6 Experimental setup

For performing the experiments, a thin planar liquid jet of 250 μm thickness was obtained using a flat metal nozzle and a liquid pump. Pure de-ionized water, a colloidal solution of silver nanoparticles, and an aqueous solution of silver nitrate were used as the liquid samples. The jet was irradiated with ultrafast laser pulses from a mode-locked chirped pulse amplifier Ti: Sapphire laser (Spectra physics TSA-10), delivering linearly polarized 100 fs pulses at 800 nm at a repetition rate of 10 Hz. The beam is focused to the jet using a plano-convex lens of 11 cm focal length. An input pulse energy of 6 mJ was used for the experiments, which results in an intensity of ~ 10^{16} W/cm^2 at the focus. A schematic of the experimental setup can be seen in figure 6.3. Since self-focusing gets limited at these high intensities, {24} there is no intensity enhancement inside the liquid. The laser interaction with the liquid in the present studies is in the intensity regime of over-the-barrier and tunnel ionization. The Rayleigh range in the present setup is slightly more than 250 μm. Hence when the jet is aligned exactly at the focus, the liquid sees a uniform intensity along the laser propagation direction. However, there will be plasma creation at the first surface of the liquid jet and the interaction of the later part of the pulse with the created plasma determines the depth of penetration of the laser light into the jet.

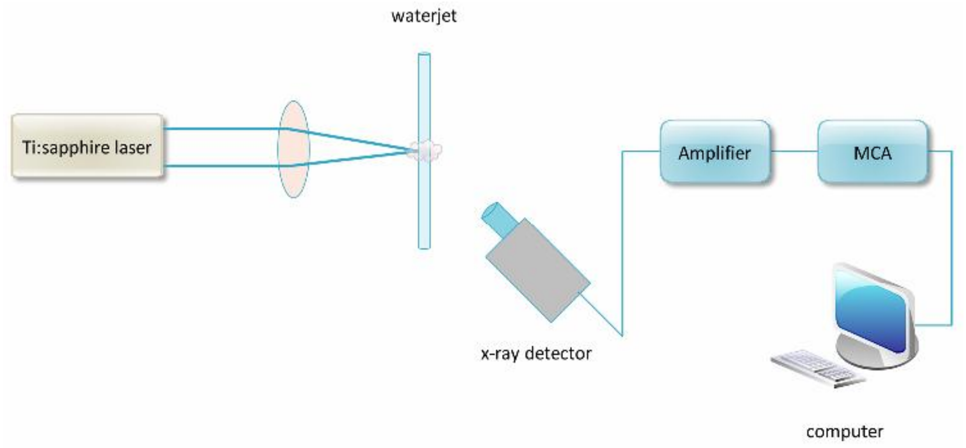

Figure 6.3: Schematic of the experimental setup.

A calibrated Si:PIN detector kept at a distance of 15 cm from the jet was used for measuring the x-ray emission spectra from the plasma. X-rays in the range of 1.5 keV to 30 keV were measured during the experiment. The x-ray counts were recorded for each laser shot and were integrated for 3000 laser shots. The laser incidence was normal to the jet. X-ray emissions at various angles with respect to the laser propagation direction were recorded, by placing the Si:PIN detector appropriately.

The Si:PIN detector was used in conjunction with the XR 100 CR amplifier. The gain of the amplifier was set to 0.5 and RTD (Real Time Discrimination) was switched on. An MCA connected to the amplifier collected the data. The MCA used was set to an ADC resolution of 2048 channels. The laser pulse energy was low enough such that there was only a feeble plasma formation in air, and no detectable x-rays were produced, when the liquid jet was switched off. This background x-ray spectrum obtained from air is shown in figure 6.4. The laser pulse energy, focusing and the detector integration time are the same as those used for measurements with the liquid jet switched on.

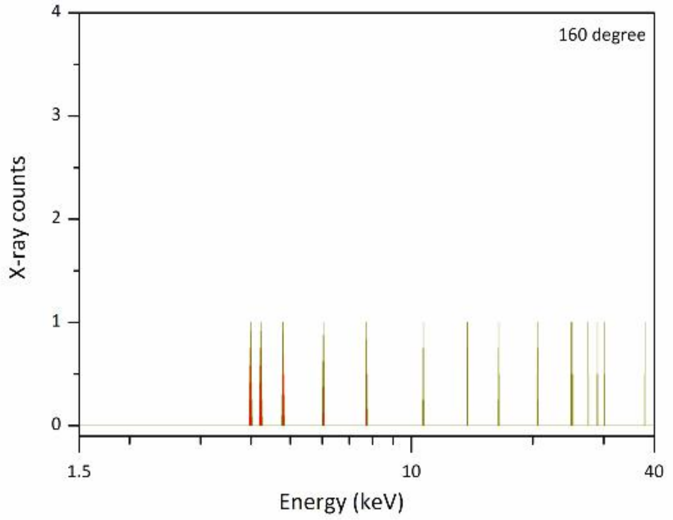

Figure 6.4: Background x-ray emission spectrum from the interaction of ultrafast laser pulses with air, when the liquid jet is switched off.

The Si:PIN detectors have an intrinsic detection efficiency (figure 6.5) and the spectrum shown above is not compensated for the detector efficiency. A polynomial fit is done to the detector intrinsic efficiency curve and the polynomial equation obtained is used for normalizing the obtained spectra. The detector efficiency in the range of 4 to 10 keV is close to 100 %. Since RTD was switched on during the measurements, the detector intrinsic efficiency curve was not valid below 2 keV. Hence for simplicity of calculation, only energies above 10 keV are considered for the polynomial fit. The detector efficiency curve along with the best polynomial fit is shown in figure 6.5.

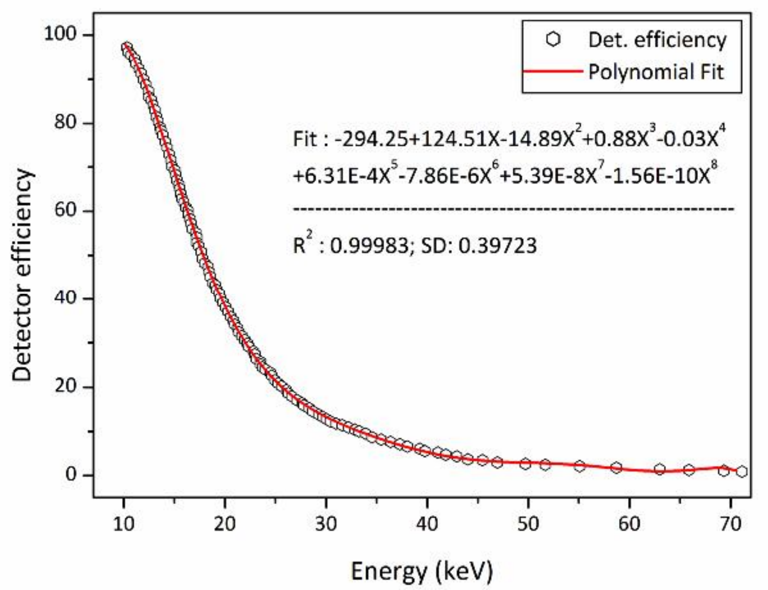

Fig.6.5: Detector intrinsic efficiency curve (hollow circles) with the best polynomial fit (solid line).

Figure 6.6 shows the as obtained and normalized spectra for the radiation of Am^{241}. It can be seen that the normalized spectrum is identical to the standard radiation spectrum of Am^{241} (given in the inset of figure 6.6) thereby validating the normalization curve. The extra peaks seen at 55 keV and 62 keV are from stray counts, which got amplified excessively during the normalization due to the low detector sensitivity in the high energy region.

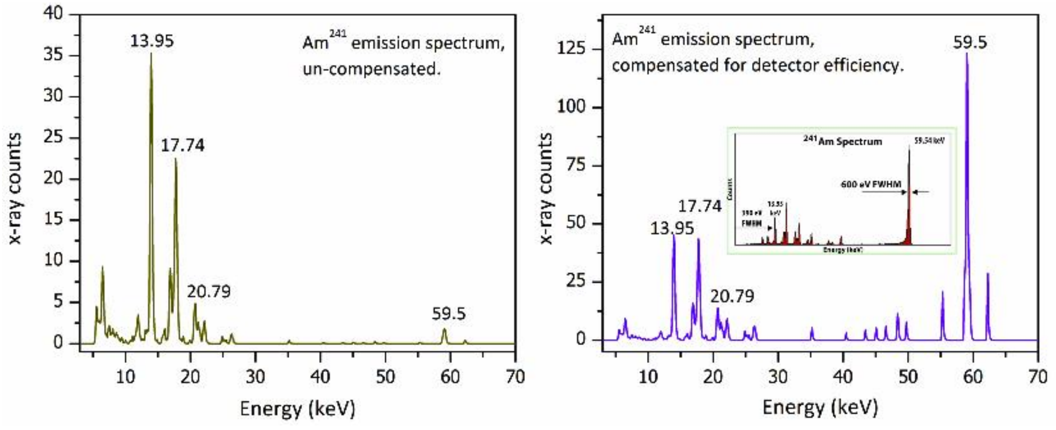

Fig.6.6: x-ray emission spectrum of Am^{241} normalized for the detector efficiency. Inset shows a standard Am^{241} emission spectrum.

All the emission spectra obtained using the Amptek XR100 CR detector were normalized for the detector efficiency by this method. The experiments were done using de-ionized water, silver nanoparticle colloidal solution and an aqueous solution of silver nitrate. The results obtained are discussed in the following sections.

6.7 X-ray emission from a water jet

De-ionized water was used as sample for the measurements. The forward laser propagation direction was taken as 0°. X-rays were measured in 10° steps around the water jet. The normalized x-ray spectra at various angles around the jet are shown in figure 6.7 and figure 6.8 respectively. Since RTD was switched on during the measurements, x-ray photons below 1.5 keV were cut off from the spectra.

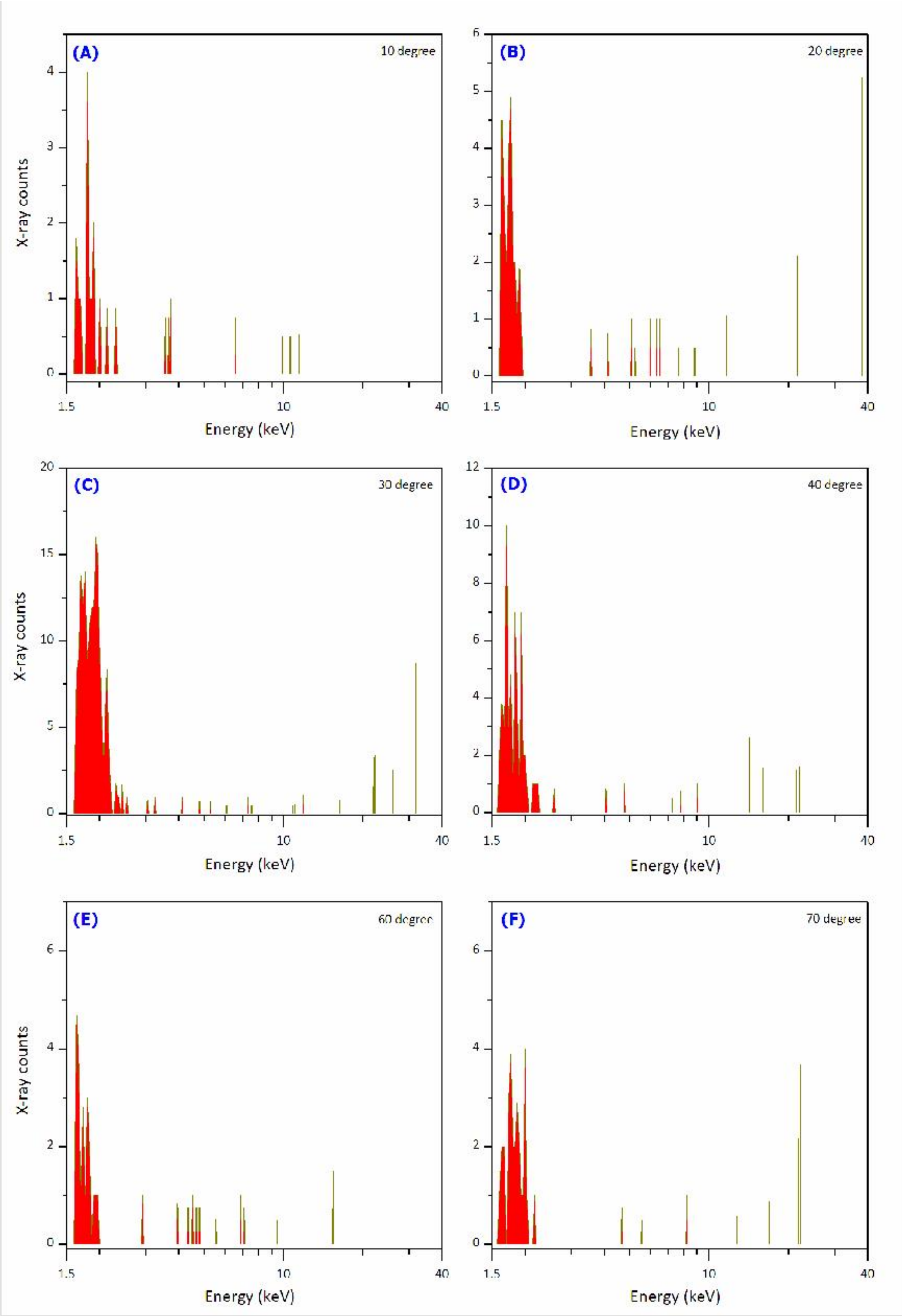

Figure 6.7: X-ray emission spectra obtained from the planar water jet for detection angles (A) 10°, (B) 20°, (C) 30°, (D) 40°, (E) 60°, and (F) 70°.

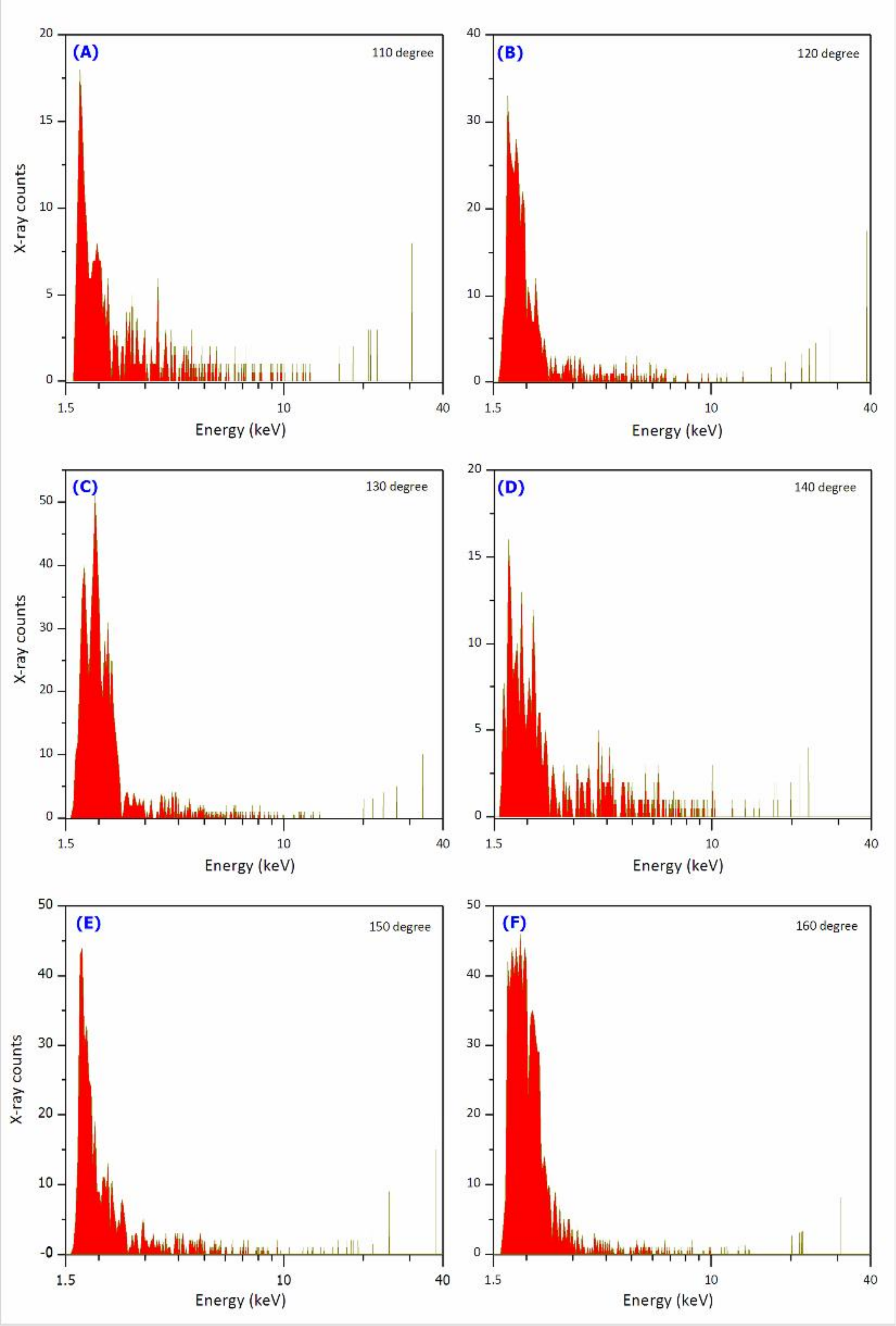

Figure 6.8: X-ray emission spectra obtained from the planar water jet for detection angles (A) 110°, (B) 120°, (C) 130°, (D) 140°, (E) 150°, and (F) 160°.

A polar diagram was plotted for the x-ray count obtained at different angles around the water jet with respect to the laser propagation direction (figure 6.9). The plot shown here is drawn by taking measurements for the 180 degrees on the right side of the beam and assuming the left side to be identical. We have confirmed this assumption by taking x-ray counts at a few corresponding points on the left side of the jet. Since the jet assembly and the liquid pump were obstructing the viewing angle on the left side, all corresponding points can not be measured but, only a few points could be taken.

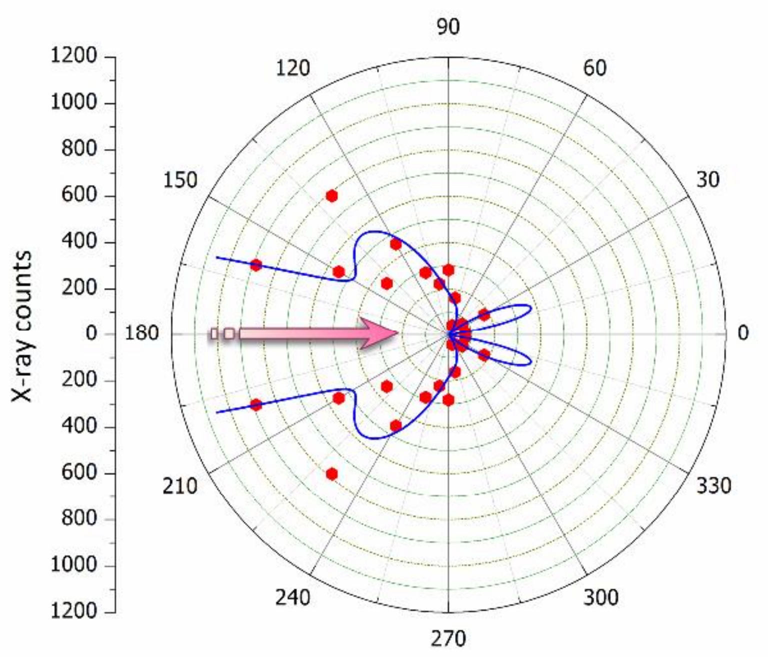

Figure 6.9: Angular distribution of x-ray emission from the laser-irradiated planar water jet. The arrow indicates the laser propagation direction. Solid line is an aid to the eye.

It can be seen that the x-rays from the water jet are preferentially emitted in the backward direction. This can be attributed to the reflection of the laser from the critical layer and the subsequent absorption of the same by the plasma already formed at the back surface of the jet by the leading part of the laser pulse.

6.8 X-ray emission from a silver nanoparticle colloidal jet

Enhancement in the x-ray emission from ultrafast laser-irradiated solids using surface modifications and by coating the surface with nanoparticles has been reported recently in literature {25,26}. To investigate this effect in the liquid phase we did x-ray emission measurements with a silver nanoparticle colloidal solution jet. Silver nanoparticles were prepared by the reduction of $AgNO_3$ by tri-sodium citrate (Details of the preparation method are given in chapter 2.). X-ray emission spectra obtained from these measurements at various angles around the liquid jet are given in figure 6.10 and figure 6.11.

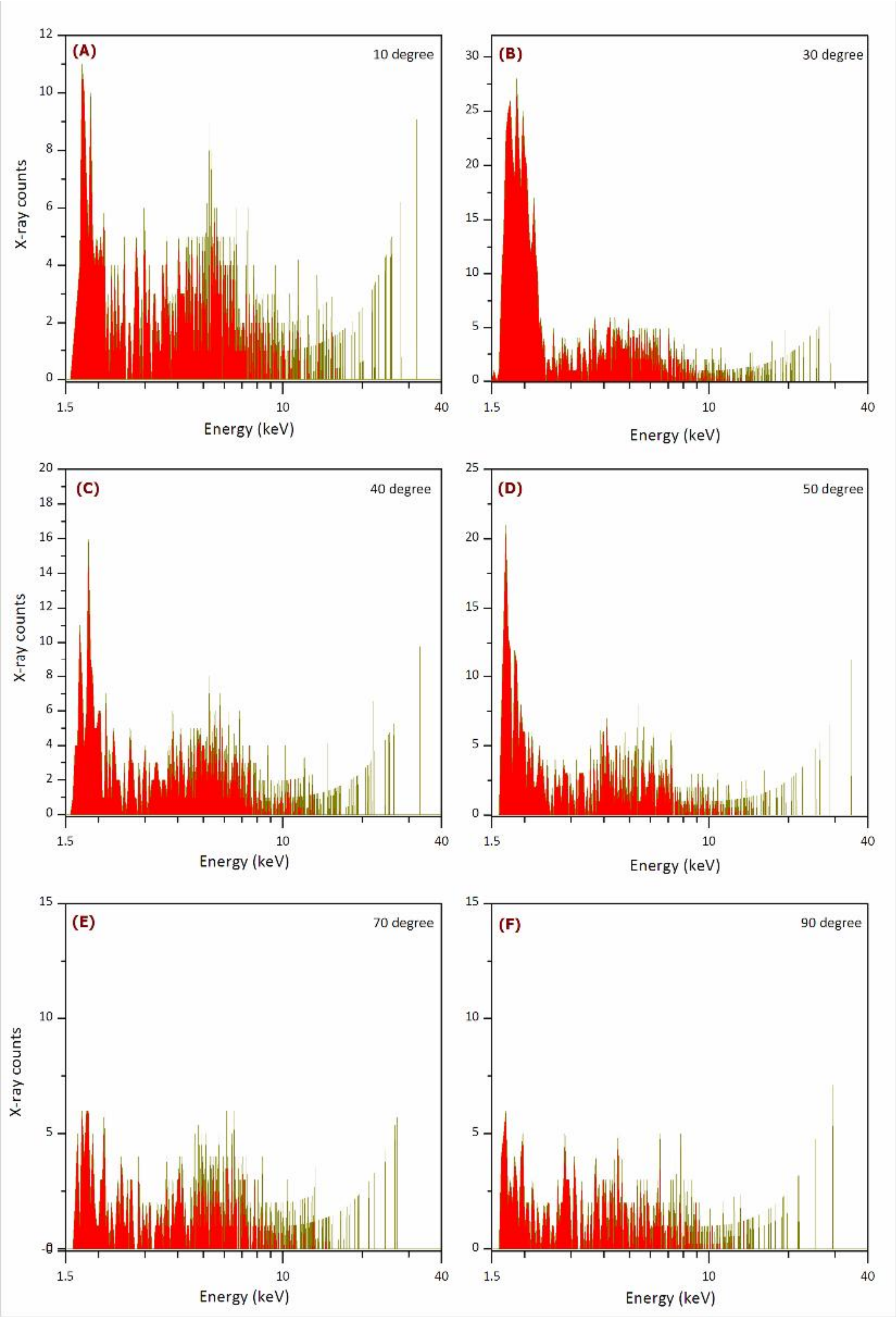

Figure 6.10: X-ray emission spectra obtained from a planar silver nanoparticle colloidal jet for detection angles (A) 10°, (B) 30°, (C) 40°, (D) 50°, (E) 70°, and (F) 90°.

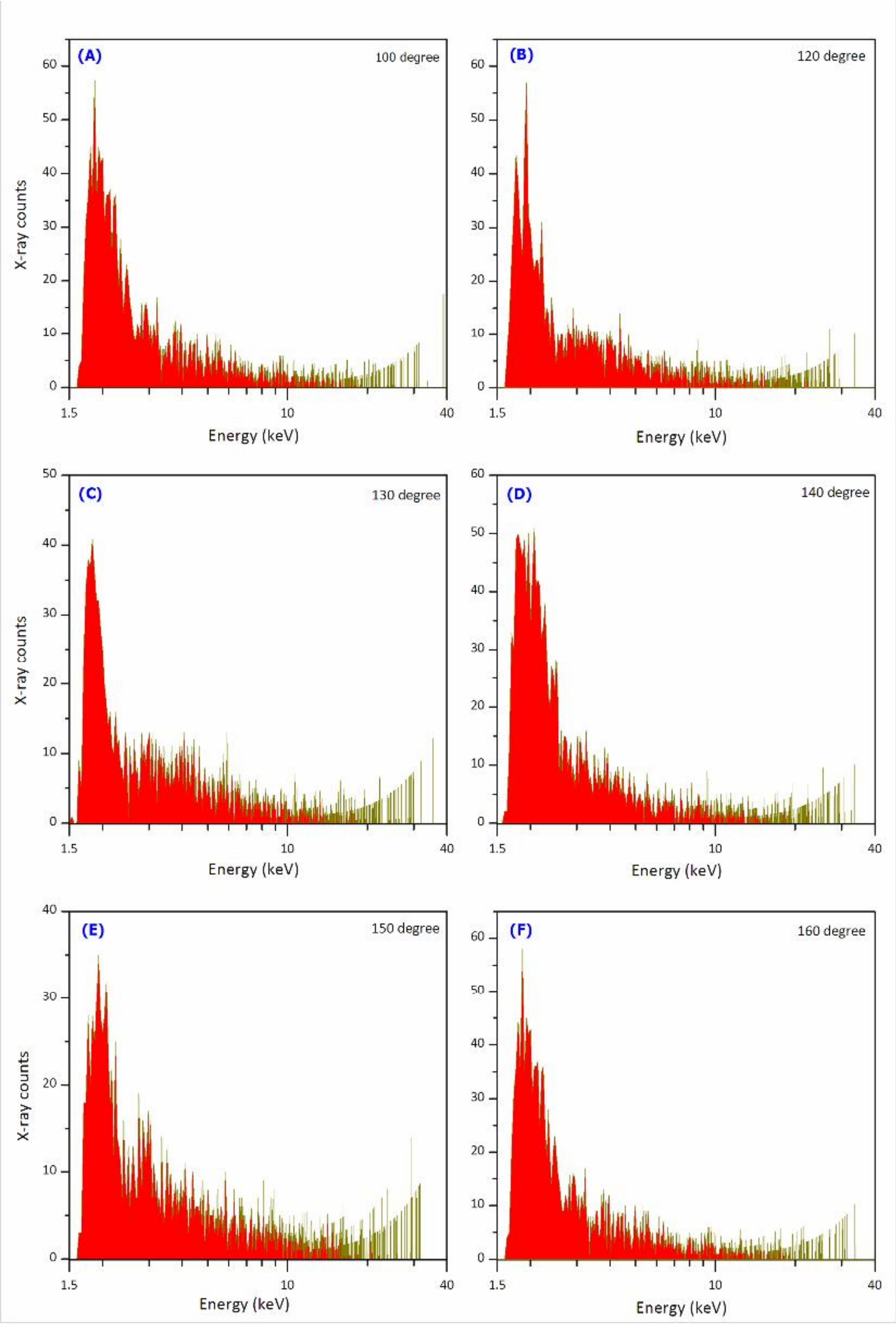

Figure 6.11: X-ray emission spectra obtained from a planar silver nanoparticle colloidal jet for detection angles (A) 100°, (B) 120°, (C) 130°, (D) 140°, (E) 150°, and (F) 160°.

Compared to the graphs obtained for water jets, it can be seen that now there is another peak around 5 keV in addition to the Bremsstrahlung emission centered around 1.8 keV seen in water. The emission counts also are quite large in this case, compared to the emission from the water jet. The polar diagram plotted for the x-ray count at different angles around the water jet with respect to the laser propagation direction is shown in figure 6.12.

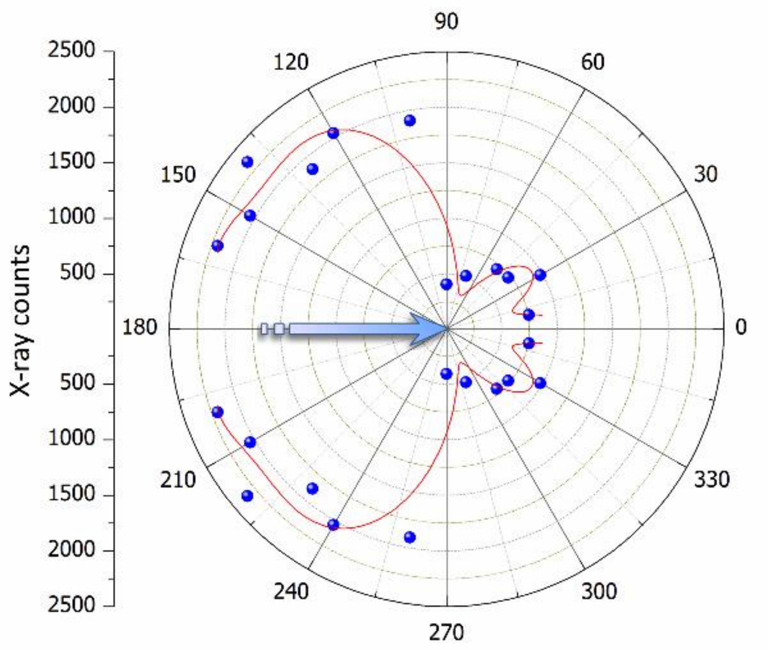

Figure 6.12: Spatial distribution of x-ray emission in the plasma produced from a planar jet of silver nanoparticle colloidal solution. The arrow indicates the laser propagation direction. Solid lines are drawn as an aid to the eye.

It can also be seen that the emission yield of x-rays from the silver nanoparticle colloid jet on average is about three times better than that from the water jet. The enhancement is as high as ten in the case of the front side emission. To investigate whether this enhancement comes from the silver and other ions present in the sample, we prepared a salt solution using all the ingredients used for the nanoparticle solution in the same amounts. The experiments were repeated on this silver nitrate + tri-sodium citrate salt solution and corresponding x-ray emissions were recorded.

6.9 X-ray emission from an $AgNO_3$ solution jet

The x-ray emission spectra obtained from the aqueous silver nitrate + tri-sodium citrate salt solution are given in figure 6.13. As can be seen from the x-ray spectra, there is only a slight enhancement in the x-ray emission yield, which is not sufficient to explain the significant enhancement seen in the silver nanoparticle colloidal solution.

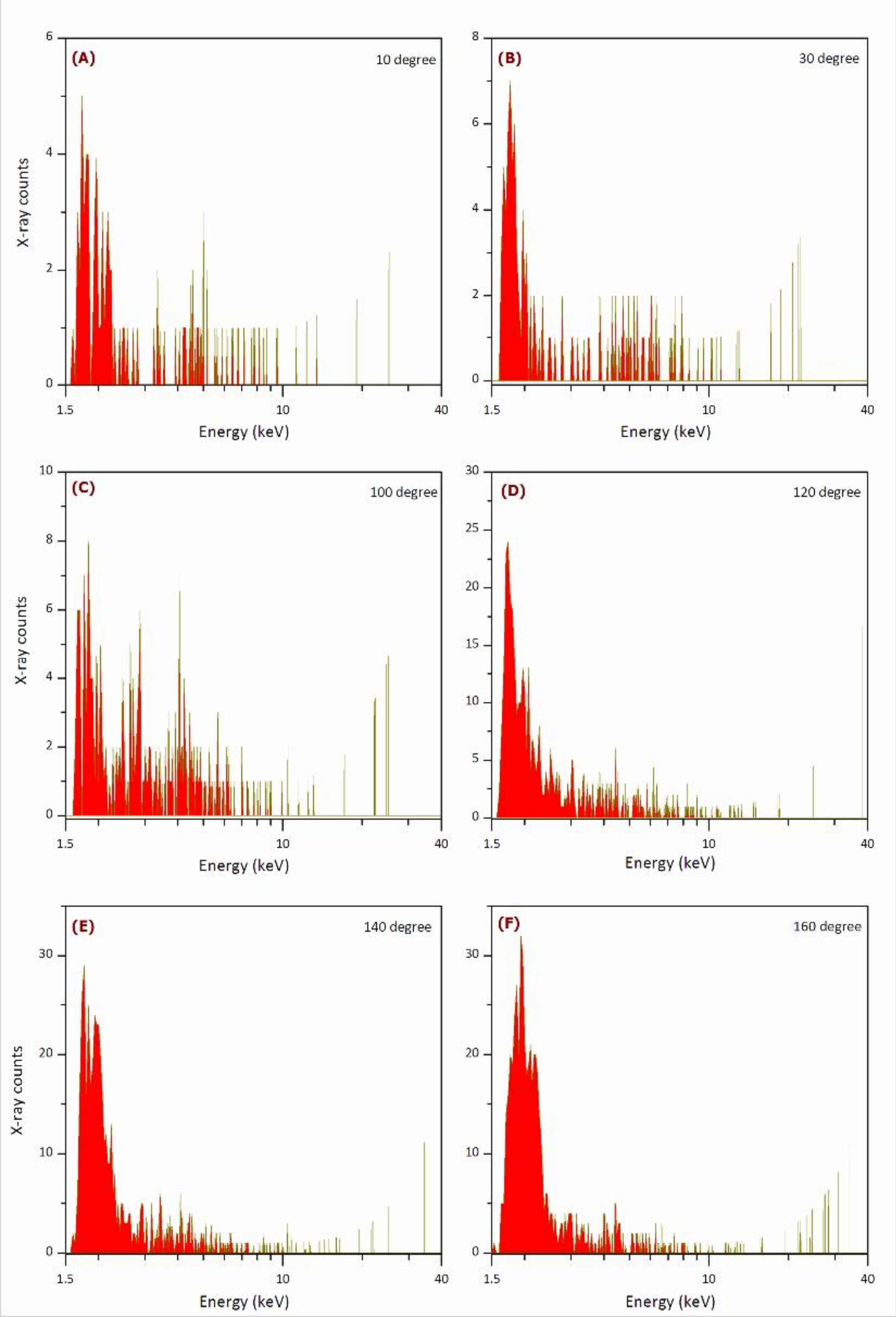

Figure 6.13: X-ray emission spectra obtained from a planar silver salt solution jet for detection angles (A) 10°, (B) 30°, (C) 100°, (D) 120°, (E) 140°, and (F) 160°.

6.10 Discussion

The fact that there is an enhancement of x-ray yield in the silver nanoparticle solution while there is almost none in the plain salt solution suggests that the metal nanoparticles are causing the enhancement. We consider a simple model to explain this as follows.

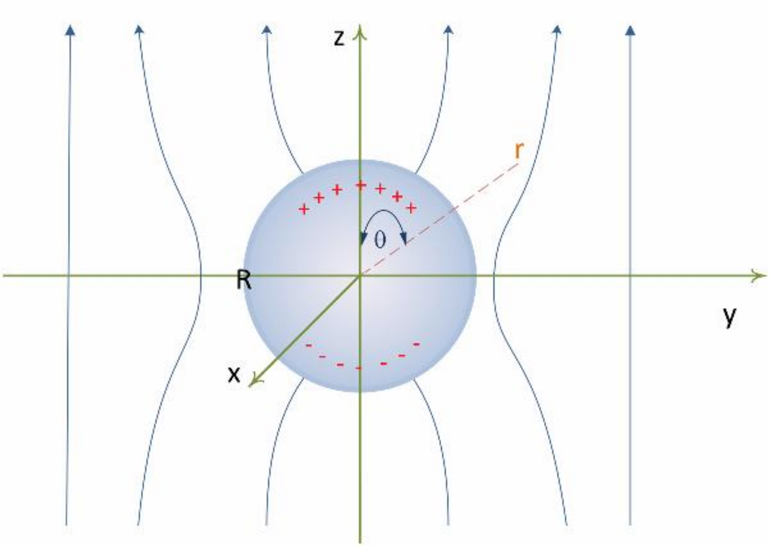

Figure 6.14: Field lines near a metallic sphere placed in an electric field.

Consider a metallic sphere placed in an electric field E$_0$. The potential *V* at a distance *r* from the centre of the sphere is given by (a simple derivation can be found in appendix II)

$$V(r,\theta)=-E_0\left(r-\frac{R^3}{r^2}\right)\cos\theta \qquad \text{- (6.13)}$$

where *R* is the radius of the sphere and θ is the angle between r and z- axis (i.e. external field vector). The electric field at the surface of the sphere can be calculated as

$$E_R=-\nabla V\,|_{r=R} \qquad \text{- (6.14)}$$

Hence from equation 6.13, we can write

$$E_R = 3E_0 \cos\theta \hat{r} \qquad - (6.15)$$

From equation 6.15 it can be seen that the local field on the metallic surfaces can have larger values than the incident field. This increase in local field intensity near the metallic nanostructure causes an increased emission from the silver nanoparticle solution sample. A similar effect with surface modified solid samples has been reported earlier in literature {24}.

6.11 Conclusions

Experiments conducted in thin planar liquid jets in ambient condition show that even in the absence of a vacuum, a substantial amount of soft x-rays can be obtained from an ultrafast laser induced plasma. It is shown that the x-ray emission range and emission yield can be enhanced by adding metal nanoparticles into a clear liquid. This enhancement is explained in terms of the increase of local electric field in the vicinity of metal spheres embedded in a dielectric medium.

References

1. *Progress in Ultrafast Intense Laser Science: volume 2,* K. Yamanouchi, S. L. Chin, and P. Agostini (Eds.), Springer-Verlag, Berlin, Heidelberg (2007).
2. *Applications of Laser-Plasma Interactions*, S. Eliezer and K. Mima, CRC press, Boca Raton, FL (2009).
3. *Ultrafast dynamics in a live cell irradiated by femtosecond laser pulses,* K. Hiroyuki, H. Chikako, G. Takeharu, and M. Atsushi, Proceedings of SPIE, the International Society for Optical Engineering, **6633**, 66330J.1-66330J.9 (2007).
4. *Hard x-ray production from high intensity laser solid interactions*, D. Perry, J. A. Sefcik, T. Cowan, S. Hatchett, A. Hunt, M. Moran, D. Pennington, R. Snavely, and S. C. Wilks, Rev. Sci. Instrum., **70**, 265 (1999).
5. *High-energy Kα radiography using high intensity, short pulse lasers,* H.S. Park, D.M. Chambers, H.K. Chung, R. J. Clarke, R. Eagleton, E. Giraldez, T. Goldsack,R. Heathcote, N. Izumi, M. H. Key, J. A. King, J. A. Koch, O. L. Landen, A. Nikroo, P. K. Patel, D. F. Price, B. A. Remington, H. F. Robey, R. A. Snavely, D. A. Steinman, R. B. Stephens, C. Stoeckl, M. Storm, M. Tabak, W. Theobald, R. P. J. Town, J. E. Wickersham, and B. B. Zhang , Phys. Plasmas, **13**, 056309 (2006).
6. *Strong Field Laser Physics*, T. Brabec, Springer, NY (2008).
7. *Laser-Plasma Interactions*, D. A. Jaroszynski, R. Bingham, and R. A. Cairns, CRC press, Boca Raton, FL (2009).
8. *Astrophysical Plasmas and Fluids*, V. Krishnan, Kluwer Academic, Dordrecht, The Netherlands (1999).
9. *High-frequency conductivity and the emission and absorption coefficients of a fully ionized plasma*, J. Dawson and C. Oberman, Phys. Fluids, **5**, 517 (1962).
10. *Correct values for high frequency power absorption by inverse bremsstrahlung in plasmas*, T. W. Johnston and J. M. Dawson, Phys. Fluids, **16**, 722 (1973).
11. *Soft x-rays and Extreme Ultraviolet Radiation*, D. Attwood, Cambridge University Press, UK (1999).
12. *The physics of Laser Plasma Interactions*, W. L. Kruer, Addison-Weasley, Redwood City, California (1988).
13. *Physics of Fully Ionized Gases,* L. Spitzer, Wiley (1956).
14. *"Coulomb logarithm" for inverse-bremsstrahlung laser absorption*, S. Skupsky, Phys. Rev. A, **36**, 5701 (1987).

15. *Skin effect and interaction of short laser pulses with dense plasmas,* W. Rozmus and V. T. Tikhonchuk, Phys. Rev. A, **42**, 7401 (1990).

16. *Inverse bremsstrahlung in strong radiation fields at low temperatures*, G. J. Pert, Phys. Rev. E, **51**, 4778 (1995).

17. *Reflectivity of steep-gradient plasmas in intense subpicosecond laser pulses*, S. C. Rae and K. Burnett, Phys. Rev. A, **44**, 3835 (1991).

18. *Nonlinear inverse bremsstrahlung in solid-density plasmas*, S. Kato, R. Kawakami, and K. Mima, Phys. Rev. A, **43**, 5560 (1991).

19. *Not-so-resonant, resonant absorption*, F. Brunel, Phys. Rev. Lett., **59**, 52 (1987).

20. *Experimental identification of "vacuum heating" at femtosecond-laser-irradiated metal surfaces*, M. K. Grimes, A. R. Rundquist, Y. S. Lee, and M. C. Downer, Phys. Rev. Lett., **82**, 4010 (1999).

21. *Efficient Kα x-ray source from femtosecond laser-produced plasmas,* A. Rousse, P. Audebert, J. P. Geindre, F. Falliès, and J. C. Gauthier, Phys. Rev. E, **50**, 2200 (1994).

22. *X-ray production ~13 nm from laser-produced plasma for projection x-ray lithography application*, R. L. Kauffman, D. W. Phillion, and R. C. Spitzer, Appl. Opt. **32**, 6897 (1993).

23. *Unresolved transition arrays*, J. Bauche, C. Bauche-Arnoult, and M. Klapish, Phys. Scr., **37**, 659 (1988).

24. *A first-order model for computation of laser-induced breakdown thresholds in ocular and aqueous media I Theory*, P. K. Kennedy, IEEE J. Q. Electron., **31,** 2250 (1995).

25. *Metal nanoplasmas as bright sources of hard x-ray pulses*, P. P. Rajeev, P. Taneja, P. Ayyub, A. S. Sandhu, and G. Ravindra Kumar, Phys. Rev. Lett., **90**, 115002 (2003).

7

X-ray emission from ultrafast laser induced plasma in a Nickel target

In this chapter we present x-ray emission measurements from an intense laser-solid target interaction. Nickel targets are irradiated at intensity levels of 10^{15} W/cm^2 in an ambient vacuum of 10^{-6} Torr. From the x-ray spectrum obtained, the hot electron temperature is calculated.

7.1 Introduction

In chapter 6 we have discussed the mechanisms of x-ray emission from ultrafast laser induced plasmas in solid density materials. In this chapter we present the results obtained from the interaction of an ultrafast laser pulse with a Nickel target in an ambient vacuum of 10^{-6} Torr.

7.1.1: Bremsstrahlung emission

When a fast electron is decelerated in the Coulomb potential of an ion a continuum emission takes place, which is known as the bremsstrahlung emission {1}. If the electron had an initial velocity v and the impact parameter is b, the interaction time is $\tau = 2b/v$. The radiated spectrum is dominated by the corresponding frequency, $\gamma \approx v/4\pi b$. On the basis of maximum acceleration during a single electron-ion impact, the energy radiated can be written as {2}

$$\Delta E = \frac{4}{3}\frac{Z^2 e^6}{m^2 c^3 b^3 v} \qquad \text{- (7.1)}$$

This expression can be integrated over a range of parameters to account for many electron-ion collisions per unit time. The number of electron-ion collisions per unit time, with an ion density n_i, with an impact parameter ranging from b to $b+db$, is $2\pi n_i v b db$. This yields the power radiated per electron as

$$w = \frac{4}{3}\frac{Z^2 e^6}{m^2 c^3} 2\pi n_i \int_{b_{\min}}^{b_{\max}} \frac{db}{b^2} \qquad \text{- (7.2)}$$

where the maximum impact parameter possible $b_{\max}$ is the Debye length and the minimum value $b_{\min}$ is given by the de Broglie wavelength. To evaluate the spectral distribution of bremmstrahlung emission, equation 7.2 can be written in terms of frequency and integrated as

$$w = \frac{4}{3}\frac{Z^2 e^6}{m^2 c^3}\frac{8\pi^2 n_i}{v}\int_{\gamma_{\min}}^{\gamma_{\max}} d\gamma \approx \frac{4}{3}\frac{Z^2 e^6}{m^2 c^3}\frac{8\pi^2 n_i}{v}\gamma_{\max} \qquad \text{- (7.3)}$$

It is assumed that $\gamma_{\max} \gg \gamma_{\min}$ since $b_{\max} \gg b_{\min}$ and $\gamma = mv^2/2h$, the frequency corresponding to the de Broglie wavelength. Now, considering a Maxwellian distribution of electron velocities

$$f_e = n_e\left(\frac{m}{2\pi k_B T_e}\right)^{3/2}\exp\left(-\frac{mv^2}{2k_B T_e}\right), \qquad \text{- (7.4)}$$

the bremsstrahlung spectral intensity can be obtained as,

$$W_B^{\nu} = \frac{1}{\sqrt{3}}\int_{2h\gamma/m}^{\infty} A f_e 4\pi v^2 dv = \frac{32\pi}{3}\left(\frac{2\pi}{3k_B T_e m}\right)^{1/2}\frac{Z^2 n_e^2 e^6}{m^2 c^3}\exp\left(-\frac{hc}{\lambda k_B T_e}\right) \qquad \text{- (7.5)}$$

Thus it is possible to obtain the energy-resolved bremsstrahlung spectrum if the temperature of the electron distribution is known.

7.1.2 Hard x-ray bremsstrahlung as signature of hot electrons

It has been shown before that the hot electrons generated in the laser plasma radiate via bremsstrahlung {3}. Since the electrons are heated to extreme energies (tens and hundreds of keV) the radiation emitted also is of similar energy. This radiation falls in the hard x-ray regime of electromagnetic spectrum. Studying the hard x-ray bremsstrahlung, therefore, provides important information about the hot electrons that generate the radiation, and their distribution in the plasma.

Hard x-ray bremsstrahlung is used as a diagnosis for the behavior of hot electrons. In particular, the temperature of different hot electron distributions can be inferred from the x-ray emission. Distributions with different temperatures are usually the products of different absorption and acceleration mechanisms discussed before. By following the scaling laws of hot electrons one can identify the mechanisms prevailing in the parameter space of the laser-matter interaction.

From equation 7.5, a bremsstrahlung spectrum caused by hot electron distribution of temperature T_e can be written as

$$N(E) \propto \frac{1}{T_e^{1/2}} \exp\left(-\frac{E}{kT_e}\right) \qquad \text{- (7.6)}$$

where E is the energy of the photon emitted. By fitting this function to an experimentally obtained energy-resolved bremsstrahlung spectrum, the temperature T_e of the hot electron distribution can be obtained. As $T_e^{-1/2}$ is a relatively slowly varying function with respect to the exponential term, a mere exponential fit yields the temperature, without much error {4}.

7.2 Experimental

We used 100 fs laser pulses from the Ti:Sapphire CPA laser, focused using a 60 cm plano-convex lens to the target inside the vacuum chamber. A pulse energy of 10 mJ was used which resulted in peak intensities of about 10^{15} W/cm^2. The experimental setup is described in detail in chapter 5. The target manipulator and controller were configured such that there was sufficient separation (~ 200 μm) between adjacent laser spots on the target. This ensures that the laser sees a fresh spot at each shot.

A calibrated NaI(Tl) detector was used to collect the spectra. The detector and calibration details can be found in chapter 5. The BK7 windows of the chamber set a low energy cutoff of around 15 keV. The detector was kept at a distance of about 75 cm from the target. In the present experiment, x-rays in the range of 30 to 200 keV are measured. The cosmic ray background noise was reduced by using appropriate time gating. We used an unpolished Nickel target (99.95 % purity, ACI Alloys) of 5 cm x 5 cm size for the measurements. The bremsstrahlung emission measured in the 30 keV - 200 keV region is shown in figure 7.1. The laser was *p*-polarized and was incident on the sample at an angle of 45 degrees. The spectrum was collected over 5000 laser shots.

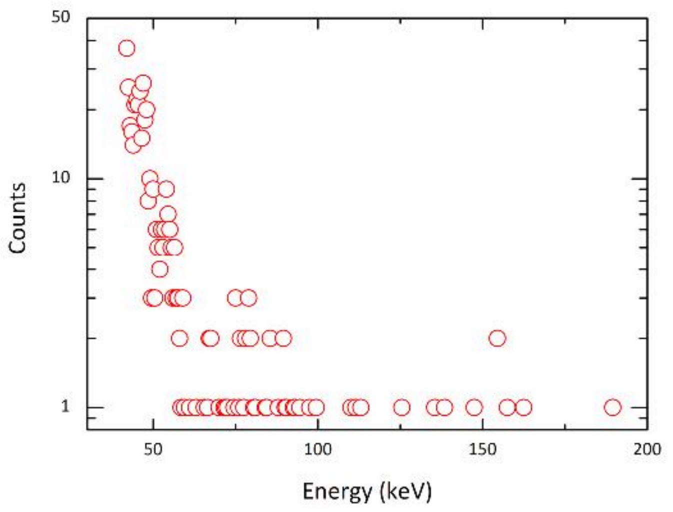

Figure 7.1: Bremsstrahlung emission from an unpolished nickel target kept at a 10^{-6} Torr vacuum irradiated with 100 femtosecond pulses at an intensity of 10^{15} W/cm^2.

The hot electron temperature can be calculated from this data by fitting an exponential to the emission spectrum using equation 7.6. The value of the hot electron temperature thus obtained is 5 ± 1 keV. The fitted curve is given in figure 7.2.

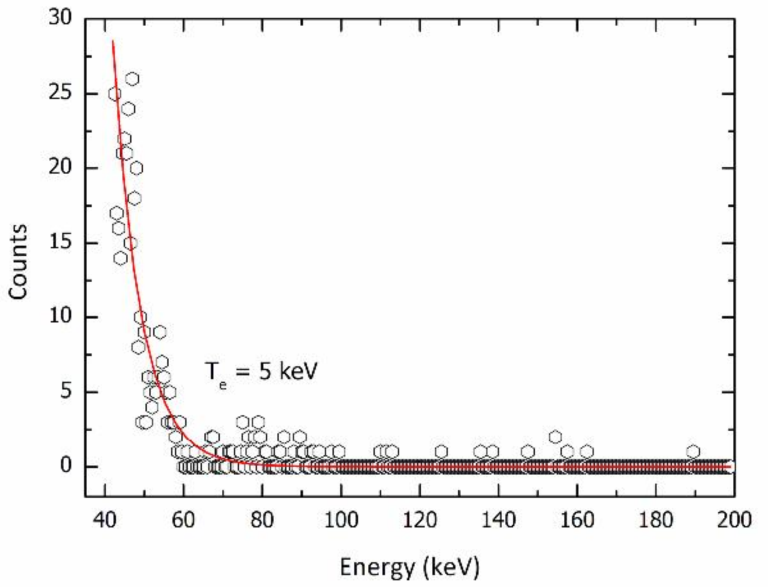

Figure 7.2: Bremsstrahlung emission from the unpolished nickel target, fitted to an exponential decay using equation 7.6.

7.3 Conclusions

We have measured the x-ray emission from an ultrafast laser induced plasma in a Nickel target. The unpolished target is moved between successive laser shots using a target manipulator and controller, so that the plasma is generated from a fresh surface every time. The hot electron temperature calculated from the bremsstrahlung emission spectrum is 5 ± 1 keV.

References

1. *Principles of Plasma Diagnostics*, I. H. Hutchinson, Cambridge University Press, Cambridge, UK (1987).
2. *X-ray emission from laser produced plasmas*, D. Giulietti, and L. A. Gizzi, La Rivista del Nuovo Cimento, **21**, 10 (1998).
3. *X-Rays from Laser Plasmas: Generation and Applications*, I. C. E. Turcu, J. B. Dance, John Wiley & Sons, NY (1999).
4. *On the distribution of hot electrons produced in short-pulse laser-plasma interaction*, M. Schnürer, R. Nolte, T. Schlegel, M. P. Kalachnikov, P. V. Nickels, P. Ambrosi, and W. Sandner, J. Phys. B: At. Mol. Opt. Phys. **30**, 4653 (1997).

8

Conclusions and visions

This thesis contains studies of the optical behavior of condensed and nanostructured media in the strong and intense laser-matter interaction regimes. Various instrumentation works carried out in the course of these experiments also are presented.

Nonlinear transmission measurements in core-shell silver nanocomposites show that they possess excellent optical limiting properties. The sample used is in thin film form, making it useful for device applications. Measurements show that the sample performs well at different wavelengths and laser pulsewidths, so that its action is truly broadband. The femtosecond response times indicate its suitability for photonic switching applications. The laser damage threshold value of this material is one of the best reported so far.

Similar studies in tellurium and silver telluride nanowires have revealed their potential as broadband optical limiters. The fact that silver telluride is a semiconducting material makes it more interesting from a hybrid device point of view.

A simple and elegant method to visually determine the sign of refractive nonlinearities in thin nonlinear samples, based on spatial self-phase modulation patterns, is devised and experimentally verified. Theoretical simulations and experimental results are found to agree well with each other.

A white-light continuum generated using femtosecond laser pulses is used for performing a nondegenerate z-scan experiment, where the spectral dispersion of the optical nonlinearity in a 200 nm wavelength range is measured in a single experiment. The white-light z-scan is a fast and cheap alternative to the use of a tunable optical parametric amplifier (OPA) in a conventional z-scan configuration.

The necessary experimental platform for intense laser-solid interaction studies in a vacuum environment is completed, which will have long term use in the laboratory. The required electronic circuits are designed and fabricated, and softwares developed. X-ray and γ-ray detectors are calibrated and detection schemes perfected. An experimental scheme for x-ray emission studies from irradiated liquid jets in ambient pressures is also realized.

The plasma emission measured from ultrafast laser irradiated planar liquid jets shows them to be good sources of soft x-rays. A scheme is devised to enhance the x-ray emission yield by adding metallic nanostructures to clear liquids. X-ray emission from an irradiated Nickel target under an ambient pressure of 10^{-6} Torr is measured, and the hot electron temperature is calculated from the bremsstrahlung emission spectrum.

The above studies which comprise this thesis are by no means exhaustive. A more detailed study of the optical nonlinearity in metal nanostructures, involving time resolved measurements, will give better insights into the electron dynamics of the media. Similarly, devising ways to improve the S/N ratio of white-light z-scan measurements will be rewarding, in view of the advantages this non-degenerate z-scan technique offers over conventional single wavelength configurations. For instance, by using crystals like barium fluoride or calcium fluoride instead of water the white-light emission yield can be enhanced, and the S/N ratio can be improved.

The results obtained from the plasma studies are very promising. Laser produced plasmas are rich sources of electromagnetic radiation, energetic ions and free electrons. More research on improving the x-ray and ion emission yields in a laser produced plasma will be of immense interest, from the viewpoints of a tabletop x-ray source and tabletop accelerator. There may be enhancements in the ion and electron yields as well, in addition to the x-ray yield, by the incorporation of metallic nanostructures into a plasma target. Metal nanostructures with sharper features which enhance the local fields even more, and with surface plasmon resonance peaks closer to the excitation wavelengths, shall be interesting materials for plasma studies. Finally, extension of plasma investigations to ion and electron spectroscopy in future will be a fitting complement to the x-ray emission studies presented in this thesis.

Appendix I

5A Regulated, Variable Power Supply

An 18V step-down transformer is used to step-down the mains. The ac output from the transformer is rectified using four 6A diodes which are in bridged configuration. The rectified output is filtered using two 2200 μF electrolytic capacitors which is then fed to an adjustable voltage regulator, IC LM 338. LM 338 is a 3-terminal positive voltage regulator capable of supplying 5A over an output range of 1.2 V to 32 V. The output from the designed power supply can be varied between 6 V to 18 V using a suitable potentiometer. A 9 V taping from another winding on the same the step-down transformer is rectified using a bridge rectifier pack and fed to a 7805 voltage regulator. The output from this fixed voltage regulator IC supplies the 5V dc required for the digital gates present in the circuit. The circuit diagram of the power supply is given below.

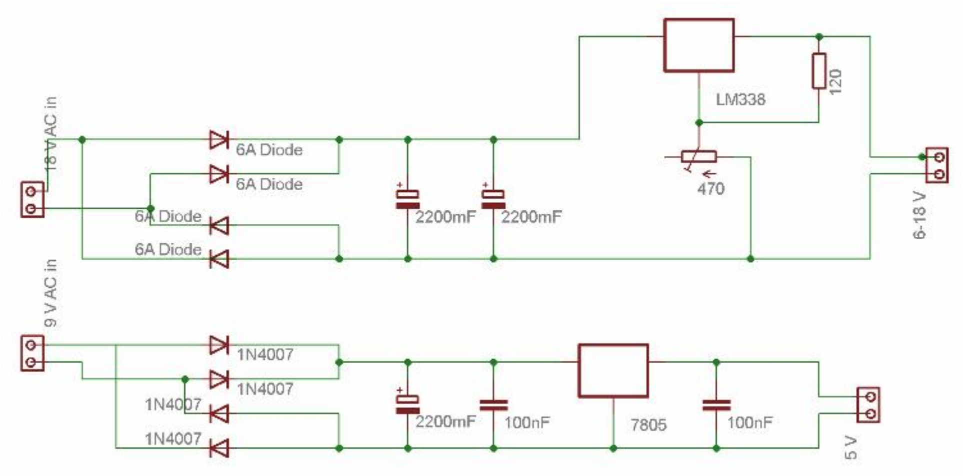

5A, variable regulated power supply.

Appendix II

Electric Field on the surface of a Metallic Sphere Placed in a Uniform Electric field

When a metallic sphere is placed in an external electric field, charges will be induced on the surface of the sphere. These induced charges produce their own fields, which cancel the field inside the metallic sphere. The potential of the sphere can be taken as zero since it is an equi-potential surface. Then by symmetry the entire xy-plane is at potential zero. But here V does not go to zero at large z. In fact, far from the sphere the field is $E_0\hat{k}$, and hence

$$V \to -E_0 z + C \qquad \text{- (1)}$$

Since V = 0 in the equatorial plane, the constant C must be zero. Accordingly, the boundary conditions for this problem are

(i) $V = 0$ when $r = R$

(ii) $V \to -E_0 r\cos\theta$ for $r >> R$

We must fit these boundary conditions with a function of the form,

$$V(r,\theta) = \sum_{l=0}^{\infty}\left(A_l r^l + \frac{B_l}{r^{l+1}}\right)P_l(\cos\theta) \qquad \text{- (2)}$$

where $P_l(\cos\theta)$ is defined by the Legendre polynomials {1}.

The first condition yields

$$A_l R^l + \frac{B_l}{R^{l+1}} = 0 \qquad \text{- (3)}$$

or

$$B_l = -A_l R^{2l+1} \qquad \text{- (4)}$$

so that

$$V(r,\theta)=\sum_{l=0}^{\infty}A_l\left(r^l-\frac{R^{2l+1}}{r^{l+1}}\right)P_l(\cos\theta) \qquad - (5)$$

For r >> R, the second term in parentheses is negligible, and therefore condition (ii) requires that

$$\sum_{l=0}^{\infty}A_l r^l P_l(\cos\theta)=-E_0 r\cos\theta \qquad -$$

(6)

Evidently only one term occurs: l=1. In fact, since $P_1(\cos\theta)=\cos\theta$, we can read off immediately, $A_l=-E_0$, all other A_l's zero.

Using these potential can be deduced as

$$V(r,\theta)=-E_0\left(r-\frac{R^3}{r^2}\right)\cos\theta \qquad - (7)$$

The first term $(-E_0 r\cos\theta)$ is due to the external field; the contribution attributable to the induced charge is evidently $E_0\frac{R^3}{r^2}\cos\theta$.

The electric field on the surface of the sphere can be calculated by taking the gradient of equation (7).i.e. $E_R=-\nabla V\,|_{r=R}$

$$E_R=3E_0\cos\theta\hat{r} \qquad - (8)$$

References

1. *Introduction to Electrodynamics*, D. J. Griffiths, Second Edition, Prentice-Hall of India Private Limited, New Delhi (1997).